UNIVERSITY OF CALIFORNIA
IRVINE

Acoustic transmission loss of perforated plates with bias flow

DISSERTATION

Submitted in partial satisfaction of the requirements

for the degree of

DOCTOR OF PHILOSOPHY

in Mechanical and Aerospace Engineering

by

Vincent Choy Phong

Dissertation Committee:
Professor Dimitri Papamoschou, Chair
Professor Feng Liu
Professor John LaRue

2014

Dedicated to my parents.

TABLE OF CONTENTS

Page

LIST OF FIGURES **v**

LIST OF TABLES **xvi**

NOMENCLATURE **xvii**

ABSTRACT OF THE DISSERTATION **xxiii**

CHAPTER 1: INTRODUCTION **1**

1.1 Motivation 1

1.2 Research objective 3

1.3 Outline 4

CHAPTER 2: LITERATURE REVIEW **6**

2.1 Fundamental Principles 6

2.1.1 Acoustical performance criteria 7

2.1.2 Acoustic impedance and Rayleigh conductivity 9

2.1.3 End effects 10

2.1.4 *Vena contracta* 11

2.1.5 Acoustic dissipation 13

2.1.6 Nonlinear effects 15

2.2 Previous theoretical developments 15

2.2.1 Transmission loss models without bias flow 15

2.2.2 Transmission loss models with bias flow 19

CHAPTER 3: CURRENT THEORETICAL MODEL **28**

3.1 Governing equations 28

3.2 Static model 30

3.3 Bias flow model 35

CHAPTER 4: EXPERIMENTAL DETAILS **51**
4.1 Perforations 51
4.2 Experiment setup 51
4.2.1 Static insertion loss experiment setup 51
4.2.2 Bias flow insertion loss experiment setup 52
4.3 Acoustic data processing 57

CHAPTER 5: RESULTS **70**
5.1 Static results 70
5.1.1 Robustness of setup 70
5.1.2 Microphone correlations 71
5.1.3 Insertion loss measurements 73
5.1.4 Comparison with previous models 74
5.1.5 Error analysis 76
5.2 Bias flow results 78
5.2.1 Robustness of setup 78
5.2.2 Signal to noise ratio 81
5.2.3 Microphone correlations 82
5.2.4 Insertion loss measurements 85
5.2.5 Comparison with previous models 86
5.2.6 Error analysis 90

CHAPTER 6: CONCLUSION **154**
6.1 Summary 154
6.2 Recommendations for future work 157

BIBLIOGRAPHY **159**

APPENDIX A: NON-ISENTROPIC DENSITY FLUCTUATIONS **166**

APPENDIX B: PITOT PRESSURE PROFILES **167**

LIST OF FIGURES

Page

Figure 1.1 Cutaway view of Rolls Royce Trent 1000 jet engine with location of intermediated and high pressure bleed valves indicated. 4

Figure 1.2 Schematic of pneumatic bleed valve assembly used on aircraft engines [2] 5

Figure 1.3 Muffler attachment to bleed valve outlet [3]. 5

Figure 2.1 Perforated plate with bias flow, indicating directions of the mean flow and pressure fluctuations. 25

Figure 2.2 Cutaway view of two holes showing the attached mass distributions associated with each hole and the interaction region between both holes [50] 26

Figure 2.3 Schematic of streamlines in a duct containing a single Contraction. Blue dashed line indicates the separation streamlines. 26

Figure 2.4 Aperture in an infinite plane with bias flow jet. Unsteady, axisymmetric vorticity is assumed to shed from the rim, convecting at a velocity U_c that is parallel to the x-axis and within the mean flow shear layer [33]. 27

Figure 3.1 Contraction chamber used for one-dimensional modeling of transmission for static case [58]. 46

Figure 3.2 End correction showing actual and idealized attached mass distribution with associated length corrections [50] 46

Figure 3.3 Contraction chamber used for modeling perforated plate acoustics **(a)** with contraction area corresponding to perforation diameter; **(b)** with contraction area corresponding to *vena contracta* area. 47
Figure 3.4 Control volume that contains the mixing region downstream of the duct expansion. 48
Figure 3.5 Correlation parameter K relating perforated plate discharge coefficient with P/d , l/d and Reynolds number [25]. 48
Figure 3.6 Perforation hole geometry: **(a)** rectilinear (square) array and; **(b)** staggered (triangular) array 49
Figure 3.7 Bias flow correction to idealized mass distribution. 49
Figure 3.8 Free jet profile for varying orifice to duct area ratio $0 < \beta < 0.5$ [57]. 50
Figure 4.1 Perforated plates used for bias flow experiments. 64
Figure 4.2 Static insertion loss experiment setup within UCI anechoic facility **(a)** represented schematically; **(b)** showing the position of the anechoic box with respect to impinging jets source. 65
Figure 4.3 Anechoic box **(a)** schematic detailing the setup of microphones in the box and relevant dimensions; **(b)** with perforated plate attached, shown in the UCI anechoic facility. 65
Figure 4.4 Bias flow insertion loss facility **(a)** schematic; **(b)** setup 66
Figure 4.5 Sample mounting plate with perforate plate (Plate 11) attached 67
Figure 4.6 Schematic detailing the setup of the microphones used in the measurement section of the BFIL facility. 67
Figure 4.7 **(a)** Microphone arm assembly with G.R.A.S. RA0173 nosecone attached to B&K 4138 microphone; **(b)** G.R.A.S. RA0173 nosecone adaptor for 3.2-mm microphone 68

Figure 4.8 Schematic detailing the pitot and static port positions relative to the perforated plate. 68

Figure 4.9 Cross section of the duct measurement section **(a)** Schematic of the measurement plane, indicating 19 points of measurement; **(b)** actual setup at measurement location $n = 1$; **(c)** setup for microphone correlation measurements with microphones at positions $n = 4$ and $n = 16$. 69

Figure 5.1 Comparison of SPL spectra between perforated plate and solid plate of equal thickness. 94

Figure 5.2 Comparison of SPL spectra between microphones in SIL **(a)** baseline; **(b)** Plate 1; **(c)** Plate 6; **(d)** Plate 11. 95

Figure 5.3 Microphone cross correlation in SIL setup, comparisons between open and **(a)** Plate 1; **(b)** Plate 2; **(c)** Plate 3; **(d)** Plate 4; **(e)** Plate 5; **(f)** Plate 6; **(g)** Plate 7; **(h)** Plate 8; **(i)** Plate 9; **(j)** Plate 10; **(k)** Plate 11. 96

Figure 5.4 Microphone coherence in SIL setup, comparisons between open and **(a)** Plate 1; **(b)** Plate 2; **(c)** Plate 3; **(d)** Plate 4; **(e)** Plate 5; **(f)** Plate 6; **(g)** Plate 7; **(h)** Plate 8; **(i)** Plate 9; **(j)** Plate 10; **(k)** Plate 11. 98

Figure 5.5 Insertion loss versus frequency comparison between **(a)** experiment and **(b)** current static model (Equation 3.23). 100

Figure 5.6 Comparisons of the range of **(a)** d/λ, **(b)** l/λ, and **(c)** β covered in the current and previous work. The ranges of d/λ, l/λ, and β are determined based on the range of experimental validation provided for the respective work. 101

Figure 5.7 Comparison of transmission loss between experiment, current static theoretical model Equation (2.39), and previous models [18,19,21] for **(a)** Plate 1; **(b)** Plate 2; **(c)** Plate 3; **(d)** Plate 4; **(e)** Plate 5; **(f)** Plate 6; **(g)** Plate 7; **(h)** Plate 8; **(i)** Plate 9; **(j)** Plate 10; **(k)** Plate 11. 102

Figure 5.8 Insertion loss error versus d/λ. 104

Figure 5.9 Transmission loss error versus **(a)** thickness scaled by hole diameter; **(b)** porosity. 104

Figure 5.10 Comparing insertion loss measurements between SIL and BFIL facilities **(a)** Plate 1; **(b)** Plate 2; **(d)** Plate 6; **(d)** Plate 11 105

Figure 5.11 SPL spectral comparisons between varying source and flow combinations 1-4. Measurements shown for Plate 1 at upstream Mach number. **(a)** $M_1 = 0.02$; **(b)** $M_1 = 0.04$; **(c)** $M_1 = 0.06$; **(d)** $M_1 = 0.08$; **(e)** $M_1 = 0.1$. 106

Figure 5.12 SPL spectral comparisons between varying source and flow combinations 1-4. Measurements shown for Plate 2 at upstream Mach number. **(a)** $M_1 = 0.02$; **(b)** $M_1 = 0.04$; **(c)** $M_1 = 0.06$; **(d)** $M_1 = 0.08$; **(e)** $M_1 = 0.1$. 107

Figure 5.13 SPL spectral comparisons between varying source and flow combinations 1-4. Measurements shown for Plate 3 at upstream Mach number. **(a)** $M_1 = 0.02$; **(b)** $M_1 = 0.04$; **(c)** $M_1 = 0.06$; **(d)** $M_1 = 0.08$; **(e)** $M_1 = 0.1$. 108

Figure 5.14 SPL spectral comparisons between varying source and flow combinations 1-4. Measurements shown for Plate 4 at upstream Mach number. **(a)** $M_1 = 0.02$; **(b)** $M_1 = 0.04$; **(c)** $M_1 = 0.06$; **(d)** $M_1 = 0.08$; **(e)** $M_1 = 0.1$. 109

Figure 5.15 SPL spectral comparisons between varying source and flow combinations 1-4. Measurements shown for Plate 5 at upstream Mach number. **(a)** $M_1 = 0.02$; **(b)** $M_1 = 0.04$; **(c)** $M_1 = 0.06$; **(d)** $M_1 = 0.08$; **(e)** $M_1 = 0.1$. 110

Figure 5.16 SPL spectral comparisons between varying source and flow combinations 1-4. Measurements shown for Plate 6 at upstream Mach number. **(a)** $M_1 = 0.02$; **(b)** $M_1 = 0.04$; **(c)** $M_1 = 0.06$; **(d)** $M_1 = 0.08$; **(e)** $M_1 = 0.1$. 111

Figure 5.17 SPL spectral comparisons between varying source and flow combinations 1-4. Measurements shown for Plate 7 at upstream Mach number. **(a)** $M_1 = 0.02$; **(b)** $M_1 = 0.04$; **(c)** $M_1 = 0.06$; **(d)** $M_1 = 0.08$; **(e)** $M_1 = 0.1$. 112

Figure 5.18 SPL spectral comparisons between varying source and flow combinations 1-4. Measurements shown for Plate 8 at upstream Mach number. **(a)** M_1 = 0.02; **(b)** M_1 = 0.04; **(c)** M_1 = 0.06; **(d)** M_1 = 0.08; **(e)** M_1 = 0.1. 113

Figure 5.19 SPL spectral comparisons between varying source and flow combinations 1-4. Measurements shown for Plate 9 at upstream Mach number. **(a)** M_1 = 0.02; **(b)** M_1 = 0.04; **(c)** M_1 = 0.06; **(d)** M_1 = 0.08; **(e)** M_1 = 0.1. 114

Figure 5.20 SPL spectral comparisons between varying source and flow combinations 1-4. Measurements shown for Plate 10 at upstream Mach number. **(a)** M_1 = 0.02; **(b)** M_1 = 0.04; **(c)** M_1 = 0.06; **(d)** M_1 = 0.08; **(e)** M_1 = 0.1. 115

Figure 5.21 SPL spectral comparisons between varying source and flow combinations 1-4. Measurements shown for Plate 11 at upstream Mach number. **(a)** M_1 = 0.02; **(b)** M_1 = 0.04; **(c)** M_1 = 0.06; **(d)** M_1 = 0.08; **(e)** M_1 = 0.1. 116

Figure 5.22 Comparison of microphone cross correlations obtained in SIL and BFIL facilities. **(a)** Plate 1; **(b)** Plate 2; **(c)** Plate 3; **(d)** Plate 4; **(e)** Plate 5; **(f)** Plate 6; **(g)** Plate 7; **(h)** Plate 8; **(i)** Plate 9; **(j)** Plate 10; **(k)** Plate 1. 117

Figure 5.23 Effect of mean flow on signal correlation for Plate 1 for varying upstream Mach number **(a)** M_1 = 0.02; **(b)** M_1 = 0.04; **(c)** M_1 = 0.06; **(d)** M_1 = 0.08; **(e)** M_1 = 0.10. 119

Figure 5.24 Effect of upstream bias flow Mach number on cross-correlation. **(a)** Plate 1; **(b)** Plate 2; **(c)** Plate 3; **(d)** Plate 4; **(e)** Plate 5; **(f)** Plate 6; **(g)** Plate 7; **(h)** Plate 8; **(i)** Plate 9; **(j)** Plate 10; **(k)** Plate 1. 120

Figure 5.25 Effect of upstream bias flow Mach number on coherence. **(a)** Plate 1; **(b)** Plate 2; **(c)** Plate 3; **(d)** Plate 4; **(e)** Plate 5; **(f)** Plate 6; **(g)** Plate 7; **(h)** Plate 8; **(i)** Plate 9; **(j)** Plate 10; **(k)** Plate 1. 122

Figure 5.26 Insertion loss measurement vs. current theory. Black line indicates experimental data that satisfy the minimum SNR and coherence requirement, and grey line indicates data points which do not satisfy one or both of the requirements **(a)** $M_1 = 0$; **(b)** $M_1 = 0.02$ **(c)** $M_1 = 0.04$; **(d)** $M_1 = 0.06$; **(e)** $M_1 = 0.08$; **(f)** $M_1 = 0.10$ 124

Figure 5.27 Insertion loss measurement vs. current theory for Plate 1. **(a)** $M_1 = 0$; **(b)** $M_1 = 0.02$; **(c)** $M_1 = 0.04$; **(d)** $M_1 = 0.06$; **(e)** $M_1 = 0.08$. 125

Figure 5.28 Insertion loss measurement vs. current theory for Plate 2. **(a)** $M_1 = 0$; **(b)** $M_1 = 0.02$; **(c)** $M_1 = 0.04$; **(d)** $M_1 = 0.06$; **(e)** $M_1 = 0.08$. 126

Figure 5.29 Insertion loss measurement vs. current theory for Plate 3. **(a)** $M_1 = 0$; **(b)** $M_1 = 0.02$; **(c)** $M_1 = 0.04$; **(d)** $M_1 = 0.06$; **(e)** $M_1 = 0.08$. 127

Figure 5.30 Insertion loss measurement vs. current theory for Plate 4. **(a)** $M_1 = 0$; **(b)** $M_1 = 0.02$; **(c)** $M_1 = 0.04$. 128

Figure 5.31 Insertion loss measurement vs. current theory for Plate 5.
(a) $M_1 = 0$; **(b)** $M_1 = 0.02$; **(c)** $M_1 = 0.04$; **(d)** $M_1 = 0.06$;
(e) $M_1 = 0.08$; **(f)** $M_1 = 0.10$ 129
Figure 5.32 Insertion loss measurement vs. current theory for Plate 6.
(a) $M_1 = 0$; **(b)** $M_1 = 0.02$; **(c)** $M_1 = 0.04$; **(d)** $M_1 = 0.06$. 130
Figure 5.33 Insertion loss measurement vs. current theory for Plate 7.
(a) $M_1 = 0$; **(b)** $M_1 = 0.02$; **(c)** $M_1 = 0.04$; **(d)** $M_1 = 0.06$. 131
Figure 5.34 Insertion loss measurement vs. current theory for Plate 8.
(a) $M_1 = 0$; **(b)** $M_1 = 0.02$; **(c)** $M_1 = 0.04$; **(d)** $M_1 = 0.06$;
(e) $M_1 = 0.08$. 132
Figure 5.35 Insertion loss measurement vs. current theory for Plate 9.
(a) $M_1 = 0$; **(b)** $M_1 = 0.02$; **(c)** $M_1 = 0.04$; **(d)** $M_1 = 0.06$;
(e) $M_1 = 0.08$; **(f)** $M_1 = 0.10$. 133
Figure 5.36 Insertion loss measurement vs. current theory for Plate 10.
(a) $M_1 = 0$; **(b)** $M_1 = 0.02$; **(c)** $M_1 = 0.04$; **(d)** $M_1 = 0.06$;
(e) $M_1 = 0.08$; **(f)** $M_1 = 0.10$. 134
Figure 5.37 Insertion loss measurement vs. current theory for Plate 11.
(a) $M_1 = 0$; **(b)** $M_1 = 0.02$; **(c)** $M_1 = 0.04$; **(d)** $M_1 = 0.06$;
(e) $M_1 = 0.08$; **(f)** $M_1 = 0.10$ 135
Figure 5.38 Comparisons of the range of **(a)** d/λ, **(b)** M_2, and **(c)** β covered in the current and previous work. The ranges of d/λ, M_p, and β are determined based on the range of experimental validation provided for the respective work. 136

Figure 5.39 Insertion loss measurement vs. current theory for Plate 1;

(a) $M_1 = 0$; **(b)** $M_1 = 0.02$; **(c)** $M_1 = 0.04$; **(d)** $M_1 = 0.06$

(e) $M_1 = 0.08$; **(f)** $M_1 = 0.10$. 137

Figure 5.40 Insertion loss measurement vs. current theory for Plate 2;

(a) $M_1 = 0$; **(b)** $M_1 = 0.02$; **(c)** $M_1 = 0.04$; **(d)** $M_1 = 0.06$

(e) $M_1 = 0.08$ 138

Figure 5.41 Insertion loss measurement vs. current theory for Plate 3;

(a) $M_1 = 0$; **(b)** $M_1 = 0.02$; **(c)** $M_1 = 0.04$; **(d)** $M_1 = 0.06$;

(e) $M_1 = 0.08$ 139

Figure 5.42 Insertion loss measurement vs. current theory for Plate 4;

(a) $M_1 = 0$; **(b)** $M_1 = 0.02$; **(c)** $M_1 = 0.04$. 140

Figure 5.43 Insertion loss measurement vs. current theory for Plate 5;

(a) $M_1 = 0$; **(b)** $M_1 = 0.02$; **(c)** $M_1 = 0.04$; **(d)** $M_1 = 0.06$

(e) $M_1 = 0.08$; **(f)** $M_1 = 0.10$ 141

Figure 5.44 Insertion loss measurement vs. current theory for Plate 6;

(a) $M_1 = 0$; **(b)** $M_1 = 0.02$; **(c)** $M_1 = 0.04$; **(d)** $M_1 = 0.06$. 142

Figure 5.45 Insertion loss measurement vs. current theory for Plate 7;

(a) $M_1 = 0$; **(b)** $M_1 = 0.02$; **(c)** $M_1 = 0.04$; **(d)** $M_1 = 0.06$. 143

Figure 5.46 Insertion loss measurement vs. current theory for Plate 8;

(a) $M_1 = 0$; **(b)** $M_1 = 0.02$; **(c)** $M_1 = 0.04$; **(d)** $M_1 = 0.06$. 144

Figure 5.47 Insertion loss measurement vs. current theory for Plate 9;

(a) $M_1 = 0$; **(b)** $M_1 = 0.02$; **(c)** $M_1 = 0.04$; **(d)** $M_1 = 0.06$. 145

Figure 5.48 Insertion loss measurement vs. current theory for Plate 10; **(a)** $M_1 = 0$; **(b)** $M_1 = 0.02$; **(c)** $M_1 = 0.04$; **(d)** $M_1 = 0.06$. 146

Figure 5.49 Insertion loss measurement vs. current theory for Plate 11; **(a)** $M_1 = 0$; **(b)** $M_1 = 0.02$; **(c)** $M_1 = 0.04$; **(d)** $M_1 = 0.06$. 147

Figure 5.50 Insertion loss difference between theory and experiment for **(a)** Plate 1; **(b)** Plate 2; **(c)** Plate 3; **(d)** Plate 4; **(e)** Plate 5; **(f)** Plate 6; **(g)** Plate 7; **(h)** Plate 8; **(i)** Plate 9; **(j)** Plate 10; **(k)** Plate 11. 148

Figure 5.51 Contour plots of L_I versus d/λ and M_2. Dashed white line indicates the bias flow Mach number M_2 which L_I reaches peak value for a given d/λ. **(a)** Plate 1; (**b)** Plate 2; (**c)** Plate 3; (**d)** Plate 4; (**e)** Plate 5; (**f)** Plate 6; **(g)** Plate 7; (**h)** Plate 8; (**i)** Plate 9; (**j)** Plate 10; (**k)** Plate 11. 149

Figure 5.52 Dependence of ΔL_I on l/d. Width of error bars indicates maximum and minimum error measurements between $0.02 < d/\lambda < 0.4$ and $M_2 < 0.25$. 150

Figure 5.53: Acoustic pressure amplitude distribution upstream of the perforated plate with: **(a)** maximum number of radial modes (m =2, n = 17); **(b)** maximum number of circumferential modes (m =50, n = 1); **(c)** intermediate number of radial and circumferential modes (m =23, n = 8).); **(d)** intermediate number of radial and circumferential modes (m =10, n = 5). m and n are the circumferential and radial modes numbers, respectively, and D =4.57-cm is the diameter of the fully converged area upstream of the perforated plate.. 153

Figure B.1: Pitot pressure profile along the measurement axis for Plate 1. **(a)** M_1 = 0.02; **(b)** M_1 = 0.04; **(c)** M_1 = 0.06; **(d)** M_1 = 0.08; **(d)** M_1 = 0.1. 167

Figure B.2: Pitot pressure profile along the measurement axis for Plate 2. **(a)** M_1 = 0.02; **(b)** M_1 = 0.04; **(c)** M_1 = 0.06; **(d)** M_1 = 0.08; **(d)** M_1 = 0.1. 168

Figure B.3: Pitot pressure profile along the measurement axis for Plate 7. **(a)** M_1 = 0.02; **(b)** M_1 = 0.04; **(c)** M_1 = 0.06; **(d)** M_1 = 0.08; **(d)** M_1 = 0.1. 169

Figure B.4: Pitot pressure profile along the measurement axis for Plate 11. **(a)** M_1 = 0.02; **(b)** M_1 = 0.04; **(c)** M_1 = 0.06; **(d)** M_1 = 0.08; **(d)** M_1 = 0.1. 170

LIST OF TABLES

Page

Table 4.1 Properties of perforated sheets used in experiments. 61

Table 4.2 Experimentally measured flow conditions for Plate 1. 61

Table 4.3 Experimentally measured flow conditions for Plate 2. 61

Table 4.4 Experimentally measured flow conditions for Plate 3. 62

Table 4.5 Experimentally measured flow conditions for Plate 4. 62

Table 4.6 Experimentally measured flow conditions for Plate 5. 62

Table 4.7 Experimentally measured flow conditions for Plate 6. 62

Table 4.8 Experimentally measured flow conditions for Plate 7. 63

Table 4.9 Experimentally measured flow conditions for Plate 8. 63

Table 4.10 Experimentally measured flow conditions for Plate 9. 63

Table 4.11 Experimentally measured flow conditions for Plate 10. 63

Table 4.12 Experimentally measured flow conditions for Plate 11. 64

NOMENCLATURE

A	reference area
a	orifice or perforation radius
BFIL	bias flow insertion loss
c	acoustic wave propagation speed
c_v	specific heat at constant volume
c_p	specific heat at constant pressure
C	spectral correction
C_D	coefficient of discharge
C_c	coefficient of contraction
C_ρ	coefficient of density
C_v	coefficient of velocity
D	duct diameter
d	perforation or orifice hole diameter
FFT	fast Fourier transform
f	frequency
h	enthalpy
He	Helmholtz number $=ka$
HIE	hole interaction effects
I	incident acoustic pressure amplitude
I	acoustic intensity
h	normalized pressure fluctuation
IJS	impinging jets source

IL	sound intensity level
i	imaginary unit $\sqrt{-1}$
k	acoustic wave number
K	bulk modulus
K_R	Rayleigh conductivity
l	plate thickness
l'	end correction length
L_T	transmission loss
L_I	insertion loss
M	Mach number
$\dot{m}$	mass flow rate
P	center-to-center distance between perforations
PL	sound power level
p	pressure
p_0	total pressure
Pr	Prandtl number
Q	volume flux
R	reflected acoustic pressure amplitude
R_0	dry air specific gas constant = 287.058 J/(kg·K)
Re	Reynolds number
R_c	reflection coefficient
S	power spectrum
s	entropy

SIL	static insertion loss
SNR	signal-to-noise ratio
SPL	sound pressure level
St	Strouhal number
T	transmitted acoustic pressure amplitude
T_c	transmission coefficient
t	time
TMM	Transfer Matrix Method
$\overline{\mathbf{U}}$	mean flow velocity
$\mathbf{u}$	total velocity
$\mathbf{u}'$	acoustic velocity
V	volume
Z	acoustic impedance
Z_0	characteristic impedance
z	normalized acoustic impedance $Z/\rho c$
α_∞	geometric tortuosity
β	porosity
γ	ratio of specific heat for dry air c_p/c_v
γ^2	magnitude squared coherence
γ_R	real component of Rayleigh conductivity normalized by $2a$
Δ	dissipation coefficient
δ_R	imaginary component of Rayleigh conductivity normalized by $2a$
ε	end correction factor

η	Stokes number
θ	angle with respect to plane containing perforations
λ	acoustic wavelength
μ	dynamic viscosity
v	kinematic viscosity
Π	acoustic power
ρ	density
δ	entropy fluctuation
σ_r	flow resistivity
τ	time lag
ψ	inverse of Fok's function [10]
$\mathbf{\Omega}$	vorticity
ω	angular frequency or vorticity
$\overline{()}$	mean value of quantity
$()'$	fluctuation of quantity about mean value
$\langle\ \rangle$	time average

Subscripts

b	bias flow component
c	convection
cav	cavity
d	diameter
e	effective

exp	experiment
FR	microphone frequency response
FF	microphone free field response
AA	atmospheric absorption
i	incident
inc	incompressible
m	mixing region
m1	microphone 1
m2	microphone 2
mod	model
p	perforation
r	reflected
ref	reference
rms	root mean square
s	static
t	transmitted
t,0	transmitted without silencing device installed
v	velocity
vc	*vena contracta*
ρ	density
ω	vorticity
0	baseline or open (without perforated plate installed in facility)
1	region upstream of contraction, orifice, or perforated plate

2	region within contraction, orifice, or perforation
3	region downstream of contraction, orifice, or perforated plate

ABSTRACT OF THE DISSERTATION

Acoustic transmission loss of perforated plates with bias flow

by

Vincent Choy Phong

Doctor of Philosophy in Mechanical and Aerospace Engineering

University of California, Irvine, 2014

Professor Dimitri Papamoschou, Chair

Perforated plates are employed in various noise control applications to attenuate sound whose direction of propagation is normal to the plate. In certain instances this is accompanied by a bias flow through the perforations. The mechanism of sound attenuation is dependent both on the physical properties of the perforated plate and on the mixing of the small jets emerging from the perforations. The objective of this study is to analyze the acoustic properties of perforates and develop a comprehensive theoretical model that is capable of predicting the sound attenuation over a wide range of bias flow speeds, porosity, hole size, and thickness values of the perforated plate. The theoretical analysis of this investigation is validated through experimentation and comparison with existing models.

As a first step in this work, a study has been conducted on the insertion loss of perforated plates at normal incidence without bias flow. The experiments comprised microphone measurements of insertion loss for eleven perforated plates that varied in thickness, hole size, and porosity. The theoretical model is based on planar wave propagation through a single contraction/expansion chamber, with modifications to account for hole interaction effects. The resulting formula for insertion loss yields superior predictions over past theories for the range of properties investigated. Deviations between experimental measurements and theoretical

predictions of insertion loss are less than about 1.5 decibels for dimensionless hole diameter d/λ <0.5, where λ is the wavelength of sound. The accuracy of the model does not show a strong dependence on plate thickness-to-diameter ratio l/d or porosity β.

An insertion loss model of perforated plates with subsonic bias flow is proposed based on the principal elements of the model without flow. Significant loss in the transmitted acoustic energy is caused by the mixing and viscous dissipation downstream of the contraction. The loss involved in this process is incorporated in the model through entropy fluctuations, which propagate downstream from the contraction at the mean flow velocity. *Vena contracta* theory was utilized in modeling the end correction of the perforated plate with bias flow. The experimental measurements and proposed theoretical model both indicate an increase in insertion loss as the bias flow Mach number in the perforations, M_2, increases to about 0.25. For M_2 >0.25, the experimental measurements indicate a saturation, followed by a decrease in insertion loss due to increasing flow noise for plates with porosity $\beta \leq 0.23$. The proposed model does not incorporate flow noise, and therefore is validated only for M_2 <0.25. Deviations between the proposed model and experimental measurements are less than 3 decibels for $M_2 \leq 0.25$ and $0.02 \leq d/\lambda \leq 0.4$ for thin plates. Larger discrepancies between the model and experiment occur at intermediate ranges of l/d, where the *vena contracta* location with respect to the perforated plate becomes unstable. Despite these discrepancies, the proposed model expression yields more reliable predictions than previous models and exhibits the same trends as the experimental measurements.

Chapter 1

INTRODUCTION

1.1 Motivation

Perforated material has been extensively employed in various noise control applications. Examples include acoustic liners for ducts and aeroengine nacelles, automotive mufflers, and silencers for flow control valves. Aeroengine acoustic liners and automotive mufflers are classified as reactive silencers [1]. In reactive silencers, the frequency response of the system is tuned to suppress sound at targeted frequencies such as, for example, the blade passing frequency of a rotor or the firing frequency of an internal combustion engine. Air or exhaust flow is usually present in these applications, which can dramatically augment or reduce the damping effectiveness.

Depending on the application, both flow speed and direction with respect to the silencer configuration may vary. The mean flow is at grazing incidence when the flow direction is parallel to the surface containing the perforations. Flow that is directed into the surface containing the perforations, thereby forcing the flow through the perforations, is referred to as bias flow. Both grazing and bias flow are commonly present in aeroengine liners. Bias flow applications in aeroengine liners were originally intended to provide a thin cooling layer to protect the liner wall from extreme temperatures in the combustion chamber. It has been found, however, that the bias flow can potentially modify the damping characteristics of the liner such that acoustically driven combustion instabilities are more effectively suppressed. A robust

model on the transmission characteristics of perforated plates that includes the effects of flow would provide guidance in optimizing the design of liners and other reactive applications.

Perforated plates are also used in mufflers for flow control valves, particularly pneumatic bleed valves on gas turbines (Figure 1.1) [2]. These valves discharge compressor air into the fan duct of a turbofan engine in order to prevent compressor surges during transients or throttle back. Noise from the bleed valves can be a significant contributor to total aircraft noise. Figure 1.2 depicts a simplified drawing of a pneumatic bleed valve. It consists of a valve body, followed by a muffler containing multiple perforated surfaces that are oriented substantially normally to the mean flow direction (Figures 1.2 and 1.3). Without the muffler, the exhaust of the valve forms a high-speed turbulent jet that is very loud. The muffler expands the cross-sectional area of the flow and dramatically reduces its bulk velocity. The small jets emerging from the perforations produce noise at very high frequency, but this noise is attenuated rapidly by atmospheric absorption. What remains, though, is transmission of sound from the internal sources, including turbulence and vortex shedding through the perforations. Recent efforts to suppress bleed valve noise underscored the lack of fundamental understanding of the dependence of sound attenuation on the properties of the perforated plate (porosity, hole size, thickness) and the bias flow speed through the perforations. This formed the basic motivation for the current study, namely the understanding and modeling of sound transmission through the perforated plates exemplified in Figure 1.2. It is evident that the noise suppression mechanism does not involve tuning and is thus fundamentally different from reactive mufflers. However, the basic physics of sound transmission through a perforation remains relevant to both reactive and non-reactive applications.

1.2 Research objectives

The goals of the present investigation can be divided into the following objectives:

1. Develop a comprehensive theoretical model of sound attenuation through perforated plates. The model should be applicable over a wide range of bias flow speeds, porosity, hole size, and thickness values of the perforated plate.
2. Identify how bias flow and the physical properties of the perforated plate affect the attenuation characteristics of the plate.
3. Construct a robust experimental facility that will provide reliable insertion loss measurements, and from the acoustic data, identify any additional physical phenomena that will assist in developing the theoretical model
4. Evaluate the current model against experimental measurements and the models of previous investigators

The research objectives were accomplished in two phases. In the first phase, the transmission characteristics of perforated plates were studied assuming no bias flow through the perforations (henceforth referred to as the static condition). This was considered as a first step to modeling the complex system illustrated in Figure 1.2, as it isolated the effect of the plate's physical properties on its damping characteristics. The established static model was then validated based on experiments and comparisons to past models. The second phase of this research focused on the effect of bias flow on the perforated plate's damping characteristics. The bias flow model established in this study was validated based on experimental measurements and comparisons with previous models.

1.3 Outline

The dissertation is presented in six chapters. Chapter 1 presents the motivation and overall objective of this study. Chapter 2 reviews the fundamental physics of sound transmission

through perforated plates, and summarizes previous efforts with emphasis on those which propose analytical models for both static and bias flow cases. Chapter 3 details the theoretical model developed in the current study for insertion loss. Chapter 4 discusses the experimental setup and data processing. Chapter 5 presents the experimental results on transmission loss, with comparisons to the present model and previous models noted in Chapter 2. Chapter 6 summarizes the findings in this study with concluding remarks and suggestions for future work.

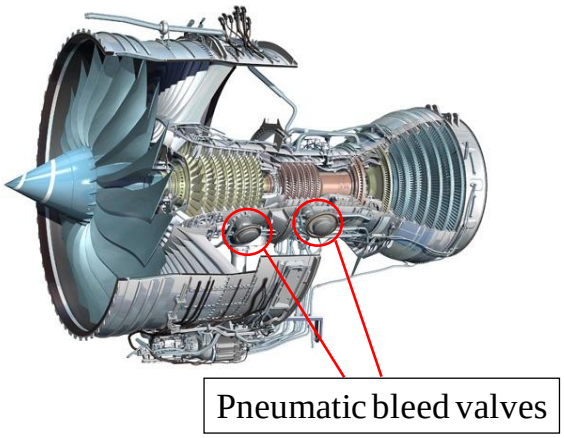

Figure 1.1: Cutaway view of Rolls Royce Trent 1000 jet engine with location of intermediate and high pressure bleed valves indicated

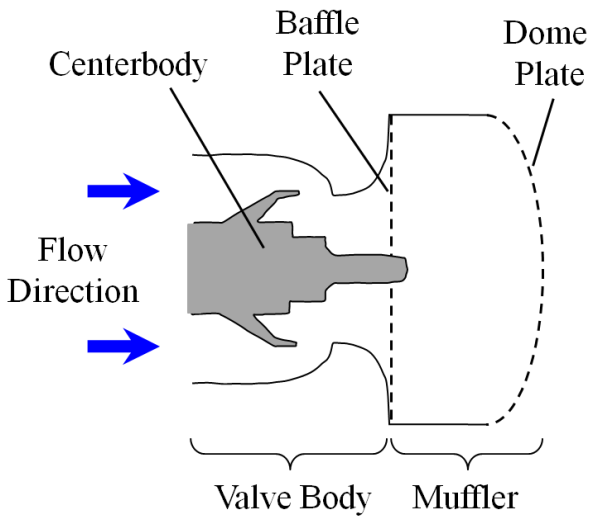

Figure 1.2: Schematic of pneumatic bleed valve assembly used on aircraft engines [2]

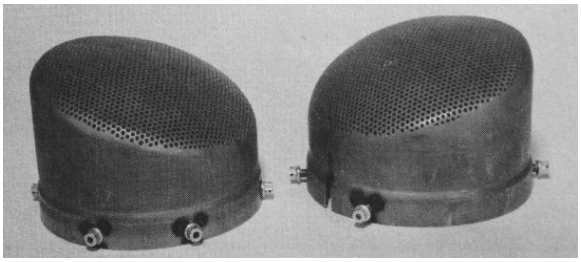

Figure 1.3: Muffler attachment to bleed valve outlet [3]

Chapter 2

LITERATURE REVIEW

This chapter reviews selected literature which focused primarily on analytical or semi-empirical modeling of the transmission characteristics of perforated plates. Prior to understanding the development of these models, an overview of fundamental principles relevant in describing the transmission behavior of silencers is reviewed. Previous models are presented along with the range of parameters over which these models are validated.

2.1 Fundamental principles

The current investigation focused on the acoustic insertion loss of perforated plates, namely the difference in measured acoustic power with and without the installation of a perforated plate. This is a process that is generally governed by inertial and viscous effects. As shown by Crandall [4], the discriminant between viscous and inertial effects on sound propagation through a short tube is the quantity

$$\eta = \frac{1}{2} d \sqrt{\frac{\rho \omega}{\mu}} \tag{2.1}$$

where d is the tube diameter, ω is the angular frequency, ρ and μ are the density and dynamic viscosity of the fluid, respectively. For $\eta \leq 1$ the propagation is dominated by viscous effects. For $\eta > 1$ inertial effects become prominent. The discriminant can be rewritten using the acoustic propagation speed, c, and wavelength, λ, as

$$\eta = \sqrt{\frac{\pi}{2}\frac{\rho c d}{\mu}}\sqrt{\frac{d}{\lambda}} \tag{2.2}$$

The argument of the first square root has the form of a Reynolds number based on the speed of sound and the hole diameter. The argument of the second square root is the non-dimensional hole size, an important parameter in the analysis that follows. For a hole diameter of 1 mm (the order of magnitude in this study), and for air at standard conditions, the discriminant becomes $\eta = 184\ (d/\lambda)^{1/2}$. This means that inertial effects dominate down to $d/\lambda \sim 10^{-4}$, i.e., frequencies on the order of 30 Hz. Aerospace applications are typically concerned with much higher frequencies associated with peak levels of annoyance. It is concluded that, for the applications that motivated this study, the sound transmission process can be treated as purely inertial with a good degree of accuracy.

2.1.1 Acoustical performance criteria

The sound field around the perforation consists of incident, reflected, and transmitted waves (subscripts *i*, *r*, and *t*, respectively). The medium far upstream of the perforation is moving at bias flow incidence with a speed defined by the Mach number M_i. The bias flow constricts and accelerates as it approaches the perforated plate, forming small jets which separate from the rim of the perforations (Figure 2.1). The jets coalesce downstream of the perforation, and resume motion predominantly at bias flow incidence with Mach number M_t. An acoustic wave is a progressive wave, where the energy of the acoustic disturbance is transported in the direction of propagation. The power of a acoustic wave is defined using the acoustic intensity, **I**, and reference area *A*

$$\Pi = \int_A \mathbf{I} \cdot \mathbf{n} dA \tag{2.3}$$

The acoustic intensity is defined for a moving medium as [5]

$$\mathbf{I} = \langle p'\mathbf{u}' \rangle + \frac{\overline{\mathbf{U}}}{\overline{\rho}} \langle p'\rho' \rangle + \overline{\mathbf{U}}\overline{\rho} \langle \mathbf{u}' \cdot \mathbf{u}' \rangle + \left(\overline{\mathbf{U}} \cdot \overline{\mathbf{U}} \right) \langle \mathbf{u}'\rho' \rangle \tag{2.4}$$

where the angle brackets $\langle\ \rangle$ denotes time averaging, p', $\mathbf{u}$', and ρ' are the acoustic pressure, velocity, and density, respectively, and $\overline{\mathbf{U}}$ and $\overline{\rho}$ are the mean (undisturbed) velocity and density. For a stationary medium, Equation 2.4 reduces to the form $\mathbf{I}_S = \langle p'\mathbf{u}' \rangle$.

The transmission loss (L_T) and insertion loss (L_I) are frequently used as performance criteria of a silencing device. The transmission loss is defined as [5,6,7]

$$L_T = 10 \log_{10} \left[\frac{\Pi_i}{\Pi_t} \right] \tag{2.5}$$

Equation 2.5 indicates that the transmission loss is defined as the level difference between the incident and transmitted sound power. Although the expression for transmission loss is easily obtainable in theory (to be shown in Chapter 3), experimentally measuring transmission loss poses difficulties. For example, a microphone placed upstream of the perforated plate in Figure 2.1 can cause interferences, such as a disturbance in the mean flow, or diffraction of the incident acoustic wave that would propagate downstream. Therefore, the sound pressure measured downstream would not be an accurate representation of the damping characteristics of the perforated plate alone. The insertion loss is a more experimentally convenient performance criteria, and is defined as

$$L_I = 10 \log_{10} \left[\frac{\Pi_{t,0}}{\Pi_t} \right] \tag{2.6}$$

Unlike the transmission loss, which requires sound power measurement at two separate locations, namely upstream and downstream of the perforated plate, the insertion loss is a comparison of the sound power at the same location downstream of the perforated plate, with (Π_t) and without ($\Pi_{t,0}$) the plate installed. The insertion and transmission losses are equal if no wave reflections occur downstream of the plate and upstream of the source. This holds true if the regions upstream and downstream of the plate are anechoically terminated [5,6,8].

2.1.2 Acoustic impedance and Rayleigh conductivity

Concerning the one-dimensional propagation of sound in a tube or lattice of tubes, we gain insight into the transmission behavior by relating the acoustic power to the acoustic impedance. The acoustic impedance of a fluid acting over a surface area A is defined as the ratio of the acoustic pressure to the acoustic velocity, or particle velocity

$$Z = \frac{1}{A}\frac{p'}{u'} \tag{2.7}$$

Expressing the particle velocity in terms of the impedance and pressure fluctuation according to Equation 2.7, the acoustic power follows the qualitative relation for a stationary medium

$$\Pi \sim \frac{\left\langle p'^2 \right\rangle}{|Z|} \tag{2.8}$$

From Equation 2.8, it is apparent that the power of the acoustic disturbance is maximized when the acoustic impedance is minimized. This occurs for disturbances at the resonance frequency of the system. Concerning the perforated plate, the incident wavefront acts as a source which disturbs the column of air inside the perforations. When the air is disturbed at integer multiples of its resonance frequency, the power of the acoustic waves inside the perforation is maximized.

This results in maximum transmission of the energy from the incident wavefront through the perforations, or minimum transmission loss, at these characteristic frequencies.

Lord Rayleigh defined an electrical analogue of conductivity for acoustic wave propagation through circular apertures [9]. The Rayleigh conductivity, K_R, is defined as the ratio of the net volume flux through the aperture to the pressure drop across the plate [10]

$$K_R = -\frac{i\omega\rho Q}{\Delta p} \tag{2.9}$$

where $Q = uA$ is the volume flux and Δp is the pressure difference across the aperture. Equation 2.9 is applicable when mean flow is either present or absent. In the absence of mean flow, it can be shown for circular apertures that $K_R = 2a$, where a is the aperture radius [9]. Combining Equations 2.9 and 2.7 results in the relation between the acoustic impedance and the Rayleigh conductivity

$$Z = \frac{-i\omega\rho}{K_R} \tag{2.10}$$

2.1.3 End effects

Acoustic disturbances that propagate within the perforations disturb the medium adjacent to the ends of the perforation. This is illustrated in Figure 2.2, where the dotted line represents the distribution of the disturbed, "attached" mass of a single hole. The disturbance inside the perforation travels a distance slightly further than the geometric thickness of the perforation as a result of this attached mass. This gives rise to an end correction to the perforation thickness, which was treated analytically by Rayleigh [9]. In the case of multiple adjacent holes, the attached mass regions overlap forming an interaction region whose extent is determined by the spacing between the holes (Figure 2.2). The consequence of this interaction has been addressed

by many authors. Fok [11] described the hole interaction effect (HIE) as a correction to Rayleigh conductivity of a single orifice. An analytical expression known as Fok's function was developed using potential theory (to be introduced in Section 3.2) and can be expressed in terms of the plate porosity β. Nesterov [12] validated Fok's work experimentally, showing that an increase in the porosity corresponds to a reduction in the end correction for thickness. Other investigators attributed HIE to the diffraction of pressure waves that radiate from the perforations. Ingard [13] showed that the pressure radiated from an orifice exerts an additional force on nearby orifices, and that this effect is strongly dependent on the separation distance between perforations. He described this acoustic interaction by a correction term, the interaction impedance, to the acoustic impedance of an isolated orifice. Christensen [14] and Hou *et al*. [15,16] concluded that the diffracted waves created acoustic modes that travel parallel to the surface of the perforated plate. The interaction between the surface modes and diffracted pressure waves from the perforations modifies the resonance condition associated with the original plate thickness to a plate that is 16% thinner [15,16]. The aforementioned works [11-16] indicated that HIE results in scaling the end correction associated with a single orifice. In the current investigation, the HIE was accounted for using Fok's function with more details on this implementation in Chapter 3.

2.1.4 *Vena contracta*

The acoustic transmission behavior through perforated plates can be significantly influenced by the introduction of bias flow, and it is therefore necessary to accurately model the mean flow dynamics in the vicinity of the perforations. Consider a cylindrical duct containing a single contraction and expansion shown Figure 2.3. The streamlines curve inward as the flow approaches and is constricted through the orifice. The blue dashed lines in Figure 2.3 are the streamlines near the wall, which separate at the upstream corner. The streamtube bound by the

separation streamlines continues to constrict due to the strong radial velocity component near the upstream surface of the contraction. The compression of the streamtube eventually ceases; due to the combination of a strong radial pressure gradient and Coandă effect both within the contraction and in the expanded duct region. At some point downstream of the contraction the streamlines become parallel, forming a minimum area, A_{vc}, known as the *vena contracta*.

A standardized method of characterizing the pressure drop across an orifice in a flow duct, such as that shown in Figure 2.3, is through the discharge coefficient

$$C_D = \frac{\dot{m}_{actual}}{\dot{m}_{ideal}} \tag{2.11}$$

The discharge coefficient is the ratio of the experimentally meausred mass flow rate through the orifice to the mass flow rate that is calculated assuming ideal (one-dimensional, isentropic) flow. Equation 2.11 can be rewritten in the form $C_D = C_\rho C_v C_c$, where the density coefficient C_ρ, velocity coefficient C_v, and contraction coefficient C_c are the ratios of the actual values of density, velocity, and area to their respective ideal values. The density coefficient is approximately unity as long as the working temperature of the fluid in the contraction is not large enough to allow dissociation [17]. The velocity coefficient has been reported to vary between 0.97 to 0.98 for a free jet discharging from a sharp edged orifice [18,19]. The ratio of the jet area at the *vena contracta* to the physical area of the contraction is the contraction coefficient, C_c.

Unlike the density and velocity coefficients, the contraction coefficient varies significantly from unity. Many standard fluid mechanics texts provide the theoretical contraction coefficient for an incompressible free jet as $C_{c,inc} = \pi/(\pi+2) = 0.611$ using hodographic transformation methods [20]. Shapiro [21] accounted for compressibility effects using a Mach number correction, and determined that an increase in the jet Mach number resulted in an increase in the contraction coefficient. Shapiro [21] and Batchelor [20] assumed the jet is issuing

from a single orifice in an infinite plane of infinitesimal thickness. In practical applications, the orifice is situated on a plate with finite size and thickness. The effect of thickness and orifice-to-duct area on the discharge coefficient has been investigated experimentally, and empirical formulas are available in several hydraulic handbooks [22,23,24].

The flow discharge through perforated plates is different from the single orifice plate due to flow interactions between neighboring jets. Smith and Van Winkle [25] experimentally determined the discharge coefficient of perforated plates for varying thickness-to-hole diameter ratio (*l/d*), hole diameter-to-pitch ratio (*d/P*), and Reynolds number based on perforation diameter $400 \leq Re_d \leq 3{,}000$. Kolodzie and Van Winkle [26] expanded this study to Reynolds number up to 20,000. Their results indicated that the discharge coefficient becomes independent of Reynolds number for $Re_d > 4{,}000$. The authors provided a correlation formula for the discharge coefficient of perforated plates, using the separation distance between the perforations and the Reynolds based on the hole diameter and mean flow velocity through the perforations. The discharge coefficient measured by the aforementioned works [25,26] yielded values that are much higher than values associated with single orifice contractions.

2.1.5 Acoustic dissipation

The addition of bias flow through the perforations introduces potential benefits in the absorptive properties of the plate. Losses in acoustic energy occur at area discontinuities, where the energy of an acoustic wave is transferred to the kinetic energy of vortical motions in the shear layer. The kinetic energy of the vortical motions is ultimately dissipated as heat. This implies a non-isentropic process downstream of the perforated plate, where changes in entropy must be factored into the propagation of the acoustic field. Mungur and Gladwell [27] linearized the energy equation in terms of entropy, and obtained an expression relating entropy fluctuations

to acoustic pressure fluctuations. Ronneberger [28], Alfredson and Davies [29], Davies [30], and Cummings [31] applied this concept to a duct containing a sudden expansion. Ronneberger and Cummings provided experimental measurements of reflection coefficient that were in good agreement for flow Mach number < 0.6. Their results [28,31] indicated a monotonic increase in losses with increasing duct Mach number. More recently, Hofmans *et al.* [1] and Durrieu *et al.* [32] developed a quasi-steady model of the acoustic response of a circular diaphragm and a perforated plate, respectively, in a duct with bias flow, using entropy fluctuations to model the dissipation of acoustic energy. For low frequency excitations, their results indicated larger transmission loss with increasing bias flow speed.

The dissipation of acoustic waves by mean flow at area discontinuities had also been approached by focusing on the acoustic-vortex layer interaction at the edge of the discontinuity. Howe [10,33] considered the canonical problem of bias flow through an aperture in an infinite plate of infinitesimal thickness, represented schematically in Figure 2.4. The aperture is circular with radius a, and the bias flow through the aperture is in line with the x-axis, at velocity U. His analysis was restricted to low Mach number, inviscid flow. The momentum equation was expressed in the following form

$$\nabla^2 h_0 = -\nabla \cdot \left(\mathbf{\Omega} \times \mathbf{u} \right) \tag{2.12}$$

where h_0 is the total enthalpy and $\mathbf{\Omega}$ is the vorticity. Howe's analytical solution of Equation 2.12 was a modified form of the Rayleigh conductivity of single aperture that included bias flow, from which he then extended his analysis to determine the transmission loss of a perforated plate. His results indicated an increase in transmission loss at low Strouhal number, St = $\omega a/U$, as the bias flow Mach number was increased. His theory was later verified by experiments [34-37]. Equation 2.12 established the framework for several other research efforts [38-44] on

characterized the bias flow effects on the transmission properties of orifices and perforated plates. The absorption or scattering of sound due to fluctuating vorticity has been investigated with varying degrees of complexity, depending on the boundary conditions imposed, and how the vortex sheet is modeled in Equation 2.12.

2.1.6 Nonlinear effects

The transmission characteristics of an orifice exhibits nonlinear behavior at high pressure amplitudes because of the dissipative effects of the jet and vortex rings formed downstream of the orifice [45,46,47]. Ingard and Ising [47] observed a linear relationship between the acoustic pressure and particle velocity for sound pressure levels (SPL) up to about 120 dB, with a quadratic relation starting above 130 dB. The SPL in the muffler cavity of Figure 1.2 is estimated not to exceed 120 dB based on far-field measurements of the jet issuing from the isolated valve body. Acoustic levels in the experiment of this study were much lower, around 60 dB. For this reason, it was concluded that non-linear effects are not significant in the actual application, the model developed in this study, and the experiments in this work for both the static and bias flow cases.

2.2 Previous theoretical models

This section gives an overview of previous models that are relevant to the scope of the current investigation. All existing models are recast in terms of transmission loss to facilitate comparison with the current theory.

2.2.1 Transmission loss models without bias flow

Chen [48] proposed a theoretical model, with experimental validation, for the transmission loss of a perforated plate under the assumption of a two-dimensional planar wave

incident on a rigid screen. The screen dimensions were assumed to be large in comparison to the wavelength. The air column inside the perforation was assumed to move in phase, behaving like a rigid piston. Viscous losses were neglected. Transmission loss predictions were provided for $3.6\times10^{-4} \leq d/\lambda \leq 0.0933$, $3.6\times10^{-4} \leq l/\lambda \leq 0.0023$, and were shown to agree well with the experiments. Chen accounted for the directivity of transmission loss by averaging over a hemisphere upstream from the perforated screen, resulting in the expression:

$$L_T = -10\log\int_0^{\pi/2}\left|\left[i\frac{(l+\varepsilon)\omega}{2\beta c}\cos\theta+1\right]^{-2}\right|\sin 2\theta\, d\theta \tag{2.13}$$

θ is the angle with respect to the normal direction of the plate surface, c is the propagation speed of the acoustic wave, and β is the porosity of the plate. The plate thickness l was augmented by an end correction factor ε, which was determined empirically to equal 1.6 times the perforation radius if the ratio of perforation radius to the distance between the holes was less than 0.2. For perforations with uniformly spaced holes, this translates to a porosity of 0.126 or less.

Tayong, Dupont and Leclaire [49] and Melling [50] defined the normal surface impedance of the perforations while incorporating Fok's function to account for HIE. Using the lumped acoustic impedance model formulated by Ingard [13], Tayong *et al*. accounted for HIE in the reactance (imaginary) term of the impedance, resulting in the expression

$$Z_p = Z_{cav} + \frac{\sqrt{8\omega\rho\mu}}{\beta}\left(1+\frac{l}{d}\right)+\frac{i\omega\rho}{\beta}\left(l+\frac{8d}{3\pi\psi(\beta)}\right) \tag{2.14}$$

where Z_{cav} is the cavity impedance and ψ is the inverse of Fok's function. Z_{cav} can be defined for a perforated panel surrounded on both sides by semi-infinite fluid media by defining Z_{cav} as the characteristic impedance of the fluid. This imposes the condition that there can be no reflected

waves in the fluid media where the transmitted waves propagate. Tayong *et al*. also included additional terms to account for nonlinear effects in their work due to high sound pressure level excitations [49]. Since the scope of the current study is concerned only with the linear regime, these terms were neglected in the model of Tayong *et al.*, resulting in Equation 2.14. Experimental validation for the authors' perforation impedance model is provided for $0.0014 \leq d/\lambda \leq 0.0024$ and $0.0013 \leq l/\lambda \leq 0.0022$. Tayong *et al*. defined the reflection coefficient, R_c, as

$$R_c = \frac{Z_p - Z_0}{Z_p + Z_0} \tag{2.15}$$

where $Z_0 = \rho c$ is the characteristic impedance of air. In order to compare directly with the experimental measurements in this study, the transmission loss expression, Equation 2.5, is rewritten using the transmission coefficient $T_c = 1 - |R_c|^2$:

$$L_T = -10\log_{10}(T_c) \tag{2.16}$$

Substituting Equation 2.15 into Equation 2.16 results in an expression for transmission loss as a function of the perforation impedance

$$L_T = -10\log_{10}\left(1 - \left|\frac{Z_P - Z_0}{Z_P - Z_0}\right|^2\right) \tag{2.17}$$

Other investigators have alternatively modeled the perforated plate as an effective fluid layer [16,51,52,53]. The perforated plate was assumed to be rigid and porous with circular cylindrical pores. The effective density, ρ_e, and bulk modulus, K, was defined using the Johnson-Champoux-Allard model [53]

$$\rho_e = \rho\alpha_\infty\left[1+\frac{\sigma_r\beta}{i\omega\rho\alpha_\infty}\left(1+i\frac{\rho\omega\alpha_\infty}{2\sigma\beta}\right)^{1/2}\right] \tag{2.18}$$

$$K = \frac{\gamma p_0}{\gamma-(\gamma-1)\left[1+\frac{\sigma_r\beta}{i\,\mathrm{Pr}\,\omega\rho\alpha_\infty}\left(1+i\frac{\rho\,\mathrm{Pr}\,\omega\alpha_\infty}{2\sigma\beta}\right)^{1/2}\right]^{-1}} \tag{2.19}$$

where the flow resistivity is $\sigma_r = 32\mu/\beta d^2$, the geometric tortuosity $\alpha_\infty = 1$, and γ, p_0, ρ, and Pr are the specific heat ratio, static pressure, density, and Prandtl number for air, respectively, at 291.15 K (γ = 1.4, $p_0 = 1.013\times10^5$ Pa, $\rho = 1.21$ kg/m^3, and Pr = 0.71). Atalla and Sgard [51] proposed a correction to the geometric tortuosity by accounting for flow distortions within the vicinity of the perforations

$$\alpha_\infty = 1+2\frac{\varepsilon}{l} \tag{2.20}$$

where ε is an end correction length defined by Jaouen and Bécot [54] as $\varepsilon = \left(1-1.13\xi-0.09\xi^2+0.27\xi^3\right)\frac{8a}{3\pi}$ with $\xi = 2\sqrt{\frac{\beta}{\pi}}$. The effective characteristic impedance and wavenumber of the perforated plate was defined using Equations 2.18, 2.19, and 2.20

$$Z_{0,p} = \sqrt{K\rho_e} \tag{2.21}$$

$$k_p = \omega\sqrt{\frac{K}{\rho_e}} \tag{2.22}$$

Assuming that the semi-infinite fluid media on both sides of the perforation is air, the Transfer Matrix Method (TMM) can be applied [5], using Equations 2.21 and 2.22, to determine the transmission loss

$$L_T = 20\log_{10}\left\{\left|\cos\left(k_p l\right)+\frac{i}{2}\left[\frac{Z_{0,p}}{\beta Z_0}+\frac{\beta Z_0}{Z_{0,p}}\right]\sin\left(k_p l\right)\right|\right\} \tag{2.23}$$

where Z_0 is the characteristic impedance of air. Atalla and Sgard provided experimental validation for their perforation impedance model for $7\times10^{-5} \leq d/\lambda \leq 7\times10^{-3}$ and $3\times10^{-4} \leq l/\lambda \leq 0.2915$.

2.2.2 Transmission loss models with bias flow

Howe [33] proposed an analytical model for the Rayleigh conductivity of a circular aperture in an infinitely thin plate, subject to low Mach number bias flow. He assumed that a circular, cylindrical vortex sheet is shed downstream of the aperture, at a strength determined by the condition that u' and p' remain finite at the rim of the aperture (Kutta condition). The theory was extended to a perforated screen with the assumption that the perforations were sufficiently separated such that the flow details of neighboring apertures do not influence each other. The results indicated significant attenuation at low Strouhal numbers based on orifice radius and orifice mean flow velocity. The level of attenuation decreased with increasing Strouhal number. The model is applicable for low Mach number flow, low porosity, and acoustic wavelengths that significantly exceed the perforation dimensions. Howe's expression for the Rayleigh conductivity is

$$K_R = 2a\left\{1+\frac{\frac{\pi}{2}I_1\left(St_a\right)e^{-St_a}-iK_1\left(St_a\right)\sinh\left(St_a\right)}{St_a\left[\frac{\pi}{2}I_1\left(St_a\right)e^{-St_a}+iK_1\left(St_a\right)\cosh\left(St_a\right)\right]}\right\} \tag{2.24}$$

where $\mathrm{St}_a = \omega a/U$ is the Strouhal number based on the bias flow velocity through the aperture and the aperture radius, and I_1 and K_1 are the modified Bessel functions of the first and second

kind, respectively. The real and imaginary components of Equation 2.24 are expressed in normalized form as γ_R=Re{K_R/(2a)} and δ_R=Im{K_R/(2a)}, respectively.

The transmission coefficient was defined as

$$T_c = \frac{\left(4\beta / \pi M_p\right)\left(\gamma_R - i\delta_R\right)}{\left|St_a + \left(i4\beta / \pi M_p\right)\left(\gamma_R - i\delta_R\right)\right|^2} \tag{2.25}$$

where the M_p = U/c is the Mach number of the flow in the perforations. The accuracy of this model in the application of perforated plates was corroborated experimentally by Hughes and Dowling [36] and by Eldredge and Dowling [37]. Collectively, these authors verified Howe's model for $2.18\times10^{-4} \leq d/\lambda \leq 0.016$, $0.02 \leq \beta \leq 0.11$, and $0 \leq M_p \leq 0.09$. The transmission loss is determined by Equations 2.25 and 2.16.

Jing and Sun [41,42] investigated the effect of thickness on the acoustic impedance of perforated plates with bias flow. The authors recast Howe's analytical expression [33] for the Rayleigh conductivity in terms of impedance. From Equation 2.10, the normalized, specific acoustic impedance of a perforation was expressed using the real and imaginary components of the Rayleigh conductivity

$$z = \left(\frac{\pi ka}{2\beta}\right)\left(\frac{\delta_R}{\gamma_R^2 + \delta_R^2} - i\frac{\gamma_R}{\gamma_R^2 + \delta_R^2}\right) \tag{2.26}$$

An additional reactance term was included to account for plate thickness

$$z_e = z + i\frac{kl}{\beta} \tag{2.27}$$

The acoustic impedance was measured experimentally using an impedance tube setup, and their model was validated over a range of for $0.0129 \leq \beta \leq 0.0254$, $0.0027 \leq d/\lambda \leq 0.0027$, and $0 \leq M_p$

$\leq$ 0.05. Jing and Sun's experimental measurements and model predicted an increase in absorption with increasing plate thickness. The authors further extended their work by solving Equation 2.12 numerically using the boundary element method [42]. Their numerical results indicated a decrease in reactance with increasing bias flow Mach number. They concluded that the damping characteristics of perforated plates behave similarly to thin plates at high flow speeds. The numerical results also indicated that the resistance can become negative, for $l/d >$ 0.75. Jing and Sun's analytical model, experiment, and numerical model indicated a linear increase in resistance with bias flow speed, for $M_p \geq 0.01$.

Bellucci, Flohr and Paschereit [43] examined the impedance characteristics of perforated plates backed by a solid walled cavity. In their analysis, the flow through the perforations was governed by the axisymmetric Navier-Stokes equations, and was assumed to be very low Mach number. *Vena contracta* effects were considered in their analysis using the discharge coefficient $C_D = 0.82$. A semi-empirical relation was used to determine the reactance component of their impedance model, where several expressions were employed to describe both orifice interaction and end corrections associated with the perforations. The model was validated with measurements from an impedance tube, modified to supply bias flow through the perforations. Their proposed semi-empirical model for the perforation impedance is [43]

$$Z_p = i\rho\omega \frac{\left(\Gamma l + l'\right)}{\beta} + Z_{cav} + \frac{\hat{\Phi}}{\beta \hat{u}_0} \tag{2.28}$$

where $\hat{\Phi}$ and $\hat{u}_0$ are the frequency-domain transforms of the pressure loss and velocity fluctuation in the perforation, respectively. Similar to the model of Tayong *et al.*, the cavity impedance Z_{cav} was defined by the characteristic impedance for a perforated panel surrounded on

both sides by semi-infinite fluid media. For bias flow speeds that are significantly larger than the velocity fluctuations, Bellucci *et al.* approximated the pressure loss term as

$$\hat{\Phi} = \rho \varsigma U \hat{u}_o \tag{2.29}$$

where Howe's vortex sheet model [33] was used to define the pressure loss coefficient

$$\varsigma = \frac{\pi a}{2}\left(\frac{\delta_R St_a}{(\gamma_R^2 + \delta_R^2)} \right) \tag{2.30}$$

The thickness was multiplied by a factor which accounted for variation in acoustic pressure [4]

$$\Gamma = 1 - \frac{2J_1(k_t a)}{k_t a J_0(k_t a)} \tag{2.31}$$

$k_t = \omega/c_t$ is the acoustic wave number in the transmitted region downstream of the plate. The end correction l' was determined by the semi-empirical relation

$$l' = \varphi(He)\chi(\beta)\psi(St_a)\theta(St_{ac}) \tag{2.32}$$

$$\varphi(He) = 2 \cdot 0.8216a\left[1 + \frac{(0.77He)^2}{1 + 0.77He} \right]^{-1} \tag{2.33}$$

$$\chi(\beta) = 1 - \sqrt{\beta/2} \tag{2.34}$$

$$\psi(St_a) = \frac{0.3\left(6/St_a^2\right) + 1}{6/St_a^2 + 1} \tag{2.35}$$

$$\theta(St_{ac}) = 1 - 0.3/St_{ac}^{0.6} \tag{2.36}$$

In order to determine the acoustic Strouhal number $St_{ac} = \omega R / |\hat{u}_o|$, $\hat{u}_0$ was determined experimentally from the authors' impedance measurement. The model of Bellucci *et al.* was validated experimentally for $5.89\times10^{-4} \leq d/\lambda \leq 0.0237$, $M_p < 0.02$, and $0.0103 < \beta < 0.0231$.

Betts [55] developed an compressible bias flow impedance model by modifying Crandall's impedance model [4,50] to account for bias flow. He obtained an expression for the normalized specific acoustic impedance

$$z_p = \frac{16\nu l}{c\beta C_D d^2} + 2.82\frac{\sqrt{\omega\nu}}{c\beta C_D}\frac{l}{d} + \frac{\rho}{\rho_p}\frac{(1-\beta^2)}{2c(\beta C_D)^2}\left[2u_b + 1.2u_{rms}\right] + \cdots$$
$$i\left(\frac{\omega l}{c\beta C_D} + 2.82\frac{\sqrt{\omega\nu}}{c\beta C_D}\frac{l}{d} + \frac{8d}{3\pi\psi(\beta)}\right) \tag{2.37}$$

ρ, c, ν, u_b and u_{rms} are the density, propagation speed, kinematic viscosity of air, bias flow and root mean square (rms) velocity, respectively, upstream of the plate. C_D is the discharge coefficient and ψ is Fok's function. Betts estimated the rms velocity experimentally, using the plane wave relation between the acoustic velocity and the sound pressure level

$$|u'| = \frac{p_{ref}\,10^{SPL/20}\sqrt{2}}{\rho c} \tag{2.38}$$

where $p_{ref} = 2\times10^{-5}$ Pa is the reference pressure. Experimental validation was provided for $0.0007 \leq d/\lambda \leq 0.0129$, $0.059 < \beta < 0.165$, and $0.00221 \leq M_p \leq 0.357$.

Recent efforts in modeling the damping characteristics of perforated plates subject to bias flow were either numerical or experimental, due to the complexity of the modeled problem [42,44,56,57]. Lee, Ih and Peat [44] applied Howe's analysis [33] to a thick orifice in a duct containing incompressible flow. The numerical approach was similar to Jing and Sun's analysis [42], however, Lee *et al*. included hole interaction effects through a correction to the orifice

thickness. Their results indicated a decrease in reactance with increasing porosity, which the authors attributed to interaction effects. Mendez and Eldredge [56] used Large-Eddy Simulation (LES) to model the unsteady behavior of the flow near the perforations. The reliability of Mendez and Eldredge's results were used to corroborate existing analytical [33] and numerical models [42,43]. They emphasized the need to model the jet profile in order to obtain more accurate predictions of the damping characteristics of perforated plates. Aygun and Attenborough [57] demonstrated experimentally an increase in insertion loss with decreasing open area ratio β, and increasing bias flow speed. The upstream Mach number of the bias flow in their experiments was subsonic ($M_1 = 0.016$). Their measurements predicted a large insertion loss increase at low frequency, which is consistent with previous investigators [33,34,35,41,43]. The authors only reported experimental evidence of the bias flow effects on insertion loss; no insertion loss or impedance model was specified in their study that accounted for the effect of bias flow.

The applicability of the aforementioned insertion loss models [33,41,43,55] are limited based on the assumptions made in the respective works. Howe [33] and Jing and Sun [41] assumed no interaction between the perforations, therefore restricting their models to low porosity plates. Betts [55] accounts for HIE, however, his model does not include possible effects of bias flow on the mass end correction associated with the perforations. The *vena contracta* of the jet was included in Bellucci *et al.* and Betts' model using the contraction coefficient, which both investigators [43,55] assumed to be constant. The models of Howe, Jing and Sun, and Bellucci *et al.* were experimentally validated only at low Mach number to be consistent with the assumption of negligible changes in the bias flow density. All previous

models [33,41,43,55] were experimentally validated only at low frequency, or low d/λ, to ensure one-dimensional wave propagation.

A bias flow model is presented in the following chapter with the aims of rectifying the shortcomings of previous models [33,41,43,55]. Interactions between the perforations are considered in this work through the use of Fok's function [11]. An estimate of the *vena contracta* location was used to determine the effect of bias flow on the end correction associated with the perforations. The *vena contracta* of the jet was not assumed constant in this study; empirical data was used to determine the jet area contraction as a function of bias flow speed and the geometric properties of the perforated plate.

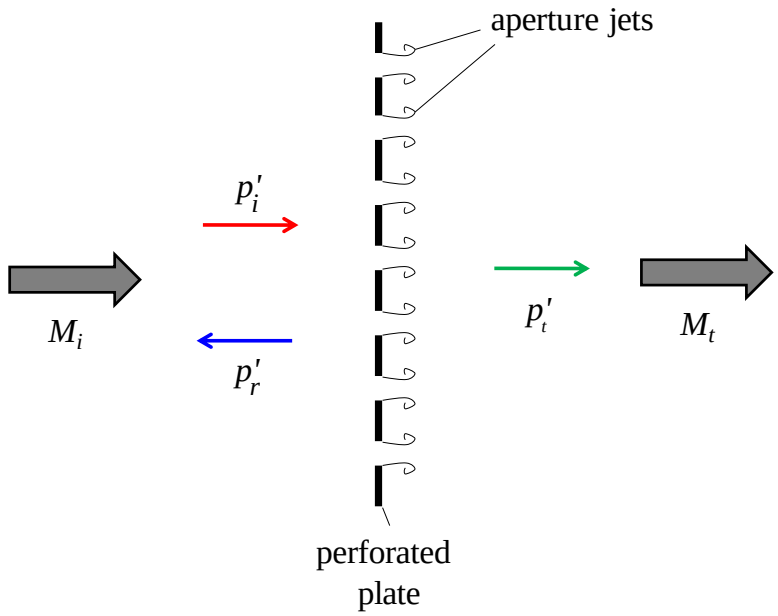

Figure 2.1: Perforated plate with bias flow, indicating directions of the mean flow and pressure fluctuations

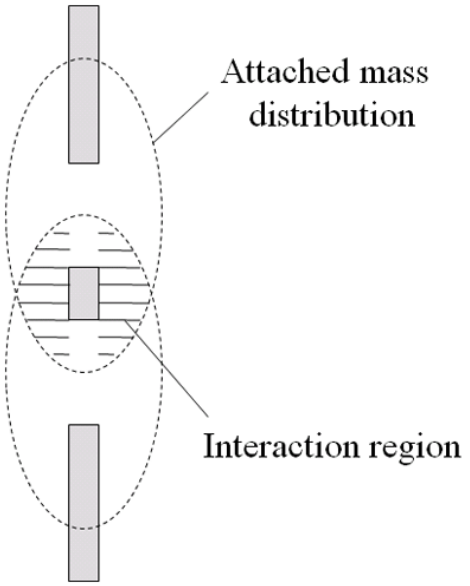

Figure 2.2: Cutaway view of two holes, showing the attached mass distributions associated with each hole and the interaction region between both holes [50]

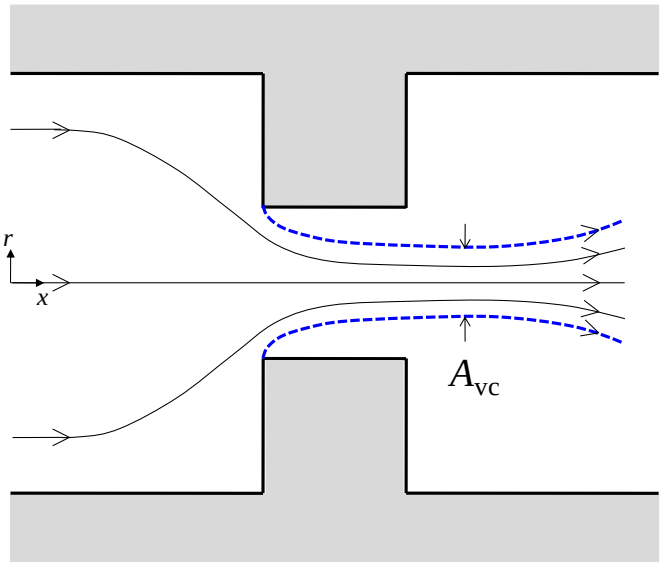

Figure 2.3: Schematic of streamlines in a duct containing a single contraction. Blue dashed lines indicate the separation streamlines

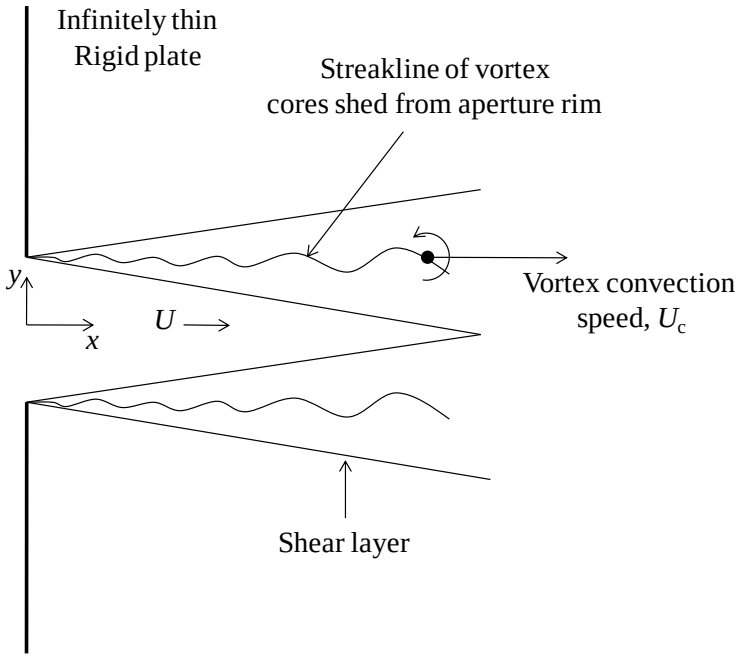

Figure 2.4: Aperture in an infinite plane with bias flow jet. Unsteady, axisymmetric vorticity is assumed to shed from the rim, convecting at a velocity U_c that is parallel to the x-axis and within the mean flow shear layer [33]

Chapter 3

CURRENT THEORICAL MODEL

In this section, the development of the insertion loss model for both static and bias flow cases are presented. The formulation of the model is detailed, beginning from fundamental principles. The transmission loss models presented are those which will be compared to the models reported in Section 2.2.1 and 2.2.2.

3.1 Governing equations

The problem considered in this work is governed by the acoustic equations, which are derived from mass continuity and Euler's equation

$$\frac{\partial \rho}{\partial t} + \nabla \cdot (\rho \mathbf{u}) = 0 \tag{3.1}$$

$$\frac{\partial (\rho \mathbf{u})}{\partial t} + \nabla \cdot (\mathbf{u} \otimes (\rho \mathbf{u})) = -\nabla p \tag{3.2}$$

where $\otimes$ denotes the tensor product. The pressure, velocity, and density are decomposed into perturbations from their mean state: $p = \bar{p} + p'$, $\mathbf{u} = \bar{\mathbf{u}} + \mathbf{u}'$, $\rho = \bar{\rho} + \rho'$, where $\bar{()}$ and $()'$ indicate the mean and perturbed states, respectively. The decomposed variables are substituted back into Equations 3.1 and 3.2, and the equations are linearized by discarding terms containing the product of two or more perturbation quantities. Further assuming that the mean quantities do not vary in space and time results in the following set of equations

$$\frac{D\rho'}{Dt} + \bar{\rho}\left(\nabla \cdot \mathbf{u}'\right) = 0 \tag{3.3}$$

$$\bar{\rho}\frac{D\mathbf{u}'}{Dt} = -\nabla p' \tag{3.4}$$

where the material derivative $\left(\frac{D}{Dt} = \frac{\partial}{\partial t} + \bar{\mathbf{u}} \cdot \nabla\right)$ has been applied. Acoustic waves are isentropic disturbances, where changes in pressure with respect to density are related through the sound speed c

$$c^2 = \left(\frac{\partial p}{\partial \rho}\right)_s = \frac{\gamma \bar{p}}{\bar{\rho}} \tag{3.5}$$

γ is the ratio of specific heat at constant pressure to specific heat at constant volume, and is equal to 1.4 for air at 293 K. For one-dimensional propagation and mean flow in a duct, $\mathbf{u} = \left(\bar{u} + u'\right)\hat{\mathbf{e}}_x$, $\nabla = \frac{\partial}{\partial x}\hat{\mathbf{e}}_x$, and $\frac{D}{Dt} = \frac{\partial}{\partial t} + \bar{u}\frac{\partial}{\partial x}$, where $\hat{\mathbf{e}}_x$ is the unit vector corresponding to the axial direction. Cross differentiating Equations 3.3 and 3.4, and combining with Equation 3.5 results in the convected wave equations for both u' and p'

$$\left(\frac{D^2}{Dt^2} - c^2\frac{\partial^2}{\partial x^2}\right)p' = 0 \tag{3.6}$$

$$\left(\frac{D^2}{Dt^2} - c^2\frac{\partial^2}{\partial x^2}\right)u' = 0 \tag{3.7}$$

Assuming time harmonic disturbances of the exponential form $e^{i\omega t}$, where $\omega = 2\pi f$ is the angular frequency, the general solutions of Equations 3.6 and 3.7 are, respectively

$$p'(x,t) = Ae^{i\left(\omega t - \frac{kx}{1+M}\right)} + Be^{i\left(\omega t + \frac{kx}{1-M}\right)} \tag{3.8}$$

$$u'(x,t) = Ce^{i\left(\omega t - \frac{kx}{1+M}\right)} + De^{i\left(\omega t + \frac{kx}{1-M}\right)} \tag{3.9}$$

where M is the mean flow Mach number, $k=\omega/c$ is the acoustic wave number, A and B are the amplitudes of the right and left running acoustic pressure waves, respectively, and C and D amplitudes of the right and left running acoustic velocity waves, respectively. The constants C and D in Equation 3.9 can be expressed in terms of A and B using Equation 3.4:

$$u'(x,t) = \frac{A}{\rho c} e^{i\left(\omega t - \frac{kx}{1+M}\right)} - \frac{B}{\rho c} e^{i\left(\omega t + \frac{kx}{1-M}\right)} \tag{3.10}$$

3.2 Static model

In the present study, the insertion loss of the perforated plate is modeled theoretically by considering a duct containing a single contraction chamber, as illustrated in Figure 3.1. The development follows the inertial model of Ffowcs Williams and Dowling [58] with important modifications related to end effects. Besides the neglect of viscous effects, the other major assumption is that the wavelength of sound is larger than the contraction diameter, which allows the approximation of the sound waves throughout the duct as one-dimensional. Acoustic waves that are confined spatially to regions such as ducts will have modes that will propagate or decay, depending on the frequency of excitation [5]. If the waves in the duct are excited at a frequency below the cutoff frequency of a certain mode, the mode is considered evanescent and will decay at appreciable distances from the source. The plane wave assumption restricts the model accuracy to only frequencies below the cutoff frequency corresponding to plane wave

propagation inside perforations. If the perforations are approximated as circular ducts, the cutoff frequency can be expressed non-dimensionally as d/λ =0.5861.

The acoustic pressure throughout the domain is expressed using Equation 3.9. In the static case, where $M = 0$, the acoustic pressure reduces to

$$\begin{aligned} p' &= I\, e^{i\omega(t-x/c_1)} + R\, e^{i\omega(t+x/c_1)} \quad , \; x < 0 \\ p' &= B\, e^{i\omega(t-x/c_2)} + C\, e^{i\omega(t+x/c_2)} \quad , \; 0 \le x \le l \\ p' &= T\, e^{i\omega(t-x/c_3)} \quad , \; x > l \end{aligned} \tag{3.11}$$

where I, R, and T are the amplitudes of the incident, reflected, and transmitted waves, respectively. The subscripts 1, 2, and 3 are used as reference to the regions upstream, inside, and downstream of the contraction respectively (Figure 3.1). The amplitudes B and C of the acoustic pressure waves inside the contraction are determined by application of the conservation equations. The mass flux into the contraction interface ($x = 0$) must equal the mass flux out of the contraction.

$$\rho A_1 u_1' = \rho A_2 u_2' \tag{3.12}$$

In addition, the energy flux into the contraction interface must equal the energy flux out of the contraction.

$$A_1 p_1' u_1' = A_2 p_2' u_2' \tag{3.13}$$

Combining Equations 3.12 and 3.13 shows that the energy flux condition is a statement of continuity in the acoustic pressure at the contraction interface, $p_1' = p_2'$. The same conditions of mass and energy flux apply at the expansion interface ($x = l$). Assuming that the pressure

fluctuations propagate at the same speed throughout the entire domain ($c = c_1 = c_2 = c_3$) and that $A_3 = A_1$, the following set of algebraic equations which relate R and T to I are obtained:

$$T = \frac{2Ie^{i\omega l/c}}{2\cos\left(\frac{\omega l}{c}\right) + i\left[\frac{A_1}{A_2} + \frac{A_2}{A_1}\right]\sin\left(\frac{\omega l}{c}\right)} \tag{3.14}$$

$$R = \frac{iI\left[\frac{A_1}{A_2} - \frac{A_2}{A_1}\right]\sin\left(\frac{\omega l}{c}\right)}{2\cos\left(\frac{\omega l}{c}\right) + i\left[\frac{A_1}{A_2} + \frac{A_2}{A_1}\right]\sin\left(\frac{\omega l}{c}\right)} \tag{3.15}$$

It can be shown from Equations 3.14 and 3.15 that the sum of the energies in the reflected and transmitted waves equals the energy of the incident wave:

$$|R|^2 + |T|^2 = |I|^2 \tag{3.16}$$

In other words, this is a lossless process as evident from the lack of any dissipative (viscous) effects in the formulation of the governing equations. Adopting Equation 2.5, Equation 2.3, and Equation 2.4 for zero bias flow, the transmission loss is

$$L_T = 10\log_{10}\left(\frac{|I|^2}{|T|^2}\right) \tag{3.17}$$

Substituting Equation 3.14:

$$L_T = 10\log_{10}\left[1 + \frac{1}{4}\left(\frac{A_1}{A_2} - \frac{A_2}{A_1}\right)^2 \sin^2\left(\frac{\omega l}{c}\right)\right] \tag{3.18}$$

In applying Equation 3.18 to a perforated plate, the porosity is $\beta = A_2/A_1$ and the plate thickness is l. The transmission loss in Equation 3.18 is symmetric in A_1 and A_2 and is therefore the same

whether the chamber is expanding ($A_2 > A_1$) or contracting ($A_2 < A_1$). With these substitutions, Equation 3.18 becomes

$$L_T = 10\log_{10}\left[1+\frac{1}{4}\left(\frac{1}{\beta}-\beta\right)^2 \sin^2(kl)\right] \tag{3.19}$$

As discussed in Section 2.1.3, an end correction for the thickness must be applied to account for the effect of acoustic interaction between the holes of the perforated plate [11-16]. The volume of the disturbed mass adjacent to the ends of the perforation can be idealized as a cylindrical volume of total length *l*' (Figure 3.2). The additional length is added to the physical thickness of the plate, resulting in an effective thickness

$$l_{e,s} = l + l' \tag{3.20}$$

where *l'* is the correction length defined as

$$l' = \frac{8d}{3\pi\psi(\xi)} \tag{3.21}$$

The $8d/(3\pi)$ term in Equation 3.21 is the end correction applicable to a single orifice in a spatially infinite plate [7]. The additional term in the denominator, $\psi(\xi)$, originates from Fok's work [11], who considered the problem of a circular tube of diameter, *D*, with a partition containing a circular orifice of diameter, *d*, located on the axis of the tube. His analysis showed that as d/D approaches unity, the orifice conductivity becomes infinite, and the end correction tends to zero. Conversely, for $d/D << 1$, the end correction approaches the value for a single orifice in an infinite plate, $8/(3\pi)$. Fok derived a function that describes this behavior:

$$M(\xi) = \begin{array}{l} 1 - 1.40925\xi + 0.33818\xi^3 + \ldots \\ 0.06793\xi^5 - 0.02287\xi^6 + \ldots \\ 0.03015\xi^7 - 0.01641\xi^8 \end{array} \tag{3.22}$$

where $\psi(\xi) = [M(\xi)]^{-1}$ is the reciprocal of Fok's function, and its argument $\xi = d/D$. Nesterov [12] showed experimentally that Equation 3.22 is valid for both single orifice and multiple orifices. The case of multiple orifices is representative of a perforated plate, where each orifice is confined within a lattice of characteristic length D, and the ratio of orifice area to lattice area is equal to the porosity β of the perforated plate. Nesterov showed that the effect of lattice geometry on Fok's function is negligible; indicating that the end correction associated with the perforations is independent of the nature of perforation grating. From this result, a circular lattice geometry of diameter D can be assumed for all perforated plates, and ratio of perforation area to lattice area, or porosity, can be defined as $\beta = d^2/D^2$. The argument in Fok's function can therefore be rewritten, using porosity, as $\xi = \sqrt{\beta}$. As β approaches zero, the lattice area effectively becomes infinite with respect to the perforation and $\psi(0) = 1$, resulting in an end correction equal to a single orifice (Equations 3.21 and 3.22). Fok's function modifies the effective thickness of a single orifice in an infinite baffle by accounting for finite lattice area. Nesterov's experiments showed that HIE are negligible for $\beta < 0.10$. The porosities of the perforations used in the current work are greater than 0.22, indicating that interaction effects must be considered for all the perforations in this study (Table 4.1). Incorporating the effective thickness, Equation 3.19 becomes:

$$L_T = 10\log_{10}\left\{1 + \frac{1}{4}\left(\frac{1}{\beta} - \beta\right)^2 \sin^2\left[k\left(l + \frac{8d}{3\pi\psi(\sqrt{\beta})}\right)\right]\right\} \tag{3.23}$$

Equation 3.23 is a variant of the original result by Ffowcs Williams and Dowling [58], modified to include end corrections and HIE. It is noted that the transmission loss model contains a sine-squared term, and therefore exhibits oscillatory behavior that is governed by the effective thickness. The oscillatory behavior is caused by standing-wave-formed resonances inside the contraction that are analogous to Fabry-Pérot resonance observed in optics [14-16].

The transmission loss was derived using one-dimensional, inviscid theory, assuming no reflections from $x = \pm\infty$, and that $A_3 = A_1$. In the absence of an area contraction, $\beta = 0$ and Equation 3.23 predicts zero transmission loss. This implies from Equation 2.5 that $\Pi_i = \Pi_t$ without a perforated plate, or from Equation 2.6, $\Pi_i = \Pi_{t,0}$. Therefore, the transmission loss expression (Equation 3.23) derived in this section is equal to the insertion loss. The predictions given by Equation (3.23) will be compared to insertion loss measurements, and to the previous theoretical models noted in Section 2.2.1.

3.3 Bias flow model

The current model for the acoustic transmission loss of perforated plates with bias flow was formulated based on the work of Durrieu *et al.* [32] and Hofmans *et al.* [1]. Similar to the static case, the perforated plate is modeled as a duct containing a single contraction chamber, only now there is flow along the duct axis (Figure 3.3(a)). The subscripts 1, 2, *j*, *m*, and 3 are used as reference to regions upstream of the contraction, within contraction, the *vena contracta* location, the mixing region downstream of the contraction, and the fully mixed region, respectively. The contraction is a discontinuous change in area at $x = 0$, and the ratio of contracted to upstream area is defined by $\beta = A_2/A_1$. The contraction expands discontinuously at $x = l$ to the original duct area, $A_3 = A_1$. The Reynolds number (Ud/ν) in the contraction was assumed to be sufficiently large so that viscosity has the sole effect of flow separation at the

upstream corner of the contraction, as illustrated in Figure 3.3(a). A jet of uniform velocity is formed at the *vena contracta*, located at $x = l_{vc}$. Irreversible losses occur in the mixing region downstream of the *vena contracta*; the losses are represented in this study through fluctuations in entropy. After some distance l_m downstream from the expansion, the flow is assumed to be fully mixed and the acoustic and mean flow properties can be approximated as one dimensional in region 3.

Recalling Section 3.1, a prerequisite of the acoustic pressure being represented by Equation 3.8 is that the mean flow cannot be varying in both time and space. The former condition is satisfied by assuming steady mean flow throughout the entire domain. Realistically, however, the fluid accelerates slightly before the contraction and within the contraction up to the *vena contracta*, violating the latter condition. In the following analysis, the change in mean flow speed is discontinuous at $x = 0$, and the separation of the jet and its profile is modeled as a contraction of constant area, equal to the *vena contracta* area (Figure 3.3(b)). This allows the *vena contracta* effect to be included such that Equation 3.8 is applicable within the contraction. The jet Mach number $M_2 = M_j$ is subsonic, and the acoustic wavelength is assumed to be much larger than the contraction diameter. This allows the approximation of one-dimensional propagation in regions 1, 2, and 3 of the duct. The acoustic pressure (Equation 3.8) can be determined only after the mean quantities, namely the density, Mach number and wave propagation speed, are known.

The flow between regions 1 and 2 is inviscid and isentopic. Therefore the following integral forms for conservation of mass and energy apply, along with the isentropic relation:

$$\rho_1 u_1 = \rho_2 u_2 \beta C_c \tag{3.24}$$

$$\frac{\gamma}{\gamma-1}\frac{p_1}{\rho_1}+\frac{u_1^2}{2}=\frac{\gamma}{\gamma-1}\frac{p_2}{\rho_2}+\frac{u_2^2}{2} \tag{3.25}$$

$$\frac{p_1}{\rho_1^{\gamma}}=\frac{p_2}{\rho_2^{\gamma}} \tag{3.26}$$

Equation 3.24 implies that the *vena contracta* area $A_2 = A_{vc} = A_1\beta C_c$. Downstream of the duct expansion, the conservation equations are applied to the control volume illustrated in Figure 3.4. The control volume (dashed black line) is defined such that the left surface is located at $x = l$. The top and bottom surfaces are coincident with the walls of the duct, and the right surface is located at length l_m that is sufficiently downstream of the expansion so that the jet has become completely mixed and the flow properties are uniform along this surface. Mass conservation between the left ($x = l$) and right ($x = l + l_m$) surfaces of the control volume requires that

$$\rho_2 u_2 \beta C_c = \rho_3 u_3 \tag{3.27}$$

Assuming that the flow expands adiabatically

$$\frac{\gamma}{\gamma-1}\frac{p_2}{\rho_2}+\frac{u_2^2}{2}=\frac{\gamma}{\gamma-1}\frac{p_3}{\rho_3}+\frac{u_3^2}{2} \tag{3.28}$$

Neglecting friction along the walls of the duct, the momentum conservation between the left and right surfaces of the control volume yields

$$p_2+\rho_2 u_2^2 \beta C_c = p_3+\rho_3 u_3^2 \tag{3.29}$$

The contraction coefficient C_c in Equations 3.24, 3.27 and 3.29 can be determined from the discharge coefficient. Assuming C_ρ=1 and C_v=0.97, from Section 2.1.4, $C_c = C_D/0.97$. The discharge coefficient C_D is determined based on the empirical correlation formula provided by Smith and Van Winkle [25] for perforated plates

$$C_{\mathrm{D}} = K\left(\frac{d}{P}\right)^{0.10} \tag{3.30}$$

where K is specified by the Reynolds number, $\mathrm{Re_d} = U_p d/v$, and l/d, using Figure 3.5. The distance between perforations, P, is determined based on the array geometry of the perforations. If the array is rectilinear (Figure 3.6(a)), P is defined as [23]

$$P = 0.89\frac{d}{\sqrt{\beta}} \tag{3.31}$$

and for the staggered array (Figure 3.6(b))

$$P = 0.9498\frac{d}{\sqrt{\beta}} \tag{3.32}$$

The mean flow quantities M_2, c_2, ρ_2, M_3, c_3, and ρ_3 are determined from Equations 3.24-3.29 if M_1, c_1, and ρ_1 are specified. Using Equations 3.24 and 3.25,

$$\frac{1}{2}M_1^2 + \frac{1}{\gamma - 1} = \frac{1}{2}\frac{M_1^2}{C_c^2\beta^2}\left(\frac{\rho_1}{\rho_2}\right)^2 + \frac{1}{\gamma - 1}\left(\frac{\rho_2}{\rho_1}\right)^{\gamma - 1} \tag{3.33}$$

ρ_2 can be determined using an iterative procedure. Equations 3.24, 3.26, and 3.5 then determine the Mach number and sound speed in region 2

$$M_2 = \left(\frac{\rho_1}{\rho_2}\right)^{\frac{\gamma+1}{2}} \frac{M_1}{C_c\beta} \tag{3.34}$$

$$c_2 = c_1\left(\frac{\rho_1}{\rho_2}\right)^{\frac{1-\gamma}{2}} \tag{3.35}$$

Equation 3.28 is rewritten in terms of Mach number

$$M_3^2 = \left(\frac{c_2}{c_3}\right)^2 \left[M_2^2 + \frac{2}{\gamma - 1}\right] - \frac{2}{\gamma - 1} \tag{3.36}$$

where the c_2/c_3 is determined by applying Equations 3.29, 3.27, and 3.5

$$\left(\frac{c_2}{c_3}\right) = \frac{C_c \beta M_j}{M_3} \frac{1 + \gamma M_3^2}{1 + \gamma M_2^2 C_c \beta} \tag{3.37}$$

Combining Equations 3.37 and 3.36 results in an implicit equation for M_3, which is then computed using an iterative procedure. Once M_3 is determined, c_3 can be solved from Equation 3.37, and by conservation of mass between regions 2 and 3

$$\rho_3 = \rho_2 \frac{M_2 c_2}{M_3 c_3} C_c \beta \tag{3.38}$$

Equations 3.24-3.29 define the mean flow properties throughout the entire domain. In order to determine the acoustic response of the contraction, acoustic perturbations are introduced in the conservation equations. The same acoustic decompositions for density, pressure and velocity introduced in Section 3.1 are applied in regions 1 and 2. The density fluctuations in region 3 are modified to include important effects associated with the mixing of the jet in the mixing region.

Irreversible flow losses occur due to mixing and viscous dissipation as the flow develops downstream of the contraction (Figure 3.4). The losses associated with the flow in the mixing region produce fluctuations in entropy that propagate downstream at the mean flow velocity in region 3. The use of entropy fluctuations to describe dissipation in acoustic energy has been used by previous researchers [27-32] with experimental validation [28,29,31,32]. The method of characterizing dissipation through entropy fluctuations can readily be integrated into the perturbed energy equation, using principles from thermodynamics (see Appendix A). Using

Equation A.6, the acoustic density fluctuation in region 3 can be expanded in terms of pressure and entropy fluctuations

$$\rho_3' = \frac{p_3'}{c_3^2} - \frac{\bar{\rho}_3 \bar{T}_3 (\gamma - 1) s_3'}{c_3^2} \tag{3.39}$$

The second term on the right hand side of Equation 3.39 indicates a perturbation from the isentropic relation defined in Equation 3.5. By dimensional analysis, the numerator of the second term on the right side of Equation 3.39 represents a pressure disturbance that is dependent on entropy fluctuation

$$\delta = -\bar{\rho}_3 \bar{T}_3 (\gamma - 1) s_3' \tag{3.40}$$

Rewriting Equation 3.39

$$\rho_3' = \frac{p_3' + \delta}{c_3^2} \tag{3.41}$$

It is noted that δ is finite only in region 3 because the entropy fluctuations produced in region *m* are convected downstream by the mean flow. Since the entropy fluctuations propagate at speeds corresponding to the mean flow, these fluctuations are not directly involved in the propagation of true sound, and therefore do not contribute to the generation of sound power in the duct. The entropy fluctuations are equal to zero in both regions 1 and 2, because the flow processes there are assumed isentropic. The acoustic pressure throughout the domain (Figure 3.2) can be expressed from Equation 3.8

$$
\begin{aligned}
p' &= I\, e^{i(\omega t - k_1^+ x)} + R\, e^{i(\omega t + k_1^- x)} \quad , \; x < 0 \\
p' &= B\, e^{i(\omega t - k_2^+ x)} + C\, e^{i(\omega t + k_2^- x)} \quad , \; 0 < x < l \\
p' &= T\, e^{i(\omega t - k_3^+ x)} \quad , \; x > l_m
\end{aligned}
\tag{3.42}
$$

where the convected wave number is related to the acoustic wave number in the static case

$$
k_n^{\pm} = \frac{k_n}{1 \pm M_n} \tag{3.43}
$$

and *n* is the index of reference to the region within the domain. The acoustic velocity and density can be determined as a function of the acoustic pressure amplitudes from Equations 3.9 and 3.41, respectively, with $s' = 0$ in regions 1 and 2. Similar to the static case, corrections to the length of the contraction were applied in order to account for inertial effects near the abrupt area changes at $x=0$ and $x=l$. Additional corrections were applied to the end correction to include the effect of bias flow. Fok accounted for the influence of neighboring perforations on the inertial reactance of a single perforation by deriving an expression based on potential theory. Therefore, it was assumed that the end correction is applicable only where the flow is potential, and hence where the mean velocity field is irrotational.

Melling [50] proposed a qualitative explanation of the effect of bias flow on the end correction associated with perforated plates. The author stated that "up to the *vena contracta* the flow is laminar and becomes turbulent beyond it… the mass reactance due to the attached mass is presumed to exist and beyond this point is destroyed." Therefore the modification to the attached mass is determined as a function of the *vena contracta* location of the jet. Figure 3.7 schematically illustrates this effect for a single perforation. The *vena contracta* length, l_{vc}, is defined as the distance between the upstream side of the plate and the *vena contracta* location. The *vena contracta* location is approximated using the jet profile determined numerically by

Rouse and Abul-Fetouh [59]. Based on their data, the jet contraction *d/D* is within 1% of the fully contracted value at *x/a* =1.4 (Figure 3.8), and therefore it was assumed in this work that the *vena contracta* is located at l_{vc}=1.4*a*. Observing Figure 3.7, three cases are defined which scale the end correction with respect to l_{vc}:

$$\begin{aligned} l_{e,b} &= l + l' \quad ; \quad l_{vc} > l'/2 \\ l_{e,b} &= l'/2 + l_{vc} \quad ; \quad l < l_{vc} < l'/2 \\ l_{e,b} &= l + l'/2 \quad ; \quad l_{vc} < l \end{aligned} \tag{3.44}$$

where *l*' corresponds to the static end correction length defined in Equation 3.21. The first condition implies that the end correction length for perforations with bias flow cannot be larger than the end correction without bias flow. The second condition follows Melling's assumption that the static end correction length on the downstream side of the plate is limited by the *vena contracta* length. The third condition implies that although the *vena contracta* location resides within the contraction, significant mixing does not occur until the mean flow leaves the perforations, and therefore the mean flow is approximately potential inside the perforation.

Applying acoustic perturbations to *p*, ρ and *u*, and making the appropriate linearization results in the following set of equations

$$\begin{aligned} &\frac{\beta C_c}{c_2}\left[(1+M_2)Be^{-ik_2^+ l_{e,b}} - (1-M_2)Ce^{ik_2^- l_{e,b}}\right] = \cdots \\ &\frac{1}{c_3}\left[(1+M_3)Te^{-ik_3^+(l_{e,b}+l_m)} + M_3\delta e^{-ik_\sigma^+(l_{e,b}+l_m)}\right] \end{aligned} \tag{3.45}$$

$$\frac{1}{c_1}\left[(1+M_1)I - (1-M_1)R\right] = \frac{C_c\beta}{c_2}\left[(1+M_2)B - (1-M_2)C\right] \tag{3.46}$$

$$\left[\beta C_c\left(M_2^2+2M_2\right)+1\right]Be^{-ik_2^+ l_{e,b}}+\left[\beta C_c\left(M_2^2-2M_2+1\right)\right]Ce^{ik_2^- l_{e,b}}=\ldots$$
$$\left(1+M_3\right)^2 Te^{-ik_3^+\left(l_{e,b}+l_m\right)}+M_3^2\delta e^{-ik_\sigma^+\left(l_{e,b}+l_m\right)} \tag{3.47}$$

$$\frac{1}{\bar{\rho}_2}\left[\left(1+M_2\right)Be^{-ik_2^+ l_{e,b}}+\left(1-M_2\right)Ce^{ik_2^- l_{e,b}}\right]=\cdots$$
$$\frac{1}{\bar{\rho}_3}\left[\left(1+M_3\right)Te^{-ik_3^+\left(l_{e,b}+l_m\right)}-\frac{\delta}{\gamma-1}e^{-ik_\sigma^+\left(l_{e,b}+l_m\right)}\right] \tag{3.48}$$

$$\frac{1}{\bar{\rho}_1}\left[\left(1+M_1\right)I+\left(1-M_1\right)R\right]=\frac{1}{\bar{\rho}_2}\left[\left(1+M_2\right)B+\left(1-M_2\right)C\right] \tag{3.49}$$

Equations 3.45 and 3.46 are the continuity equations applied from regions 2 to 3, and 1 to 2, respectively; Equation 3.47 is the momentum conservation between the jet and fully mixed flow in region 3; and Equations 3.48 and 3.49 are the energy conservation equations from regions 2 to 3, and 1 to 2, respectively. Equations 3.45-3.49 are a linear system of equations

$$\begin{pmatrix} 0 & K_5 & K_6 & -K_3 & -K_4 \\ K_2 & -K_7 & -K_8 & 0 & 0 \\ 0 & K_9 & K_{10} & -K_{11} & -K_{12} \\ 0 & -K_{17} & -K_{18} & K_{15} & K_{16} \\ K_{14} & -K_{19} & -K_{20} & 0 & 0 \end{pmatrix}\begin{pmatrix} R \\ B \\ C \\ T \\ \delta \end{pmatrix}=\begin{pmatrix} 0 \\ -K_1 \\ 0 \\ 0 \\ -K_{13} \end{pmatrix}I \tag{3.50}$$

where K_1 through K_{20} are defined on the following page:

$$K_1 = \frac{1+M_1}{c_1} \qquad K_6 = -\beta C_c \frac{1-M_2}{c_2} e^{ik_2^- l_{e,b}} \qquad K_{11} = (1+M_3)^2 e^{-ik_3^+ (l_{e,b}+l_m)} \qquad K_{16} = \frac{-1}{\bar{\rho}_3(\gamma-1)} e^{-ik_\delta (l+l_m)}$$

$$K_2 = -\frac{1-M_1}{c_1} \qquad K_7 = \beta C_c \frac{1+M_2}{c_2} \qquad K_{12} = M_3^2 e^{-ik_\delta (l_{e,b}+l_m)} \qquad K_{17} = \frac{1+M_2}{\bar{\rho}_2} e^{-ik_2^+ l_{e,b}}$$

$$K_3 = \frac{1+M_3}{c_3} e^{-ik_3^+ (l+l_m)} \qquad K_8 = -\beta C_c \frac{1-M_2}{c_2} \qquad K_{13} = \frac{1+M_1}{\bar{\rho}_1} \qquad K_{18} = \frac{1-M_2}{\bar{\rho}_2} e^{ik_2^- l_{e,b}}$$

$$K_4 = \frac{M_3}{c_3} e^{-ik_\delta (l+l_m)} \qquad K_9 = \beta C_c \left[M_2^2 + 2M_2\right] e^{-ik_2^+ l_{e,b}} \qquad K_{14} = \frac{1-M_1}{\bar{\rho}_1} \qquad K_{19} = \frac{1+M_2}{\bar{\rho}_2}$$

$$K_5 = \beta C_c \frac{1+M_2}{c_2} e^{-ik_2^+ l_{e,b}} \qquad K_{10} = \beta C_c \left[M_2^2 - 2M_2\right] e^{ik_2^- l_{e,b}} \qquad K_{15} = \frac{(1+M_3)}{\bar{\rho}_3} e^{-ik_3^+ (l_{e,b}+l_m)} \qquad K_{20} = \frac{1-M_2}{\bar{\rho}_2}$$

The system of equations was solved using MATLAB's inbuilt reduced row echelon function. The acoustic energy flux of a wave propagating in a moving medium (Equation 2.4) is rewritten for plane wave propagation as

$$I = \frac{1}{\bar{\rho}_n c_n} \left[(1+M)^2 \left\langle p'^2_{+,n} \right\rangle - (1-M)^2 \left\langle p'^2_{-,n} \right\rangle \right] \tag{3.51}$$

The power associated with the forward and reflected waves is determined by multiplying by the appropriate reference area (Equation 2.3). Since $A_1 = A_3$, the transmission loss is therefore determined from Equations 2.3, 2.5, and 3.51

$$L_T = 10 \log_{10} \left(\frac{\bar{\rho}_3 c_3}{\bar{\rho}_1 c_1} \frac{(1+M_1)^2}{(1+M_3)^2} \frac{|I|^2}{|T|^2} \right) \tag{3.52}$$

where T is determined through the solution of Equation 3.50. If no area change is present in the duct, the incident wave in region 1 propagates downstream to region 3 without any loss in power. Therefore, like Equation 3.23, Equation 3.52 is also a valid expression for the insertion loss.

As mentioned in Chapter 2, the bias flow model proposed in this study (Equation 3.52) aims to overcome the shortcomings of previous models [33,41,43,55]. The proposed model

takes in account the variation of mean flow density, and is therefore not restricted to low subsonic bias flow. A combination of HIE and an estimate of the *vena contracta* location were used to model the effect of bias flow on the end correction length. The jet contraction diameter is determined based on measurements of the discharge coefficient [25] for perforated plates. Unlike previous works [43,55], the variations in the contraction coefficient with bias flow speed are included in the proposed model. The insertion loss predictions from Equation 3.52 will be validated against the previous models presented in Section 2.2.2, and experimental results reported in Chapter 5.

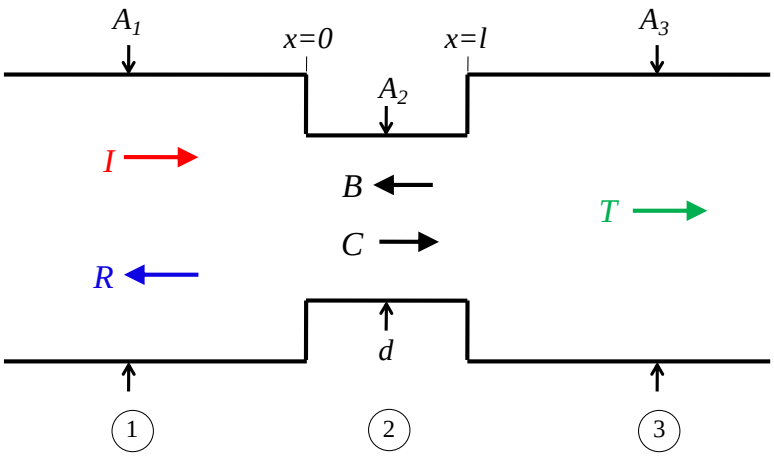

Figure 3.1: Contraction chamber used for one-dimensional modeling of transmission for static case [58]

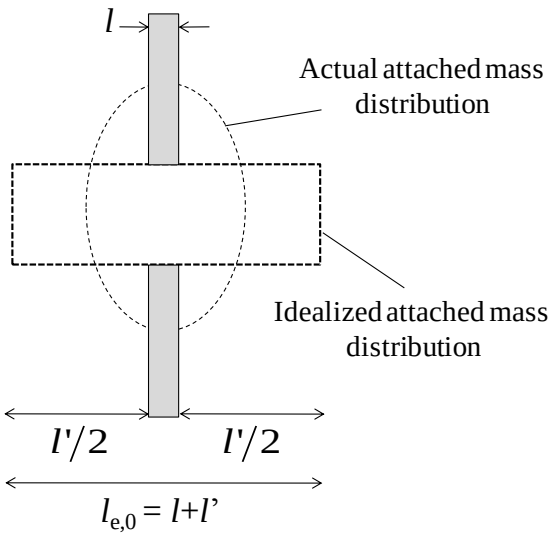

Figure 3.2: End correction showing actual and idealized attached mass distribution with associated length corrections [50]

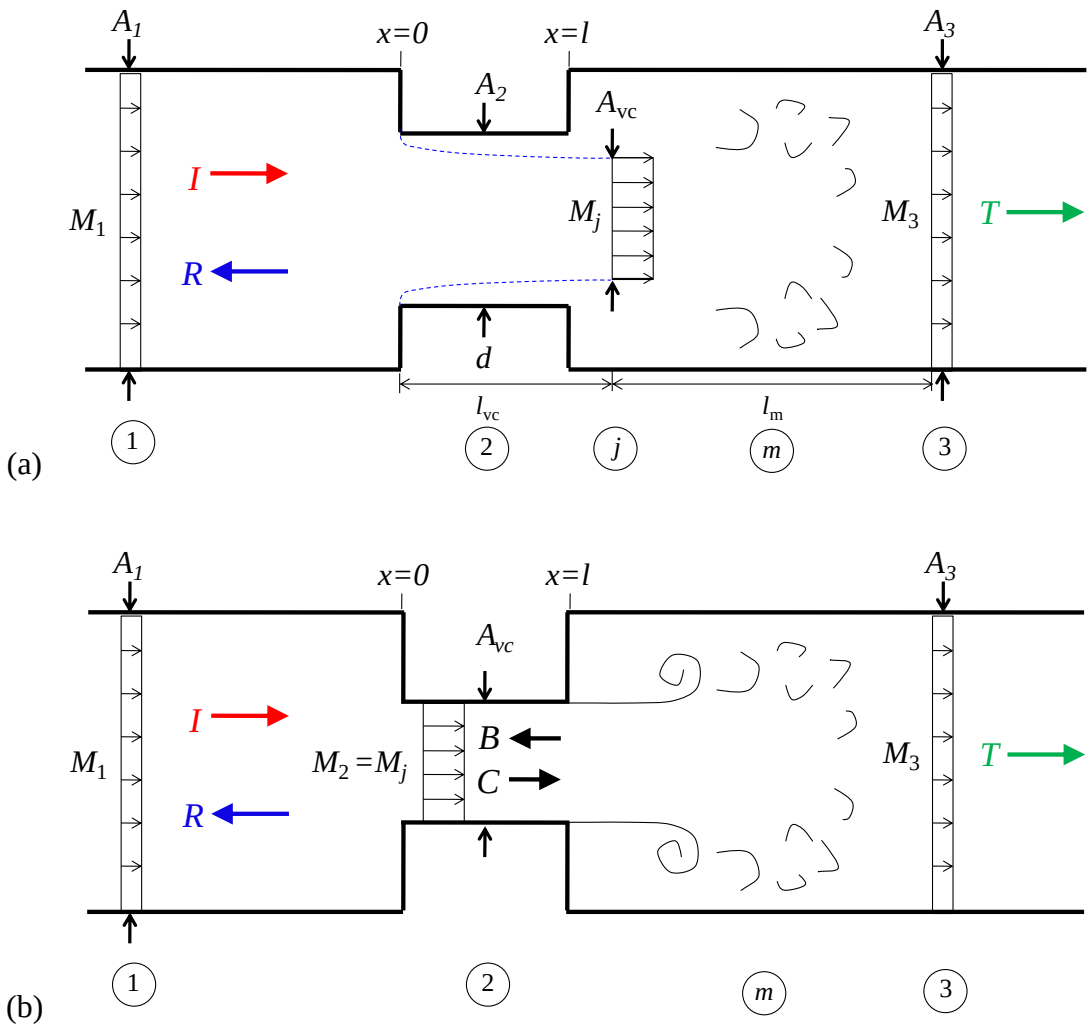

Figure 3.3: Contraction chamber used for modeling perforated plate acoustics **(a)** with contraction area corresponding to perforation diameter; **(b)** with contraction area equal to *vena contracta* area

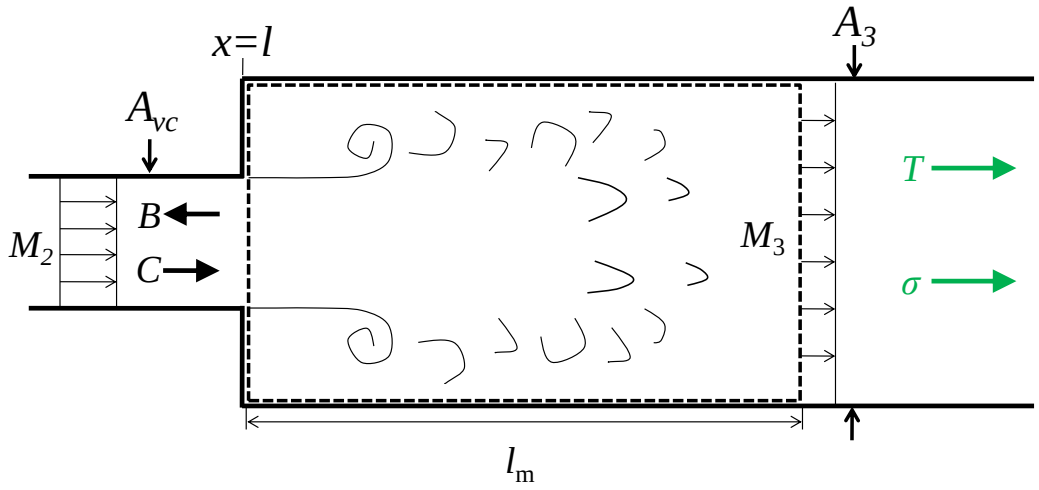

Figure 3.4: Control volume that contains the mixing region dowstream of the expansion

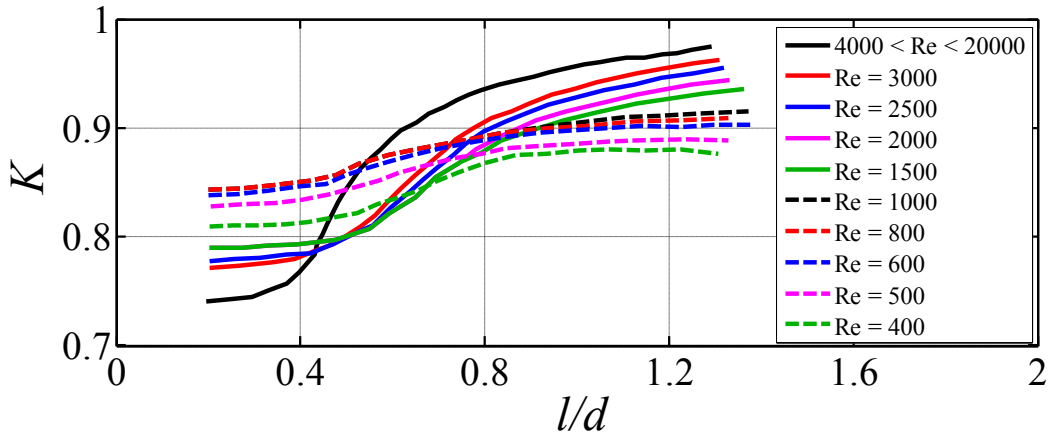

Figure 3.5: Correlation parameter *K* relating perforated plate discharge coefficient with *P*/*d* , *l*/*d* and Reynolds number [25]

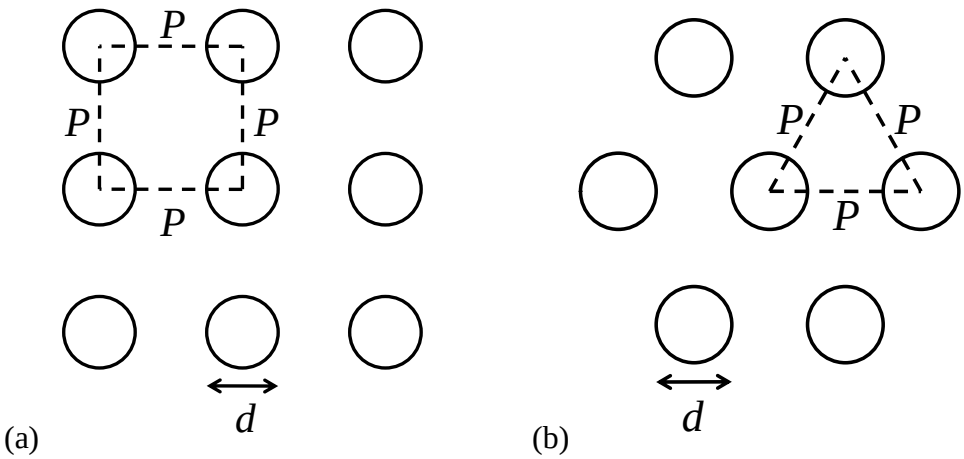

Figure 3.6: Perforation hole geometry: **a)** rectilinear (square) array and; **b)** staggered (triangular) array

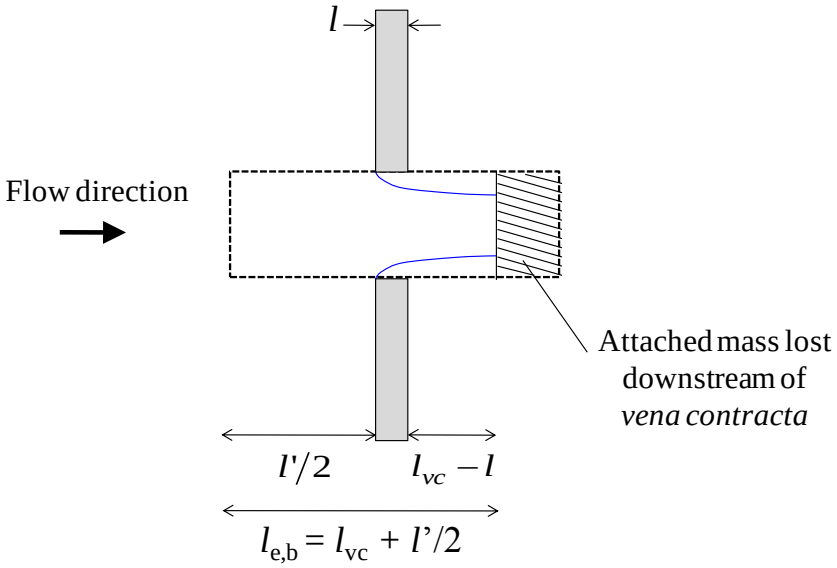

Figure 3.7: Bias flow correction to idealized mass distribution.

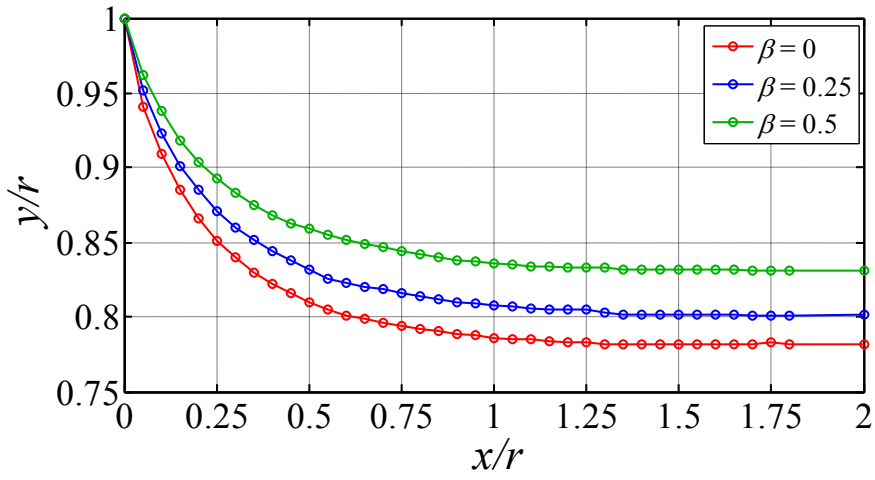

Figure 3.8: Free jet profile for varying orifice to duct area ratio $0 < \beta < 0.5$ [59]

Chapter 4

EXPERIMENTAL DETAILS

4.1 Perforations

Eleven perforated plates of varying porosity, hole size, and thickness were investigated (Figure 4.1). Table 4.1 lists the geometric properties of the perforated plates used for both static and bias flow cases. All the plates were made of sheet metal: either brass or steel. It was noted in a previous study [48] that the transmission characteristics of the plate are independent of its material composition. The test matrix includes a solid perforated plate (Experiment S) and the free-field, baseline case (Experiment 0). The gratings of the perforations on the plates were either square or triangular patterned (Figure 3.6).

4.2 Experiment setup

Two separate experiment facilities were utilized to determine the insertion loss of the perforated plates. The static insertion loss (SIL) facility was set up within the UCI anechoic chamber. To accommodate bias flow, a separate facility (bias flow insertion loss (BFIL) facility) was built. The details of the experimental setup are given in this chapter, followed by a description of the acoustic data processing

4.2.1 Static insertion loss experiment setup

The static insertion loss experimental setup has some similarity to the arrangement used by Chen [48]. The basic layout is shown in Figure 4.2. Acoustic measurements were conducted inside an anechoic facility using two 3.2-mm condenser microphones (Brüel & Kjaer, Model

4138), with frequency response of 120 kHz. The microphones were mounted inside a separate small anechoic box located within the anechoic facility (Figure 4.2(b)). The anechoic box, detailed in Figure 4.3, had one open side on which the perforated plates were mounted. The other sides were lined with anechoic wedges with cut-off frequency of 200 Hz. The microphones were held on an arm at the opposite end of the box, and were separated from each other by a distance of 7.6-cm. The distance between the microphone tips and plane of the opening was approximately 7.6-cm. The microphone signals were acquired simultaneously, which allowed microphone correlation assessments that would validate the assumption of plane wave propagation used in the static theory.

A localized broadband acoustic source ("point source") was generated using four small impinging jets, each issuing from a 2.54-mm diameter tube and supplied at a pressure of 200 kPa. The design of the impinging-jets source was similar to that used by Gerhold and Clark [60]. The distance between the impinging-jets source and the perforated plate was 1.48-m. The perforated sheets were attached to the open end of the box using spring clamps. The box was hinged in one corner to allow variation of the incidence angle relative to the wave front. In the present experiments, the incidence angle was normal to the perforations.

4.2.2 Bias flow insertion loss experiment setup

In order to investigate the effect of bias flow on the transmission properties of the perforated plate, a separate facility was constructed which accommodated a steady flow of dry air flow to the perforations. The facility is schematically represented in Figure 4.4(a). The material selected for the main duct and coupling was polyvinyl chloride (PVC) for ease of manufacturing. The internal diameter of the duct was 26.35-cm, with an average wall thickness of 0.475-cm. A 3.81-cm duct liner (SoundVAC^{TM}, with a cutoff frequency of 500 Hz) was used

to prevent signal contamination by internal reflections from the duct wall. The BFIL facility was divided into three sections, each connected by flanges at the tube ends. The coupling between the flanges was sealed with an Aramid/Buna-N flange gasket to minimize air leakage during experiments.

The first section was constructed with the objective of conditioning the incoming flow. The section was 0.762-m in length and contained four inlet ports into which compressed air was supplied. The supplied air was injected in the radial direction with respect to the duct axis (see Figure 4.4). A honeycomb grid and a series of screens were placed downstream of the inlet ports to reduce turbulence levels of the incoming flow. The selection of the coarseness and positioning of the wire mesh was based on the initial design for the NASA Langley 8-foot transonic pressure tunnel by McKinney and Scheiman [61]. The honeycomb selected was 2.54-cm in length with circular cell sizes of 3.18-mm diameter. Downstream of the honeycomb, a 20 x 20 wire mesh was placed, followed by two 42 x 42 wire mesh. The screens and honeycomb were separated by 12.7-cm. To prevent over pressurization of the BFIL facility, a burst diaphragm with a burst pressure of about 5 psig was installed in the flow conditioning section, upstream of the 20 x 20 wire mesh.

The second section (0.762-m in length) was used to hold the impinging jets source and the convergent section upstream of the sample plate. The impinging jets were supplied by four 1.6-mm diameter tubes. An additional screen (42 x 42 wire mesh) was placed slightly downstream of the piping for the source in order to reduce fluctuations in the flow due to shedding in the wake of the pipe. At the end of the source section, a smoothly convergent section was constructed using open cell, insulation foam sealant to ensure uniform axial flow at the plane of the perforation. The overall length of the convergent section was 20.32-cm. A

sample mounting plate located immediately downstream of the convergent section was used to hold the perforation in place (Figure 4.5). The plate was sandwiched between the flanges of the source section and the measurement/termination section.

The measurement/termination section (1.52-m in length) held the microphone arm and termination cone. The microphone arm consisted of an aluminum rod (1.27-cm diameter), mounted perpendicular to the duct axis, 25.4-cm from the sample mounting plate. Two 3.2-mm condenser microphones (Brüel & Kjaer, Model 4138) were inserted into slotted wedges, which were held by the microphone arm. Figure 4.6 details the setup used to obtain the microphone correlations in the BFIL facility. The measurement plane, defined as the plane intersecting the two microphone tips, was located 19.7-cm from the sample mounting plate. The microphones were fixed at the locations shown in Figure 4.6, and were separated by a distance of 7.6-cm to compare with the correlations obtained in the SIL facility. The sound power downstream of the perforated plate was determined by multiple acoustic measurements from a single microphone, traversed within the measurement plane. Details of the sound power measurement obtained in the BFIL facility are provided in Section 4.3. The sample mounting plate had a 4.57-cm diameter hole bored in its center that allowed airflow through from the convergent section.

To be consistent with the theory developed in Section 3.3, it was necessary to ensure anechoic termination so that acoustic measurements would not be contaminated by reflections from the downstream end of the duct. The use of duct area expansion for anechoic termination was not a practical choice for the current setup due to the large duct diameter [62]. Instead, a termination cone 0.45-m in length was attached at the end of the termination section. The frame of the cone was constructed from balsa wood, and was both filled and wrapped with 3.81-cm of R-19 Ecotouch FIBERGLAS insulation.

Unlike the SIL facility, a single spatial measurement of sound pressure level is not an accurate indication of the acoustic power in the duct. The wave propagation in the duct is confined by the liner surface, creating an effective duct diameter D = 18.73-cm. If $D/\lambda > 0.5861$, the first higher order duct mode is cut-on, and the pressure fluctuations will vary with position in the measurement plane [5]. Multiple acoustic measurements on the measurement plane were needed in order to obtain an accurate measurement of the sound power level in a duct [63,64]. The microphone arm was therefore attached to a linear traverse, and acoustic measurements were acquired at different spatial locations in the measurement plane, at a fixed axial distance from the perforated plate (see Figure 4.6). Further details on the acoustic power measurement for the BFIL setup are provided in Section 4.3. The microphones were held at zero-incidence angle with respect to the sample mounting plate.

In order to protect the B&K 4138 condenser microphone from flow impact, an aerodynamic forebody (Figure 4.7) was attached to the microphone tip in place of the standard protective grid. Discriminating between the noise due to turbulent fluctuations from the mean flow and the noise from the acoustic source is generally accomplished using two measurements under the same source and flow conditions. One measurement is made in which the nose-cone forebody is used, while another is obtained using a slit-tube windscreen [63,64]. However, due to unavailability of a slit-tube windscreen for the microphone size used in this study, only measurements obtained with the nose-cone attachment were used. Post-filtering of noise due to pressure fluctuations from the mean flow will be described in Chapter 5.

The total and static pressure upstream of the perforated plate were measured to determine experimentally the upstream Mach number. The total pressure was measured using a Pitot tube. The Pitot tube was installed in the source section of the duct, 11.43-cm upstream of the

convergent section inlet in order to minimize flow interference between the Pitot tube and the perforated plate (Figure 4.8). A static port was installed 2.54-cm upstream of the perforated plate. Using static and Pitot pressure measurements, the Mach number upstream of the plate was determined from the isentropic relation

$$M_1 = \sqrt{\frac{2}{\gamma - 1}\left[\left(\frac{p_{pitot}}{p_1}\right)^{\frac{\gamma-1}{\gamma}} - 1\right]} \tag{4.1}$$

For the BFIL experiments, acoustic measurements were conducted for M_1 = 0, 0.02, 0.04, 0.06, 0.08, and 0.1. The insertion loss model proposed in this study (Equation 3.52) is dependent on the contraction coefficient. The contraction coefficient was estimated from Smith and Van Winkle's experimental data, which required the Reynolds number of the flow through the perforations [25]. The perforation Reynolds number is defined as

$$\mathrm{Re}_p = \frac{M_p d}{c\nu} \tag{4.2}$$

The Mach number of flow in the perforation was estimated using Equation 4.1 along with static pressure measurements downstream of the perforated plate (see Figure 4.6). Assuming the total temperature T_0 = 293 K and is constant throughout the duct, the adiabatic relation was used to determine the local temperature

$$T_p = \frac{T_0}{1 + \frac{\gamma - 1}{2} M_p^2} \tag{4.3}$$

And the speed of sound in the perforation was determined from the equation of state

$$c = \sqrt{\gamma R_0 T_p} \tag{4.4}$$

Tables 4.2-4.12 lists the experimentally determined values of the Reynolds number Re_d, using the flow conditions specified for $0.02 < M_1 < 0.1$.

4.3 Acoustic data processing

The voltage time traces represent the raw acoustic data acquired from the microphones used in the experiments. The raw data was post processed to obtain the sound pressure level (SPL) spectrum of the acoustic signal. The normalized pressure is obtained from the pressure fluctuation

$$h(t) = \frac{p'(t)}{p_{ref}} \tag{4.5}$$

where the pressure fluctuation in the time domain was determined by multiplying the voltage time trace by the appropriate sensitivity factor, and $p_{\text{ref}} = 20\ \mu$Pa. For the SIL facility, both microphones were connected to a conditioning amplifier (Brüel & Kjaer, model 2690-A-0S4). The outputs of the amplifiers were sampled simultaneously at a rate of 250 kS/s per channel using a multifunction data acquisition board (National Instruments PCI-6143) installed in a Dell Precision T7400 computer with a Xeon quad-core processor. For the BFIL facility, the microphones were connected to a dual channel power supply/conditioning amplifier (Brüel & Kjaer Type 5935L). The outputs of the amplifier were sampled at 250 kS/s by a multifunction data acquisition board (National Instruments PCI-6070E) installed in a Dell Optiplex 380 computer with an Intel Core 2 Duo processor. The voltage signals for both SIL and BFIL facilities were conditioned with a high-pass filter set at 350 Hz and a low-pass filter set at 140 kHz. The power spectrum, S_{raw}, of Equation 4.5 was then computed using a 4096 point Fast Fourier transform, resulting in a spectral resolution of 61.03 Hz. The spectra of each of the microphones represent the power spectral density of the acoustic signal. Accounting for

microphone sensitivity and adjusting for amplifier gains, the raw, narrowband sound pressure level spectrum was obtained from the power spectrum of the normalized pressure

$$\mathrm{SPL}_{raw}(f) = 10\log_{10}\left[S_{raw}(f)\right] \tag{4.6}$$

The raw sound pressure level was corrected for microphone actuator C_{FR} and free field response C_{FF}, both of which are based on data provided from the microphone manufacturer. Atmospheric absorption corrections C_{AA}, were also applied using relative humidity and temperature of the ambient air. All corrections were applied in the frequency domain. The resulting corrected sound pressure level spectrum is expressed as

$$\mathrm{SPL}(f) = \mathrm{SPL}_{raw}(f) - C_{\mathrm{FR}}(f) - C_{\mathrm{FF}}(f) + C_{\mathrm{AA}}(f) \tag{4.7}$$

The microphone measurements were not shown to vary significantly with spatial location in the SIL setup, and therefore a single point measurement was sufficient in determining the insertion loss (to be shown in Chapter 5). In the BFIL setup, however, it was necessary to obtain SPL measurements at multiple spatial locations. The acoustic measurements were taken at the 19 locations indicated by the filled dark circles on the measurement axis (Figure 4.9(a)). The microphone arm was aligned with the *z*-axis. The slotted wedge was mounted on the arm, and the microphone was inserted through the slot (Figure 4.9(b)). The microphone tips were oriented at normal incidence to the sample plate. Due to the microphone-arm setup, the measurement axis was offset from the *z*-axis by 12.7-mm (Figure 4.9(a)). Position 10 corresponded to the measurement location intersecting the *y*-axis. Acoustic measurements were taken at 19 different locations along the measurement axis in increments of ±6.4-mm. The acoustic intensity level for a plane wave in a non-stationary medium is related to the sound pressure through Equation 3.51

$$\mathrm{IL}_n = 10\log_{10}\left[(1+M_n)^2\,\frac{p_n'^2}{\rho c I_{ref}}\right] \tag{4.8}$$

n corresponds to the measurement position indicated in Figure 4.9(a), M_n is the Mach number, and $I_{ref} = 10^{-12}$ W·m^{-2}. The intensity is assumed to be constant over the strip of area, dA_n, where the radii used to determine dA_n was selected to intersect the midpoint between the *n* and *n-1*, and the *n* and *n+1* location along the measurement axis. M_n was measured using Pitot pressure measurements of the flow field downstream of the perforated plate, wall static pressure measurements in the measurement plane (Figure 4.6). The microphone shown in Figure 4.7(a) was replaced by a Pitot tube with an internal diameter of 3.2 mm. Pitot pressure was obtained at the 19 positions shown in Figure 4.9a. The Pitot tube was connected to a Setra Model 209 transducer that was sampled at a rate of 1 kHz by a data acquisition board (National Instruments PCI-6070E) installed on a Dell Optiplex 380 computer with an Intel Core 2 Duo processor. The Pitot pressure was monitored using National Instruments Labview software. The measured static and Pitot pressures led to determination of the local Mach number, M_n, by Equation 4.1. In the current experiments, the Mach number in the measurement plane did not exceed 0.2 for all perforated plates (see Appendix B). Therefore the variation in density and temperature from a stationary medium did not exceed 2% and 1%, respectively, and the approximation $p_{ref}^2 = \rho c I_{ref}$ holds satisfactorily, where $p_{ref} = 20\,\mu$Pa. This allowed the acoustic intensity level spectrum to be recast in terms of SPL, by combining Equations 4.6 and 4.8

$$\mathrm{IL}_n(f) = 10\log_{10}\left[(1+M_n)^2 \cdot 10^{0.1\cdot \mathrm{SPL}_n(f)}\right] \tag{4.9}$$

The sound power level over the measurement plane was determined using Equation 2.3

$$\mathrm{PL}_{t,\exp} = \sum_{n=1}^{19} \mathrm{IL}_n(f)\, dA_n \tag{4.10}$$

and the resulting expression for the experimentally determined insertion loss is

$$L_{I,\exp} = \mathrm{PL}_{t,0,\exp} - \mathrm{PL}_{t,\exp} \tag{4.11}$$

Equation 4.11 is the general expression for the insertion loss measurement used in both the SIL and BFIL facilities. For the SIL facility, only a single point measurement of the acoustic field behind the perforated plate was needed, reducing Equation 4.11 to

$$L_{I,s,\exp} = \mathrm{SPL}_{t,0,\exp} - \mathrm{SPL}_{t,\exp} \tag{4.12}$$

Here $\mathrm{SPL}_{t,0,\exp}$ refers to the sound pressure level measurement without the plate installed (baseline case), and $\mathrm{SPL}_{t,\exp}$ is the sound pressure level measurement with the plate installed. To facilitate the interpretation of the insertion loss measurements in the SIL facility, the spurious wiggles from the SPL spectra were removed by using a Savitzky-Golay filter [65]. The filter removes the wiggles but does not alter the fundamental shape of the spectrum.

Table 4.1: Properties of perforated sheets used in experiments

Experiment	Porosity β	Thickness l, mm	Hole Diameter d, mm	Perforation Grating	Hole Pitch P, mm
S	0.00	0.6096	--	--	--
0	1.00	--	--	--	--
1	0.37	0.6096	1.1430	Square	1.672
2	0.48	0.4064	2.6162	Square	3.361
3	0.37	0.4064	1.1430	Square	1.672
4	0.29	0.4064	1.0160	Square	1.679
5	0.45	0.7620	1.7526	Triangular	2.481
6	0.23	0.7620	1.5875	Triangular	3.144
7	0.23	0.9144	1.5875	Triangular	3.144
8	0.23	0.4064	0.6858	Square	1.273
9	0.23	0.4064	0.6096	Square	1.131
10	0.22	0.4064	0.5080	Triangular	1.029
11	0.22	0.4064	0.4064	Triangular	0.823

Table 4.2: Experimentally Determined Flow Conditions for Plate 1

Flow Condition	M_1	M_p	U_p	Re_d
1	--	--	--	--
2	0.020	0.056	19.25	1441
3	0.040	0.108	37.07	2776
4	0.060	0.160	55.00	4118
5	0.080	0.211	72.56	5433
6	0.100	0.276	95.03	7116

Table 4.3: Experimentally Determined Flow Conditions for Plate 2

Flow Condition	M_1	M_p	U_p	Re_d
1	--	--	--	--
2	0.020	0.048	16.60	2845
3	0.040	0.096	32.93	5643
4	0.060	0.141	48.53	8318
5	0.080	0.189	65.17	11169
6	0.100	0.256	88.19	15114

Table 4.4: Experimentally Determined Flow Conditions for Plate 3

Flow Condition	M_1	M_p	U_p	Re_d
1	--	--	--	--
2	0.020	0.057	19.53	1472
3	0.040	0.114	39.14	2951
4	0.060	0.169	57.95	4369
5	0.080	0.227	77.85	5869
6	0.100	0.310	106.42	8023

Table 4.5: Experimentally Determined Flow Conditions for Plate 4

Flow Condition	M_1	M_p	U_p	Re_d
1	--	--	--	--
2	0.020	0.083	28.65	1927
3	0.040	0.168	57.76	3884
4	0.060	0.246	84.57	5686
5	0.080	0.327	112.41	7558
6	0.100	0.472	162.03	10895

Table 4.6: Experimentally Determined Flow Conditions for Plate 5

Flow Condition	M_1	M_p	U_p	Re_d
1	--	--	--	--
2	0.020	0.040	13.66	1579
3	0.040	0.078	26.79	3097
4	0.060	0.114	39.20	4531
5	0.080	0.140	47.98	5547
6	0.100	0.184	63.24	7310

Table 4.7: Experimentally Determined Flow Conditions for Plate 6

Flow Condition	M_1	M_p	U_p	Re_d
1	--	--	--	--
2	0.020	0.090	31.05	3240
3	0.041	0.193	66.30	6919
4	0.060	0.280	96.32	10051
5	0.080	0.384	132.04	13778
6	0.098	0.527	181.25	18913

Table 4.8: Experimentally Determined Flow Conditions for Plate 7

Flow Condition	M_1	M_p	U_p	Re_d
1	--	--	--	--
2	0.020	0.103	35.35	3676
3	0.040	0.187	64.51	6709
4	0.060	0.261	89.94	9353
5	0.080	0.366	126.10	13114
6	0.100	0.523	179.93	18712

Table 4.9: Experimentally Determined Flow Conditions for Plate 8

Flow Condition	M_1	M_p	U_p	Re_d
1	--	--	--	--
2	0.020	0.079	27.15	1228
3	0.040	0.166	57.16	2585
4	0.060	0.248	85.19	3853
5	0.080	0.323	111.12	5026
6	0.100	0.439	150.71	6817

Table 4.10: Experimentally Determined Flow Conditions for Plate 9

Flow Condition	M_1	M_p	U_p	Re_d
1	--	--	--	--
2	0.020	0.082	28.10	1126
3	0.041	0.155	53.35	2138
4	0.060	0.226	77.70	3114
5	0.080	0.301	103.45	4145
6	0.100	0.413	142.06	5692

Table 4.11: Experimentally Determined Flow Conditions for Plate 10

Flow Condition	M_1	M_p	U_p	Re_d
1	--	--	--	--
2	0.020	0.086	29.60	988
3	0.040	0.158	54.21	1810
4	0.060	0.234	80.37	2684
5	0.080	0.319	109.69	3663
6	0.100	0.436	150.02	5009

Table 4.12: Experimentally Determined Flow Conditions for Plate 11

Flow Condition	M_1	M_p	U_p	Re_d
1	--	--	--	--
2	0.020	0.084	28.78	774
3	0.040	0.150	51.45	1384
4	0.060	0.215	73.68	1982
5	0.080	0.285	97.81	2631
6	0.100	0.386	132.40	3561

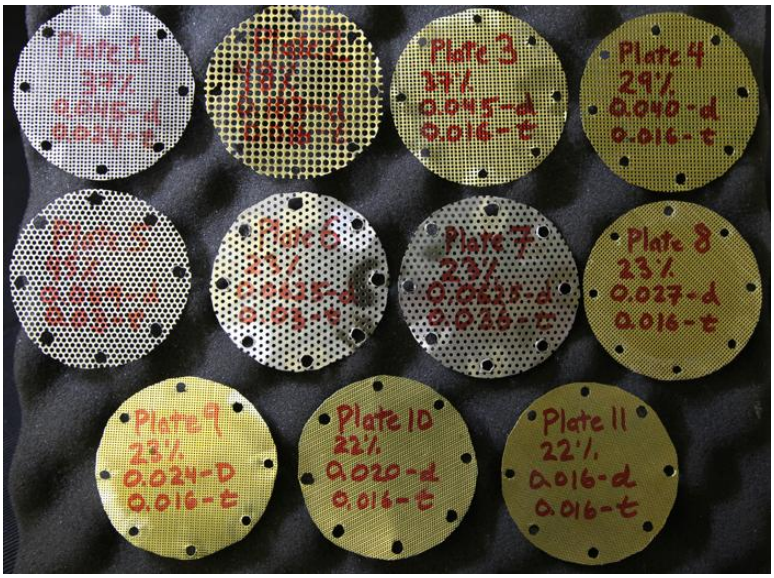

Figure 4.1: Perforated plates used for bias flow experiments.

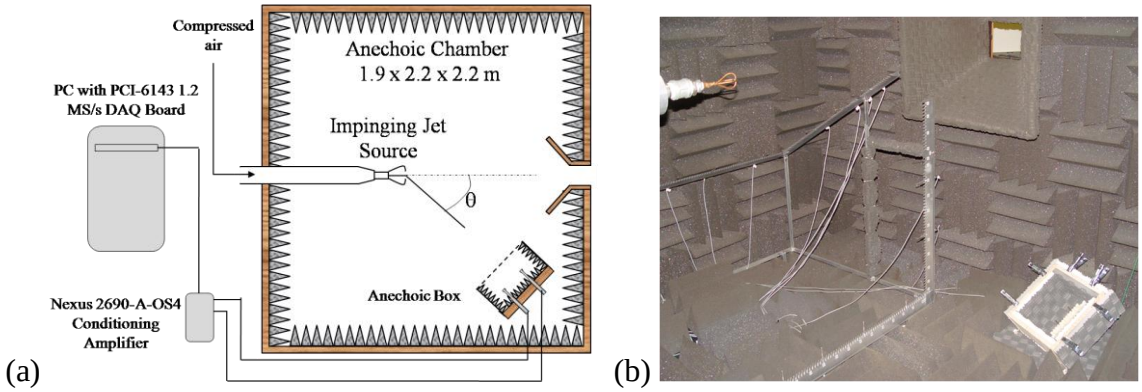

Figure 4.2: Static insertion loss experiment setup within UCI anechoic facility **(a)** represented schematically; **(b)** showing the position of the anechoic box with respect to impinging jets source.

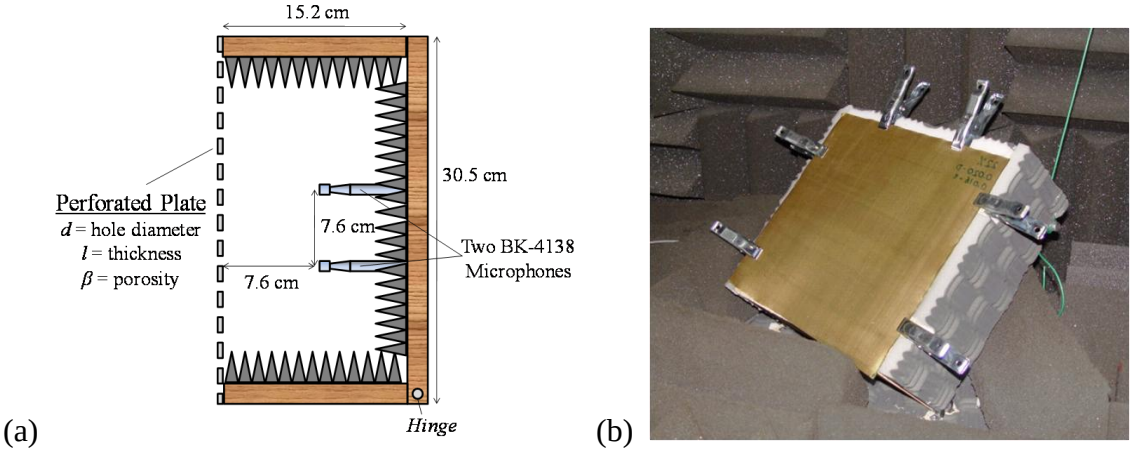

Figure 4.3: Anechoic box **(a)** schematic detailing the setup of microphones in the box and relevant dimensions; **(b)** with perforated plate attached, shown in the UCI anechoic facility.

(a)

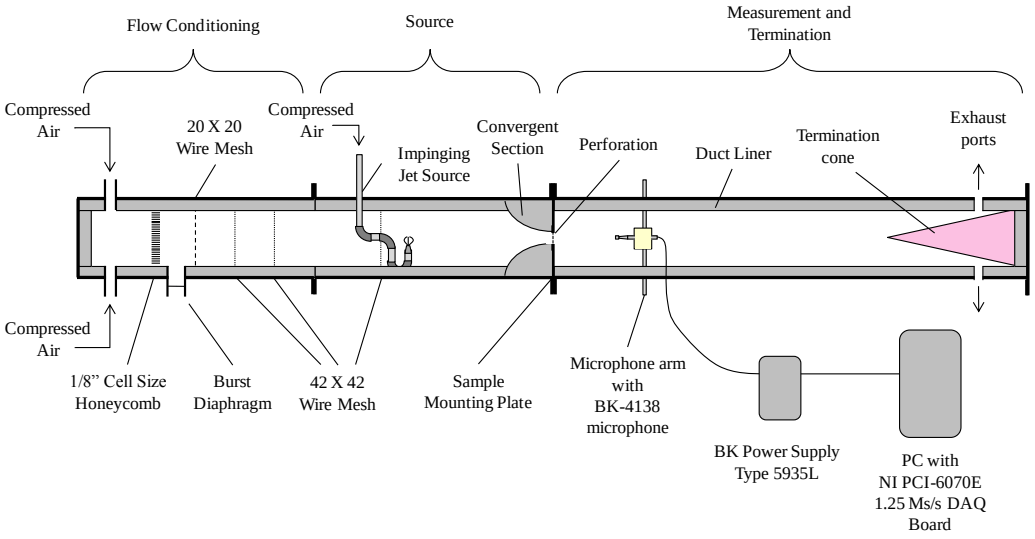

(b)

Figure 4.4: Bias flow insertion loss facility **(a)** schematic; **(b)** setup.

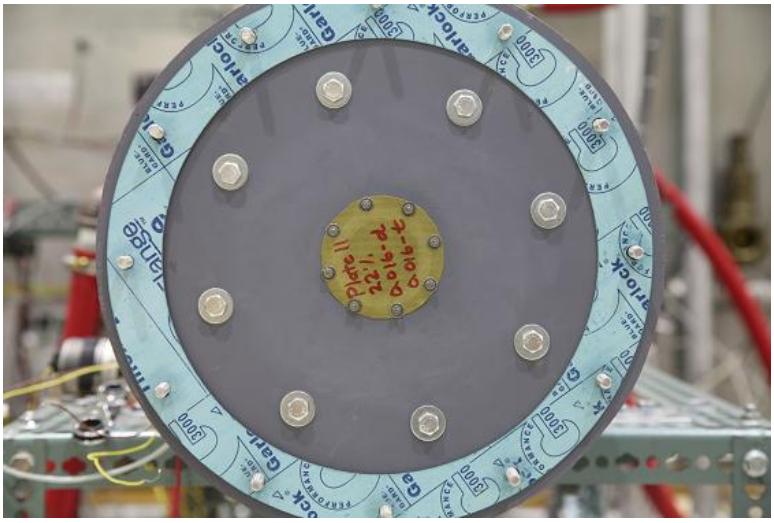

Figure 4.5: Sample mounting plate with perforated plate (Plate 11) attached.

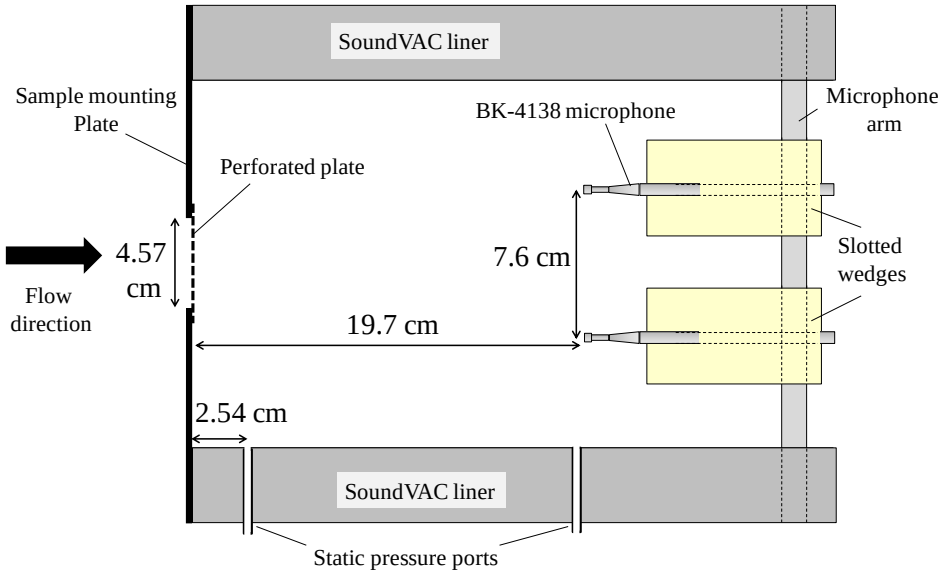

Figure 4.6: Schematic detailing the setup of the microphones used in the measurement section of the BFIL facility.

(a)

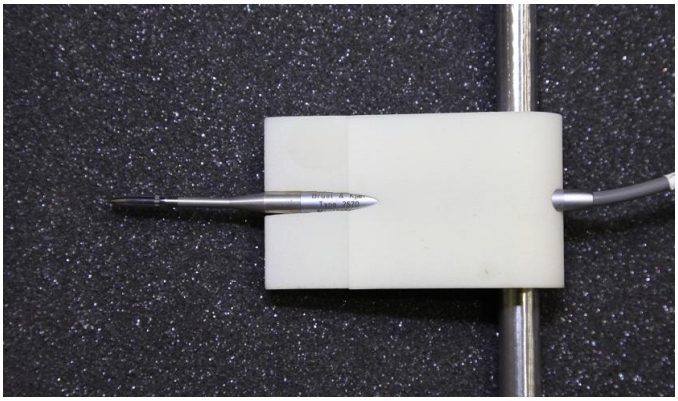

(b)

Figure 4.7: **(a)** Microphone arm assembly with G.R.A.S. RA0173 nosecone attached to B&K 4138 microphone; **(b)** G.R.A.S. RA0173 nosecone adaptor for 3.2-mm microphone.

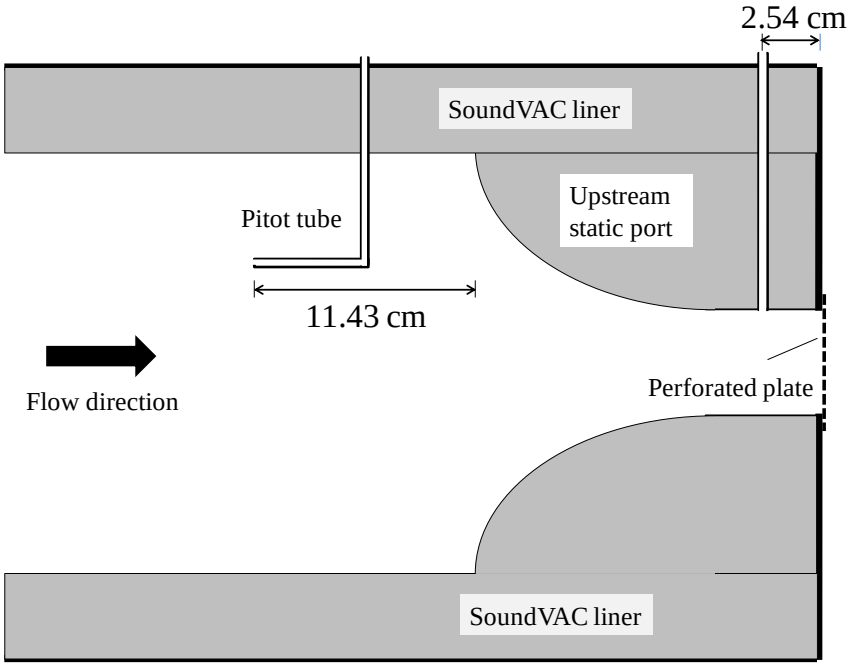

Figure 4.8: Schematic detailing the Pitot and static port positions relative to the perforated plate.

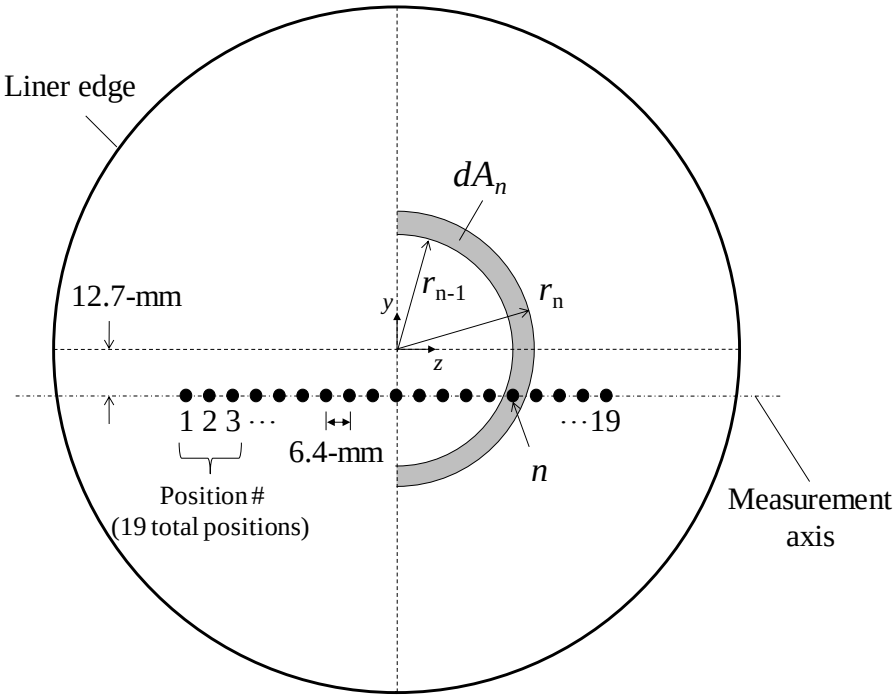

(a)

(b)

(c)

Figure 4.9: Cross section of the duct measurement section, **(a)** Schematic of the measurement plane, indicating 19 points of measurement; **(b)** actual setup at measurement location $n = 1$; **(c)** setup for microphone correlation measurements with microphones at positions $n = 4$ and $n = 16$.

Chapter 5

RESULTS

The results are presented in two sections. The first section and second section presents the measurements and validation of the SIL facility and the BFIL facility, respectively. Both sections first evaluate the robustness of the experimental facility in determining the insertion loss of perforated plates. This is done through an analysis of the SPL spectra and microphone cross-correlations. The experimental results are then compared with the current theoretical models, Equations 3.23 and 3.52, and previous models presented in Chapter 2. The sections conclude with an analysis of the error between the current theoretical models and experimental measurements.

5.1 Static results

5.1.1 Robustness of setup

It was necessary to check for any possible sources of error in the experiment setup in order to ensure accuracy in the insertion loss measurements. Acoustic contamination could result from leaks due to inadequate sealing of the contact area between the perforated plate and the structure of the anechoic box. An additional source of concern was vibrations of the plate itself, which could lead to discrepancies in the transmission loss measurement. In order to assess these possible sources of error, experiments were conducted with a solid plate, and the results were compared to a perforated plate of equal thickness.

Figure 5.1 shows the raw SPL spectra (before smoothing) comparisons between three cases: the solid plate, the perforated plate, and the background noise with the source turned off

and the solid plate installed. It was noted that the spectrum for the solid plate is well below the spectrum of the perforated plate. The difference is 20 dB at low frequency increasing to 40 dB at high frequency. This shows that the effects of vibration and leakage were very small and did not have any impact on the measured transmission loss. It was also noted that the spectrum for the solid plate was higher than the background spectrum, indicating some transmission of sound through the sealed anechoic box. It is natural that some sound will be transmitted through the box, particularly though the un-insulated solid plate. However, this transmission was extremely weak to influence the results.

Chapter 4 also discussed the capability of the SIL facility in determining sound power using a single point measurement. This was confirmed by comparing the SPL spectra of the signals acquired by each microphone. Figure 5.2 shows the spectral comparisons between the baseline (no plate attached), Plates 1, 2, 6, and 11. The plates selected for this comparison covered both extrema and intermediate values of thickness, hole size, and porosity used in this study. The comparisons show that the spectra were nearly identical, with the exception of Plate 2 (Figure 5.2(c)), where differences are noticeable at f >100 kHz. Based on these results, multiple spatial acoustic measurements in the SIL box was deemed unnecessary, and an average of the spectra between the two microphones was taken as representative of the acoustic power transmitted through the plate.

5.1.2 Microphone correlations

To confirm that the incident waves were normal to the perforations, the signals of the two microphones were cross-correlated. The microphone voltage signals were cross-correlated using MATLAB's inbuilt cross correlation function. Figure 5.3 compares the cross-correlation coefficient R_{m1m2} for the open box and the box covered with a perforated plate. For both the

open and covered box, the cross-correlation peaks at τ = 7.8 μs. This time lag corresponds to a propagation distance of 2.7-mm, which is very small compared to the 76-mm separation between the microphones. For all practical purposes, the sound arrived at the two microphones simultaneously and the wavefronts were aligned with the plane of the perforation. It is interesting that the magnitude of the cross-correlation does not decline with installation of the perforated plate. This indicates that the diffraction process is largely deterministic.

Further insight was gained by examining the coherence between the microphone signals, plotted in Figure 5.4. The magnitude squared coherence γ^2 was computed using MATLAB's inbuilt coherence function, using an FFT size of 4096 with a 1024 point Hanning window. The coherence plots are virtually identical for the open and covered box, except at f >100 kHz. The coherence is very strong for f <100 kHz, then falls off rapidly for higher frequency. The decline has to do with the turbulent nature of the impinging-jets noise source wherein the variance of source location becomes large compared to the acoustic wavelength.

The cross-correlation results, in conjunction with the geometry of the setup depicted in Figure 4.3(a), allowed us to assess the applicability of the one-dimensional propagation model, proposed in Section 3.2, to the present experiments. The strong coherence for f <100 kHz indicates a highly coherent wavefront impinging on the plate - a prerequisite for the aforementioned model. On the other hand, the decline in coherence for f >100 kHz indicates that the wavefronts impinging on individual holes become progressively uncorrelated. For this reason, only the results below 100 kHz were used in evaluating the model.

The large distance between the sound source and the perforated plate ensured that the wave approaching each hole is planar. Near the center of the plate, the incidence of the plane wave is normal. Towards the edge of the plate, the incidence is slightly off-normal with an

obliquity angle no larger than 6.4 deg. Sustained propagation at such angle requires high-order radial and circumferential modes whose cutoff frequency is much higher than the planar-propagation cutoff frequency mentioned in Section 3.2 [66,67]. Therefore, it was concluded that the obliquity of the incident wave on the perforations did trigger any transverse modes and thus did not alter the insertion-loss relations developed in this study.

5.1.3 Insertion loss measurements

The experimental results for transmission loss of the perforated plates listed in Table 4.1 are plotted in Figure 5.5(a). For all the cases investigated, the transmission loss is practically zero at very low frequency. With increasing frequency, the transmission loss for plates with thickness l=0.4046-mm increases monotonically within the frequency range investigated. For the three cases with l >0.4046-mm (Plates 5, 6, and 7), the transmission loss curves rise then fall. As indicated in Section 3.2, the saturation and decline of transmission loss for the thick plates is a result of Fabry-Pérot-like resonance. The theoretical predictions for transmission loss are plotted in Figure 5.5(b). A quick comparison between Figures 5.5(a) and 5.5(b) shows that the model captures the experimental trends. In the cases with l >0.4046 mm Equation 3.23 is able to accurately predict the frequency at which the maximum transmission loss occurs. The frequency limitation of the experiment prevented resolution of the frequency of peak transmission loss for plates with thickness l=0.4046 mm; therefore no distinct transmission loss maxima were observed for these cases. The comparisons in Figure 5.4 also indicate a significant deviation between model and experiment at high frequency for Plate 2. This deviation may be attributable to diffraction effects similar to Wood's anomaly [14,15,16,68], which occurs when the wavelength becomes similar to the hole spacing, P. Plate 2 was the only case that may be impacted by Wood's anomaly within the experimental frequency range.

5.1.4 Comparison with previous models

It was necessary to determine the range where the non-dimensional parameters of the previous classical models were validated so that comparisons with the current model can appropriately be made. The ratio of plate thickness to acoustic wavelength, l/λ, and perforation diameter to acoustic wavelength, d/λ, were selected as the relevant non-dimensional parameters. The range of d/λ and l/λ where the classical models were considered valid was determined based on their respective experimental constraints, and is illustrated in Figure 5.6. A region of significant overlap, $0.002 \leq d/\lambda \leq 0.09$, was chosen to compare the insertion loss results. It is shown in Figure 5.6 that the current work investigates values of $d/\lambda > 0.1$, a region where previous static models [48,49,51] lack validation.

Figure 5.7 compares the current insertion loss measurements with the predictions of the current static model, Equation 3.23, and the predictions by Chen [48], Tayong *et al.* [49], and Atalla and Sgard [51]. Equations 2.17 and 2.23 were used to recast the impedance expressions of Tayong *et al*. and Atalla and Sgard, respectively, into transmission loss. The aforementioned models [48,49,51] were derived with the assumptions that no reflected waves are present downstream of the perforated plate or upstream from the source, and therefore the insertion loss and transmission loss are identical. Figures 5.7(b), 5.7(d), 5.7(h), 5.7(i), 5.7(j), and 5.7(k) focus on insertion loss between $0.002 \leq d/\lambda \leq 0.09$, the region of validity of the classical models. Figures 5.7(a), 5.7(c), 5.7(e), 5.7(f), and 5.7(g) include results for $d/\lambda \geq 0.09$, and a vertical dashed line marking the upper d/λ limit at which previous models [48,49,51] were validated.

Within the region of validated d/λ, Chen's theory over-predicted the insertion loss with increasing error at higher d/λ for all perforates except for Plate 4. It is important to note that the end correction value used in Chen's theory is 0.8 times the perforation diameter for $\beta < 0.126$.

Since no specification was given for perforates with larger values of porosity, Chen's theory is expected to be inaccurate for higher porosity cases, such as Plates 1, 2, 3, and 5 (Figures 5.7(a), 5.7(b), 5.7(c), and 5.7(e)). Both transmission loss predictions using the surface impedance model of Tayong *et al.* and applying the TMM to Atalla and Sgard's model agree well with the current experimental data within the region of validated d/λ, except for Plates 8-11 (Figures 5.7(h), 5.7(i), 5.7(j), and 5.7(k)), where deviations from the experiment occur with increasing d/λ.

The capability of the classic and current models in predicting the resonance phenomena shown in the experiments (Figure 5.5(a)) is compared next. Figures 5.7(a), 5.7(e), 5.7(f), and 5.7(g) indicate that resonance effects become apparent for $d/\lambda > 0.1$, a region which previous classical models [48,49,51] lack validation. This effect is an essential physical mechanism that cannot be ignored when modeling the transmission behavior of perforated plates. This underscores the distinguishing advantage of the current model over Tayong *et al*. and Chen's model. As discussed in Section 2.2.1, the insertion loss was obtained from the model of Tayong *et al*. [49] by examining the classic problem of acoustic wave transmission between two semi-infinite fluid media: one defined by characteristic impedance of air, and the other by the perforation impedance. Conservation equations were applied at the interface separating the media, resulting in the well known expression for reflection coefficient Equation 2.15. The transmission loss was then obtainable from the reflection coefficient, as shown in Equation 2.17. In the current model, boundary conditions were applied at the two cross sectional area changes of contraction chamber (Figure 3.1). Reflected waves form within the contraction, resulting in a Fabry-Pérot-like resonance behavior when the acoustic wavelength approaches the order of the plate thickness l. This effect was captured in the transmission loss expression, Equation 3.23, through the sine-squared term, and was confirmed by experimental results for thicker plates.

Atalla and Sgard's [51] model was used in conjunction with the TMM in order to assess the accuracy to which their model can capture the resonance behavior shown in the current experiments. The results indicate that the Fabry-Pérot resonance behavior for thick plates is resolved, with good accuracy in predicting the d/λ value of peak transmission loss. However, the model also yields large errors in transmission loss amplitude for Plates 1, 5, and 7 (Figures 5.7(a), 5.7(c), and 5.7(g)) at high d/λ. It is not expected, however, for Atalla and Sgard's model to be accurate at high frequencies, or high d/λ, because their model was designed to focus on visco-inertial and thermal dissipative effects on the transmission behavior of porous media at low frequencies.

5.1.5 Error analysis

To assess the range of validity of the current predictive model, Equation 3.23, the deviation of the prediction from the experiment was examined systematically. The error in transmission loss was defined as the difference between the model prediction and experimental measurement

$$\Delta L_I = L_{I,\text{model}} - L_{I,\text{exp}} \tag{5.1}$$

Equation 5.1 is plotted versus the relevant non-dimensional parameters of the problem. In the formulation of the current theory it was assumed that the wavelength of sound is much greater than the perforation diameter. To examine the effect of this assumption, Figure 5.8 plots ΔL_I against the ratio of perforation diameter to wavelength of sound, d/λ, for all the plates examined. There is a very modest increase in ΔL_T with increasing d/λ, the deviation being less than about 1.5 dB for d/λ <0.5. For d/λ above this value, ΔL_T increases significantly, as shown in the case of Plate 2.

Since the current experiments include d/λ greater than the cutoff value of 0.5861 (Section 3.2), we expect the departure from the model, Equation 5.1, to increase for $d/\lambda \geq 0.5861$ because the acoustic excitations can sustain non-planar modes. This is evident in the ΔL_I trends shown in Figure 5.8. For Plate 2, ΔL_I increases to about 2 dB at $d/\lambda = 0.6$, and continues to increase monotonically with increasing d/λ. It is concluded that the assumption of one-dimensional propagation holds satisfactorily for $d/\lambda \leq 0.5$, where $|\Delta L_T| \leq 1.5$ for all cases.

In addition to higher-order duct modes, it is expected that the diffracted pressure field significantly influences the experimental results. The simplified analysis and assumptions made in formulating the problem did not allow a rigorous analysis of diffraction effects. It is believed, however, that diffraction effects are inherent in the application of end corrections. As discussed in Section 3.2, recent studies have attributed the effects of diffraction as a link between acoustic modes within the perforations and evanescent modes along the surface of the perforated plate [14,15,16]. It was shown in the work of these authors that the coupling between modes results in decreasing the Fabry-Pérot predicted resonance frequency. In the current model, the end correction with HIE increases the effective thickness of the plate, which also results in decreasing the resonance frequency. The similarity between these results implies a coupling between diffraction effects and the implementation of HIE using end corrections with Fok's function. The validity of this assumption is corroborated by the accuracy in predicting the d/λ of peak transmission loss (Figures 5.7(e), 5.7(f), and 5.7(g)).

Next, the effects of dimensionless thickness and porosity on the model accuracy for $d/\lambda \leq 0.5$ are examined. The effect of thickness-to-diameter ratio, l/d, on the insertion loss error is shown in Figure 5.9(a) for several values of d/λ. The trends in Figure 5.9(a) indicate that the transmission loss error is not a strong function of l/d. The magnitude of the error is less than 1.2

dB. Similarly, Figure 5.9(b) plots ΔL_I against the range of perforation porosities tested, $0.22 \leq \beta \leq 0.48$. The results of Figure 5.9(b) show that the current model predicts the transmission loss within an error of about 1.2 dB or less for all the porosities tested. Unlike the trends seen in Figure 5.8, where ΔL_I increases with d/λ, there does not appear to be any definable trend between ΔL_I and l/d or β.

Estrada et al. [68] and other authors [14,15,16] indicated deviations from expected transmission behavior, known as Wood's anomaly, when the acoustic wavelength approaches the same length as the spacing between perforations. This phenomenon occurs as a result of diffraction of higher order acoustic modes, which cannot be resolved by the current model's plane wave based approach. It is therefore expected that ΔL_I increases as λ approaches P. The spacing between the perforations in Plate 2 approach this limit, which may possibly explain the large departure of experiment from the model prediction shown in Figure 5.5.

5.2 Bias flow results

5.2.1 Robustness of setup

As described in Section 4.2.2, an in-duct method was used to determine the total power of the acoustic wave propagating in the measurement section of the duct. When obtaining experimental measurements of sound power in a duct containing flow, one must consider the following issues [64]:

1. Pressure fluctuations that propagate from the source down the duct experiences reflections at discontinuous area changes in the duct
2. The sound pressure varies with location along a fixed axial plane in the duct if the source frequency is higher than the cut-on frequency of the first non-planar mode

3. In addition to sound pressure fluctuations, the microphone is also subject to unsteady turbulent pressure fluctuations associated with the flow itself, requiring a windscreen or forebody attachment to the microphone tip
4. If only the transmission properties of the acoustic signal are desired, signal contamination due to pressure fluctuations from the flow must be filtered.

The first item emphasized caution to possible reflections that could contaminate the noise signal acquired in the measurement plane. In the current study, this problem was addressed by terminating the duct anechoically. The termination cone height was constructed to 0.45-m, or about 2.4 effective duct diameters in length, to allow for gradual area change at the exit. The flow was exhausted radially (Figure 4.4a), 15.2-cm upstream from the duct end. The direction of the reflected waves from the exhaust ports were predominantly radially inward, and were therefore reflected back towards the termination cone. This termination setup allowed ventilation of the supplied air and minimized acoustic reflections through gradual area changes at the duct exit.

The second item addressed the possible need to account for higher order mode effects of wave propagation. Except for Plate 2, the laboratory scale frequencies resolved in the current experiments were well below the cut-off frequencies for acoustic higher order modes corresponding to the perforation diameter. However the influence of these modes cannot be neglected within the duct itself. The sound power at a particular cross section of the duct was not appropriately represented by a single point measurement in the duct, and therefore, acoustic measurements were taken at multiple spatial locations within the measurement plane. In order to validate this method of measurement, the insertion loss results measured in the SIL facility were compared to insertion loss results measured in the BFIL facility with no bias flow. Figure 5.10

compares the insertion loss measured from each of the facilities. Plates 1, 2, 6 and 11 were selected for comparison. Overall, the trends observed in the insertion loss measurements acquired in the BFIL facility were similar to those observed in the SIL facility, notably the thickness effect captured in Figure 5.10(c). This indicates that, although the sound pressure distribution in the duct is not one-dimensional, the insertion loss based on the sound power level computation (Equation 4.10) exhibits similar trends as the one-dimensional SIL experiments. The peculiarity of this result is discussed in Section 5.2.6. The BFIL measurements indicated a large magnitude of insertion loss at low frequency, followed by a rapid decline with increasing frequency. This behavior is not exhibited in the SIL measurement, and can be attributed to the difference in the experiment setup. Both facilities utilized an impinging jets source supplied by compressed air. Unlike the SIL facility, where the air is exhausted freely in an anechoic chamber (Figure 4.2(a)), the air supplied in the BFIL facility can only be vented at exhaust ports which are downstream of the perforations (Figure 4.4a). Therefore, the flow that is used to operate the source also provides a small amount of bias flow through the perforations. The increase in insertion loss at low frequency may be attributed to the transfer of acoustic energy to the kinetic energy of vortical motions, a low frequency phenomena that was noted by previous authors [10,34,35,41]. It will be shown in Section 5.2.4, however, that the increase in insertion loss is overcome by wind noise with increasing bias flow.

The third and fourth items emphasized that noise due to turbulence fluctuations in the flow must be filtered from the acoustic signal if a measurement of sound power associated only with the impinging jets source is desired. Assuming that the sound emitted from the source and the flow noise signal are mutually uncorrelated, the intensity of the pressure fluctuations measured at the microphone tip is the sum of the intensity associated with fluctuations from the

source, p'^2_{IJS} , and the intensity of turbulence pressure fluctuations associated with the bias flow, p'^2_{flow} . Therefore, the experimental data needs to be analyzed in order to discriminate between pressure disturbances from turbulent fluctuations and pressure disturbances from the impinging jets source. This task was accomplished in two steps: examination of the signal-to-noise ratio between the acoustic signal and flow noise; and cross-correlation of the microphone signals. Details are provided in the next two sections.

5.2.2 Signal to noise ratio

This step comprised of a series of measurements for varying source and flow conditions. Acoustic measurements were acquired for the following run conditions

1. Impinging jets source on, mean flow on $(p'_{IJS} \neq 0, p'_{flow} \neq 0)$
2. Impinging jets source on, mean flow off $(p'_{IJS} \neq 0, p'_{flow} = 0)$
3. Impinging jets source off, mean flow on $(p'_{IJS} = 0, p'_{flow} \neq 0)$
4. Impinging jets source off, mean flow off $(p'_{IJS} = 0, p'_{flow} = 0)$

The sound power level (PL) spectra for these four run conditions are plotted and compared in Figures 5.11-5.21. The SPL spectra for condition 2 (green line) indicates that the impinging jets source emits noise with predominantly high frequency content. The noise associated with the flow (condition 3, blue line) is predominantly low frequency content. When both the source and the mean flow are on (condition 1, red line), the resulting spectrum reflects the combination of conditions 2 and 3. As the mean flow speed increases, the noise magnitude and the frequency bandwidth associated with the flow increases. While the spectral shape of the high frequency content associated with acoustic source does not appear to change with increasing bias flow, the SPL decreases uniformly over these frequencies (Figures 5.11(a)-5.11(e)). In some cases,

particularly at the highest flow condition (M_1 = 0.10), the spectral shape at high frequencies resembles that of the mean flow only (Figure 5.17(e)) indicating that the sound field associated with the impinging jets source has become significantly contaminated by the turbulence due to bias flow.

The focus of this work is on the transmission of acoustic waves from the source alone, without consideration to noise amplification from the turbulence fluctuations of the bias flow. Therefore, only frequencies where the SPL of the source is significantly greater than the SPL of the flow will be considered. Based on existing literature on in-duct acoustic measurements [63,64,69], a minimum signal-to-noise ratio (SNR) of sound pressure level from the source to noise due to turbulence is 6 dB, however, 10 dB is recommended. Referring back to the SPL spectra in Figures 5.11-5.21, only frequencies where the difference between the blue and red lines is $\geq$ 10 dB were considered valid in determining the insertion loss experimentally in this study.

5.2.3 Microphone correlations

Microphone correlation data provided additional guidance in determining the amount of signal contamination due to turbulence fluctuations from the bias flow. The microphones tips were positioned approximately 19.7-cm downstream of the perforated plate. The microphones were fixed at positions 4 and 16 (Figure 4.9(a)), which corresponded to a separation distance of 7.6-cm between the microphone tips. These positions were chosen to allow comparisons with the correlations obtained in the SIL facility. The cross-correlations between the microphone voltage signals are plotted in Figures 5.22 and 5.23. The cross-correlations plotted in Figure 5.22 are comparisons between the correlations measured in the BFIL and the SIL facility. We see in both facilities a maximum correlation at very nearly zero time lag. For Plates 6-11

(Figures 5.22(f)-5.22(k)), the magnitude of the peak correlation is somewhat lower than the peak correlation value measured in the SIL facility. It is suspected, as previously mentioned, that this departure is due to bias flow effects from the air supplied to the impinging jets source. This argument is corroborated by the smaller decline in peak magnitude for the higher porosity Plates 1-5. Since the open area ratio is larger, the bias flow velocity in the perforations will be smaller. This results in a weaker influence from the turbulence fluctuations of bias flow that form downstream of the perforations.

The influence of bias flow on the acoustic field was further evaluated by examining the cross-correlation of the microphone signals at varying bias flow conditions. Figure 5.23 compares the effect of increasing upstream Mach number on the microphone correlation for Plate 1. The blue line plots the microphone correlation for the condition where both the IJS source and bias flow are on, while the red line plots the microphone correlation with only the bias flow on. The signal correlation decreases with increasing Mach number, indicating an increasing dominance of flow noise over the original acoustic signal from the impinging jets source. This trend of decreasing cross correlation was also observed for the remaining plates and is plotted in Figure 5.24. There is a discernable peak near zero time lag that is reminiscent of the static condition for M_1 =0.02, however, the magnitude of the peak is significantly reduced. When increasing the bias flow to M_1 =0.04, Plates 6-8 (Figures 5.24(f), 5.24(g), and 5.24(h)) do not exhibit any distinguishable peak, and a further increase to M_1 = 0.06 results in very small peaks for Plates 1, 2, 5, 9, 10, and 11 (Figures 5.24(a), 5.24(b), 5.24(e), 5.24(i), 5.24(j), and 5.24(k)). In the range of $M_1 > 0.08$, no peaks are shown in the correlation plots, which indicated that the acoustic pressure field was largely contaminated by turbulence fluctuations associated with the bias flow. It was also noted that the time lag associated with peak correlation does not

shift appreciably with increasing bias flow, indicating weak diffraction of the wave front due to mean flow.

In the BFIL setup, the coherence between the microphones was not used to ascertain one-dimensionality of the wave front. The coherence measurements were instead used to indicate the extent to which the signal becomes contaminated by turbulence fluctuations from the flow, and at which frequencies the signal contamination is most prominent. Figure 5.25 plots the dependence of coherence on the upstream Mach number. With increasing bias flow, the magnitude of coherence decreases initially at high frequencies for all plates. Plates 4 and 7 (Figures 5.25(d) and 5.25(g)) represent this effect most clearly. Further increasing the bias flow Mach number to $M_1 = 0.04$ results in decreasing coherence levels at high frequency nearly to zero for Plates 1, 4, 6, and 8 (Figures 5.25(a), 5.25(d), 5.25(f), and 5.25(h)). At $M_1 \geq 0.08$, the signal coherence is nearly zero at all frequencies for Plates 4, 6, 7 and 8. It was also noted that the limit at which low frequencies are incoherent broadens with increasing M_1. For all plates, the signal coherence rises from about 3 kHz at $M_1 = 0$, to about 22 kHz at $M_1 = 0.1$. These frequency values correspond very closely to the frequency values in Figures 5.11-5.21 where the shape of the PL spectra associated with the source becomes distinct from the flow noise PL spectra. The coherence levels plotted in Figure 5.25 indicated the extent to which noise from the source is affected by flow noise, and which frequencies are most affected. To ensure that the incoherent frequency components of noise associated with flow was not factored into the insertion loss, an additional criterion of $\gamma^2 \geq 0.05$ was imposed in addition to the SNR requirement defined in Section 5.2.2.

5.2.4 Insertion loss measurements

The insertion loss was determined from experiments with the constraints of $\gamma^2 \geq 0.05$ and SNR $\geq$10 dB. Figure 5.26 plots the insertion loss for Plate 9, with emphasis on the components of the spectra that meet both of the aforementioned constraints. The red line is the insertion loss predicted using the current bias flow theory (Equation 3.52), while the black and grey lines are the measured insertion loss from experiment. The black line represents the measurements at which the SNR $\geq$ 10 dB and $\gamma^2 \geq 0.05$, and the grey line represents the measurements that fail to meet either one or both of the SNR and γ^2 requirements. Figure 5.26 indicates that the amount of signal contamination from turbulence fluctuations increases with M_1, and is reflected by the increase in the amount of unusable experimental data (grey lines). Two distinct features were noted from the experimentally measured insertion loss. For a finite value of M_1, the insertion loss measurement is negative at low frequencies, indicating sound pressure amplification with increasing bias flow speed. Furthermore, the range of low frequencies over which amplification occur increases monotonically with increasing M_1. The second feature that was noted was the sharp drop in the insertion loss at f = 106 kHz, shown in Figure 5.26(d). This is due to a tone in the SPL spectra, shown by the red curve in Figure 5.19(d), and can be attributed to a "whistling" effect which has been reported for single orifices with bias flow [70,71]. The phenomenon is related to the shear layer instability forming downstream of the perforations. Energy is transferred from the bias flow to self-sustained oscillations due to hydrodynamic feedback between the vortex layers shed from the perforation rims [70]. The data presented in Figure 5.26 indicate that the imposed SNR and coherence criteria filter both flow and whistling noise.

Figures 5.27-5.37 plot the insertion loss results for the remaining plates, showing only data which satisfy both SNR and coherence criteria. Figures 5.27(a)-5.37(a) compare the

insertion loss measured by experiment with no flow and the current model (Equation 3.52). Since the current model does not allow a zero input for the upstream Mach number, a small value, $M_1 = 10^{-5}$, was used to assess the applicability of Equation 3.52 in a static medium. Equation 3.52 predicts the experimental measurements very well between 10 kHz < f < 100 kHz. It was noted in Section 5.3.1 that even with the mean flow inoperative, a small amount of bias flow is supplied to the perforations from the source. It is suspected that the error at f <10 kHz is a result of dissipation due to a small amount of bias flow supplied by the impinging jets source.

Figures 5.27-5.37 also plot the effect of increasing upstream Mach number. Both the current bias flow model (Equation 3.52) and experiments show an increase in insertion loss as M_1 is increased from 0 to 0.02, however, Equation 3.52 overestimates the insertion loss increase for some cases Plates 1, 3 and 5 (Figures 5.27(b), 5.29(b), and 5.31(b)). Similar to the static case, the insertion loss with bias flow exhibited resonance behavior for thick plates (Plates 5, 6 and 7). It is shown in Figures 5.31 and 5.32 that the frequency corresponding to peak loss is reduced as M_1 is increases. The effect of convection on the acoustic wave propagation within the perforations produces a shift in the frequency corresponding to peak insertion loss. A considerable amount of deviation is shown at high frequencies for Plates 2, 6, and 7 (Figures 5.28, 5.32, and 5.33), which is attributed to effects of higher order mode propagation within the perforations. Also, at moderate bias flow speeds for Plate 7 (Figures 5.33(c), (d), and (e)), the measured insertion loss is much larger than the model prediction.

5.2.5 Comparison with previous models

Before comparing with previous models, it was first necessary to determine the range of experimental parameters used in each study to determine the previously validated parameter space. Section 2.2.2 summarized the validated parametric space as cited by the authors

referenced in this work [33,41,43,55]. Comparison between previous and the current experimental parameter space for d/λ, and M_2 are illustrated in Figures 5.38(a) and 5.38(b). For the majority of previous experiments, the Mach number inside the perforations was in the low subsonic range of $M_2 < 0.3$, and the range of valid d/λ was well below the cut-on limit for higher order modes of wave propagation When comparing the current bias flow model to previous bias flow models [33,41,43,55], a parameter space was selected to appropriately evaluate the current model. For comparison with previous models, the parameter range selected was $0.001 \leq d/\lambda \leq 0.03$, and $0 \leq M_2 \leq 0.35$.

Figures 5.39-5.49 compare the insertion loss predictions of the current bias flow model (Equation 3.52), previous bias flow models [33,41,43,55], and the insertion loss measurements from this study. The vertical dashed line is drawn at $d/\lambda = 0.03$ to indicate the maximum d/λ validated for previous bias flow models. Figures 5.39(a)-5.49(a) indicate that both current and previous bias flow models fail to capture the insertion loss peak at low frequencies. All plates except for Plates 2, 6 and 7 had valid experimental data that were within the range of previously validated d/λ for $M_2 > 0$. Except for Plate 4, the current model is in better agreement with the experimental data than previous models where $M_2 > 0$ and for $d/\lambda < 0.03$.

The performance of the current and previous bias flow models for $d/\lambda > 0.03$ was then evaluated against experimental measurements. For $M_1 = 0$, the insertion loss predictions using Howe's model [33] agrees with the current experimental data for plates with low porosity (Figures 5.44(a)-5.48(a)). The agreement between his model and the current experiments increases over a larger range of d/λ as the perforation hole diameter decreases (Figures 5.46(a), 5.47(a)). This result is expected because the hole spacing scales inversely with the porosity (see Equation 3.32, for example), and therefore interaction effects weaken as porosity decreases. As

porosity increases, Howe's assumption of no interaction between the perforations [33] is no longer valid, and therefore his model becomes unreliable for large β. This explains the large error between Howe's model and the experimental measurements for Figures 5.40 and 5.43, where $\beta \geq 0.45$. Howe's model is also shown to be fairly accurate for low perforation Mach number (Figures 5.46(b), 5.47(b)), which is expected because Equation 2.28 was derived assuming low Mach number flow. Howe's model predicts a monotonic increase in insertion loss as the bias flow speed increases, which is consistent with the current experimental data for $0 \leq M_2 \leq 0.35$. His model, however, over predicts the insertion loss increase due to bias flow at small d/λ (Figures 5.46(b), 5.47(b), and 5.48(b)).

Jing and Sun [41] modified Howe's model [33] with an impedance correction to include the effect of plate thickness. Jing and Sun's results show an increase in insertion loss in comparison to Howe's model at higher d/λ. Since their model [41] is an extension of Howe's analysis, Jing and Sun's model also predicts additional low frequency dissipation when bias flow is present. Figures 5.39-5.49 indicate that, aside from Plate 7 (Figure 5.45(d)), the agreement between Jing and Sun's model and the current experimental data is very poor. The authors had noted in their work [41] that the additional reactance term corresponding to the thickness correction in their model resulted in an overestimate of the reactance when compared to their experiments. They claimed that the reactance error was large at high bias flow speeds due to the effect of flow separation, which was not included in their model.

Figures 5.44(b)-5.49(b) indicate that the model of Bellucci *et al*. [43] agrees well with the current experimental data at low β and low M_2. This is expected, as the model was validated only for perforation Mach numbers less than 0.02 and $\beta < 0.0231$. The model fails to predict the static insertion loss with accuracy, except at low d/λ where the model has been validated (Figures

5.46(a)-5.49(a). It is also important to note that the model of Bellucci *et al.* [43] predicts a monotonic decrease in insertion loss with increasing bias flow. This result is inconsistent with the expected increase in insertion loss at low subsonic perforation Mach number.

Betts' impedance model yielded similar trends as the models of Howe [33] and Jing and Sun [41]: an increase in insertion loss over the entire range of d/λ with increasing bias flow Mach number. The trends in his model are consistent with the current experimental results, however, his model slightly over predicts the insertion loss for many cases with low bias flow Mach number (Figures 5.39(b), 5.41(b), 5.43(b), 5.46(b), and 5.47(c)). His model is also very accurate for Plate 2 (Figure 5.40), which is the plate of highest porosity in this experiment. The large porosity implies a strong interaction between perforations, which Betts included in his model using Fok's function [11]. The importance of including HIE in the modeling of perforated plates with bias flow is emphasized by the greater accuracy in which Betts' [55] and the current bias flow model (Equation 3.52) predicts the insertion loss measurements for higher porosity plates, such as Plates 2 and 5 (Figures 5.40 and 5.43). Betts' model, however, assumes no difference in the treatment of HIE between the static and bias flow cases.

The current bias flow model developed in this study was shown to have greater accuracy than previous bias flow models [33,41,43,55] when compared to experimental measurements. The development of the current static model (Section 3.2) and the results presented in Section 5.1.3 indicated that the Fabry-Pérot-like resonance behavior was captured by applying the appropriate boundary conditions at the contraction and expansion location of the contraction chamber. This analysis was repeated for the current bias flow model (Section 3.3), and the agreement between the proposed bias flow model (Equation 3.52) with the experimental results shown in Section 5.2.4 indicated that the resonance behavior was resolved successfully by the

current model. The inclusion of hole interaction effects using Fok's function [11] was an essential element of the current static model (Equation 3.23), and was therefore also utilized in the current bias flow model. The attached mass was modified, assuming that any portion of the idealized attached mass downstream of the *vena contracta* location was destroyed [50]. Betts also used Fok's function to account for HIE, however, no consideration was given to the region downstream of the perforations, where the flow is no longer potential and Fok's function becomes invalid. Both Howe [33] and Jing and Sun's [41] model did not include HIE, which possibly explains the poor comparison between their models [33,44] and the experimental data shown in Figures 5.39-5.43. The previous bias flow models [33,41,43,55] had also failed to predict the static insertion loss with consistent accuracy whereas the current bias flow was able to do so. Observing that the current model predicts insertion loss with superior accuracy over previous bias flow models, under both static and bias flow conditions, underpins the advantage of the current bias flow model over previous models.

5.2.6 Error analysis

Equation 5.1 was used to determine the insertion loss difference between the current bias flow model and experiments as a function of d/λ for Plates 1 through 11 (Figure 5.50). Except for Plate 7 (Figure 5.50(g)), ΔL_I stays within 2.5 dB for $d/\lambda < 0.4$ and $0 < M_1 < 0.02$. As M_1 is increased to 0.04, ΔL_I increases beyond 2.5 dB for Plates 6, 7 and 8 (Figures 5.50(e), (f), and (h)), while the remaining plates keep within 2.5 dB level difference. Increasing M_1 even further results in larger ΔL_I for Plate 5, with a maximum of 7 dB difference for Plate 11 at $M_1 = 0.1$. Plates 1, 2, and 3 did not seem to illustrate any increase in ΔL_I with increasing M_1 towards 0.1. The discrepancy between the current model and experiment for Plate 2 at $d/\lambda > 0.7$ and $M_1 = 0$ is consistent with the error seen in the static experiments (Figure 5.8). This is due to higher order

mode propagation, as d/λ becomes larger than the cut-off frequency for plane waves. Discrepancies in L_I were also observed for $d/\lambda > 0.5$ for both Plates 6 and 7, which was suspected to be an effect of high order mode propagation as the wavelength approaches the thickness of the plate.

Figure 5.51 plots L_I contour levels versus M_2 and d/λ. All subfigures indicate negative insertion loss, or noise amplification, at small d/λ. This result is consistent with the signal-to-noise analysis in Section 5.2.2, where the flow noise power spectrum was shown to progressively contaminate the low frequency content of the acquired signal as the mean flow speed increases. The white dashed lines in Figure 5.51 indicate the perforation Mach number where maximum insertion loss occurs for a specified d/λ. The perforations with high porosity (Figures 5.51(a), 5.51(b), 5.51(c) and 5.51(e)) do not provide conclusive information about peak insertion loss; however, the lower porosity plates indicate a saturation of insertion loss at about $M_2 = 0.25$ followed by decline with further increase in M_2. The decline in insertion loss is due to high-frequency amplification from the mean flow. The proposed model (Equation 3.52) does not predict this behavior, and therefore the validity of the model is verified only for $M_2 < 0.25$.

Figure 5.52 plots ΔL_I versus l/d for Plates 1 through 11. The upper and lower limits of the error bars correspond to the maximum and minimum ΔL_I for $0.02 < d/\lambda < 0.4$ and $M_2 < 0.25$. The upper limit in d/λ was selected to exclude large error magnitudes due to higher order modes (see Figures 5.50(b),(f),(h)), while the limit in M_2 was selected to exclude error from flow noise amplification. Figure 5.52 indicates a large amount of error localized between $0.45 < l/d < 0.6$. The large error can be explained by the assumption of a stable *vena contracta* downstream of the perforated plate. The location of the *vena contracta* was determined based on the jet profile by Rouse and Abul-Fetouh [59], and it was assumed in this study that the *vena contracta* location is

steady. Also, Rouse and Abul-Fetouh's analysis was based on a free jet issuing from a sharp edged orifice. The orifice thickness, which was not considered in their analysis [59], can have significant impact on the details of the jet profile. Smith [22] described multiple flow regimes for an orifice in a duct that depend on l/d. The separation streamlines depicted in Figure 2.3 expand in the positive radial direction due to Coandă effect and positive radial pressure gradient (Section 2.1.4). Smith identified a regime of thickness-to-orifice diameter ratio, $0.5 < l/d < 0.8$, where the jet may intermittently detach and reattach to the wall of the orifice. This transitional regime of separated or reattached flow implies unsteadiness of the *vena contracta*. Since both the insertion loss and end correction in this study are modeled based on steady flow, discrepancies between predictions and experiments could be attributed to the transitional regime of the jet described by Smith.

Unlike the SIL facility, where the wavefronts from the impinging jets source radiate freely in an anechoic environment, disturbances in the BFIL experiments are confined within a duct. Although the acoustic liner in the duct minimizes internal reflections, higher order acoustic modes are sustainable in the regions both upstream and downstream of the perforated plate. Despite the propagation of these modes, it was shown in Section 5.2.1 (Figure 5.10) that the insertion loss measurements in the BFIL facility exhibited similarity to measurements in the SIL facility. The similarity between the SIL and BFIL experimental measurements is explained by an analysis of the acoustic pressure non-uniformity associated with non-planar modes upstream of the perforated plate. Based on the diameter of the contracted duct upstream of the perforated plate, D =4.57-cm, and the highest frequency resolved in the BFIL experiments, f_{max} = 125 kHz, the impinging wave from the source contains 50 circumferential and 17 radial cut-on modes. Acoustic pressure amplitude contours associated with cut-on modes upstream of the plate are

plotted in Figures 5.53(a)-5.53(d). The red and blue regions in the figures indicate peak and minimum pressure fluctuation amplitudes, respectively, *m* is the circumferential mode number, and *n* is the radial mode number. Figures 5.53(a) and 5.53(b) indicate a minimum distance of 2.86-mm between peak pressure fluctuations. The non-uniformity in pressure fluctuation is confined to the outer perimeter of the duct wall for the highest circumferential mode (Figure 5.52(b)). An intermediate mode shape (Figure 5.53(c)) indicates a minimum distance of 2.77-mm between peak pressure amplitude. Except for Plate 2, the diameter of the perforations in this study is less than 1.75-mm. Although acoustic pressure non-uniformity is present due to higher order modes of wave propagation upstream of the perforated plate, the non-uniformity is small with respect to the individual perforations. This is represented clearly for lower circumferential and radial mode numbers (Figure 5.53(d)). The pressure non-uniformity of the impinging wave is small, relative to the perforation diameter, and therefore the process governing sound transmission through each perforation is approximately one-dimensional.

The current analysis is valid only in quantifying the amount of transmitted energy from a known source upstream of the perforation. The experimental measurements indicated that noise regeneration as a result of turbulence fluctuations from the bias flow can significantly contaminate the fluctuations from the source, producing large errors between the current theory (Equation 3.52) and experimental measurements. This was evident in Figure 5.26, where flow noise and potential orifice whistling resulted in negative insertion loss measurements. These effects were not included in the model, and therefore care was taken to isolate and omit any error arising from these sources of sound. The process of isolating these effects involved an examination of both signal-to-noise ratio and the microphone coherence in the measurement plane. The effectiveness of this method is critical in the validation of this study.

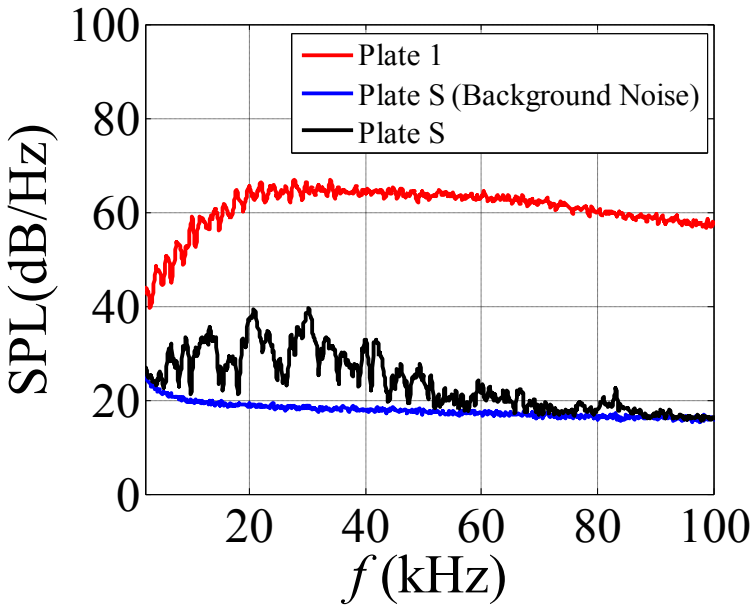

Figure 5.1: Comparisons of SPL spectra between perforated plate and solid plate of equal thickness.

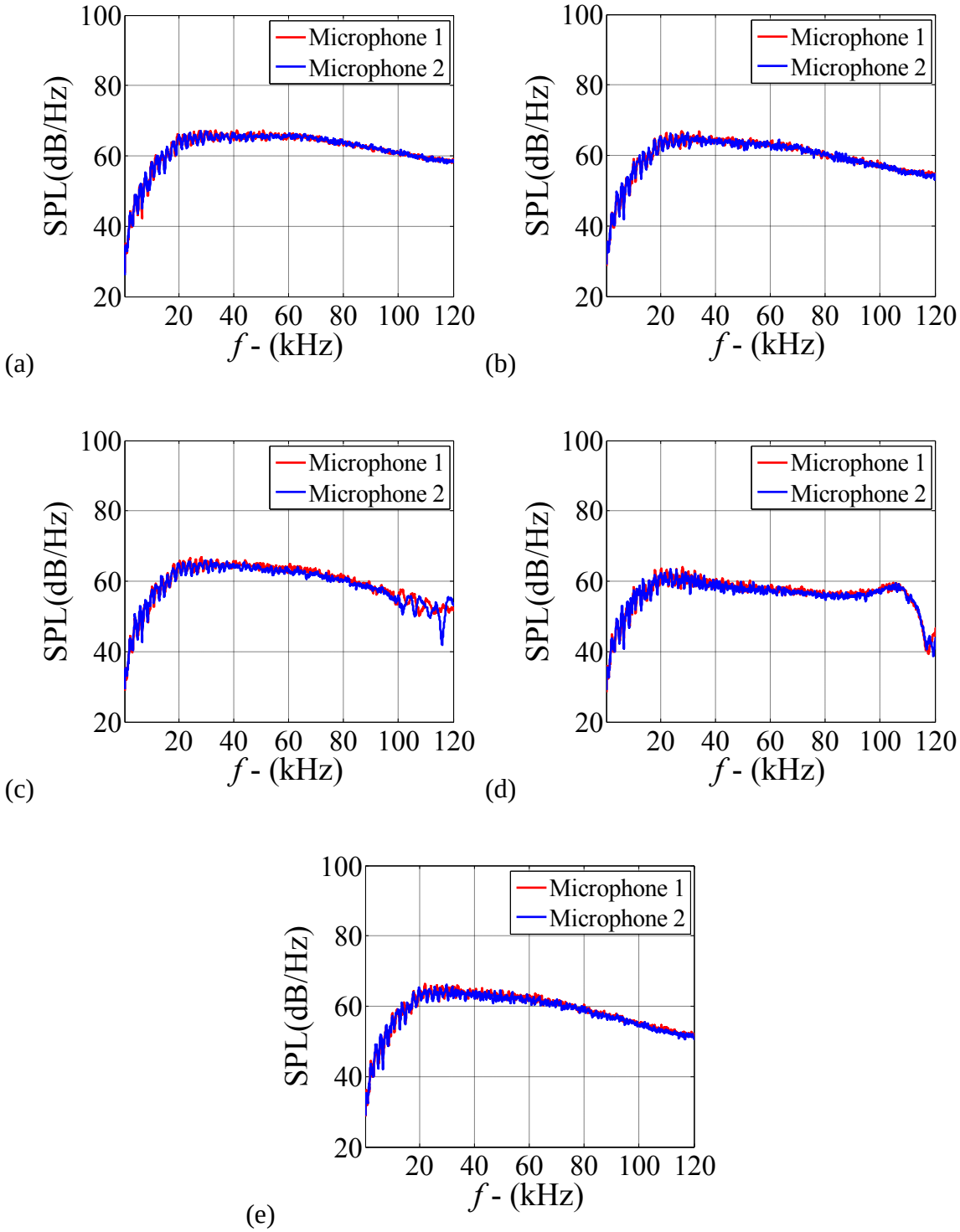

Figure 5.2: Comparisons of SPL spectra between microphones in SIL **(a)** baseline; **(b)** Plate 1; **(c)** Plate 2; **(d)** Plate 6; **(e)** Plate 11

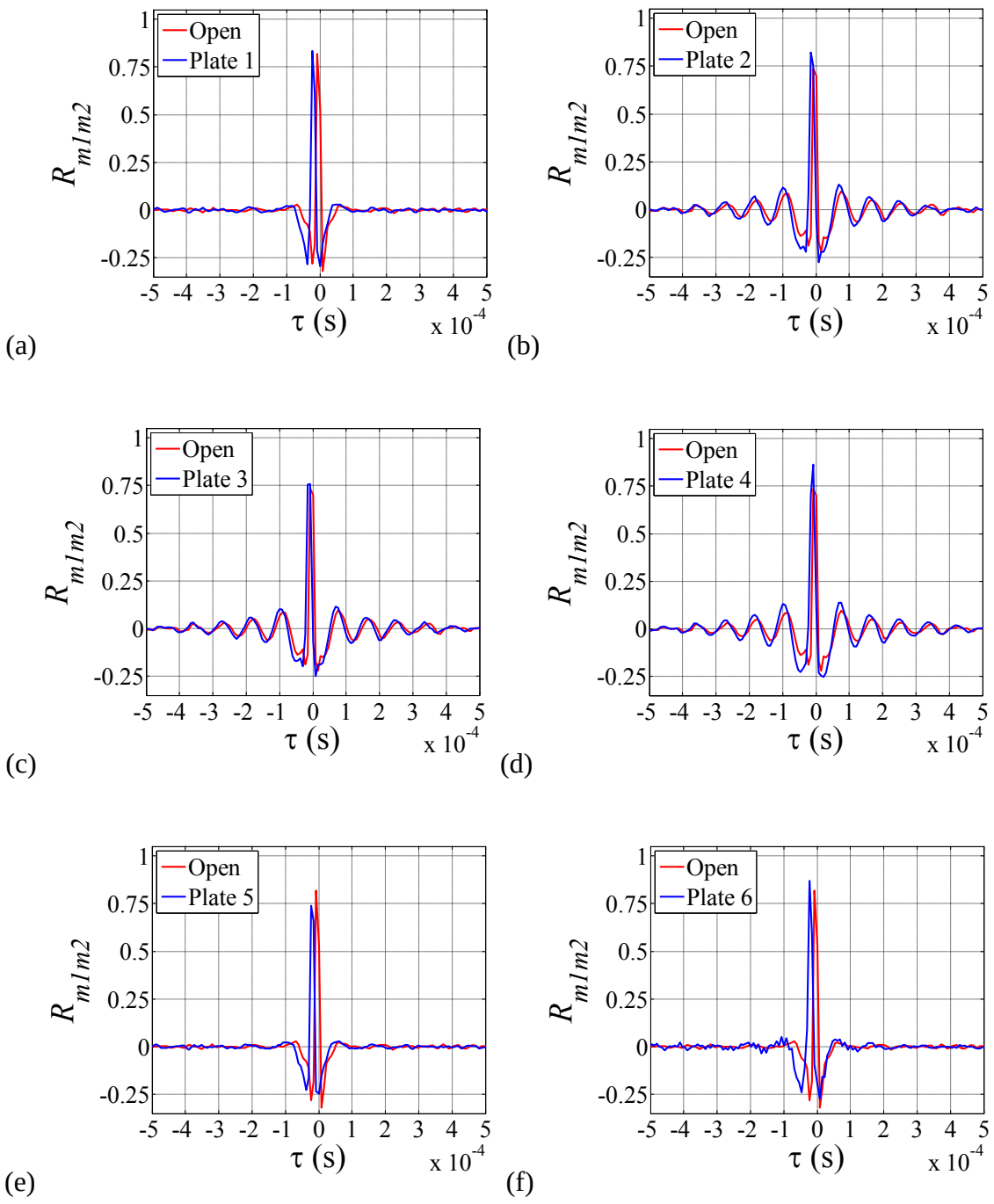

Figure 5.3: Microphone cross correlation in SIL setup, comparisons between open and **(a)** Plate 1; **(b)** Plate 2; **(c)** Plate 3; **(d)** Plate 4; **(e)** Plate 5; **(f)** Plate 6; **(g)** Plate 7; **(h)** Plate 8; **(i)** Plate 9; **(j)** Plate 10; **(k)** Plate 11

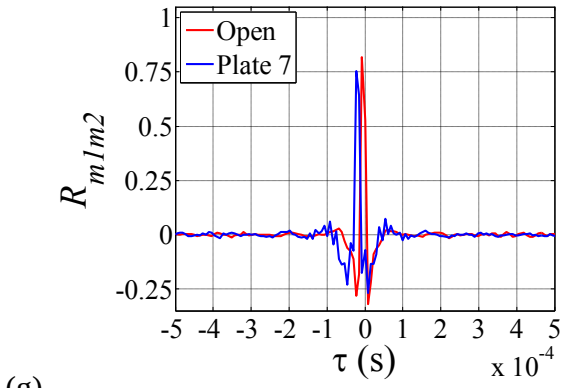

(g)

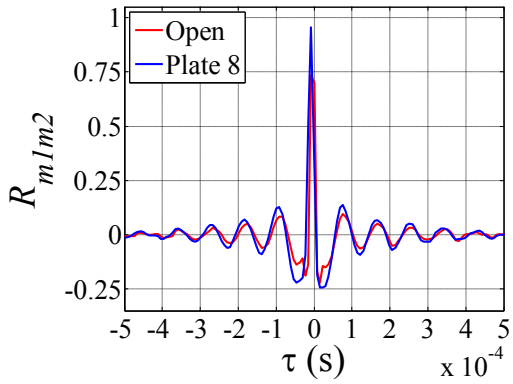

(h)

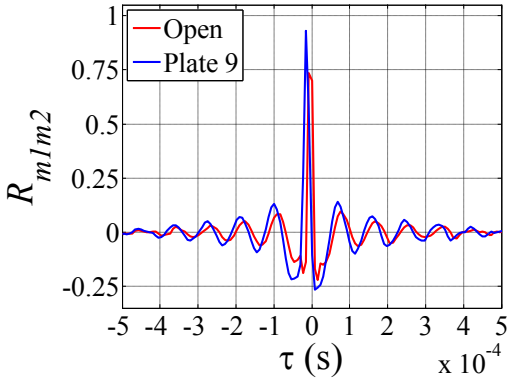

(i)

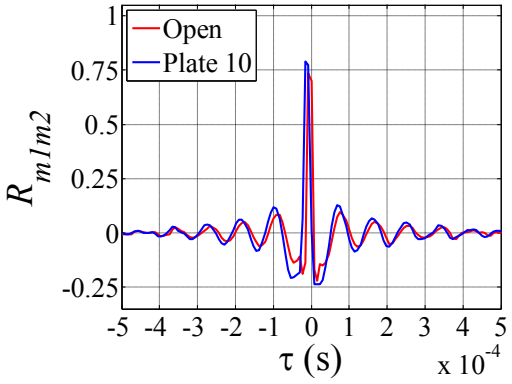

(j)

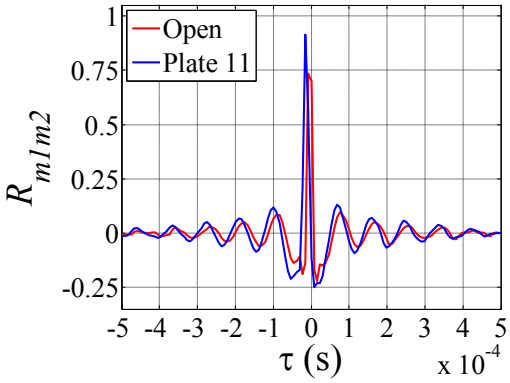

(k)

Figure 5.3: (cont.)

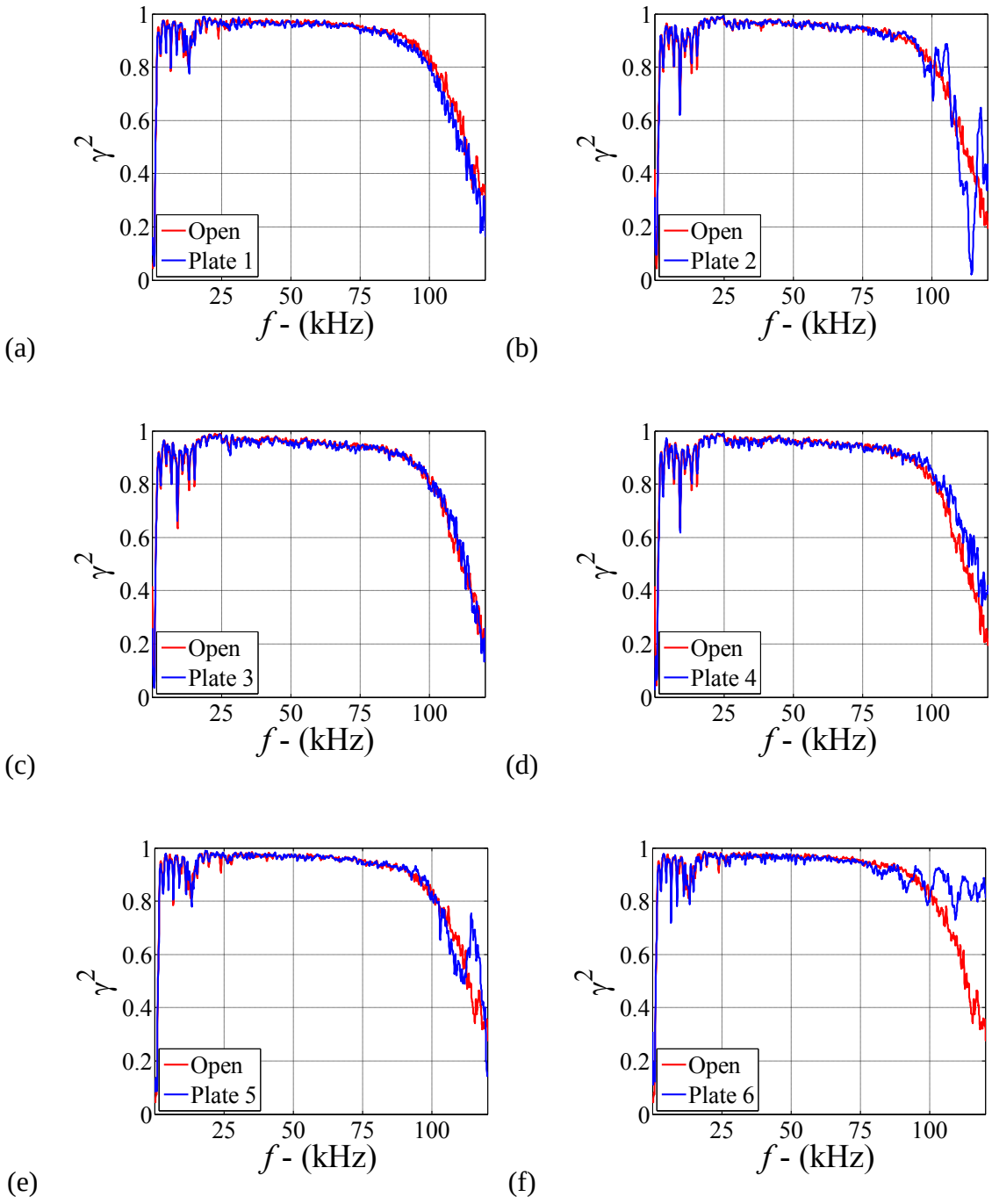

Figure 5.4: Microphone coherence in SIL setup, comparisons between open and **(a)** Plate 1; **(b)** Plate 2; **(c)** Plate 3; **(d)** Plate 4; **(e)** Plate 5; **(f)** Plate 6; **(g)** Plate 7; **(h)** Plate 8; **(i)** Plate 9; **(j)** Plate 10; **(k)** Plate 11

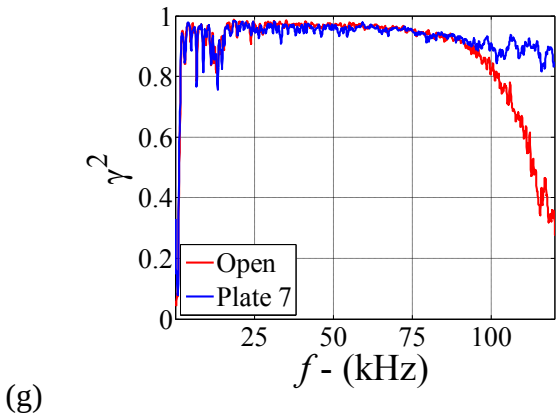

(g)

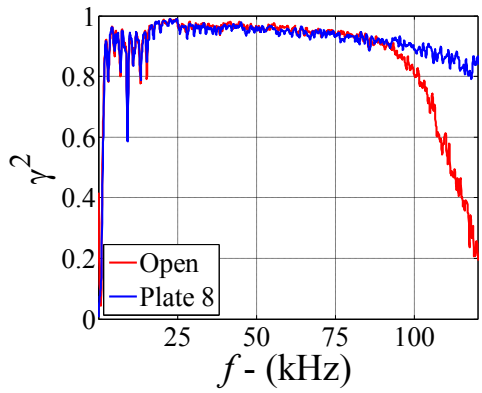

(h)

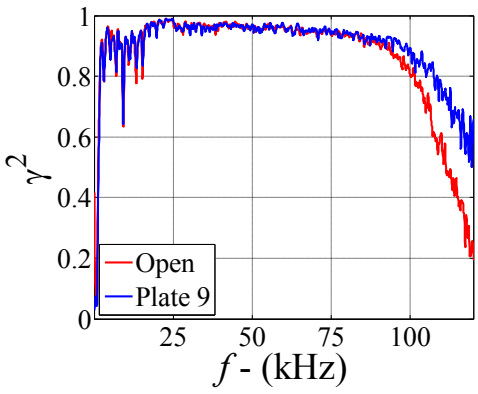

(i)

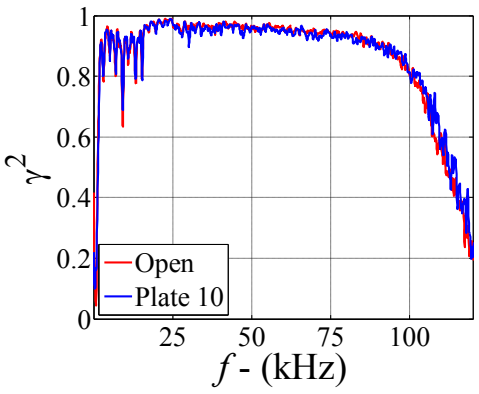

(j)

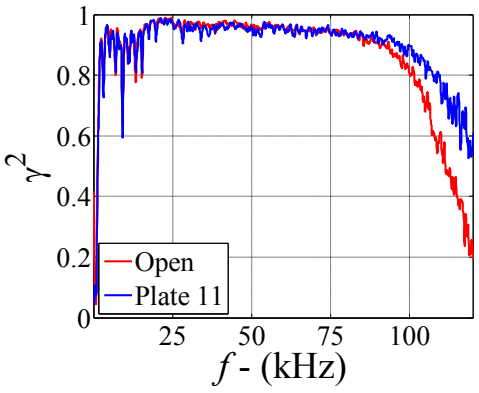

(k)

Figure 5.4: (cont.)

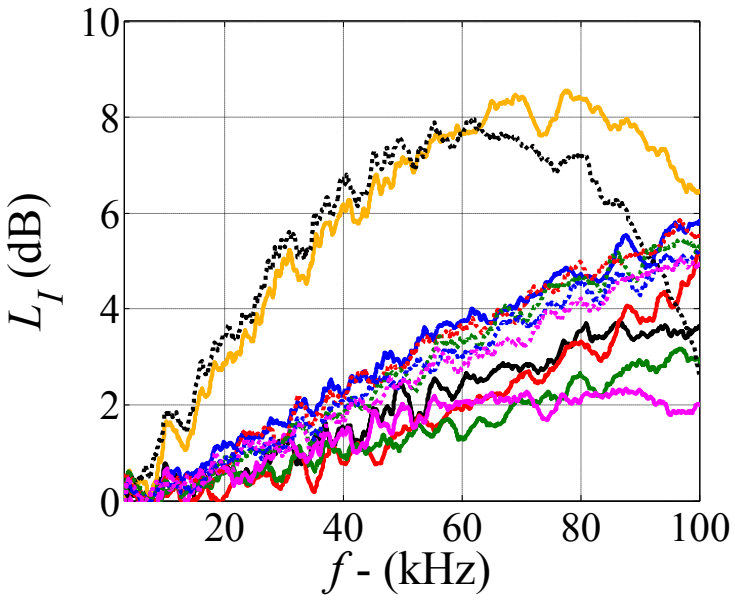

(a)

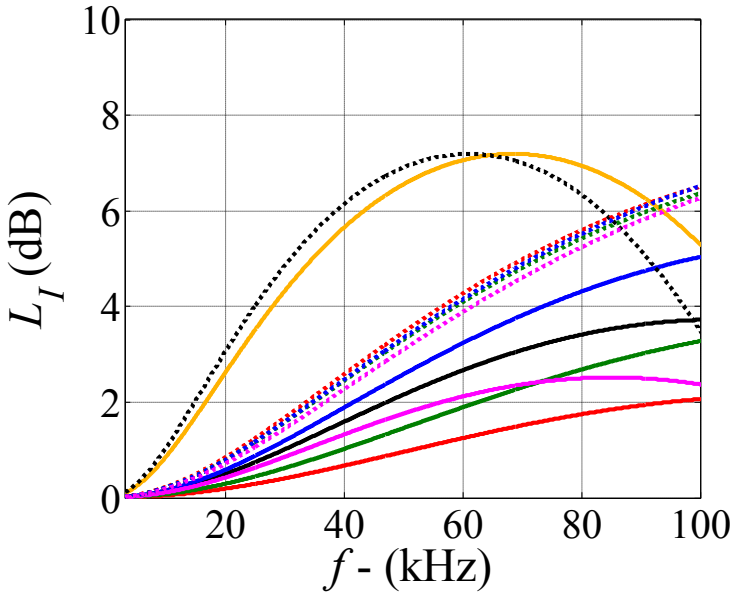

(b)

Figure 5.5: Insertion loss versus frequency comparison between **(a)** experiment and **(b)** current static model (Equation 3.23); Plate 1 Plate 2 Plate 3 Plate 4 Plate 5 Plate 6 Plate 7 Plate 8 Plate 9 Plate 10 Plate 11

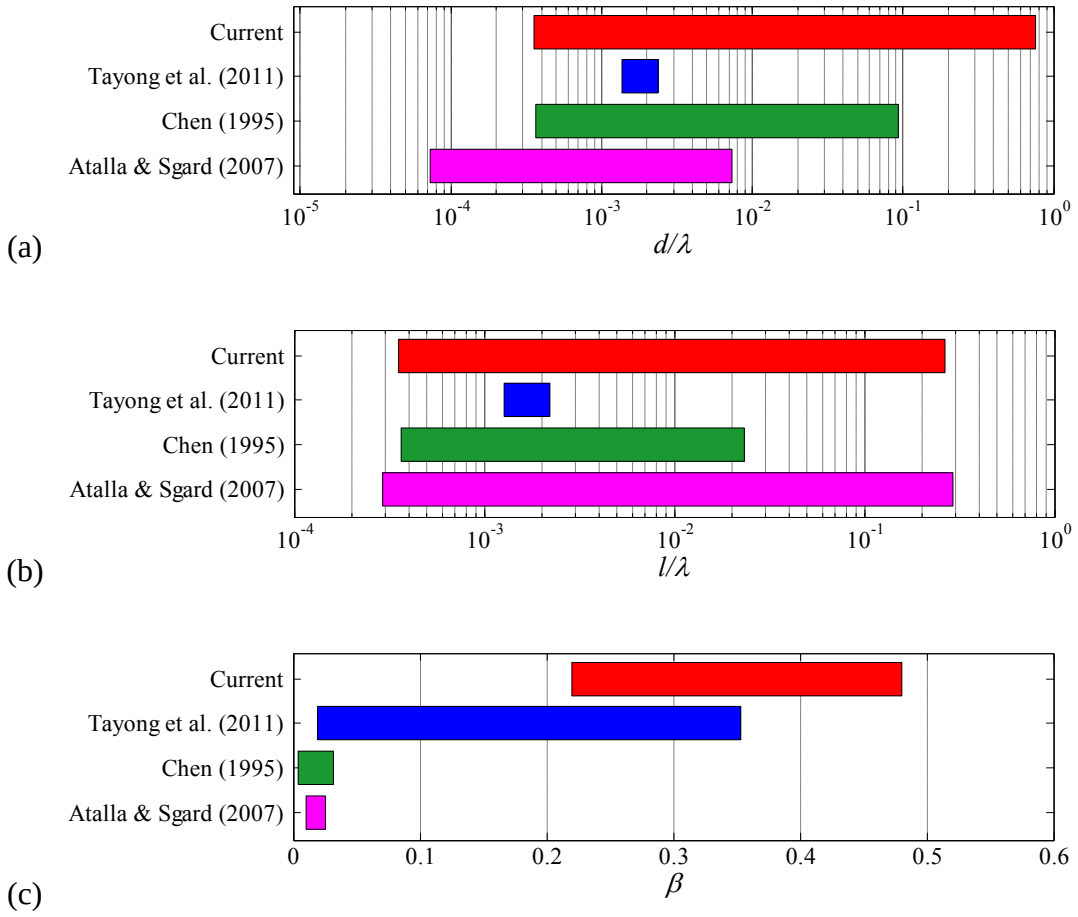

Figure 5.6: Comparisons of the range of **(a)** d/λ, **(b)** l/λ, and **(c)** β covered in the current and previous work. The ranges of d/λ, l/λ, and β are determined based on the range of experimental validation provided for the respective work.

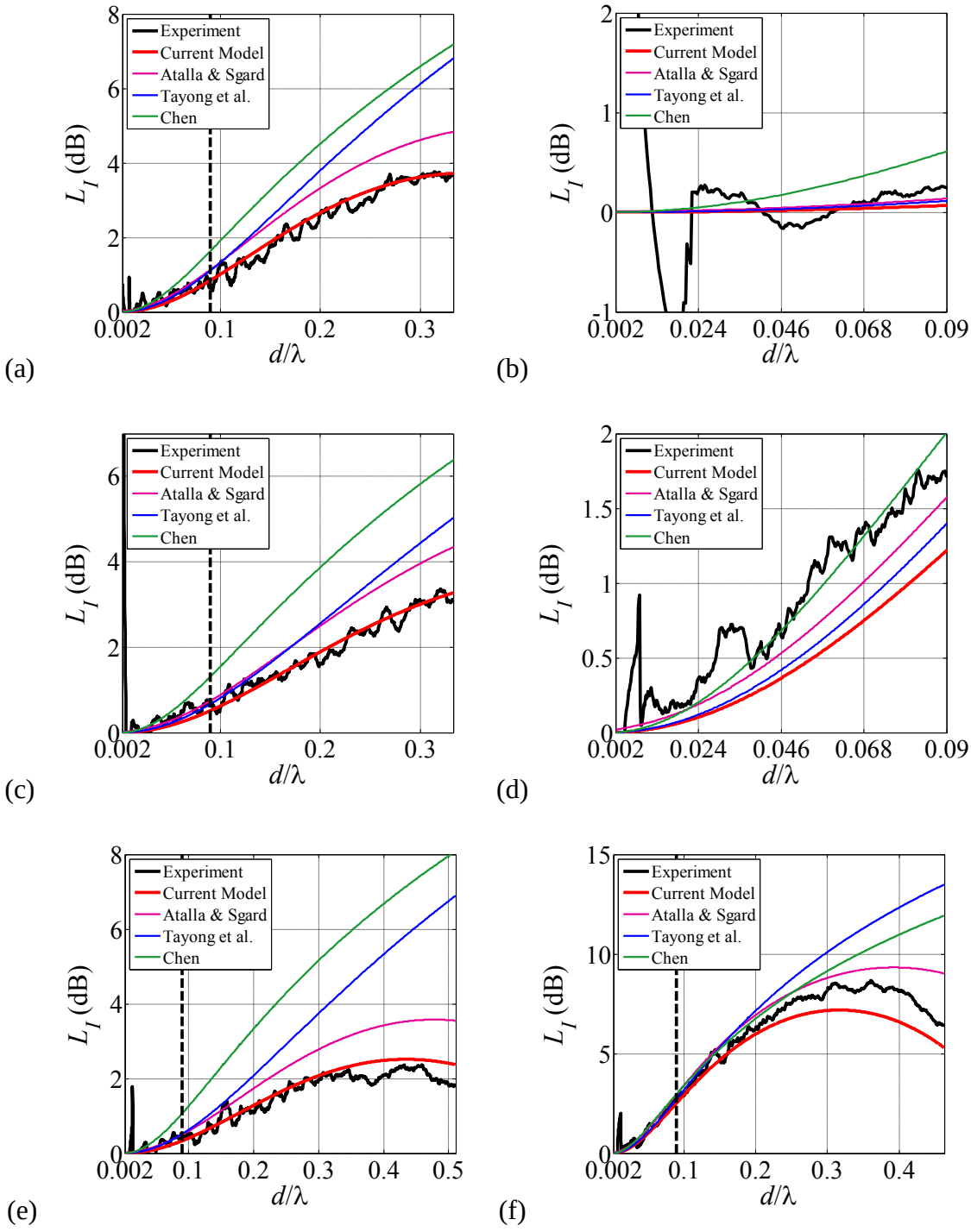

Figure 5.7: Comparison of transmission loss between experiment, current static theoretical model Equation (2.39), and previous models [18,19,21] for **(a)** Plate 1; **(b)** Plate 2; **(c)** Plate 3; **(d)** Plate 4; **(e)** Plate 5; **(f)** Plate 6; **(g)** Plate 7; **(h)** Plate 8; **(i)** Plate 9; **(j)** Plate 10; **(k)** Plate 11

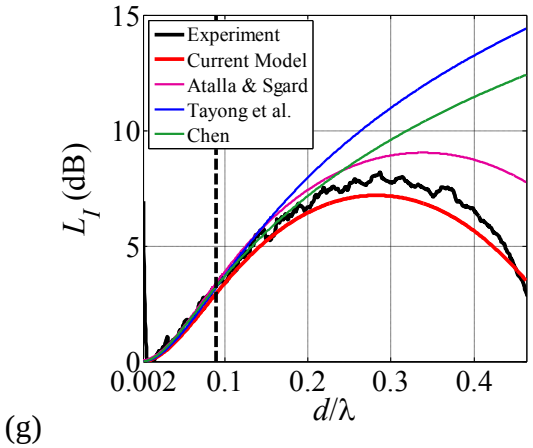

(g)

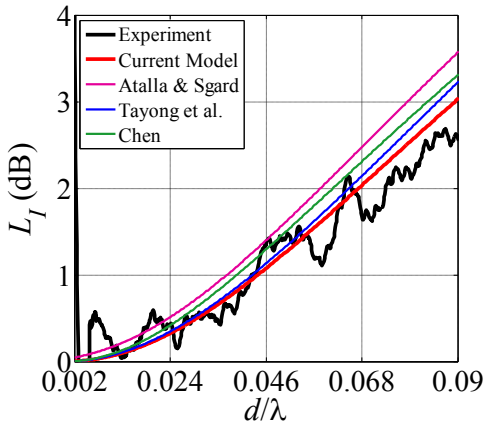

(h)

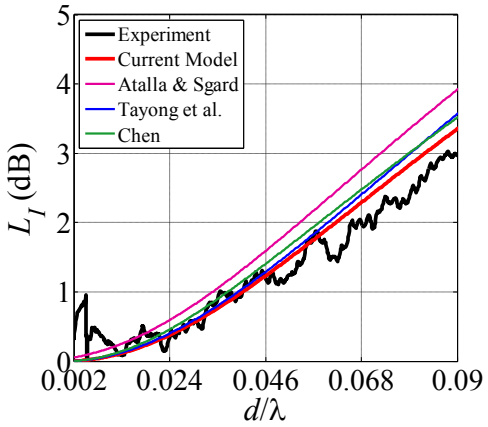

(i)

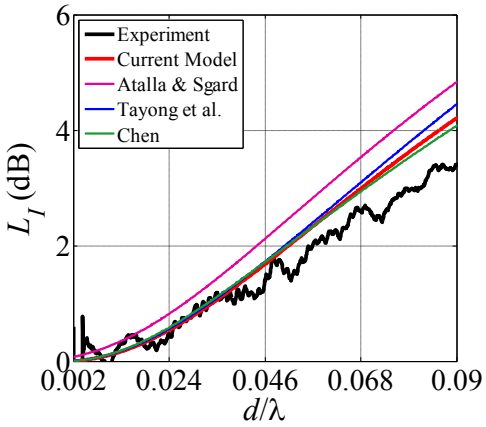

(j)

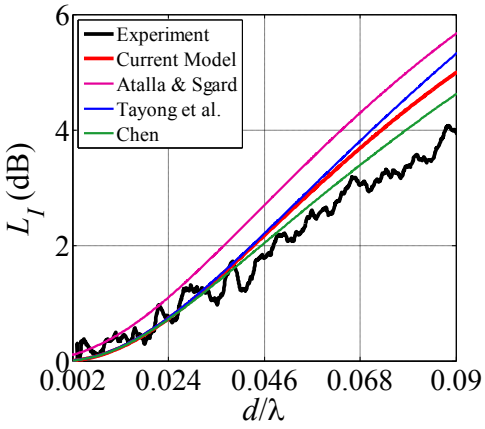

(k)

Figure 5.7: (cont.)

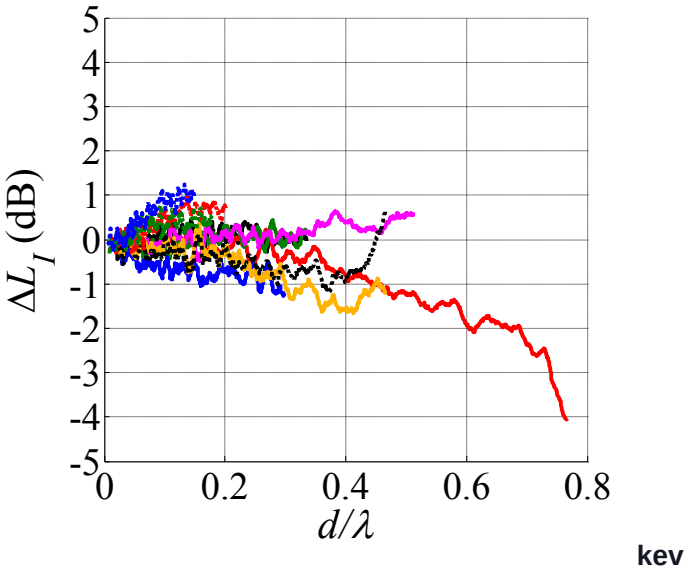

Figure 5.8: Insertion loss error versus d/λ:

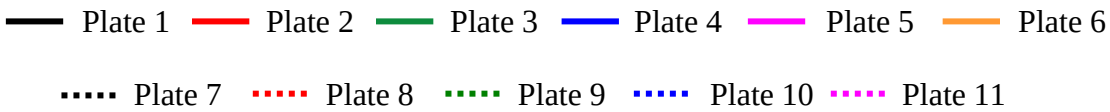

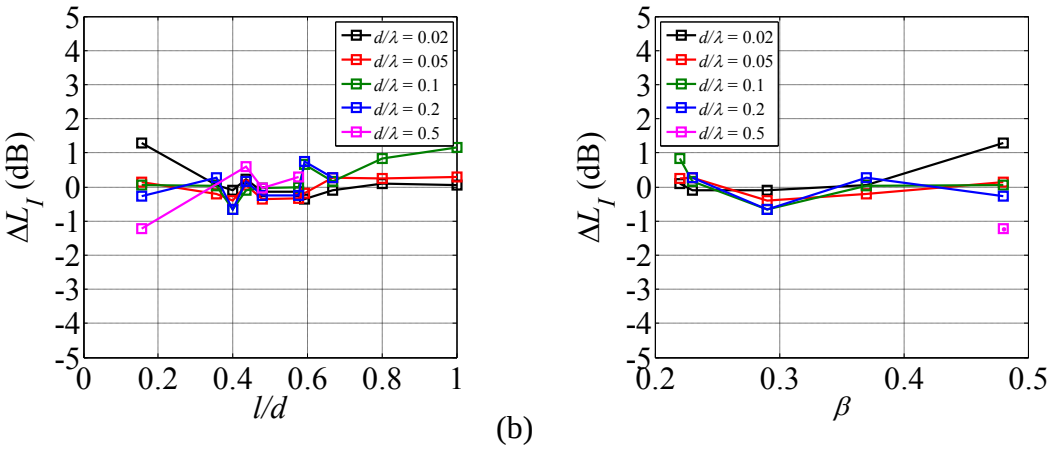

(a) (b)

Figure 5.9: Transmission loss error versus **(a)** thickness scaled by hole diameter;

(b) porosity

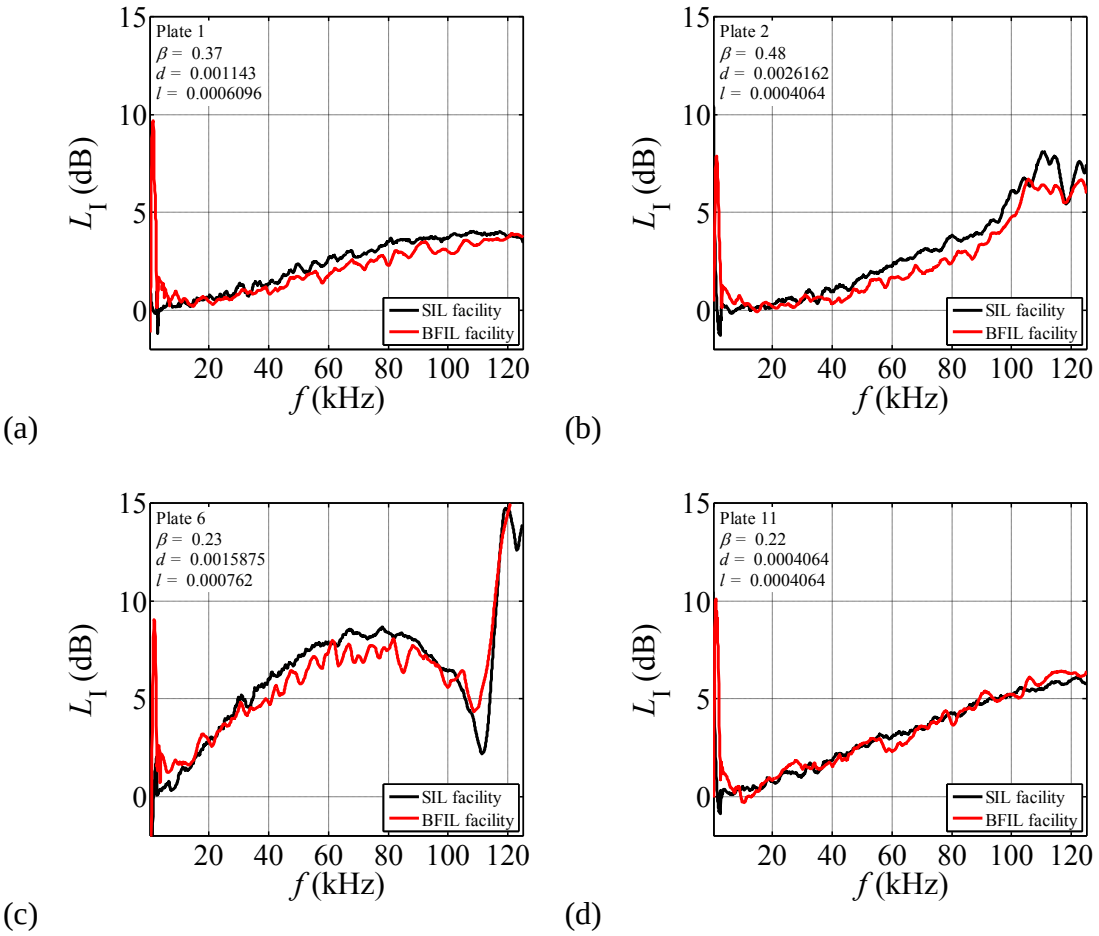

Figure 5.10: Comparing insertion loss measurements between SIL and BFIL facilities;

(a) Plate 1; **(b)** Plate 2; **(d)** Plate 6; **(d)** Plate 11

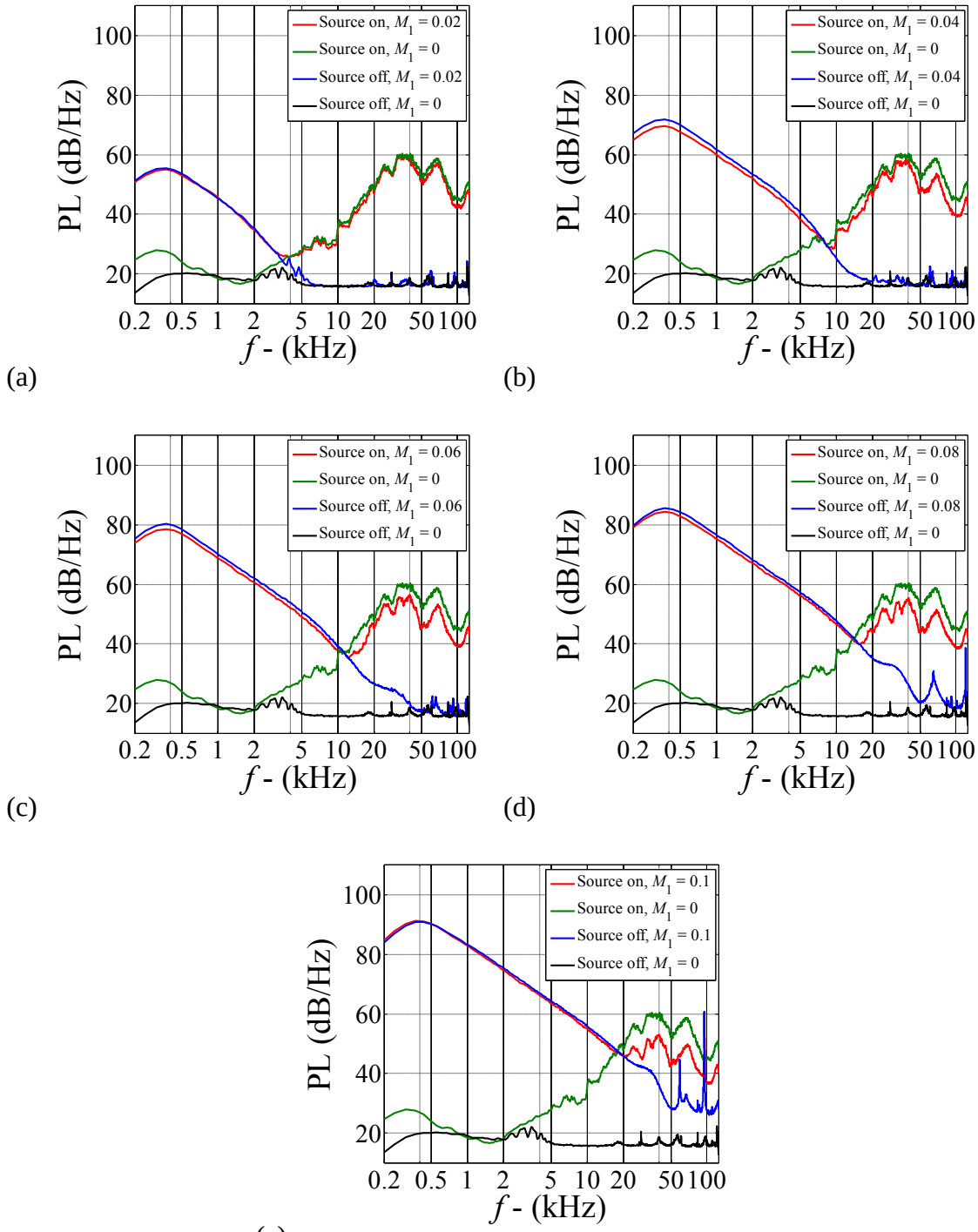

Figure 5.11: SPL spectral comparisons between varying source and flow combinations 1-4.

Measurements shown for Plate 1 at upstream Mach number

(a) M_1 = 0.02; **(b)** M_1 = 0.04; **(c)** M_1 = 0.06; **(d)** M_1 = 0.08; **(e)** M_1 = 0.1

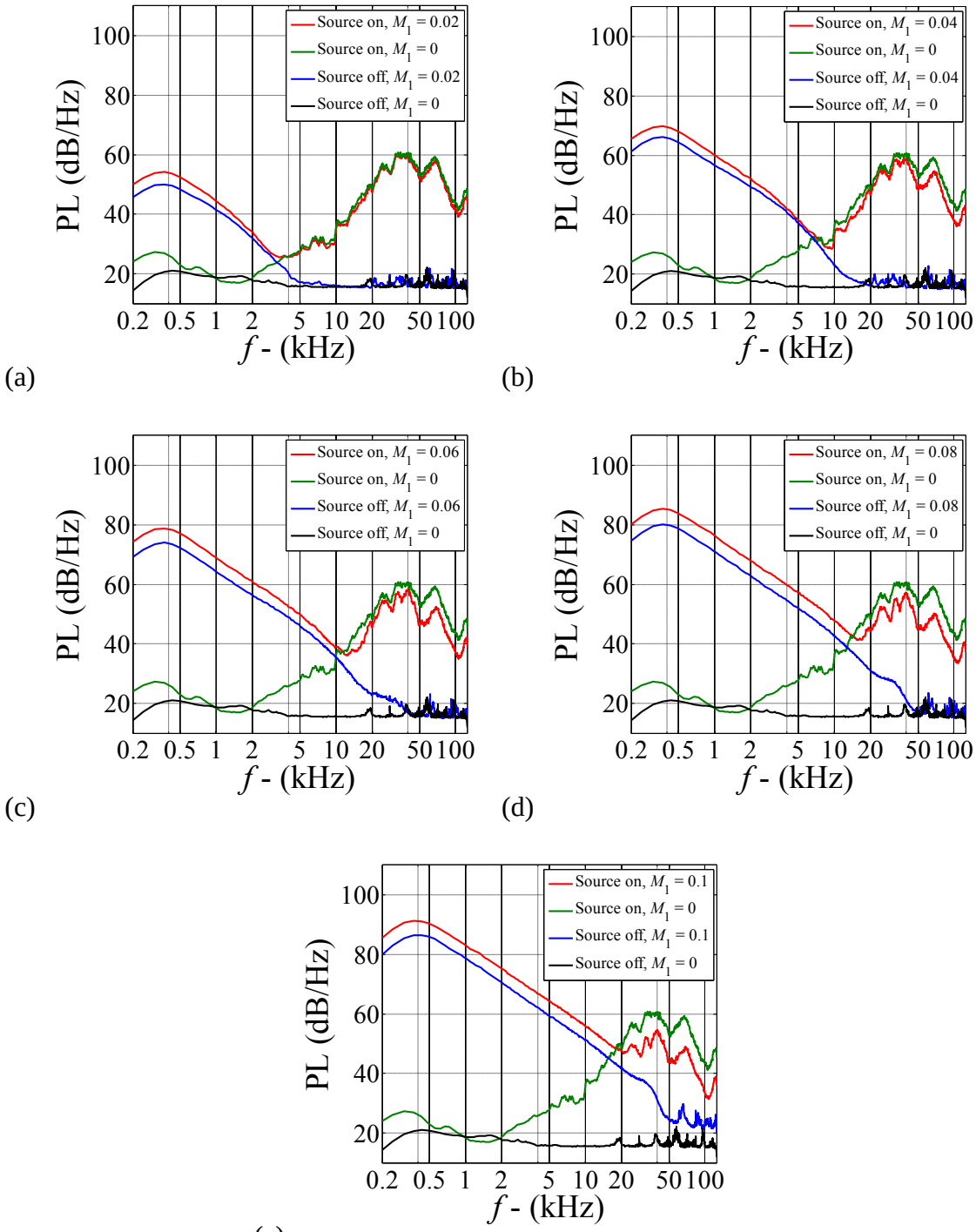

Figure 5.12: SPL spectral comparisons between varying source and flow combinations 1-4.

Measurements shown for Plate 2 at upstream Mach number

(a) M_1 = 0.02; **(b)** M_1 = 0.04; **(c)** M_1 = 0.06; **(d)** M_1 = 0.08; **(e)** M_1 = 0.1

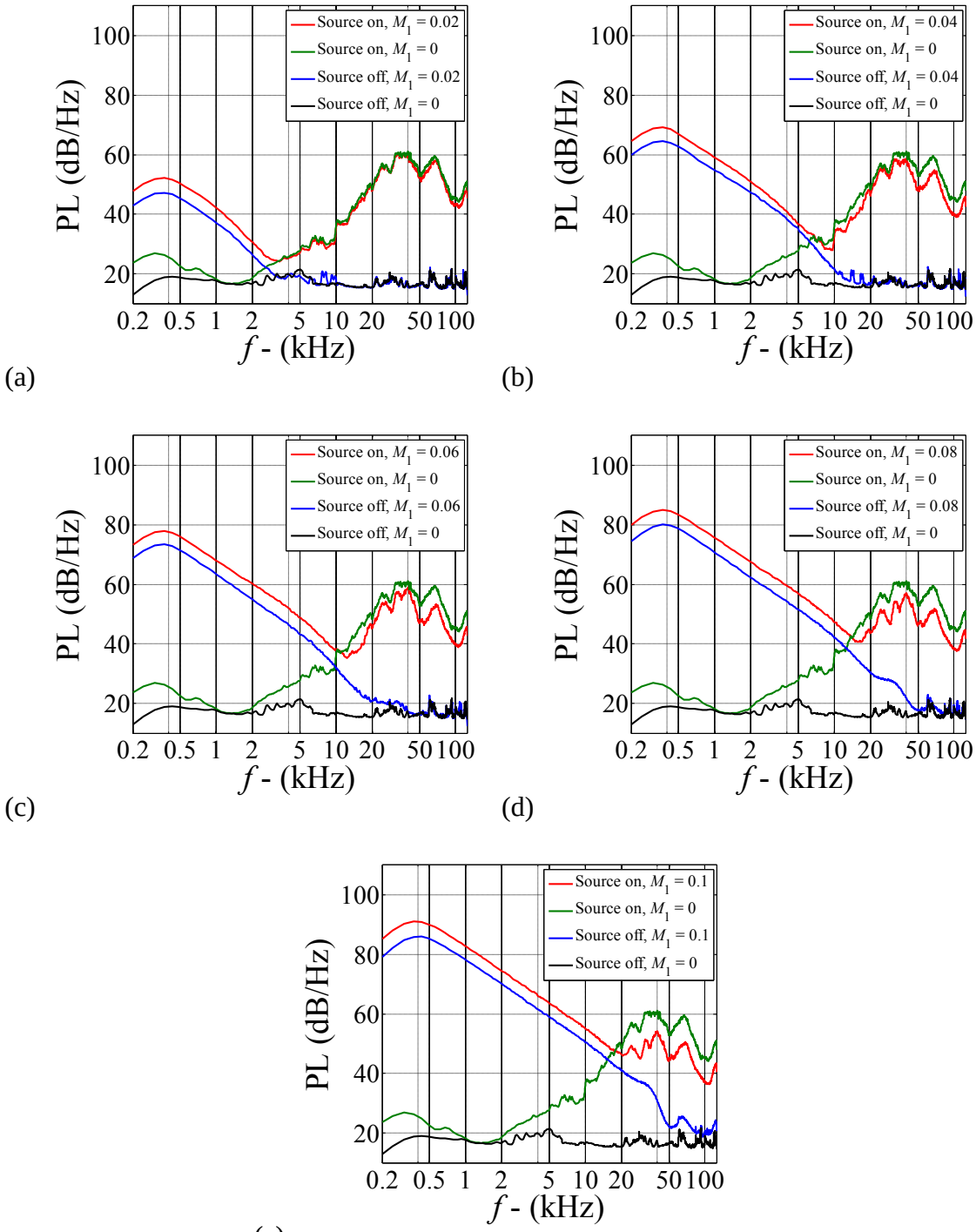

Figure 5.13: SPL spectral comparisons between varying source and flow combinations 1-4.

Measurements shown for Plate 3 at upstream Mach number

(a) M_1 = 0.02; **(b)** M_1 = 0.04; **(c)** M_1 = 0.06; **(d)** M_1 = 0.08; **(e)** M_1 = 0.1

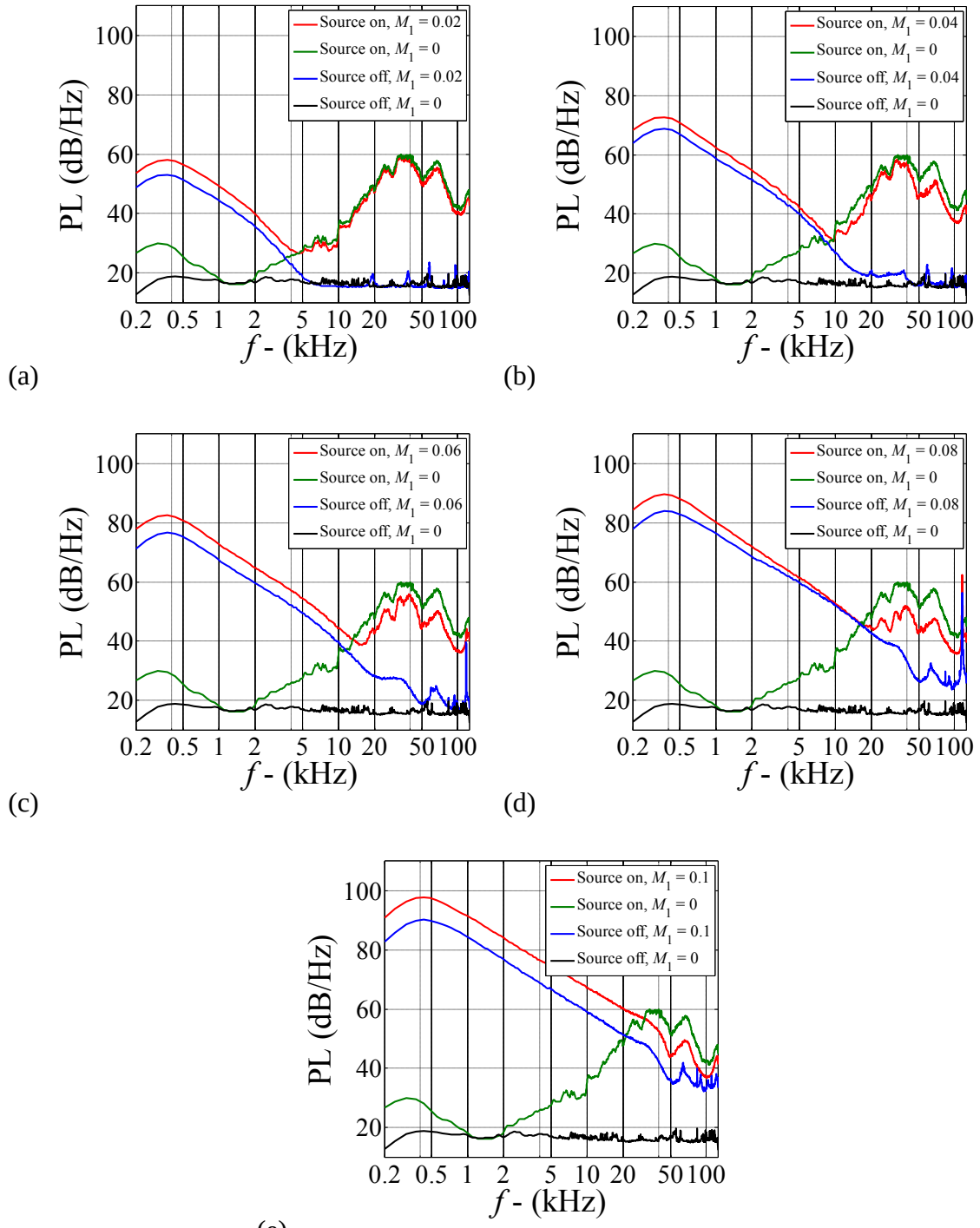

Figure 5.14: SPL spectral comparisons between varying source and flow combinations 1-4.

Measurements shown for Plate 4 at upstream Mach number

(a) M_1 = 0.02; **(b)** M_1 = 0.04; **(c)** M_1 = 0.06; **(d)** M_1 = 0.08; **(e)** M_1 = 0.1

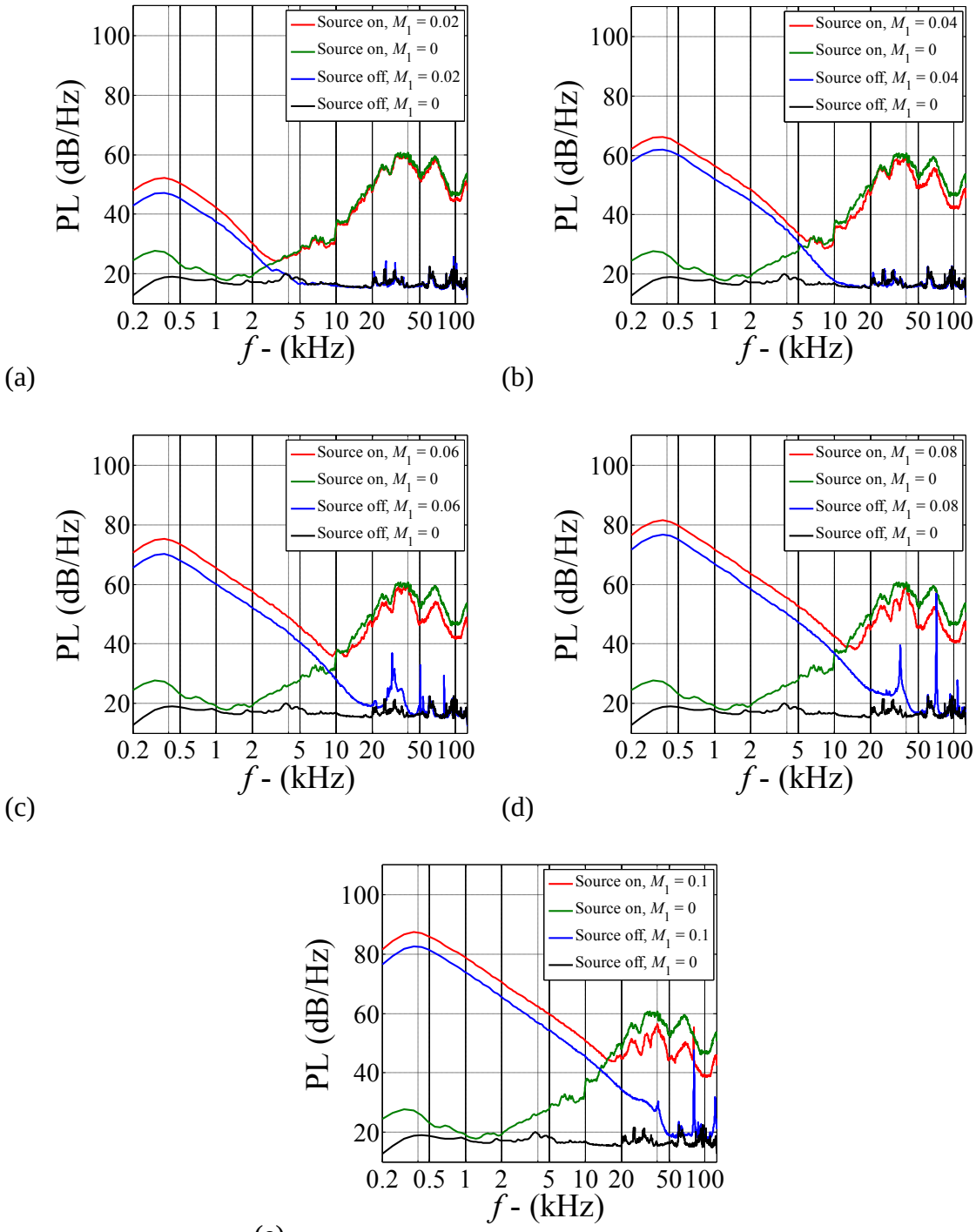

Figure 5.15: SPL spectral comparisons between varying source and flow combinations 1-4.

Measurements shown for Plate 5 at upstream Mach number

(a) M_1 = 0.02; **(b)** M_1 = 0.04; **(c)** M_1 = 0.06; **(d)** M_1 = 0.08; **(e)** M_1 = 0.1

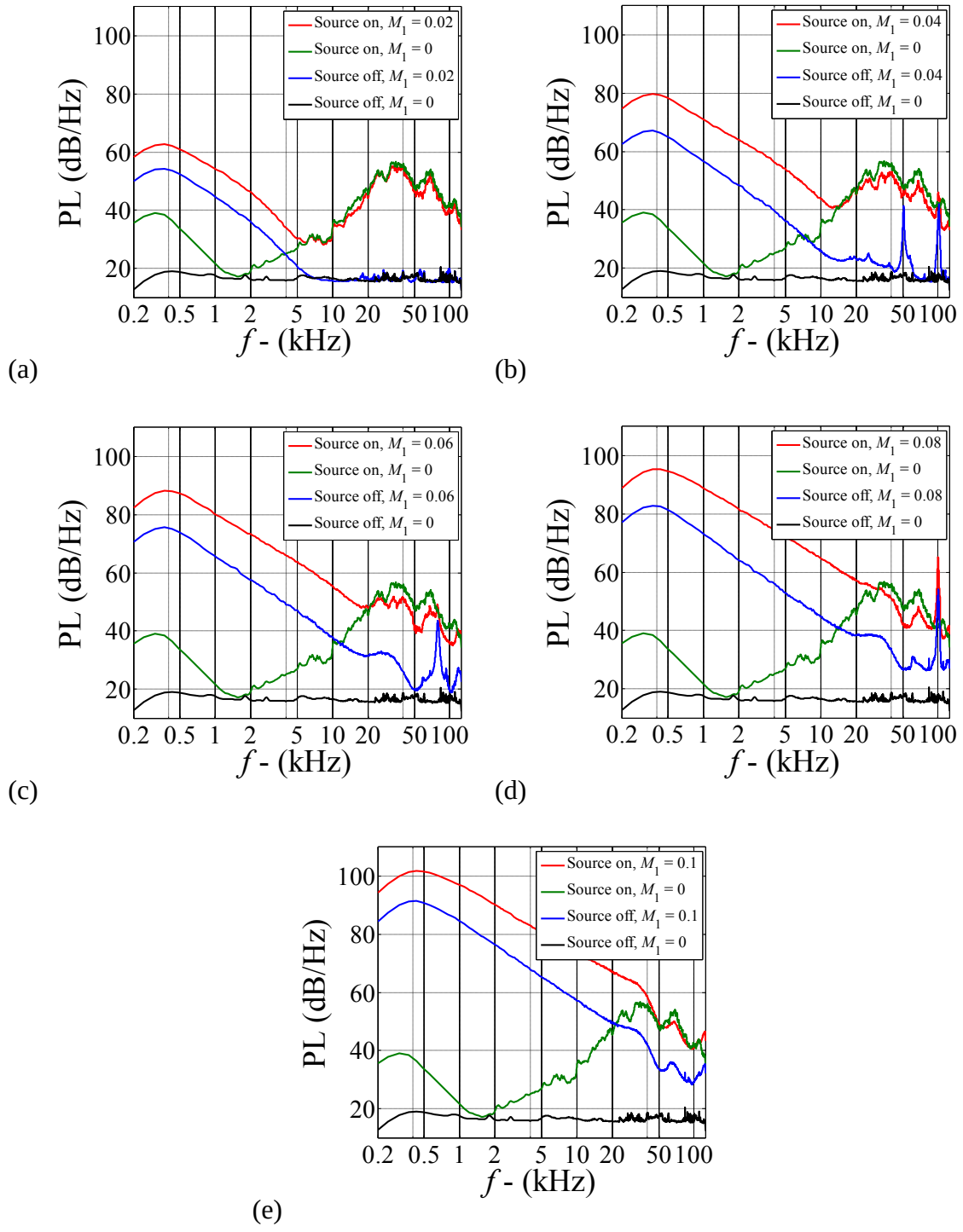

Figure 5.16: SPL spectral comparisons between varying source and flow combinations 1-4.

Measurements shown for Plate 6 at upstream Mach number

(a) M_1 = 0.02; **(b)** M_1 = 0.04; **(c)** M_1 = 0.06; **(d)** M_1 = 0.08; **(e)** M_1 = 0.1

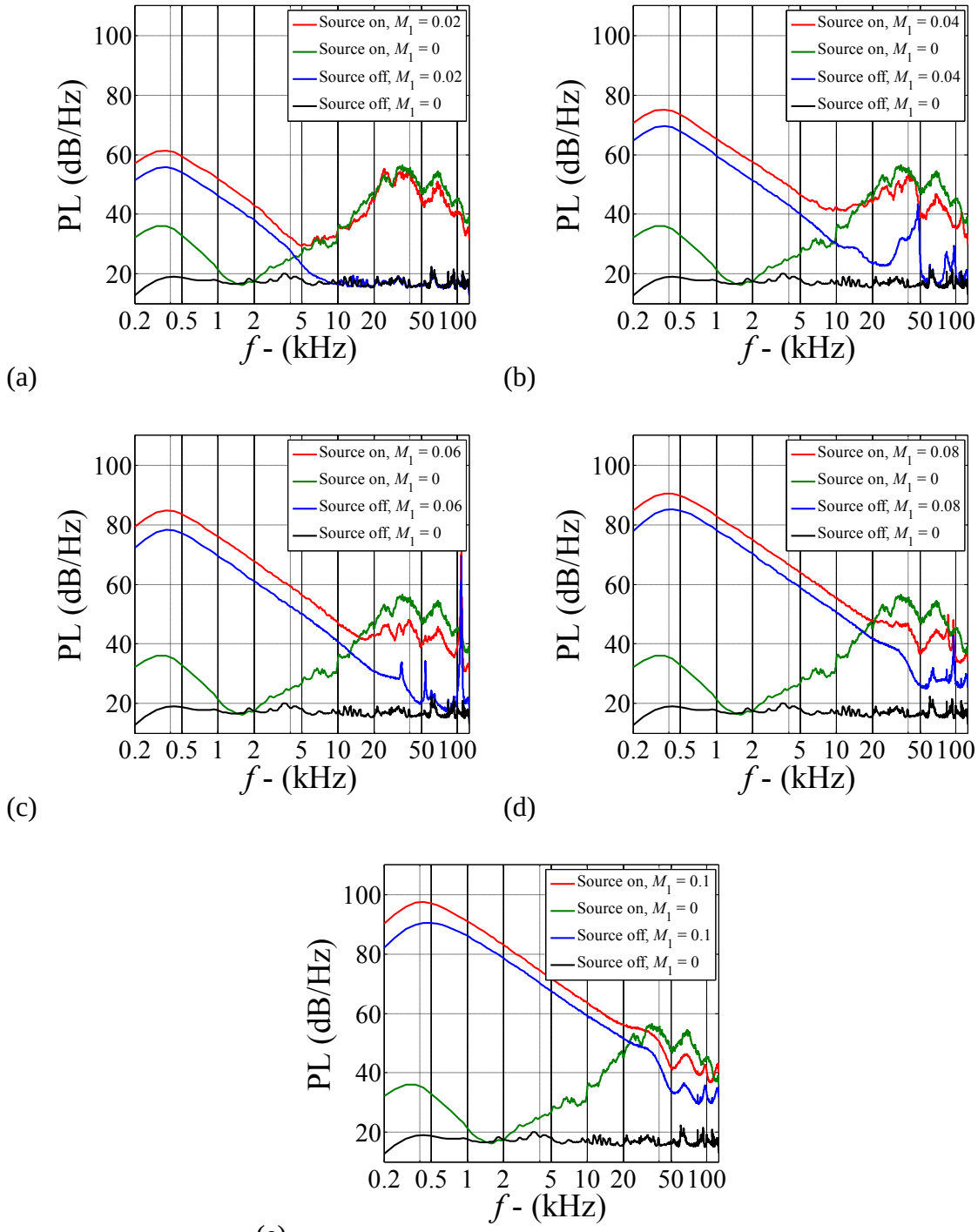

Figure 5.17: SPL spectral comparisons between varying source and flow combinations 1-4.

Measurements shown for Plate 7 at upstream Mach number

(a) M_1 = 0.02; **(b)** M_1 = 0.04; **(c)** M_1 = 0.06; **(d)** M_1 = 0.08; **(e)** M_1 = 0.1

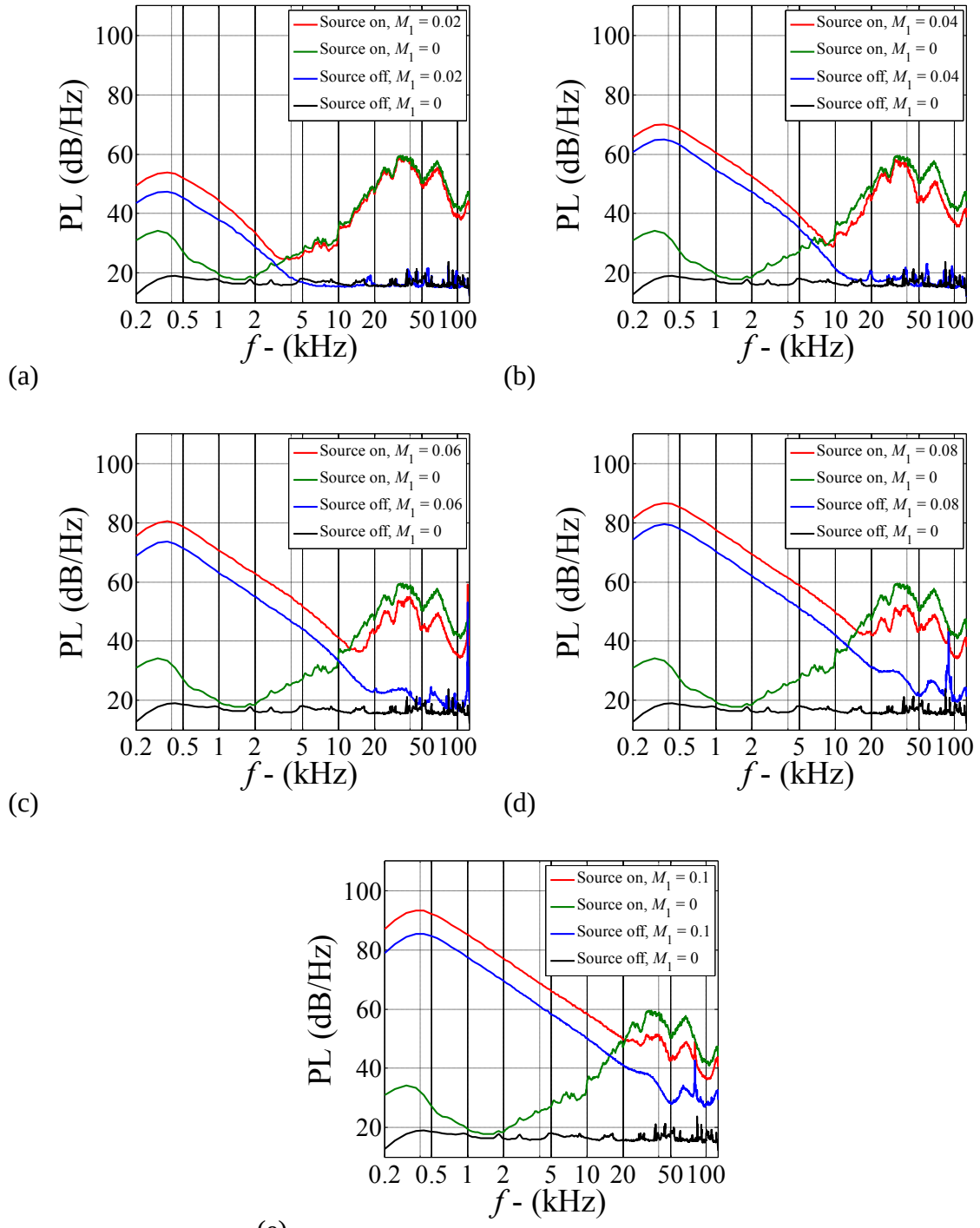

Figure 5.18: SPL spectral comparisons between varying source and flow combinations 1-4.

Measurements shown for Plate 8 at upstream Mach number

(a) M_1 = 0.02; **(b)** M_1 = 0.04; **(c)** M_1 = 0.06; **(d)** M_1 = 0.08; **(e)** M_1 = 0.1

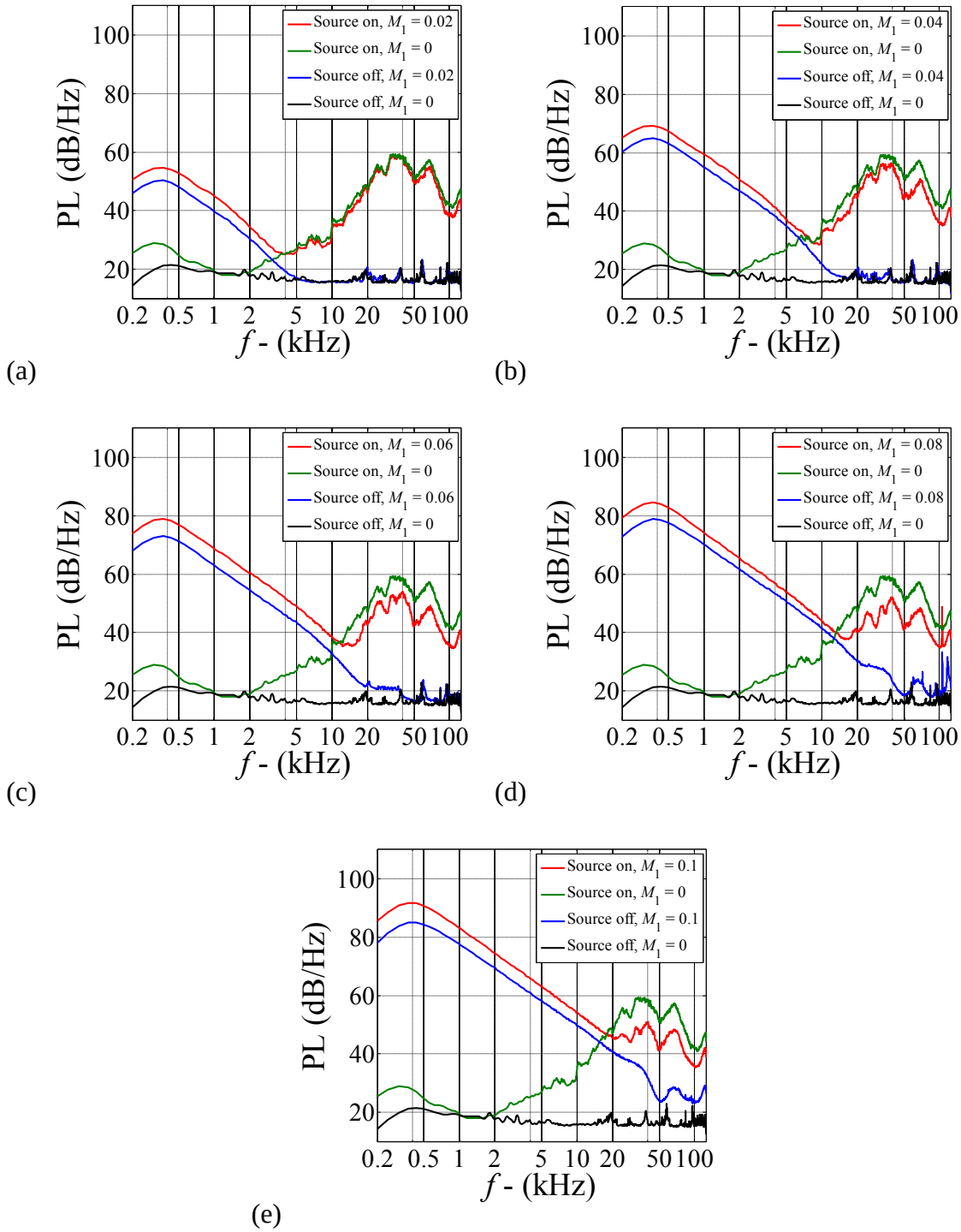

Figure 5.19: SPL spectral comparisons between varying source and flow combinations 1-4.

Measurements shown for Plate 9 at upstream Mach number

(a) M_1 = 0.02; **(b)** M_1 = 0.04; **(c)** M_1 = 0.06; **(d)** M_1 = 0.08; **(e)** M_1 = 0.1

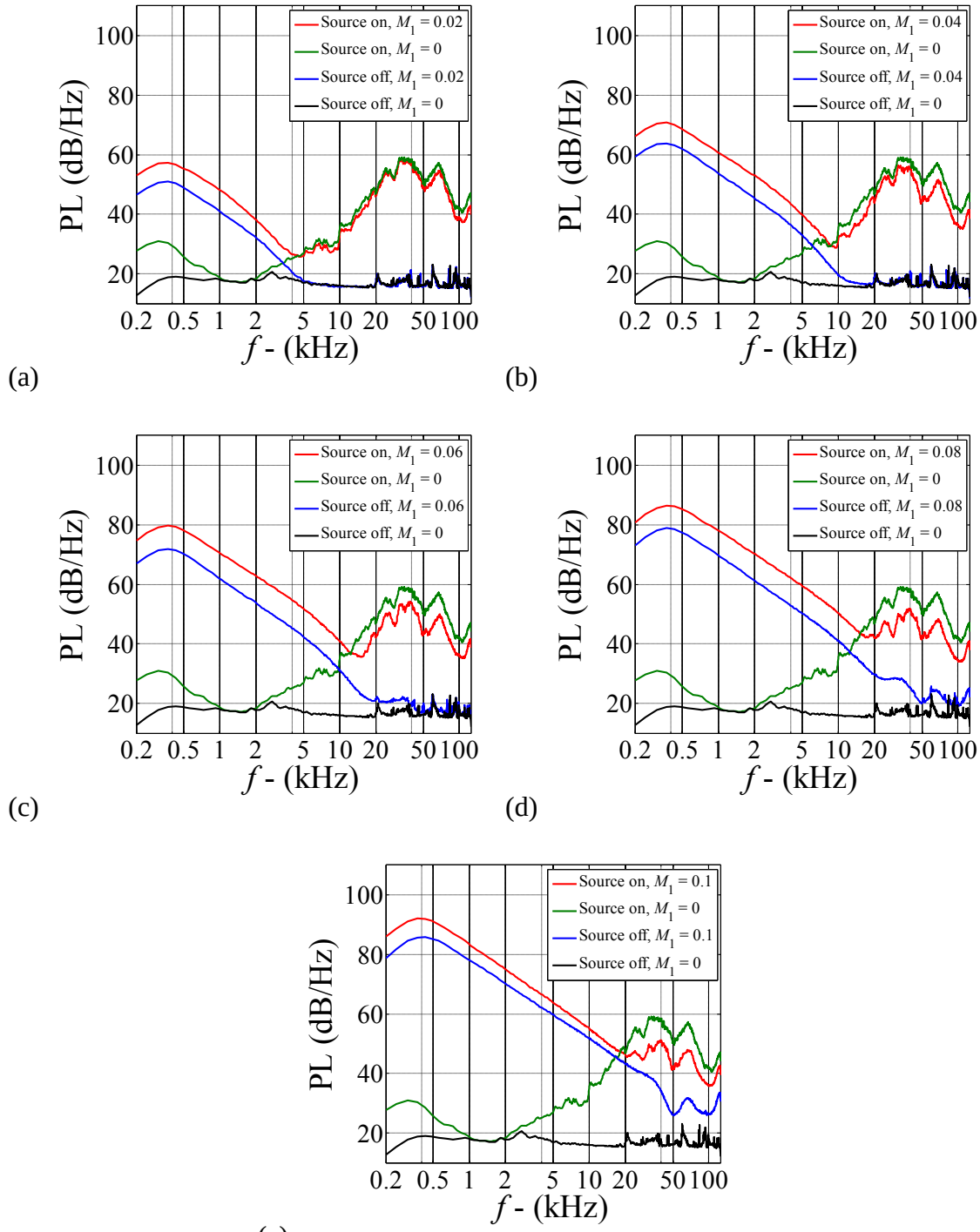

Figure 5.20: SPL spectral comparisons between varying source and flow combinations 1-4.

Measurements shown for Plate 10 at upstream Mach number

(a) M_1 = 0.02; **(b)** M_1 = 0.04; **(c)** M_1 = 0.06; **(d)** M_1 = 0.08; **(e)** M_1 = 0.1

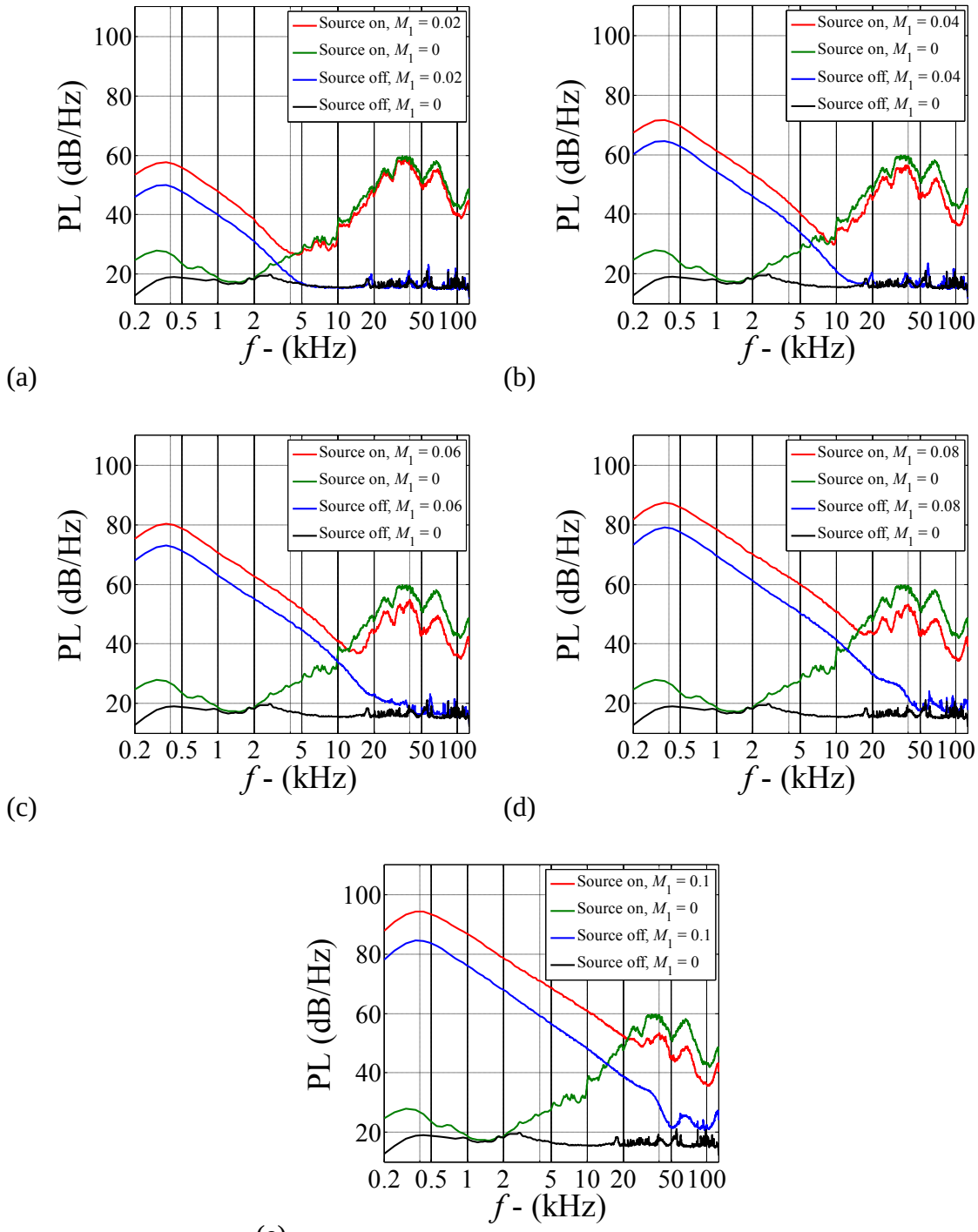

Figure 5.21: SPL spectral comparisons between varying source and flow combinations 1-4.

Measurements shown for Plate 11 at upstream Mach number

(a) M_1 = 0.02; **(b)** M_1 = 0.04; **(c)** M_1 = 0.06; **(d)** M_1 = 0.08; **(e)** M_1 = 0.1

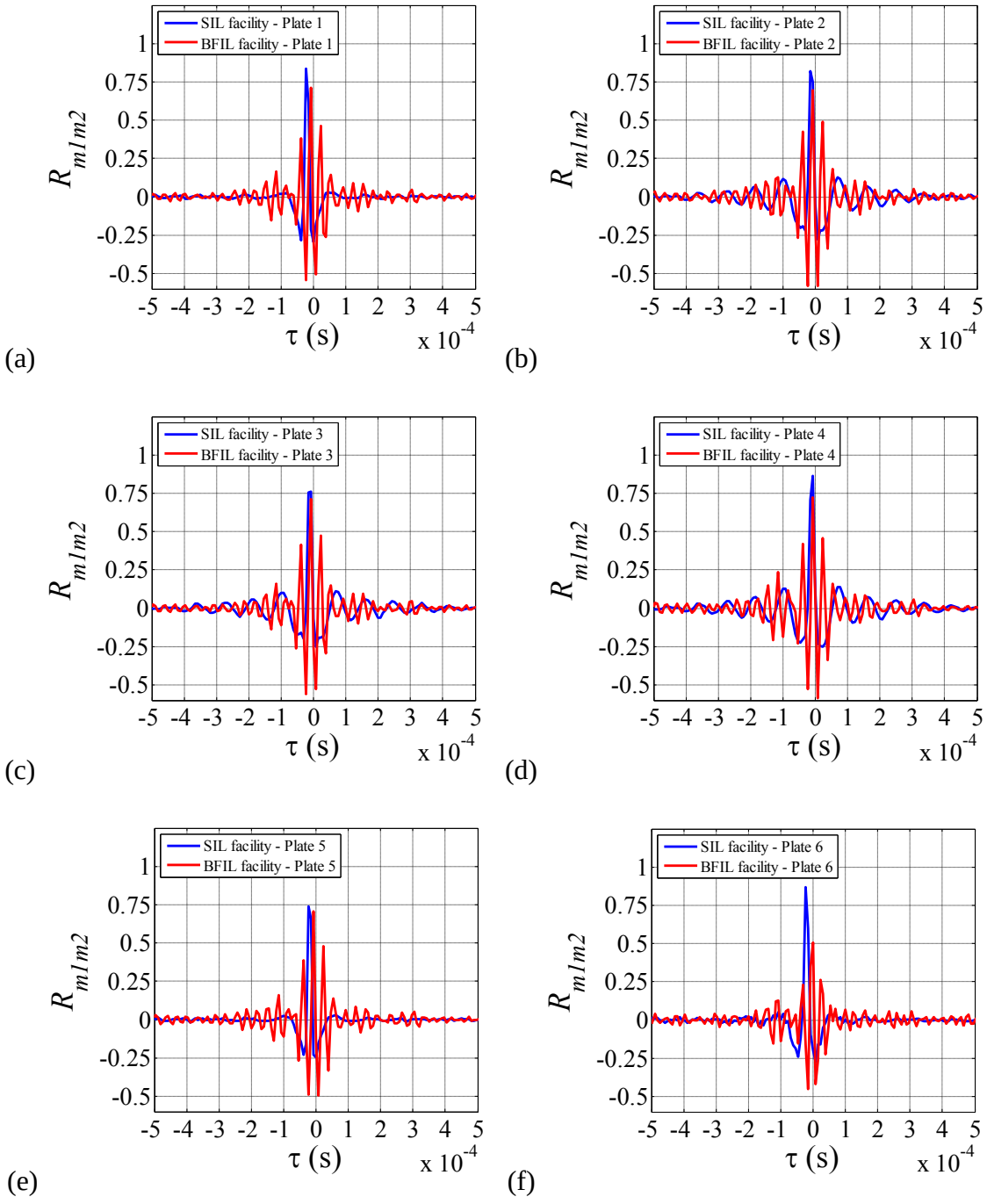

Figure 5.22: Comparison of microphone cross correlations obtained in SIL and BFIL facilities.

(a) Plate 1; **(b)** Plate 2; **(c)** Plate 3; **(d)** Plate 4; **(e)** Plate 5; **(f)** Plate 6;

(g) Plate 7; **(h)** Plate 8; **(i)** Plate 9; **(j)** Plate 10; **(k)** Plate 11

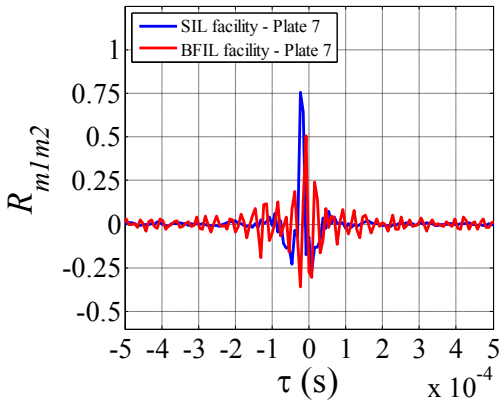

g.)

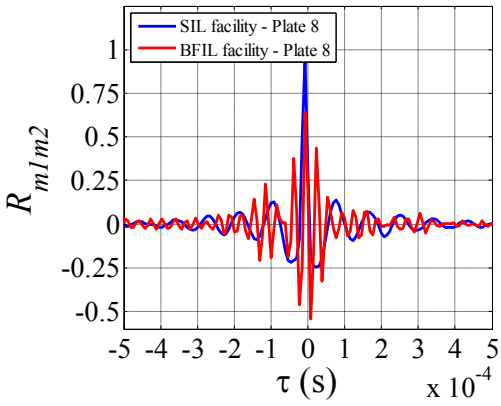

h.)

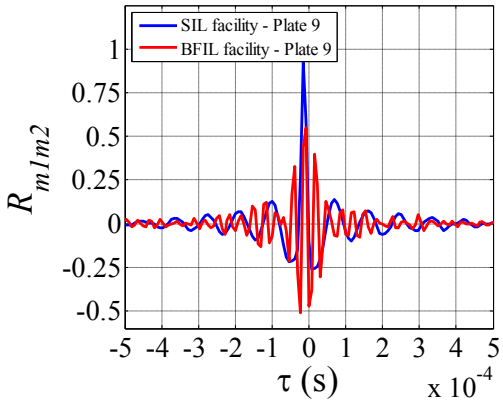

i.)

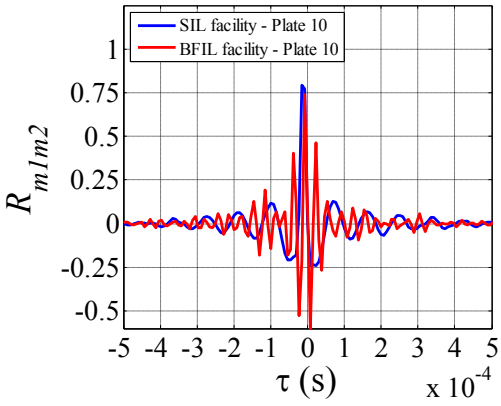

j.)

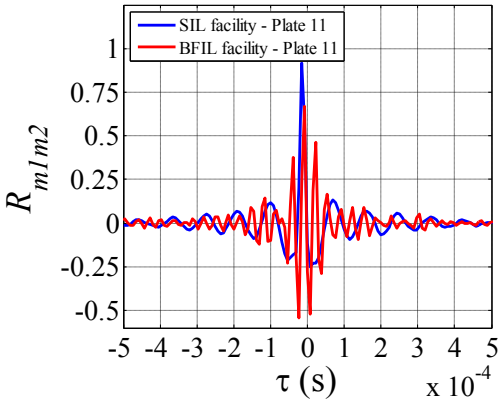

k.)

Figure 5.22: (cont.)

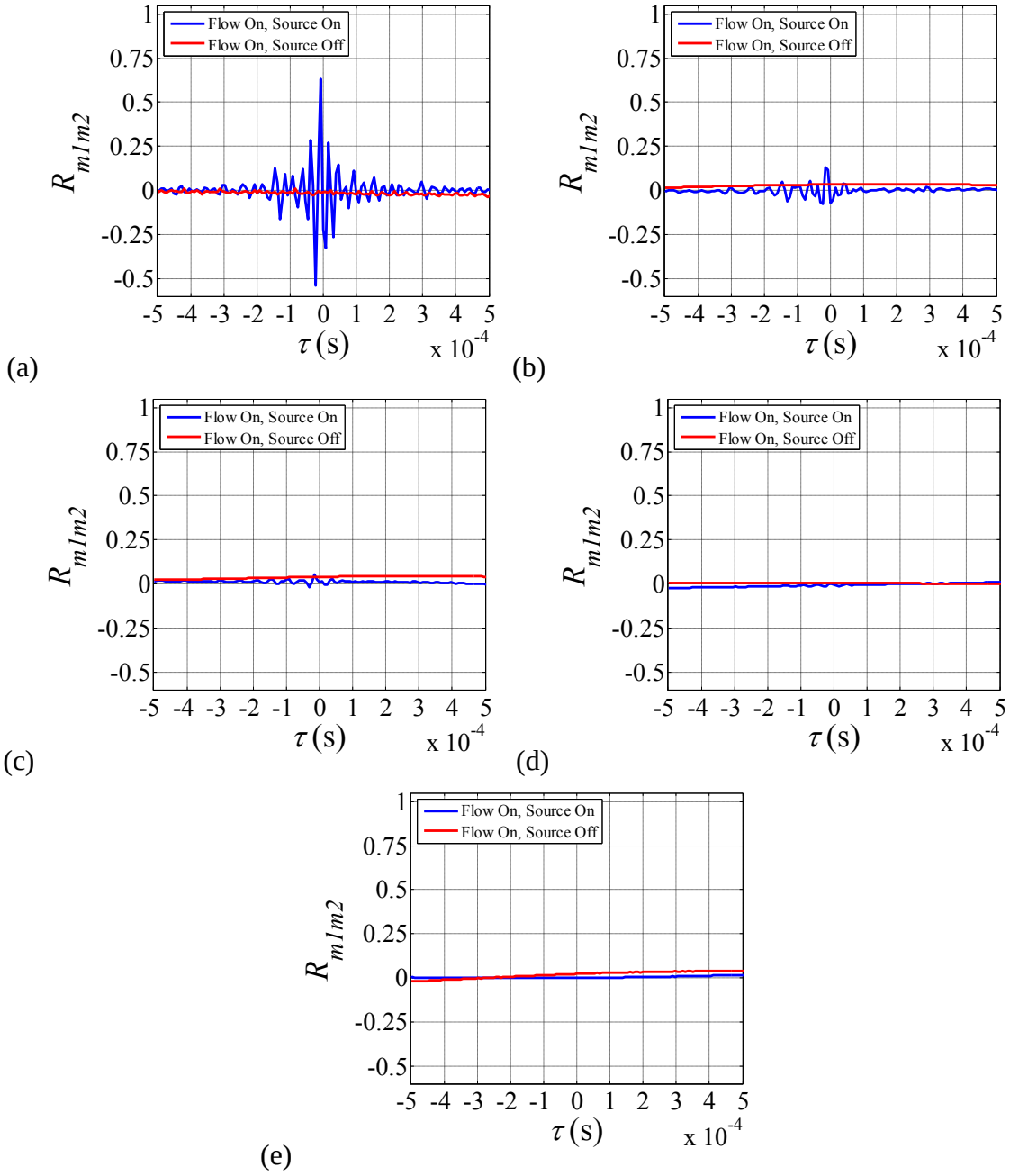

Figure 5.23: Effect of mean flow on signal correlation for Plate 1, and signal correlation of flow only at varying upstream Mach number; **(a)** $M_1 = 0.02$; **(b)** $M_1 = 0.04$; **(c)** $M_1 = 0.06$; **(d)** $M_1 = 0.08$; **(e)** $M_1 = 0.10$

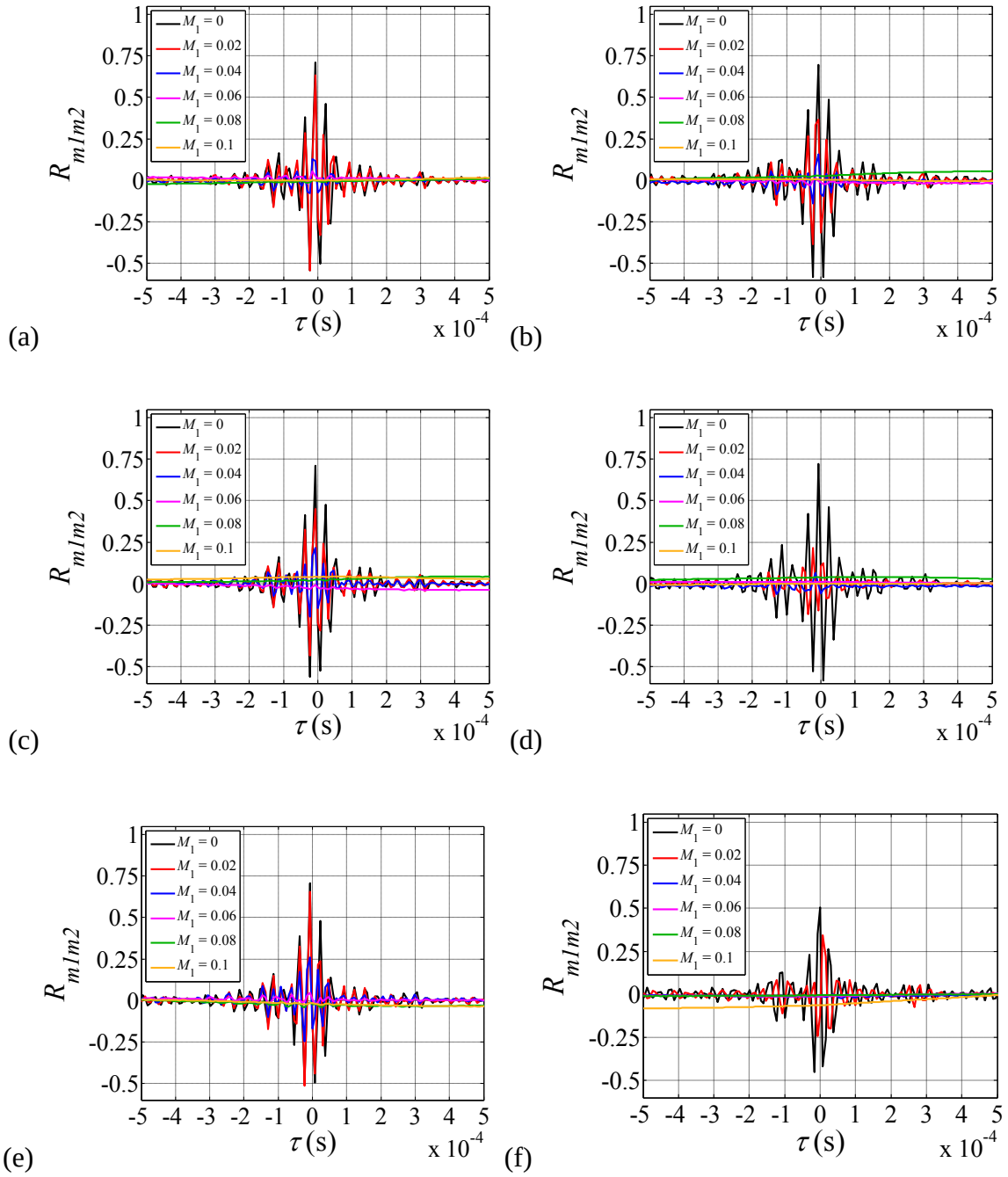

Figure 5.24: Effect of upstream bias flow Mach number on cross-correlation.

(a) Plate 1; **(b)** Plate 2; **(c)** Plate 3; **(d)** Plate 4; **(e)** Plate 5; **(f)** Plate 6;

(g) Plate 7; **(h)** Plate 8; **(i)** Plate 9; **(j)** Plate 10; **(k)** Plate 11

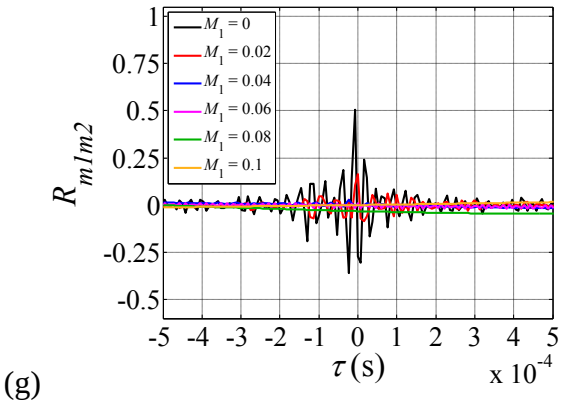

(g)

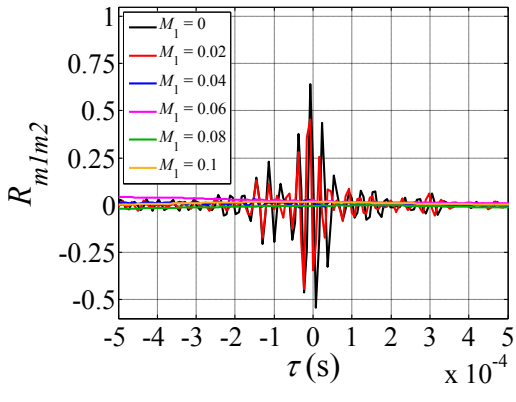

(h)

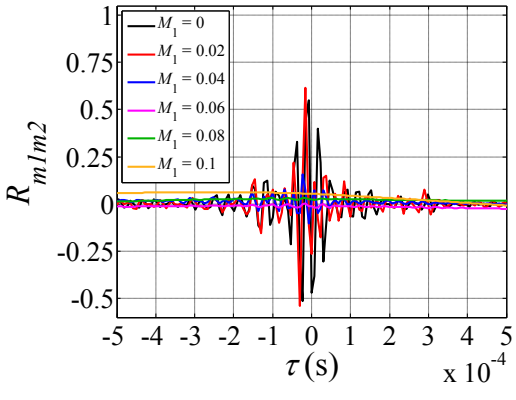

(i)

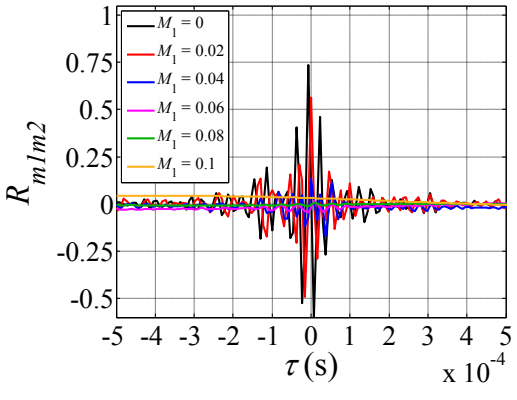

(j)

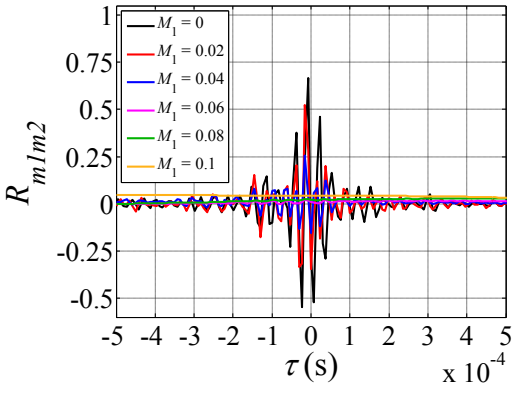

(k)

Figure 5.24: (cont.)

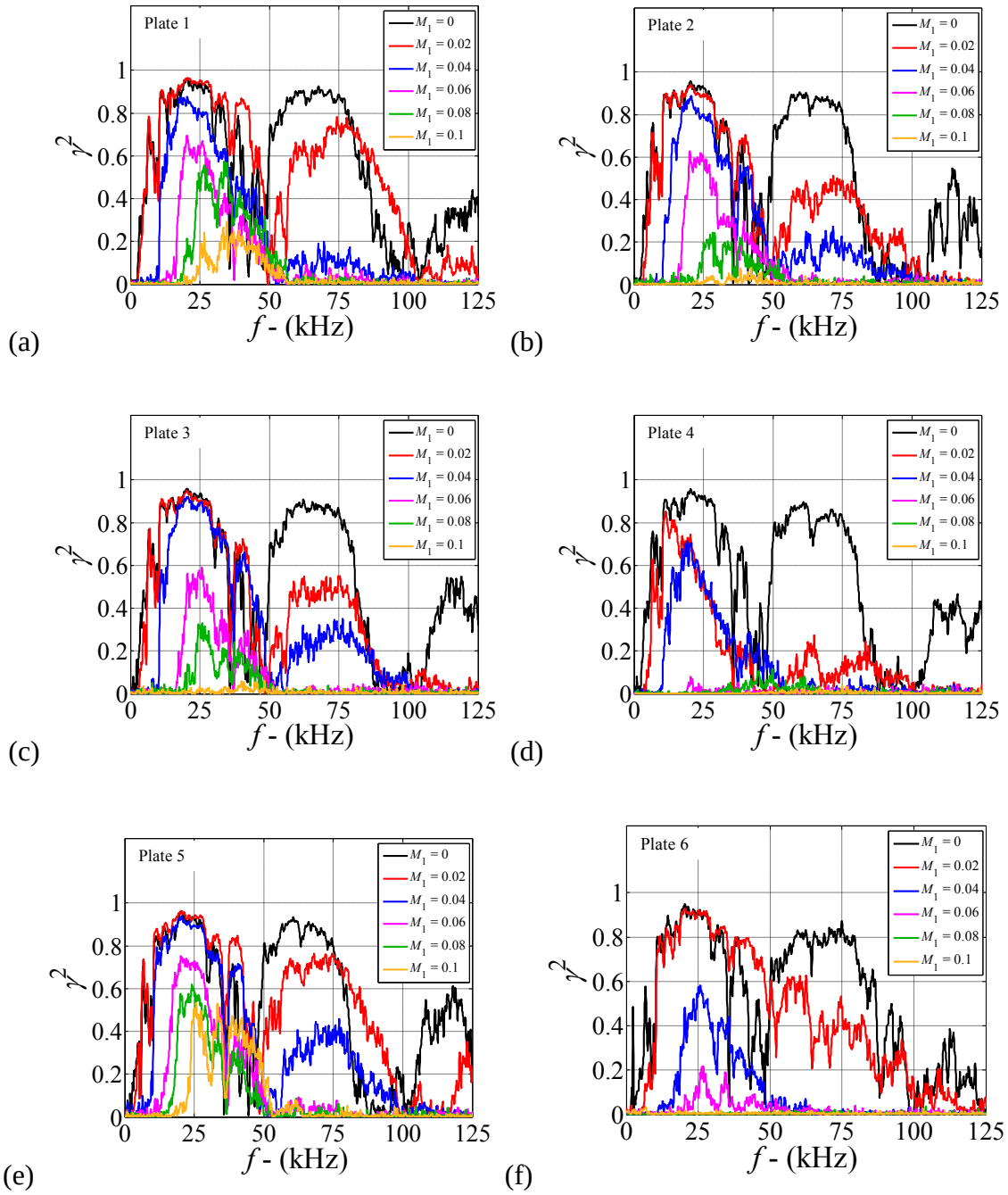

Figure 5.25: Effect of upstream bias flow Mach number on microphone coherence

(a) Plate 1; **(b)** Plate 2; **(c)** Plate 3; **(d)** Plate 4; **(e)** Plate 5; **(f)** Plate 6;

(g) Plate 7; **(h)** Plate 8; **(i)** Plate 9; **(j)** Plate 10; **(k)** Plate 11

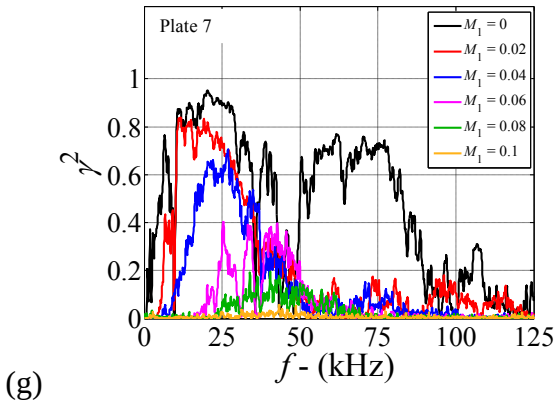

(g)

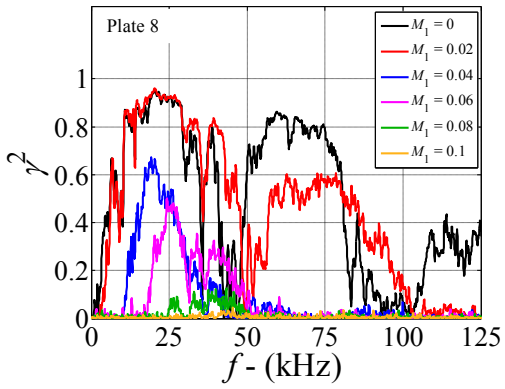

(h)

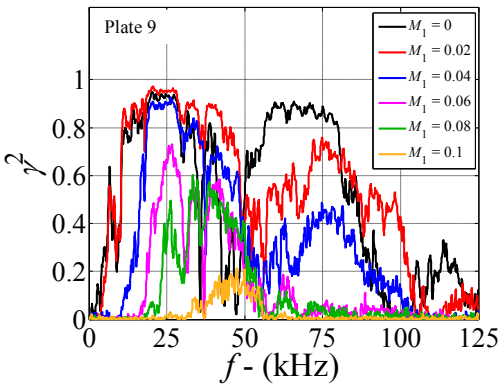

(i)

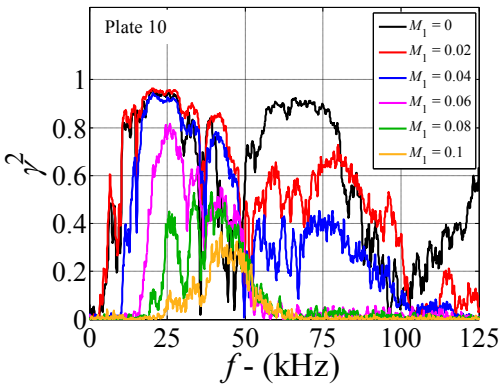

(j)

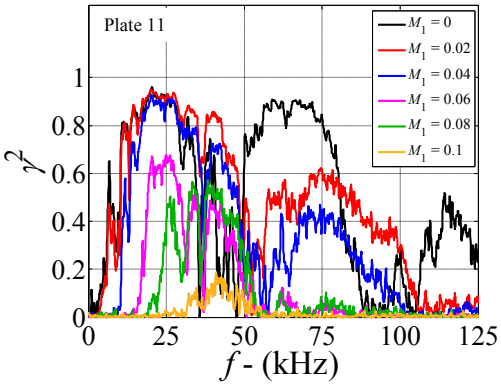

(k)

Figure 5.25: (cont.)

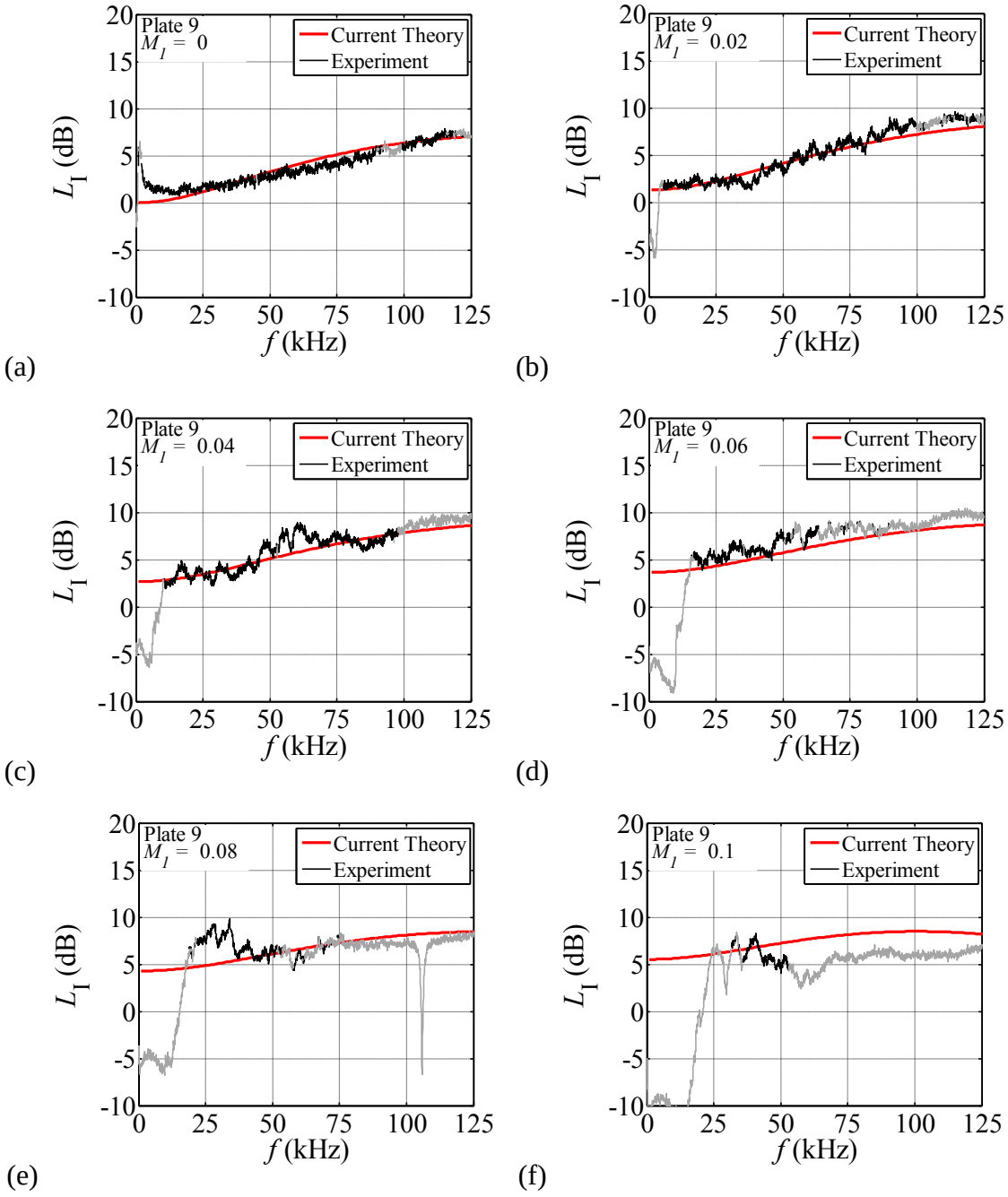

Figure 5.26: Insertion loss measurement vs. current theory. Black line indicates experimental data that satisfy the minimum SNR and coherence requirement, and grey line indicates data points which do not satisfy one or both of the requirements

(a) $M_1 = 0$; **(b)** $M_1 = 0.02$; **(c)** $M_1 = 0.04$; **(d)** $M_1 = 0.06$; **(e)** $M_1 = 0.08$; **(f)** $M_1 = 0.10$

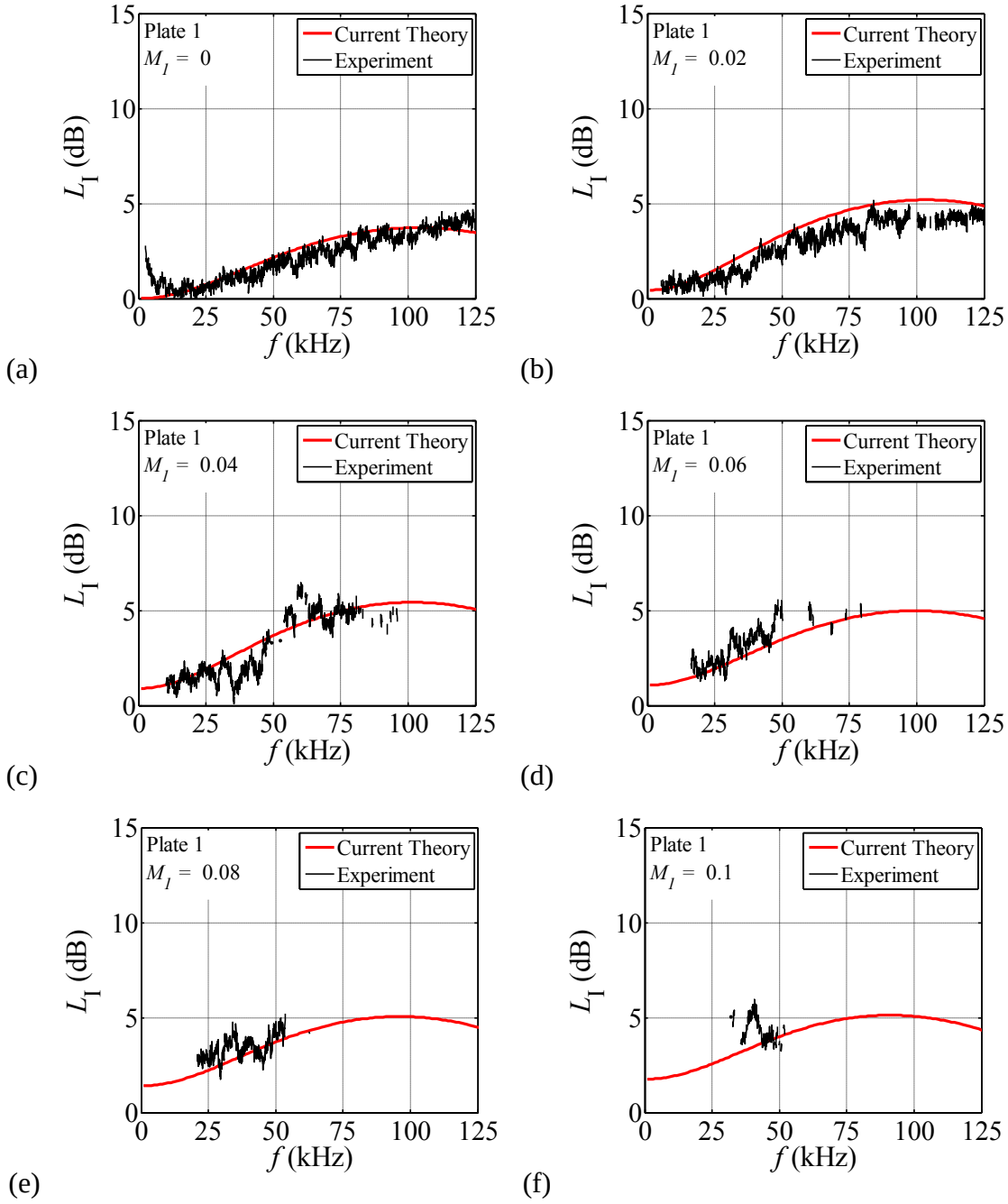

Figure 5.27: Insertion loss measurement vs. current theory for Plate 1; **(a)** $M_1 = 0$; **(b)** $M_1 = 0.02$; **(c)** $M_1 = 0.04$; **(d)** $M_1 = 0.06$; **(e)** $M_1 = 0.08$; **(e)** $M_1 = 0.1$

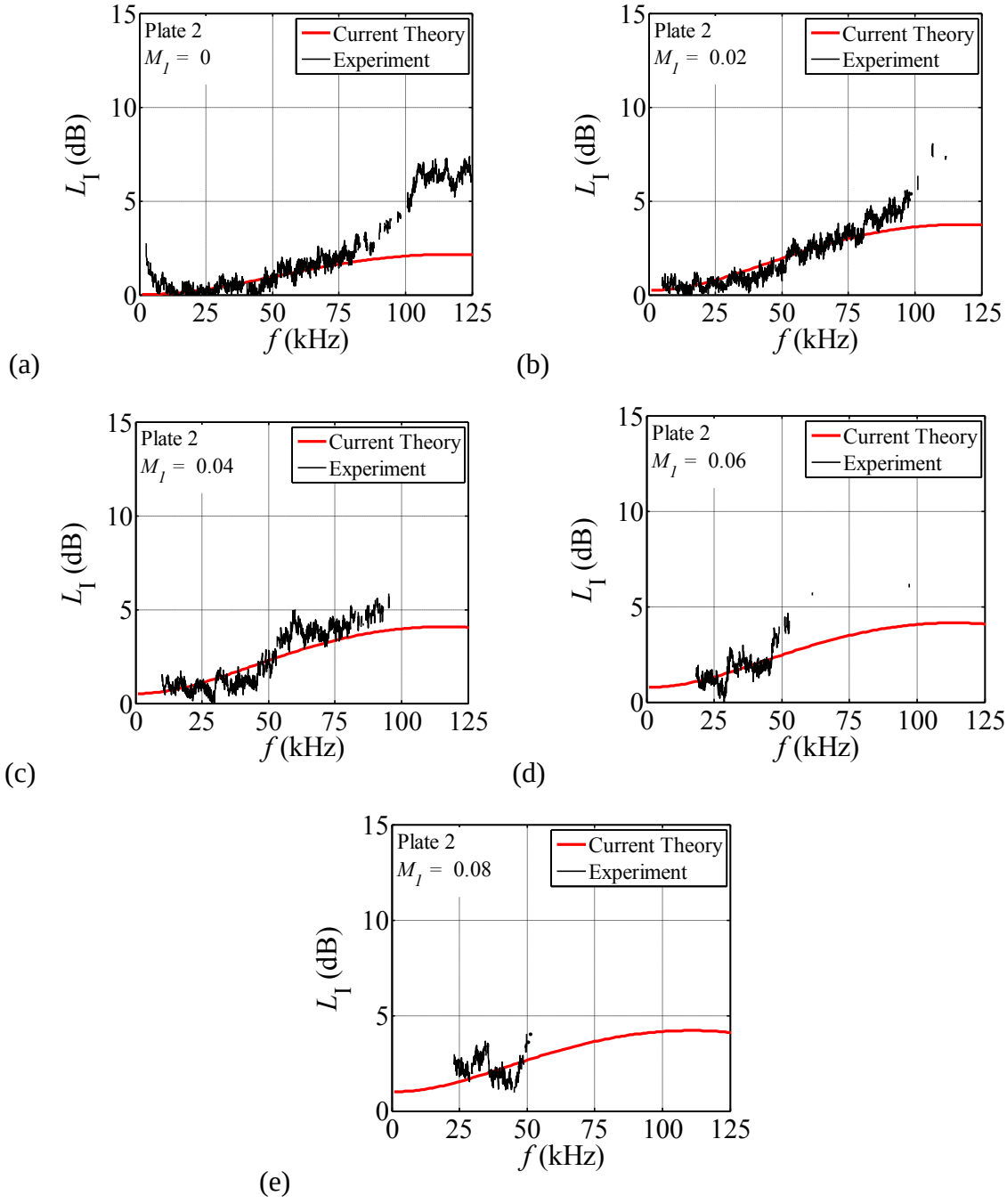

Figure 5.28: Insertion loss measurement vs. current theory for Plate 2; **(a)** $M_1 = 0$; **(b)** $M_1 = 0.02$; **(c)** $M_1 = 0.04$; **(d)** $M_1 = 0.06$; **(e)** $M_1 = 0.08$

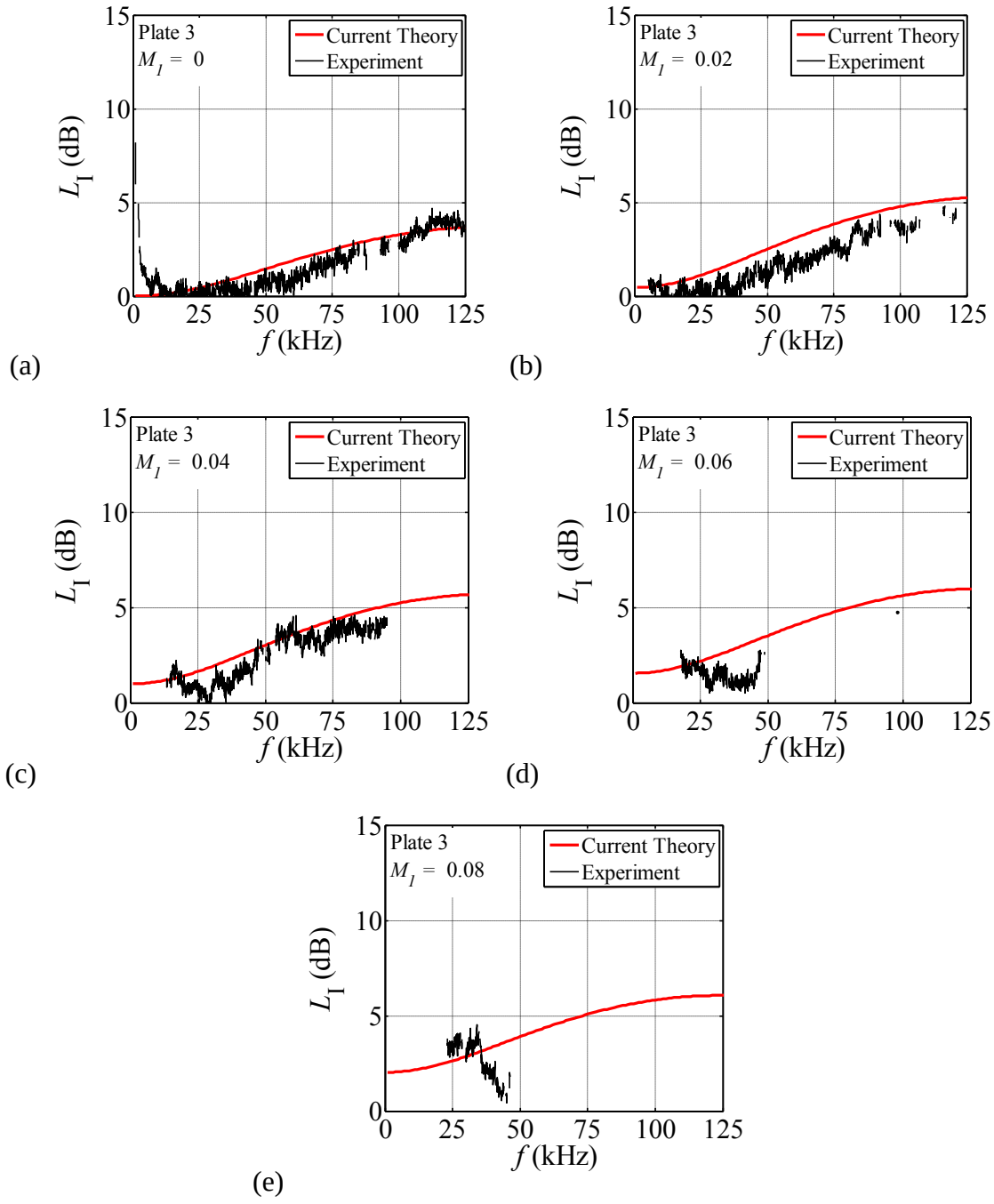

Figure 5.29: Insertion loss measurement vs. current theory for Plate 3; **(a)** $M_1 = 0$; **(b)** $M_1 = 0.02$; **(c)** $M_1 = 0.04$; **(d)** $M_1 = 0.06$; **(e)** $M_1 = 0.08$

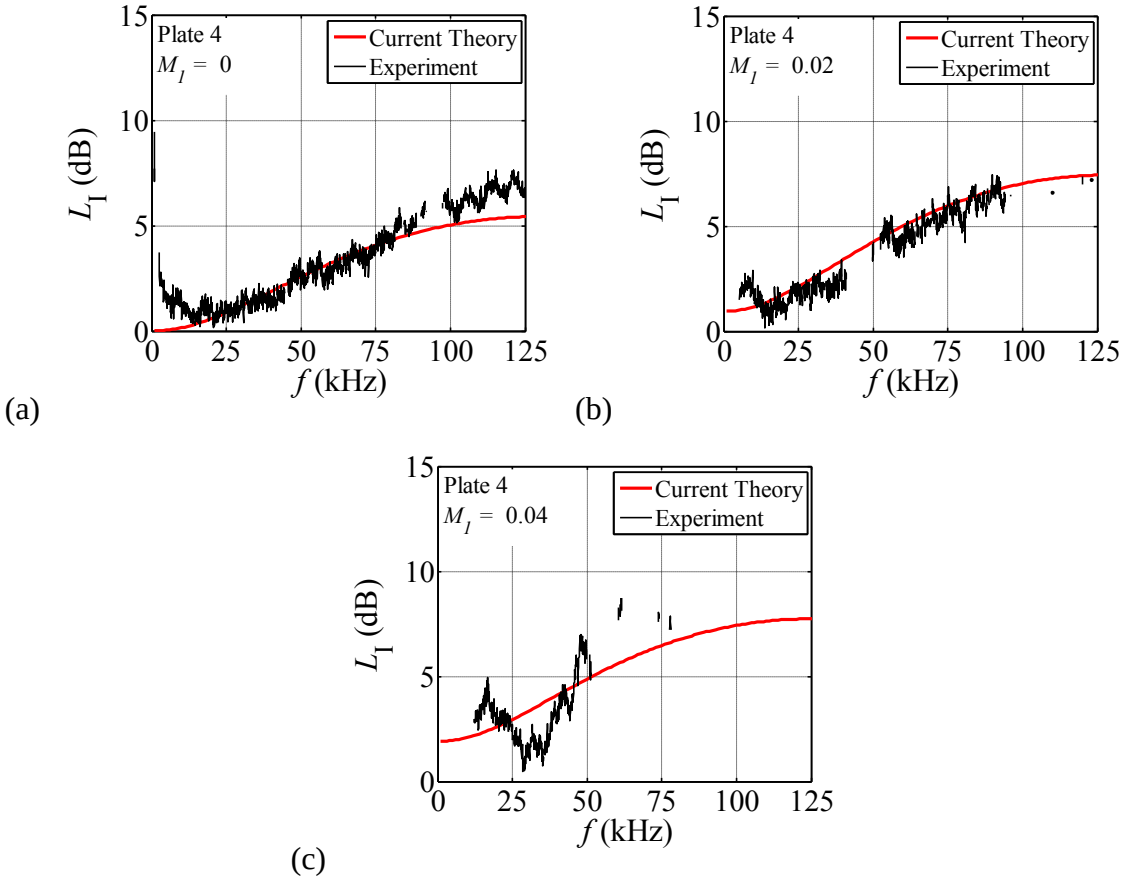

Figure 5.30: Insertion loss measurement vs. current theory for Plate 4; **(a)** $M_1 = 0$; **(b)** $M_1 = 0.02$; **(c)** $M_1 = 0.04$

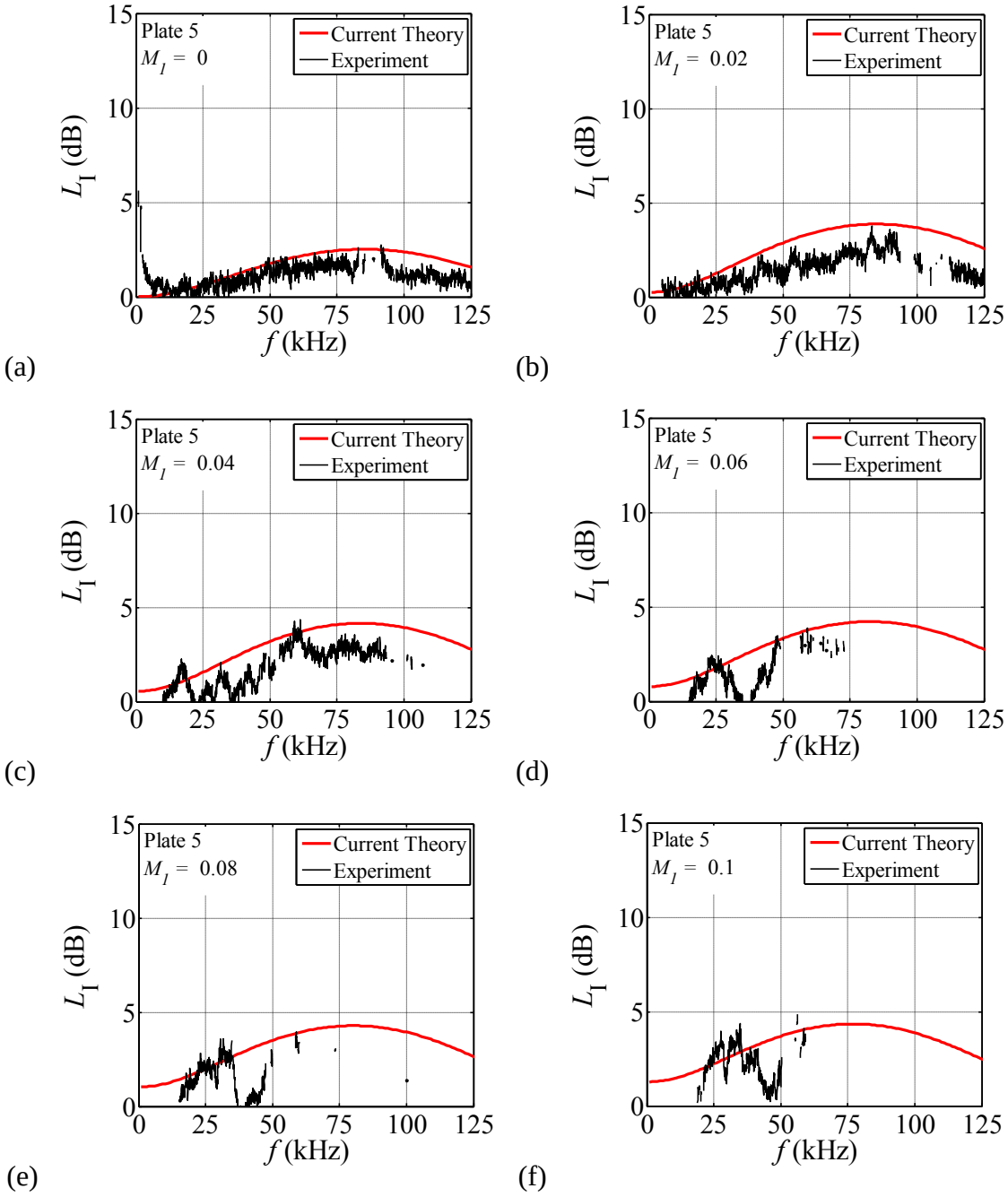

Figure 5.31: Insertion loss measurement vs. current theory for Plate 5; **(a)** $M_1 = 0$; **(b)** $M_1 = 0.02$; **(c)** $M_1 = 0.04$; **(d)** $M_1 = 0.06$; **(e)** $M_1 = 0.08$; **f.)** $M_1 = 0.10$

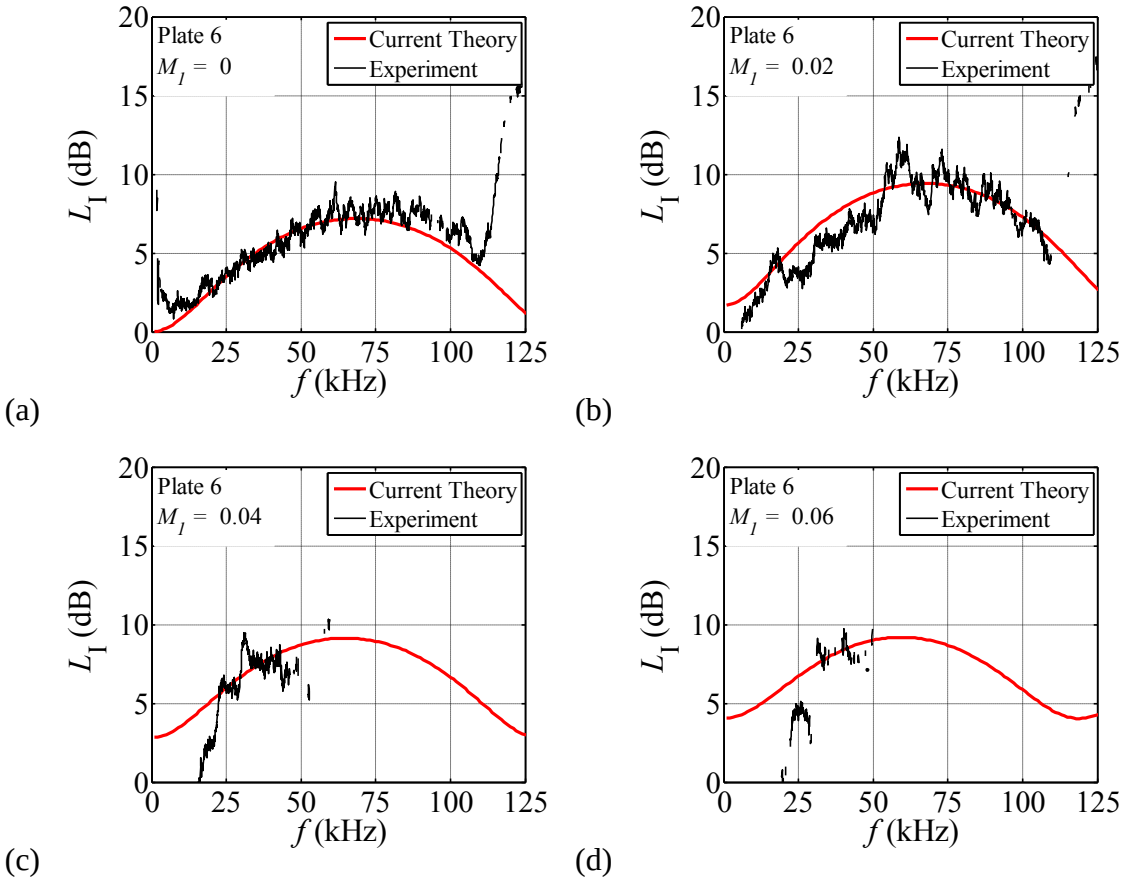

Figure 5.32: Insertion loss measurement vs. current theory for Plate 6; **(a)** $M_1 = 0$; **(b)** $M_1 = 0.02$; **(c)** $M_1 = 0.04$; **(d)** $M_1 = 0.06$

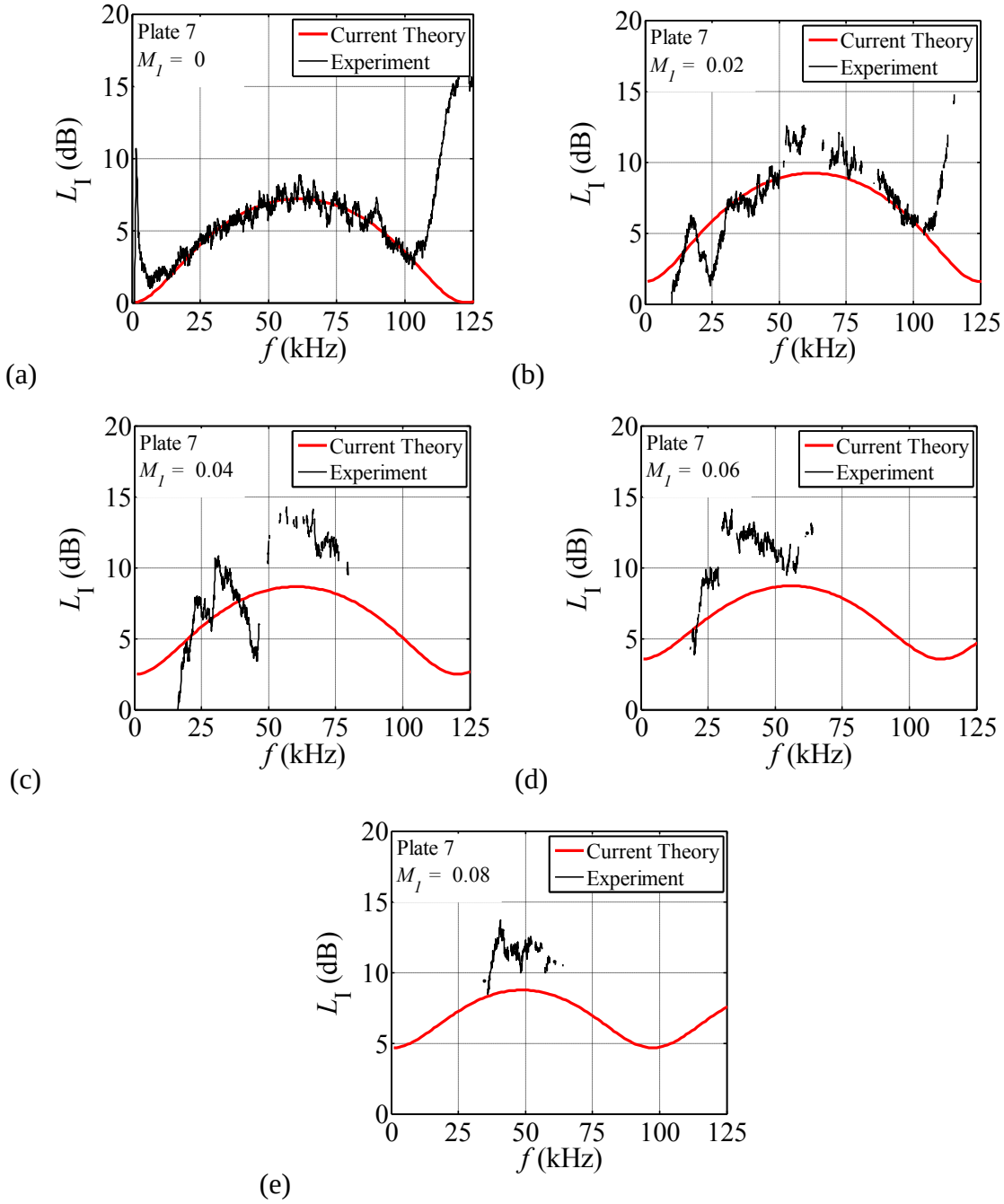

Figure 5.33: Insertion loss measurement vs. current theory for Plate 7; **(a)** $M_1 = 0$; **(b)** $M_1 = 0.02$; **(c)** $M_1 = 0.04$; **(d)** $M_1 = 0.06$

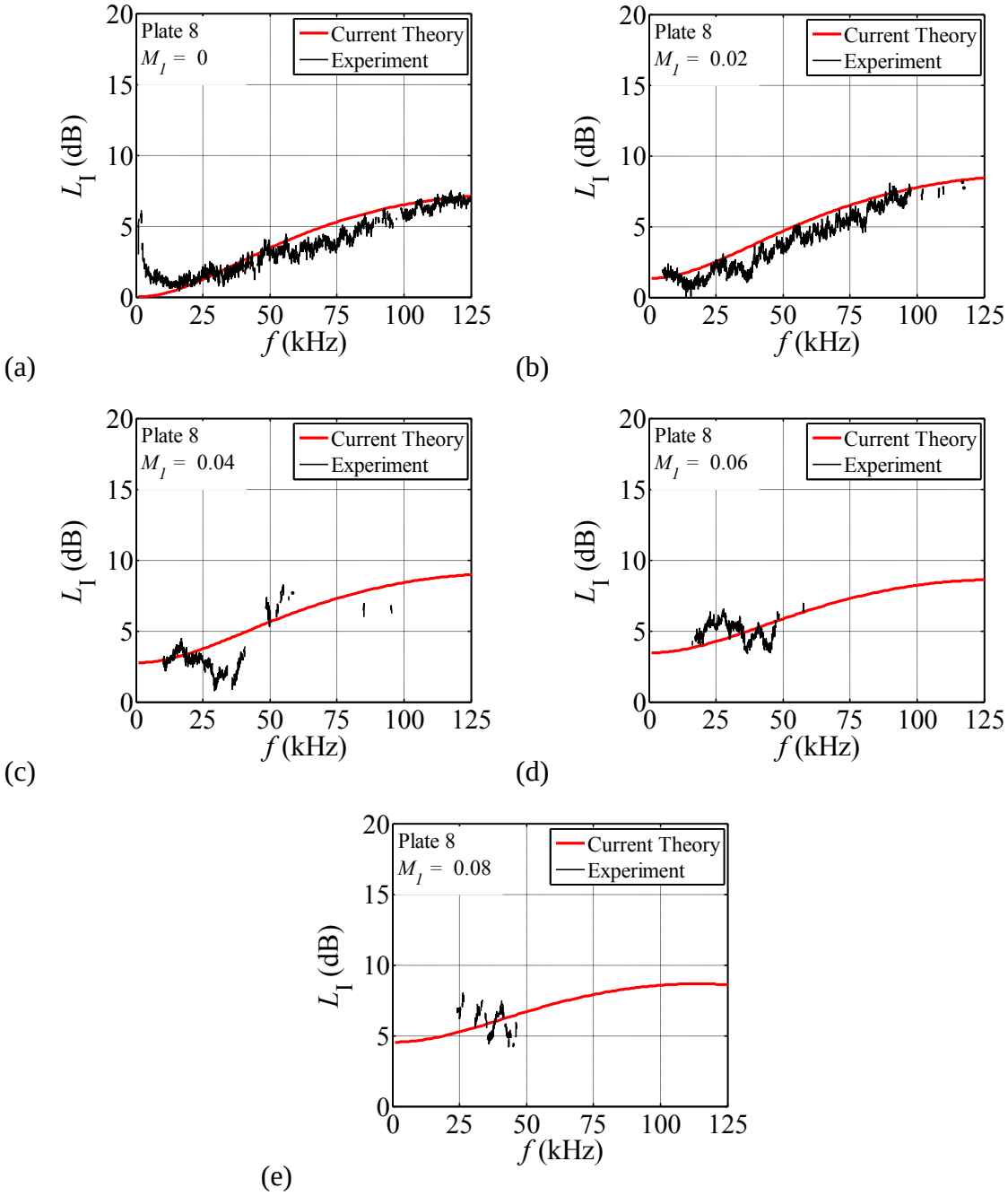

Figure 5.34: Insertion loss measurement vs. current theory for Plate 8; **(a)** $M_1 = 0$; **(b)** $M_1 = 0.02$; **(c)** $M_1 = 0.04$; **(d)** $M_1 = 0.06$; **(e)** $M_1 = 0.08$

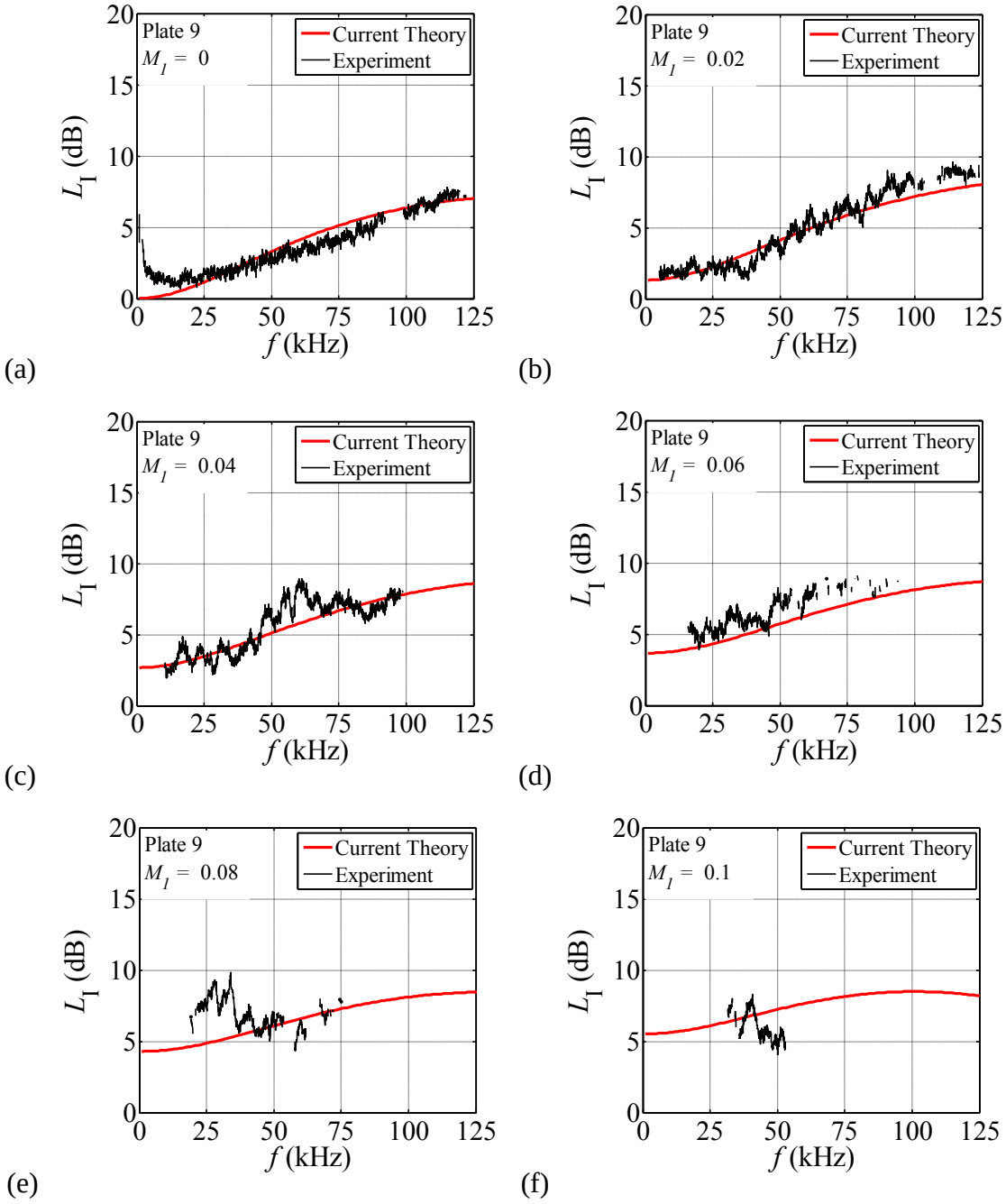

Figure 5.35: Insertion loss measurement vs. current theory for Plate 9; **(a)** $M_1 = 0$; **(b)** $M_1 = 0.02$; **(c)** $M_1 = 0.04$; **(d)** $M_1 = 0.06$; **(e)** $M_1 = 0.08$; **(f)** $M_1 = 0.1$

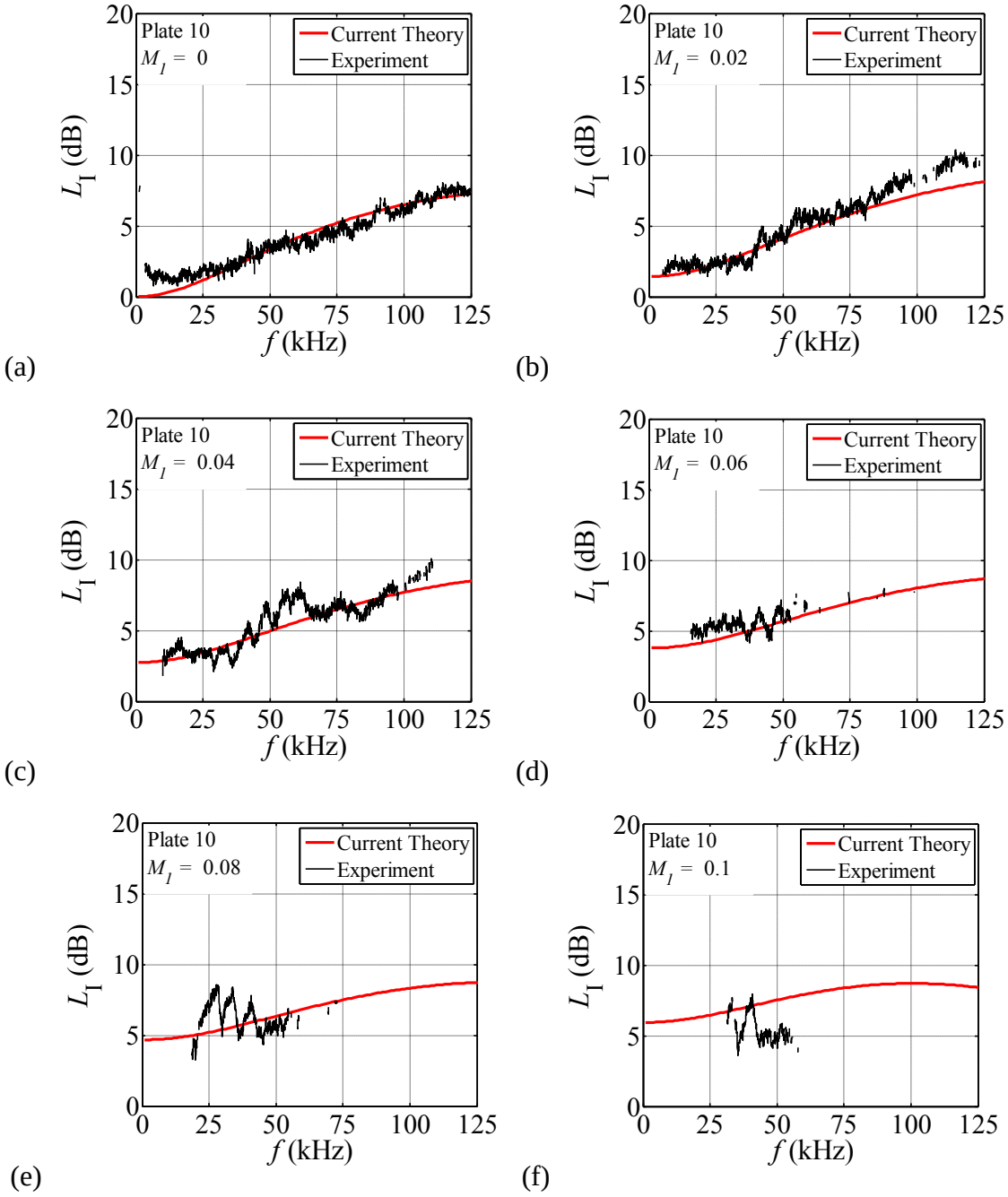

Figure 5.36: Insertion loss measurement vs. current theory for Plate 10; **(a)** $M_1 = 0$; **(b)** $M_1 = 0.02$; **(c)** $M_1 = 0.04$; **(d)** $M_1 = 0.06$; **(e)** $M_1 = 0.08$; **(f)** $M_1 = 0.1$

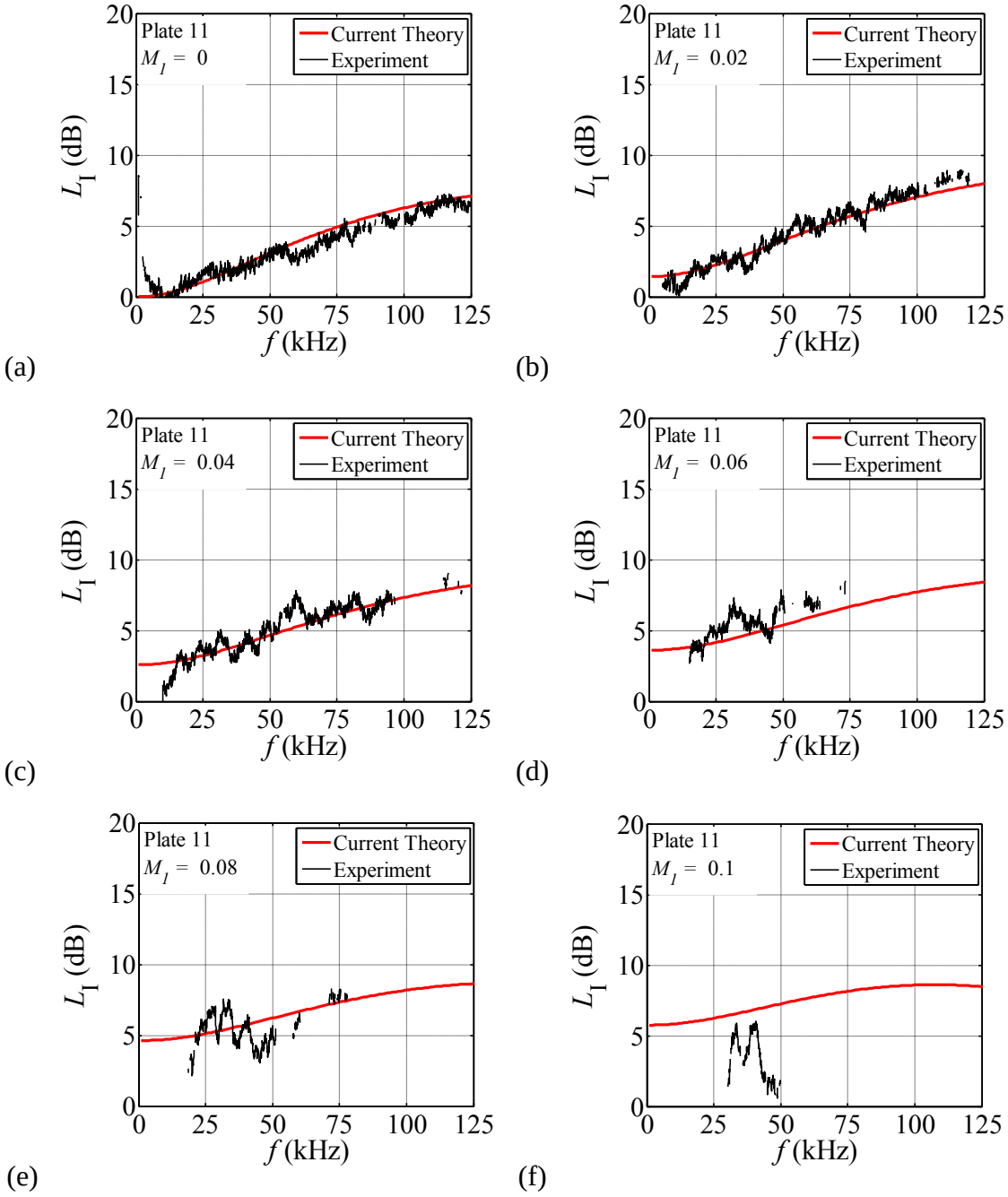

Figure 5.37: Insertion loss measurement vs. current theory for Plate 11; **(a)** $M_1 = 0$; **(b)** $M_1 = 0.02$; **(c)** $M_1 = 0.04$; **(d)** $M_1 = 0.06$; **(e)** $M_1 = 0.08$; **(f)** $M_1 = 0.10$

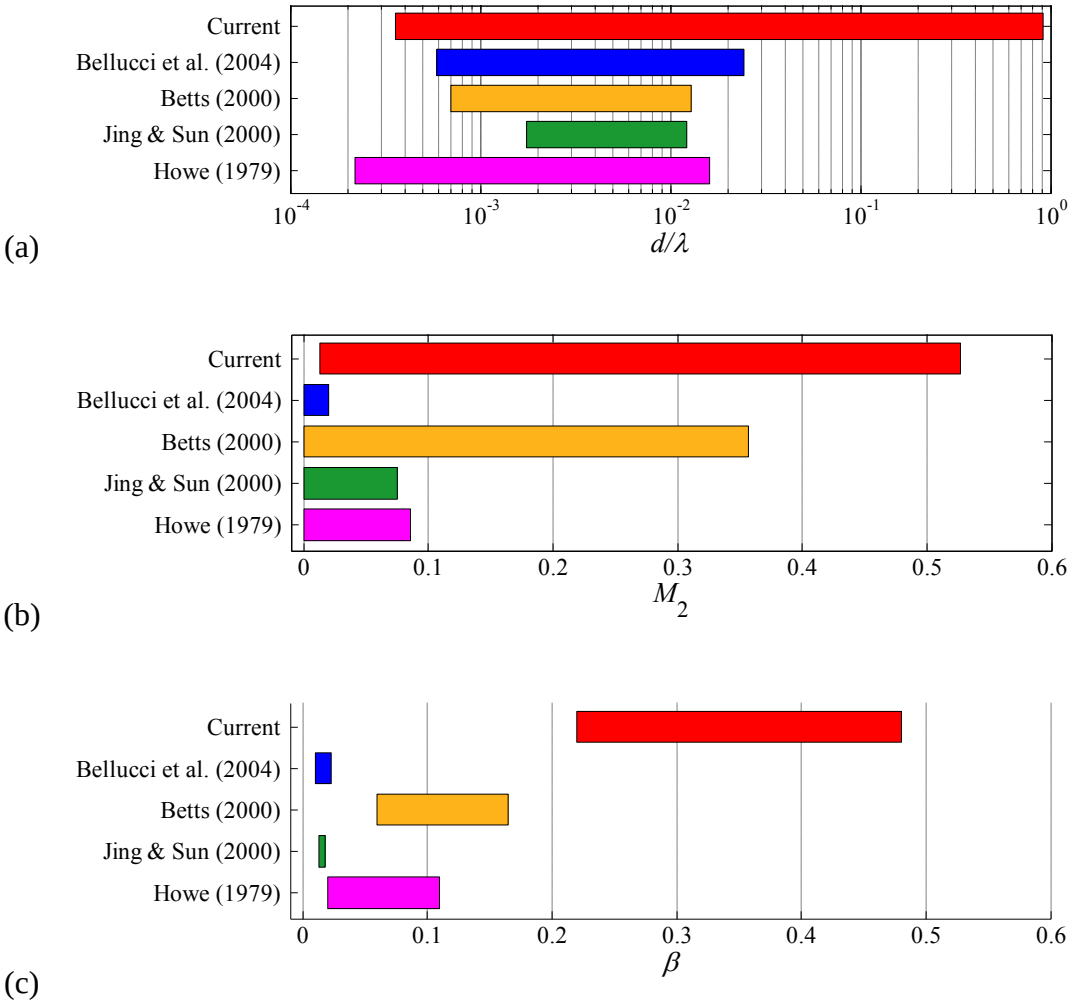

Figure 5.38: Comparisons of the range of **(a)** d/λ, **(b)** M_2, and **(c)** β covered in the current and previous work with bias flow. The ranges of d/λ, M_2, and β are determined based on the range of experimental validation provided for the respective work.

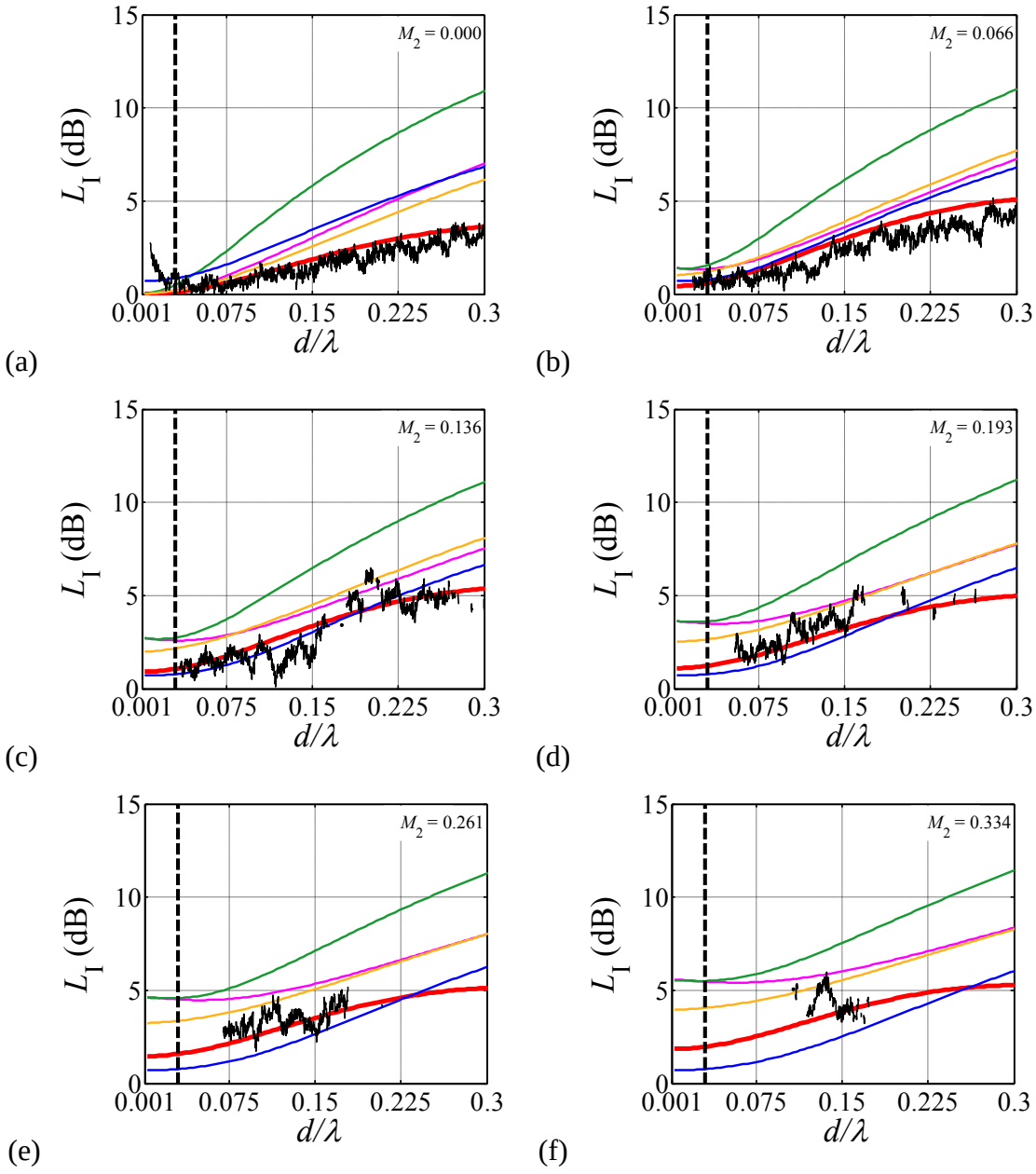

Figure 5.39: Insertion loss measurement vs. current theory for Plate 1; **(a)** $M_1 = 0$; **(b)** $M_1 = 0.02$; **(c)** $M_1 = 0.04$; **(d)** $M_1 = 0.06$; **(e)** $M_1 = 0.08$

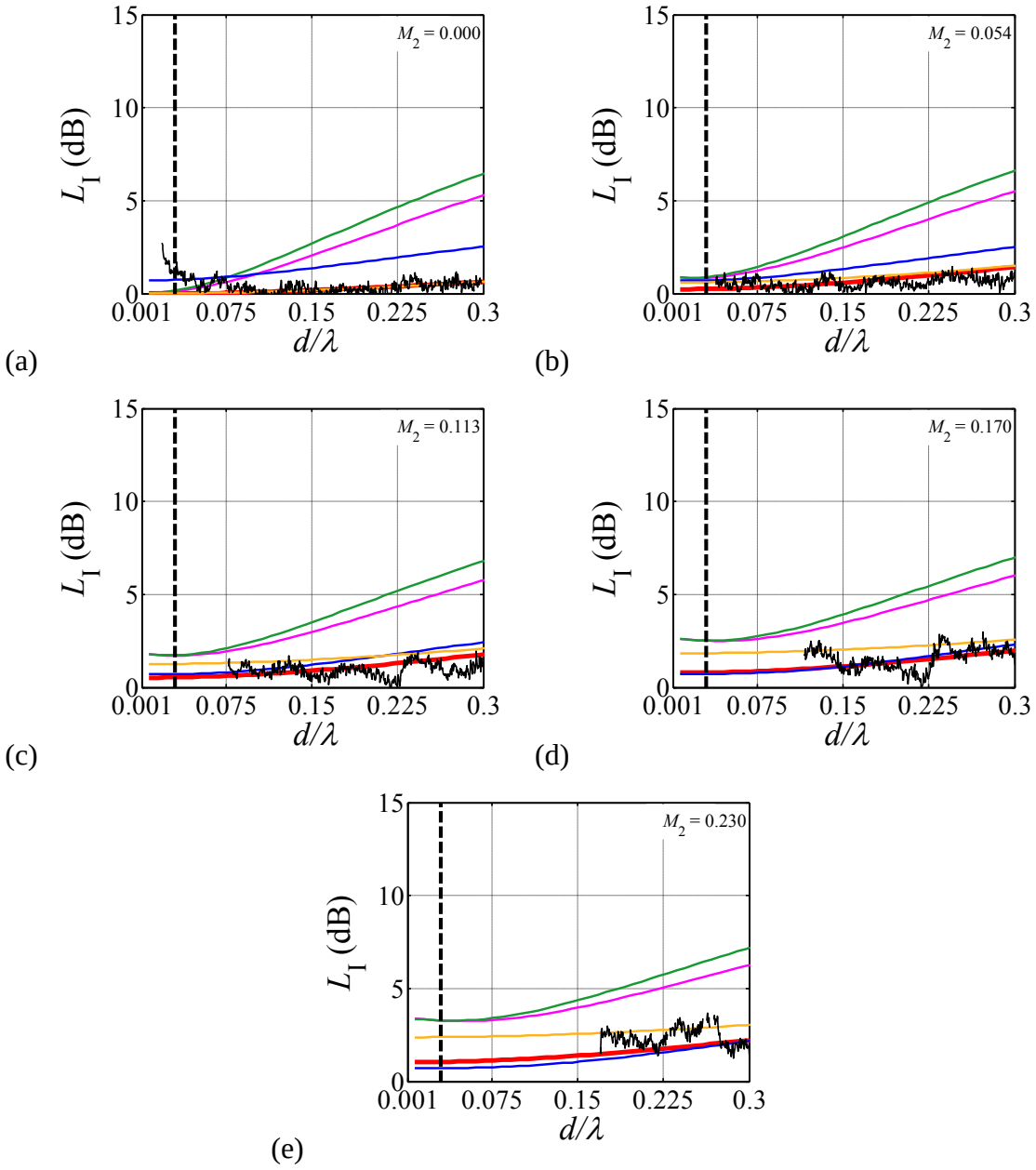

Figure 5.40: Insertion loss measurement vs. current theory for Plate 2; **(a)** $M_1 = 0$; **(b)** $M_1 = 0.02$; **(c)** $M_1 = 0.04$; **(d)** $M_1 = 0.06$; **(e)** $M_1 = 0.08$

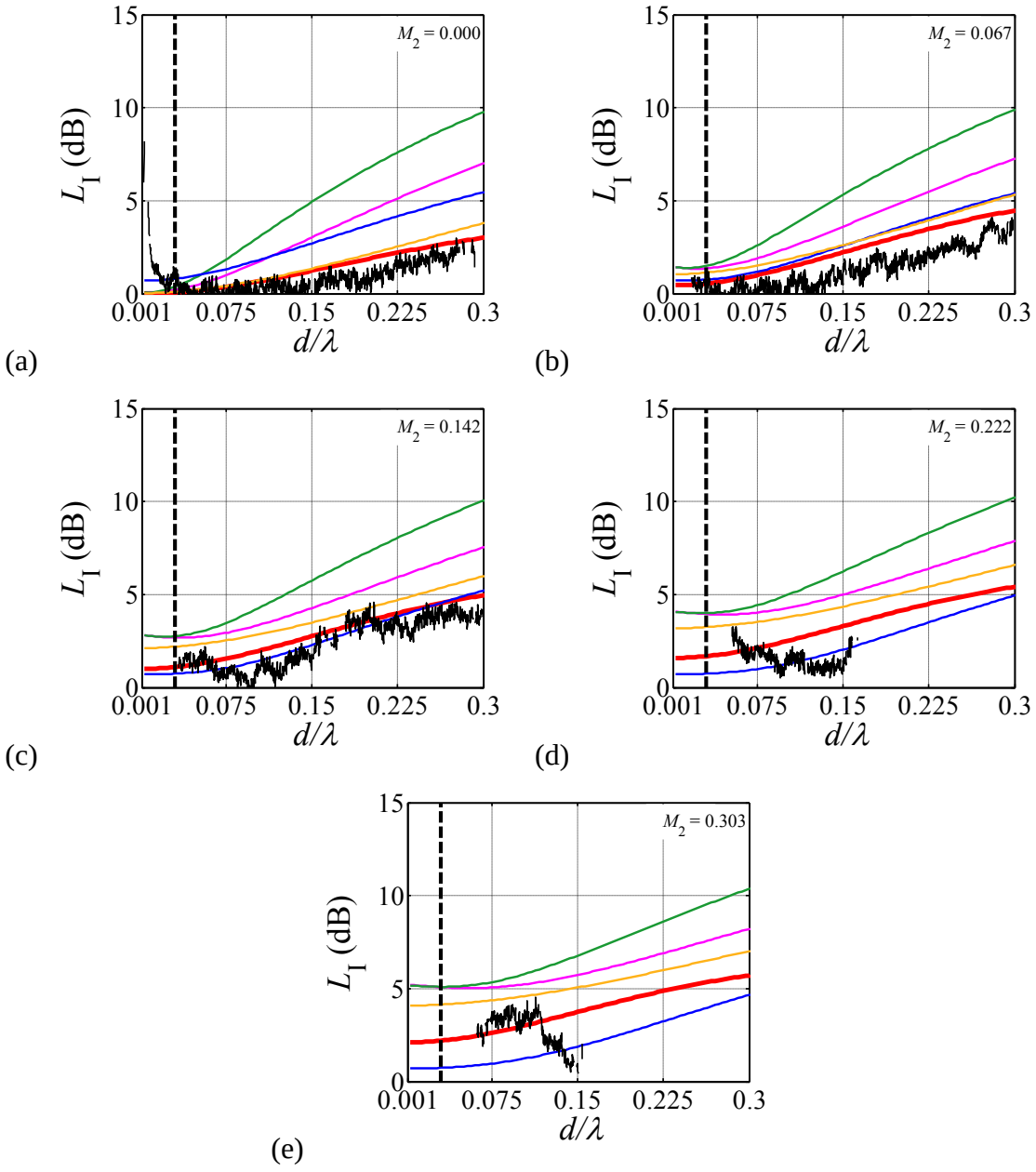

Figure 5.41: Insertion loss measurement vs. current theory for Plate 3; **(a)** $M_1 = 0$; **(b)** $M_1 = 0.02$; **(c)** $M_1 = 0.04$; **(d)** $M_1 = 0.06$; **(e)** $M_1 = 0.08$

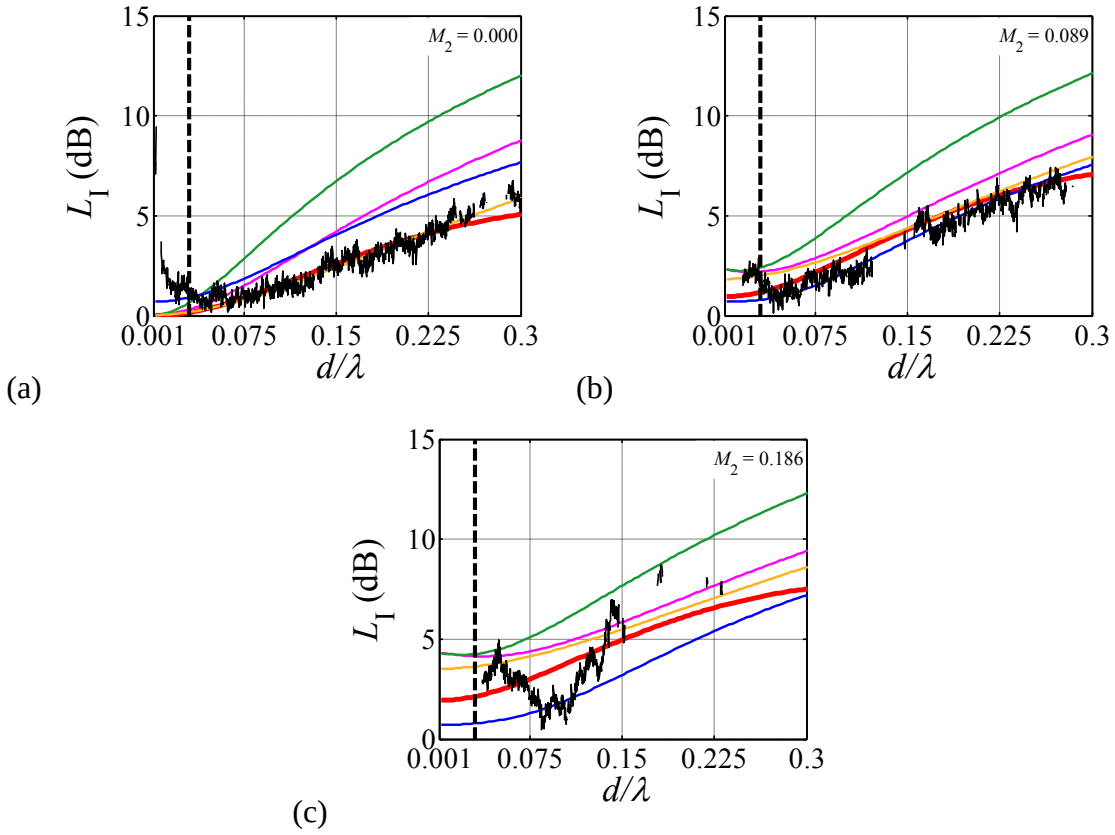

Figure 5.42: Insertion loss measurement vs. current theory for Plate 4; **(a)** $M_1 = 0$; **(b)** $M_1 = 0.02$; **(c)** $M_1 = 0.04$

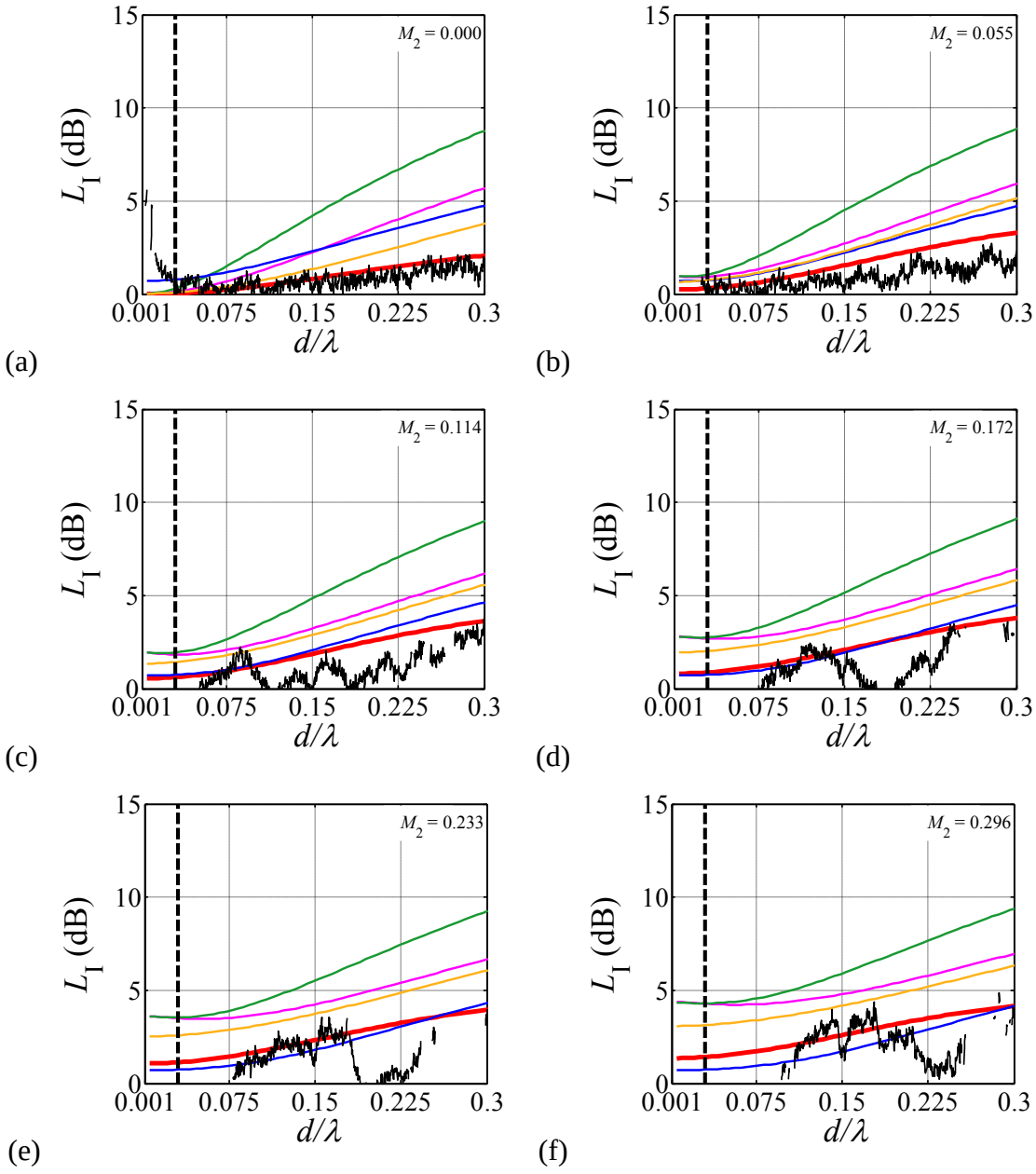

Figure 5.43: Insertion loss measurement vs. current theory for Plate 5; **(a)** $M_1 = 0$; **(b)** $M_1 = 0.02$; **(c)** $M_1 = 0.04$; **(d)** $M_1 = 0.06$; **(e)** $M_1 = 0.08$; **(f)** $M_1 = 0.10$

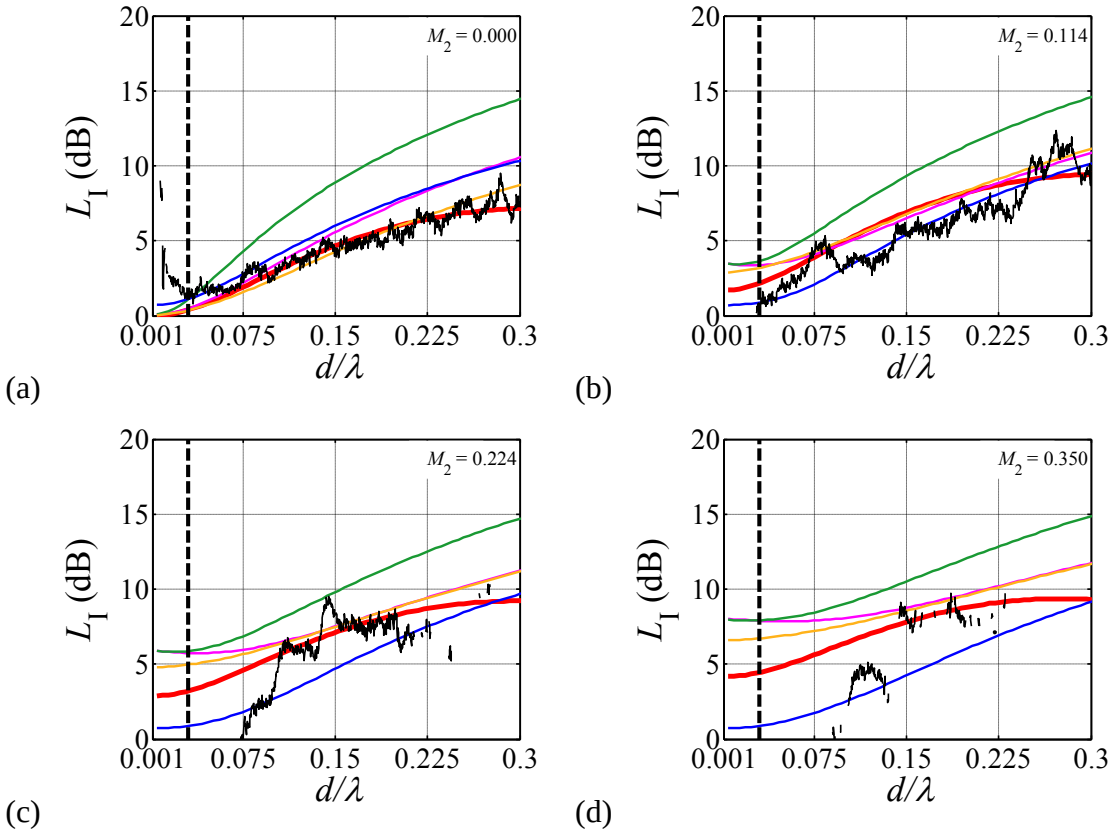

Figure 5.44: Insertion loss measurement vs. current theory for Plate 6; **(a)** $M_1 = 0$; **(b)** $M_1 = 0.02$; **(c)** $M_1 = 0.04$; **(d)** $M_1 = 0.06$

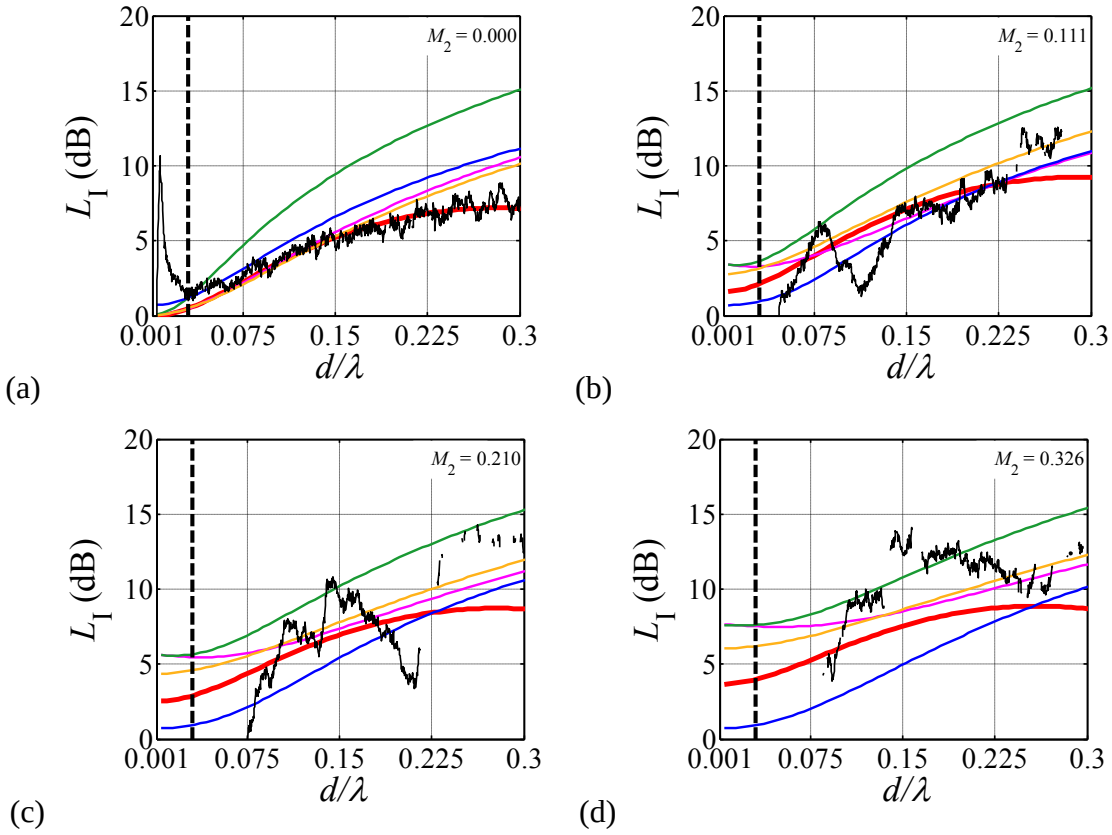

Figure 5.45: Insertion loss measurement vs. current theory for Plate 7; **(a)** $M_1 = 0$; **(b)** $M_1 = 0.02$; **(c)** $M_1 = 0.04$; **(d)** $M_1 = 0.06$

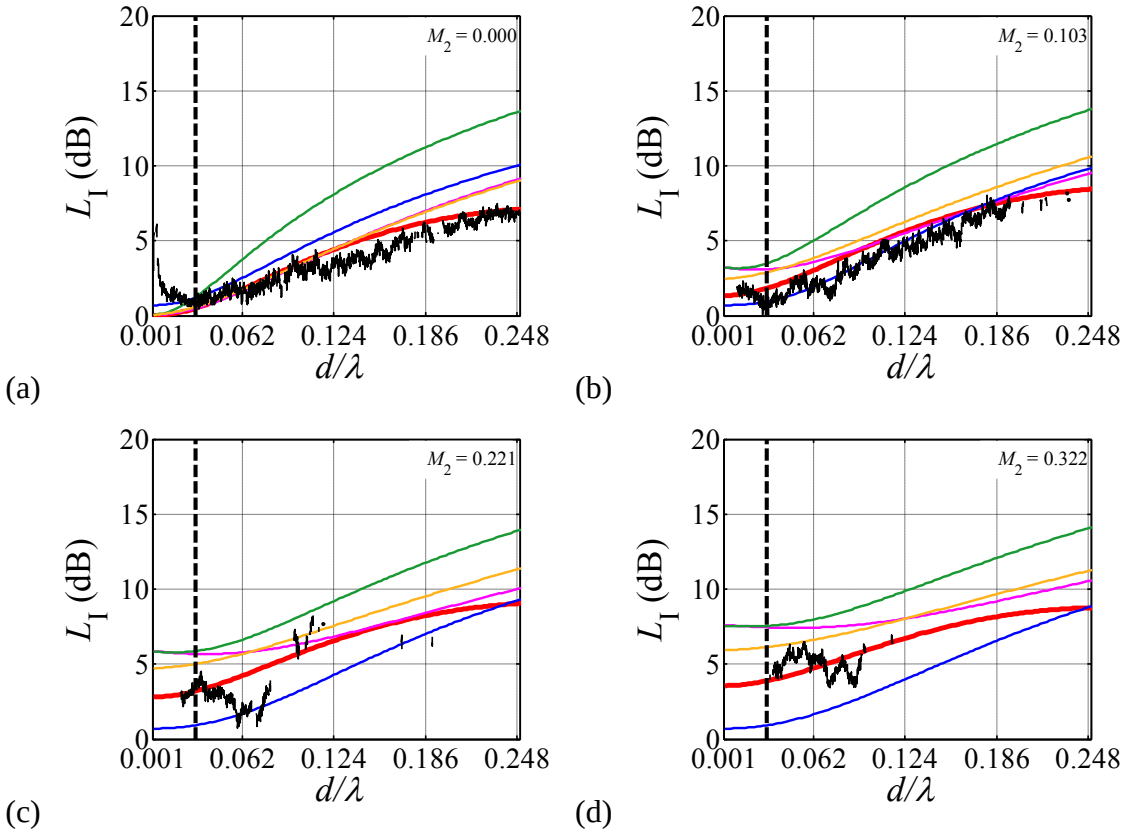

Figure 5.46: Insertion loss measurement vs. current theory for Plate 8; **(a)** $M_1 = 0$; **(b)** $M_1 = 0.02$; **(c)** $M_1 = 0.04$; **(d)** $M_1 = 0.06$

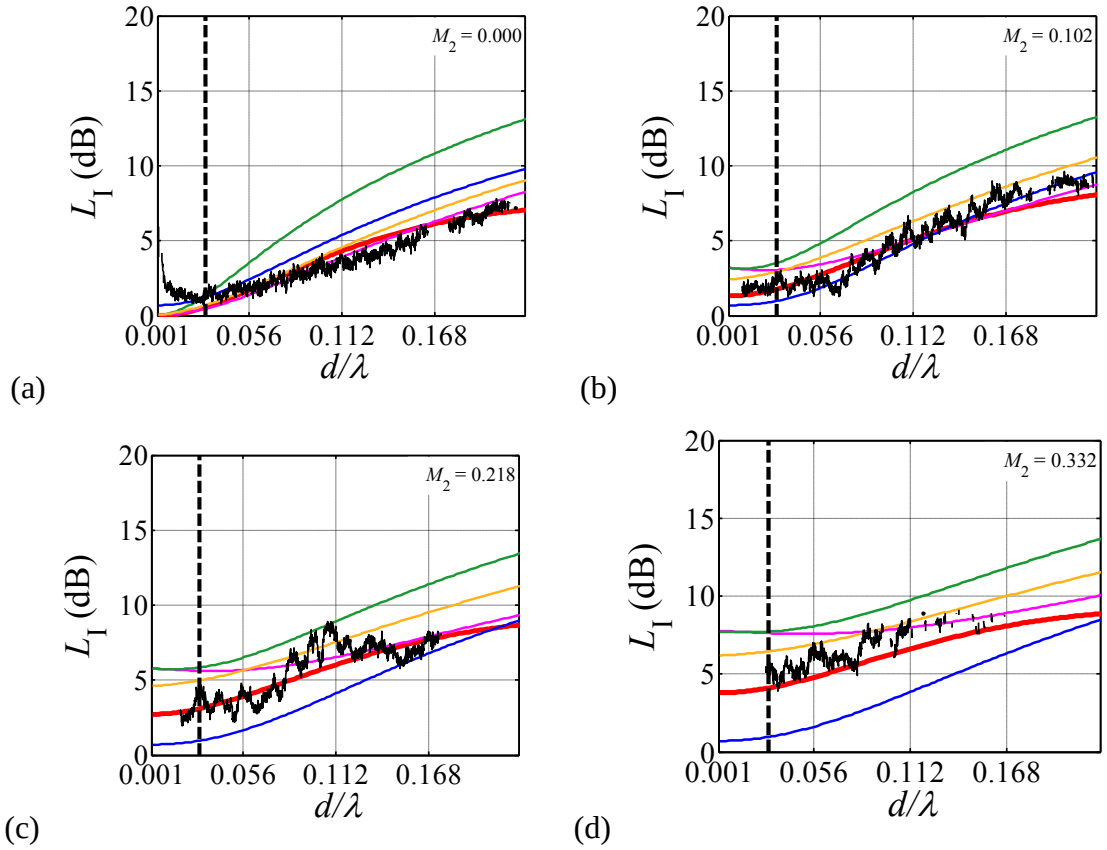

Figure 5.47: Insertion loss measurement vs. current theory for Plate 9; **(a)** $M_1 = 0$; **(b)** $M_1 = 0.02$; **(c)** $M_1 = 0.04$; **(d)** $M_1 = 0.06$

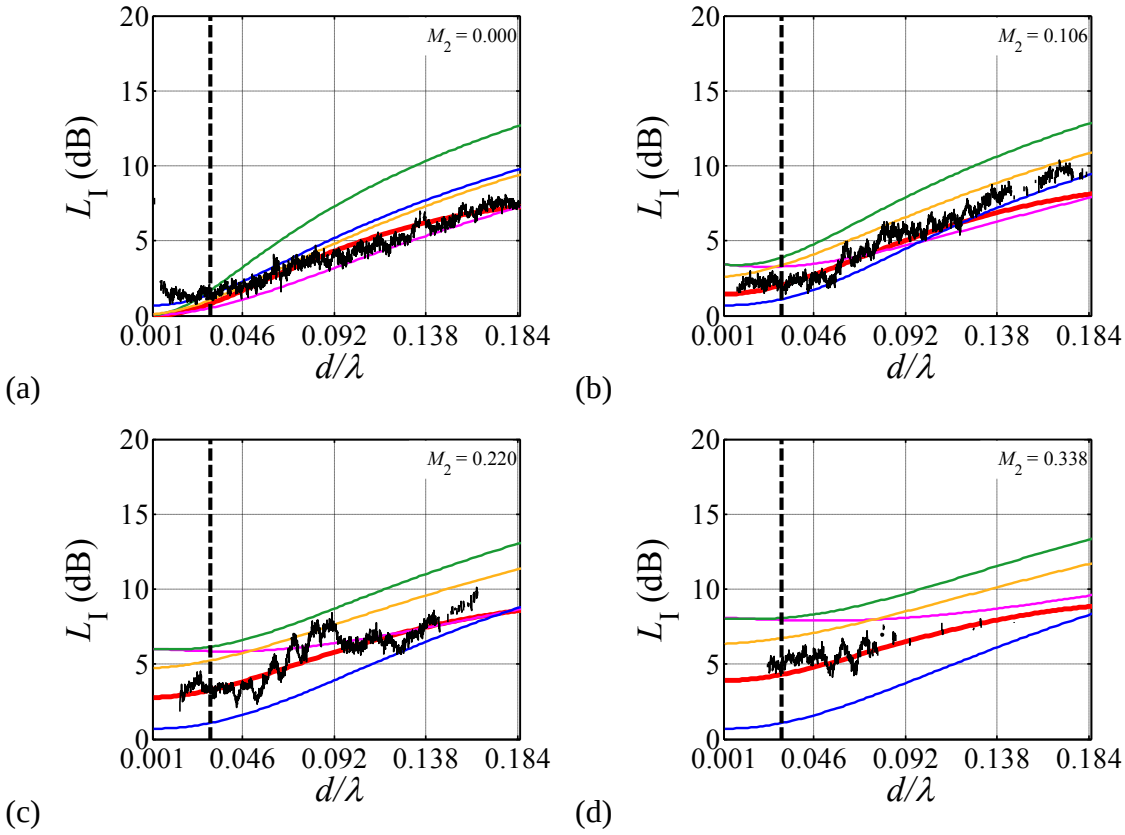

Figure 5.48: Insertion loss measurement vs. current theory for Plate 10; **(a)** $M_1 = 0$; **(b)** $M_1 = 0.02$; **(c)** $M_1 = 0.04$; **(d)** $M_1 = 0.06$

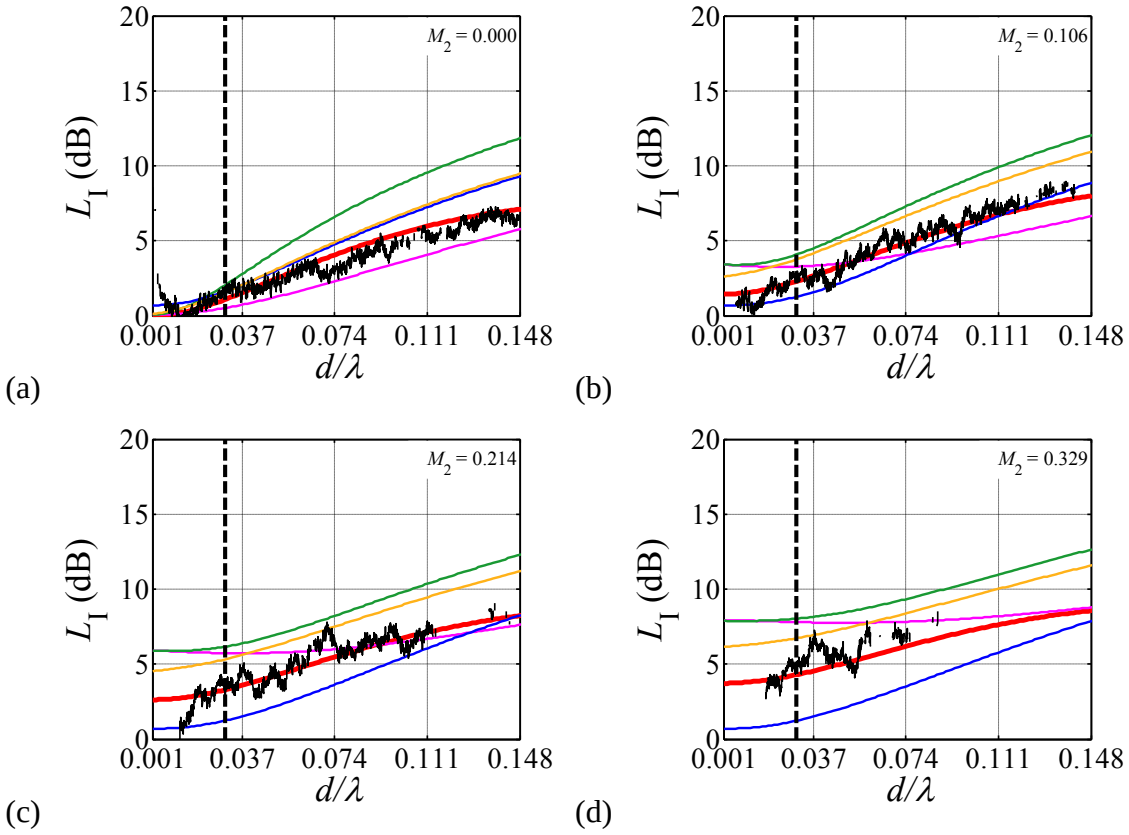

Figure 5.49: Insertion loss measurement vs. current theory for Plate 11; **(a)** $M_1 = 0$; **(b)** $M_1 = 0.02$; **(c)** $M_1 = 0.04$; **(d)** $M_1 = 0.06$

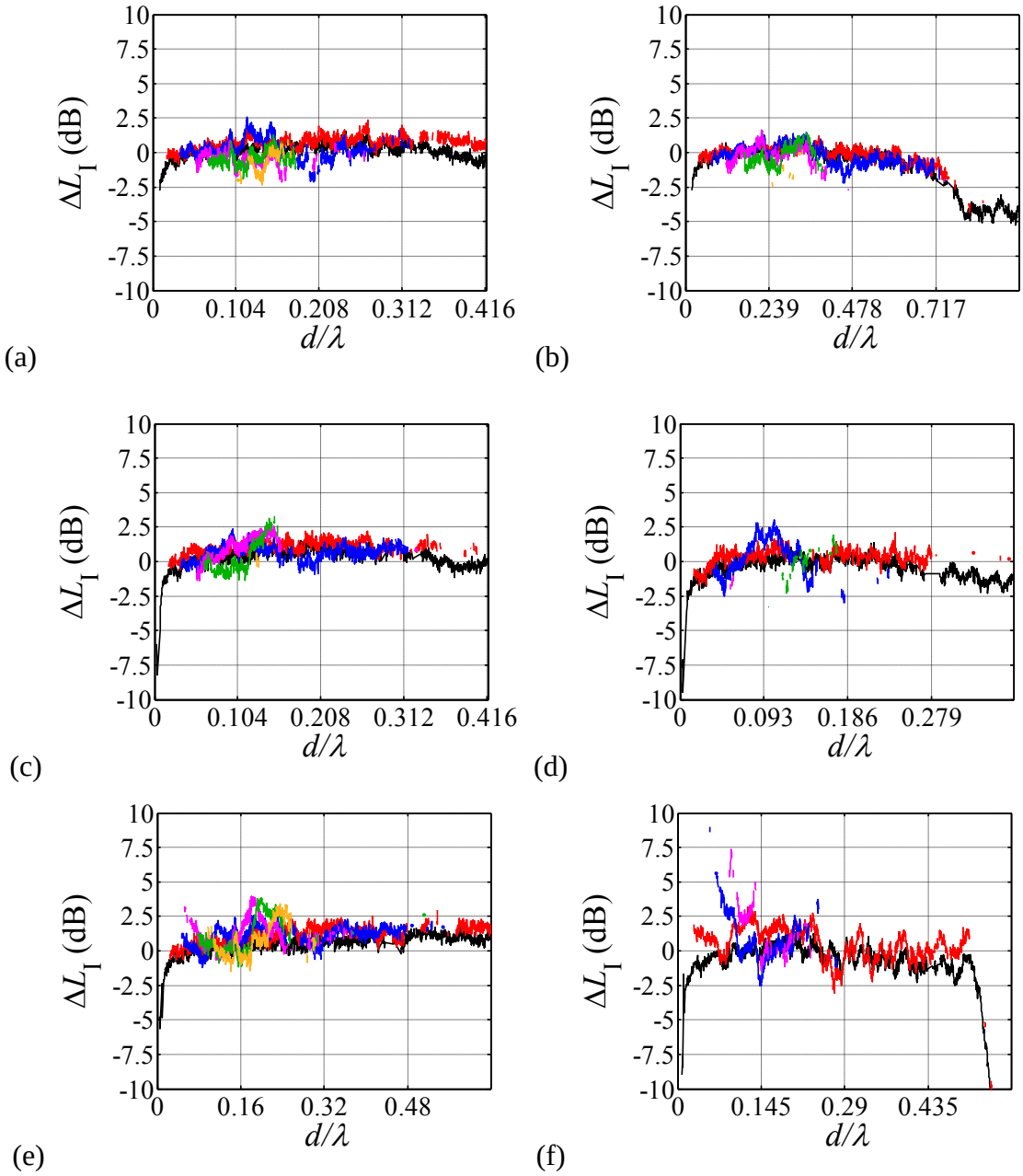

Figure 5.50: Insertion loss difference between theory and experiment for **(a)** Plate 1; (**b)** Plate 2; (**c)** Plate 3; (**d)** Plate 4; (**e)** Plate 5; (**f)** Plate 6; **(g)** Plate 7; (**h)** Plate 8; (**i)** Plate 9; (**j)** Plate 10; (**k)** Plate 11

— $M_1 = 0$; — $M_1 = 0.02$; — $M_1 = 0.04$; — $M_1 = 0.06$; — $M_1 = 0.08$; — $M_1 = 0.1$

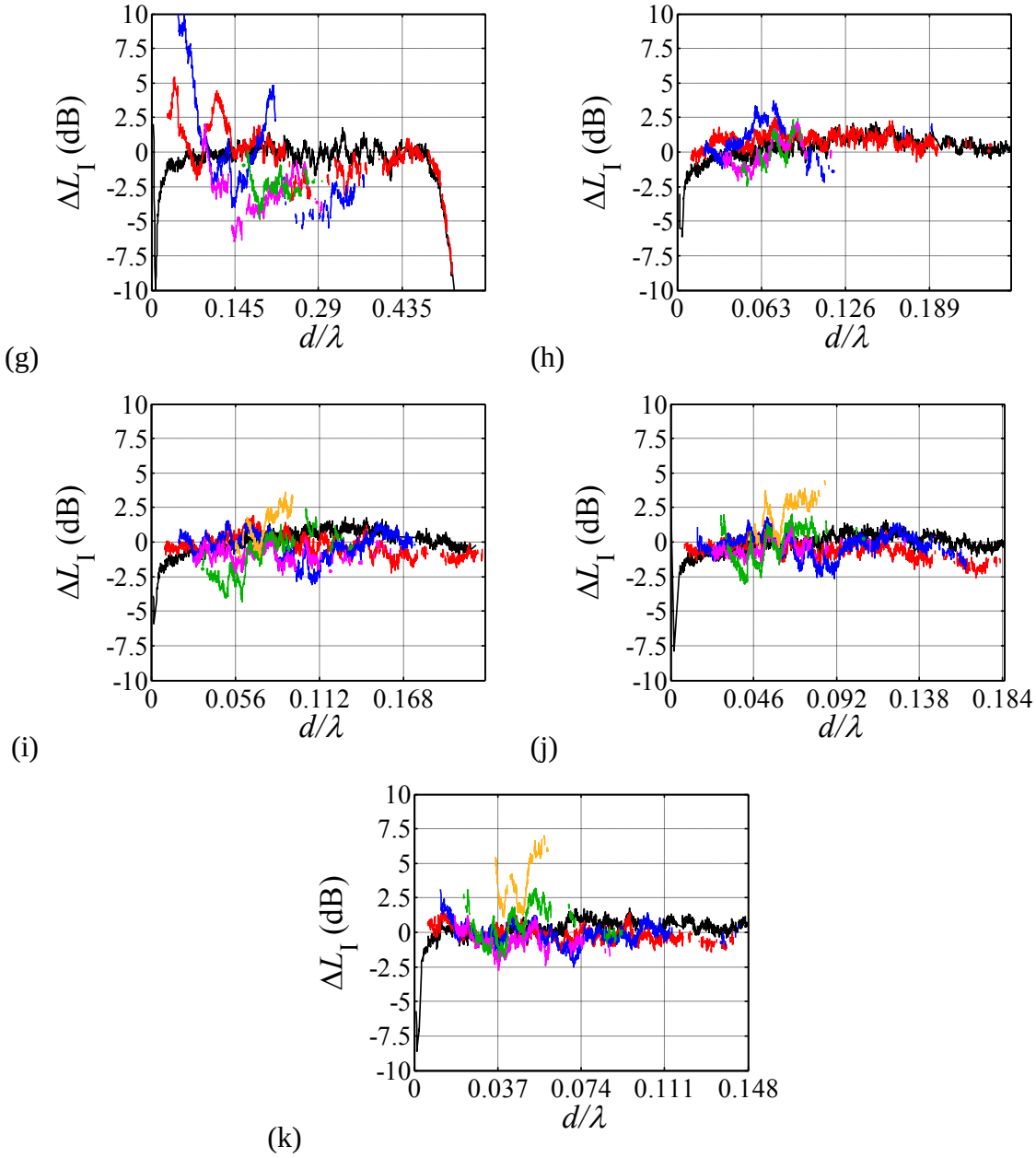

Figure 5.50: (cont.)

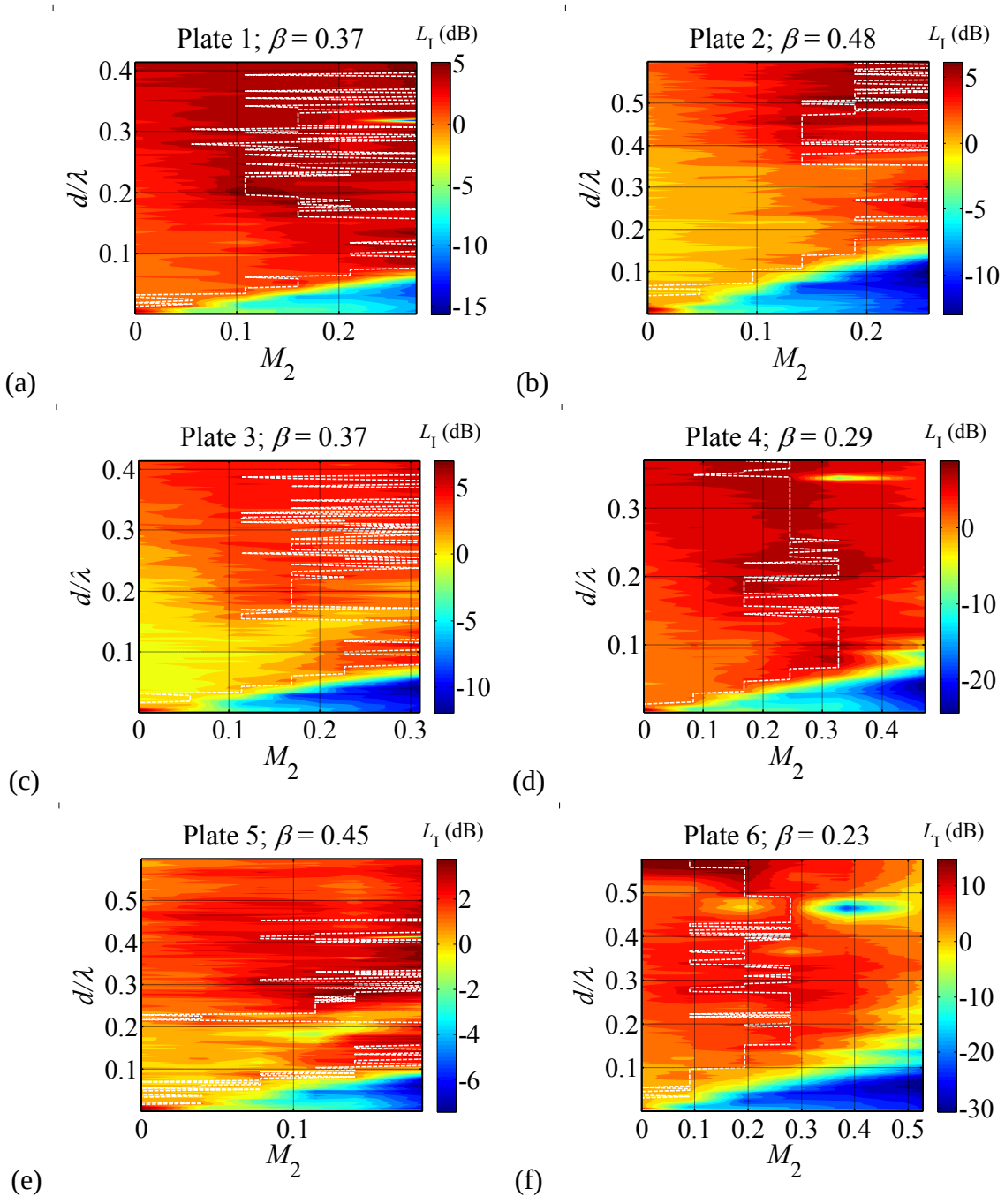

Figure 5.51: Contour plots of L_I versus d/λ and M_2. Dashed white line indicates the bias flow Mach number M_2 which L_I reaches peak value for a given d/λ. **(a)** Plate 1; **(b)** Plate 2; **(c)** Plate 3; **(d)** Plate 4; **(e)** Plate 5; **(f)** Plate 6; **(g)** Plate 7; **(h)** Plate 8; **(i)** Plate 9; **(j)** Plate 10; **(k)** Plate 11

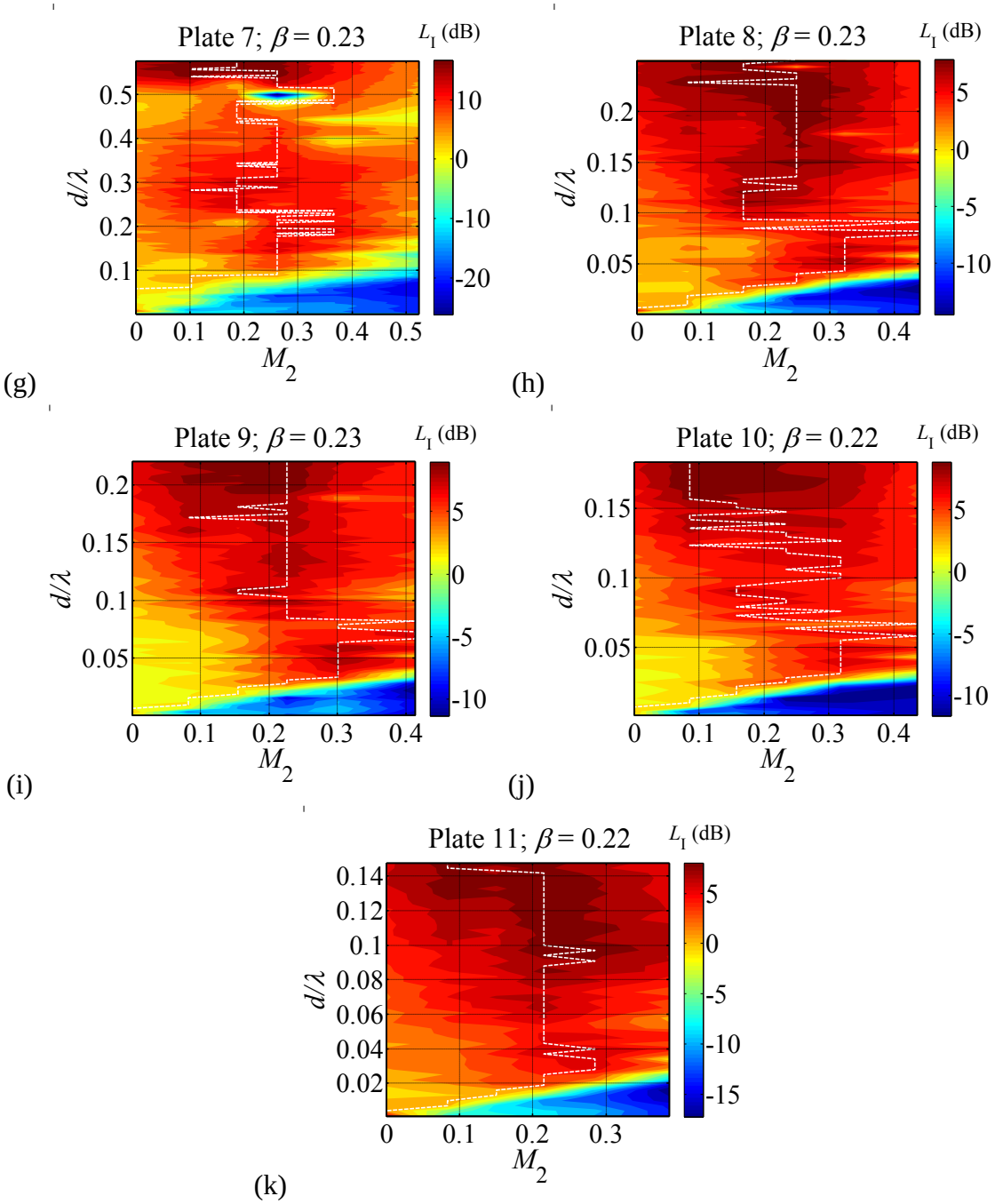

Figure 5.51: (cont.)

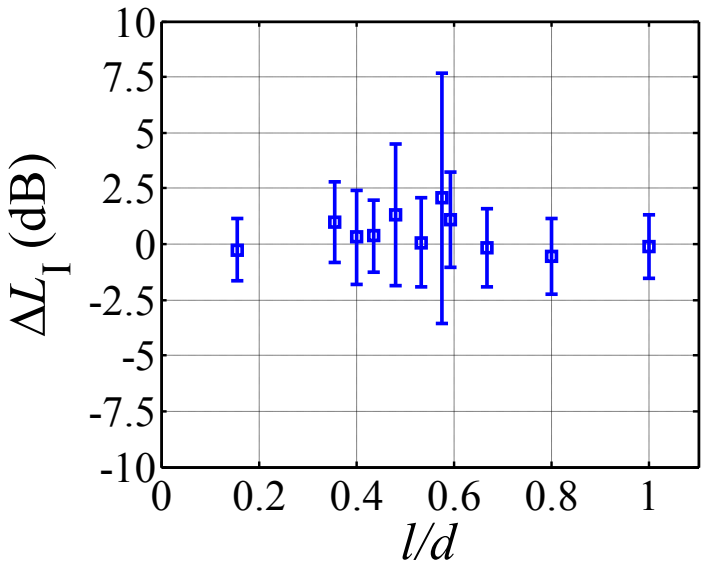

Figure 5.52: Dependence of ΔL_I on l/d. Width of error bars indicates maximum and minimum error measurements between $0.02 < d/\lambda < 0.4$ and $M_2 < 0.25$.

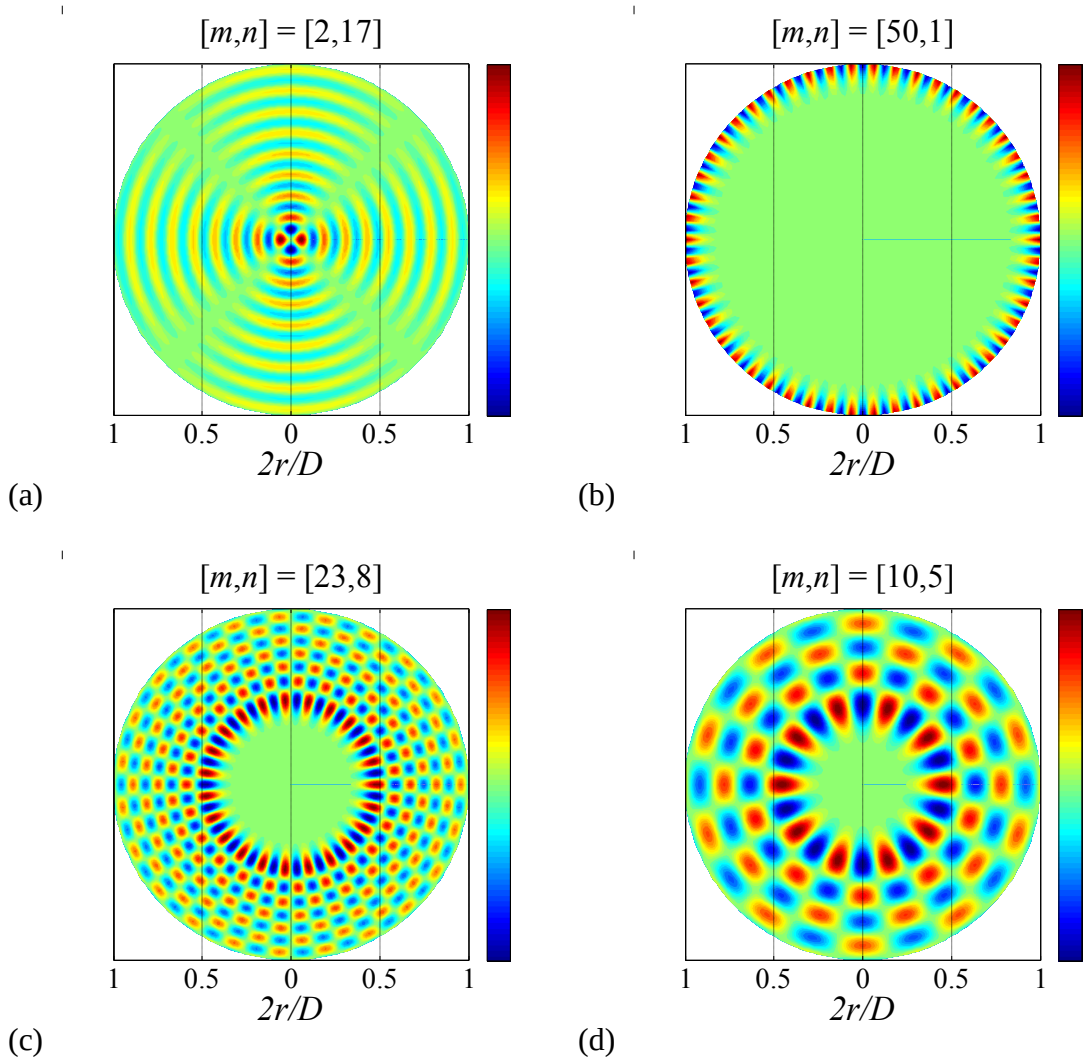

Figure 5.53: Acoustic pressure amplitude distribution upstream of the perforated plate with: **(a)** maximum number of radial modes (m =2, n = 17); **(b)** maximum number of circumferential modes (m =50, n = 1); **(c)** intermediate number of radial and circumferential modes (m =23, n = 8).); **(d)** intermediate number of radial and circumferential modes (m =10, n = 5). m and n are the circumferential and radial modes numbers, respectively, and D =4.57-cm is the diameter of the fully converged area upstream of the perforated plate.

Chapter 6

CONCLUSION

6.1 Summary

An experimental and theoretical parametric study of the acoustic damping characteristics of perforated plates at normal incidence, without and with bias flow, was conducted. The investigation included experiments in specially designed facilities and the development of a theoretical model for the prediction of insertion loss. Two distinct experimental setups were designed and built for the measurement of insertion loss without and with bias flow: the static insertion loss (SIL) facility and the bias flow insertion loss (BFIL) facility. The theoretical model was first developed for the static case and later expanded to include the effects of the bias flow.

The static model combines one-dimensional planar wave theory through a single contraction chamber with end corrections that include hole interaction effects. The model is based on the acoustic wavelength being much larger than the hole diameter. Experiments were conducted in the UCI anechoic facility to provide validation for the static model (Equation 3.23). The SIL experiments comprised a broadband point source to evaluate the insertion loss of eleven perforated plates with varying porosity, hole size, and thickness. The robustness of the SIL facility was assessed by examining the simultaneously acquired acoustic signal of two microphones downstream of the perforated plate. A comparison of the sound pressure level (SPL) spectra and microphone correlations confirmed the one-dimensional acoustic wave propagation through the perforated plate. This was a prerequisite of the static model (Equation

3.23). The experimental matrix covered porosities $0.22 \leq \beta \leq 0.48$, non-dimensional hole size $7\times10^{-5} \leq d/\lambda \leq 0.75$, and non-dimensional thickness $0.15 \leq l/d \leq 1.0$. The static model predictions are in good agreement with the experimental measurements, with errors of about 1.5 dB or less for $d/\lambda \leq 0.5$. The static model also provides much higher fidelity predictions than past models over most of the range of the experiments in this study. A systematic analysis of the error between the static model and SIL experimental measurements did not show any specific trends versus plate thickness-to-diameter ratio or porosity. The results of the static model and experimental comparisons emphasized the importance of correctly modeling resonance effects exhibited in thicker plates and hole interaction effects between the perforations.

The bias flow model developed in this study is based on similar elements as the static model: one-dimensional wave propagation through an contraction chamber with end corrections that include hole interaction effects. The *vena contracta* of the jet that forms due to flow separation from the upstream corner of the contraction was modeled as an additional area reduction to the open area ratio. The mean flow upstream of the contraction is approximately potential, and therefore the mass end correction upstream of the contraction was assumed equal to the end correction length used in the static model. The mean flow downstream of the *vena contracta* is no longer potential due to the mixing process between the jet and surrounding fluid. The end correction downstream of the contraction was therefore modified assuming that the attached mass downstream of the *vena contracta* location is destroyed. The bias flow mixing and viscous dissipation are sources of irreversible losses, which were included in the insertion loss model through entropy fluctuations.

A different experimental setup than the SIL facility was needed to provide insertion loss measurements for perforated plates with bias flow. The BFIL facility was similar to an

impedance tube setup, with modifications that included bias flow. An impinging jets noise source was also used in the BFIL experimental setup. An in-duct method was used to determine the acoustic power in the duct, which was accomplished by spatially averaging the acoustic intensity inside the duct. The accuracy of this method at static conditions was validated by comparing the BFIL and SIL insertion loss measurements without bias flow. In the BFIL facility, the insertion loss measurement can be contaminated by noise from the turbulent mixing of the jets emerging from the perforations. To mitigate this effect, signal-to-noise and spatial coherence criteria were enforced to filter out the contaminated results. The signal-to-noise criterion entailed that the combined power level of flow plus source must exceed by at least 10 dB the power level of the flow alone. The spatial coherence criterion required that the magnitude of coherence squared γ^2 of the signals of two laterally displaced microphones at the measurement plane exceed 0.05. Any experimental data that did not meet both of these requirements were considered unusable.

The bias flow model (Equation 3.52) indicated two primary trends associated with increasing bias flow Mach number. The first was a monotonic increase in the insertion loss with increasing bias flow over all frequencies. The second is a decrease in the frequency corresponding to the peak value of insertion loss. The former observation is a result of flow losses due to mixing downstream of the area expansion. The latter observation is a convection effect on the acoustic wave propagation by mean flow within the contraction. The trends of increasing insertion loss and decrease in the frequency corresponding peak loss with increasing bias flow were also observed in most of the BFIL experiments. The exceptions were the plates with the low open area ratio (Plates 4, 6, 7, 8, 9, 10 and 11), where the experimental measurements had indicated a decrease in insertion loss when the Mach number inside the

perforations M_2 was increased above 0.25. It was concluded that there exists a bias flow Mach number where optimal sound attenuation occurs; further increasing the bias flow Mach number results in a decrease in the sound attenuation capability of the perforated plate. Further experimental work is needed to confirm this trend with the remaining perforated plates.

The bias flow model agreed with experimental data to within 3 dB for $0.02 < d/\lambda \leq 0.4$ at $M_1 < 0.08$ for thin plates. For thicker plates (Plates 6 and 7), the discrepancy between the bias flow insertion loss model and the BFIL measurements increased with increasing upstream Mach number. The model also appears to be more accurate at values of $l/d \leq 0.4$, where the *vena contracta* location of the jet is far downstream of the perforated plate. The large departure between the bias flow model and experiments for intermediate values of l/d may be due to instability of the *vena contracta* as its location approaches the downstream side of the perforated plate. Despite the discrepancy between the current bias flow model and experiments at large M_1 and intermediate values of l/d, the current bias flow model predicts insertion loss with higher fidelity than previous models over the range of experiments in this study.

6.2 Recommendations for future work

The effect of bias flow on the transmission of plane wave propagation through a perforated plate has been examined theoretically and experimentally. An integral part of interpreting the bias flow experimental data was the signal-to-noise ratio and coherence measurement. Increasing the signal-to-noise ratio would allow a broader set of experimental data points that could be used to validate the model. The signal-to-noise ratio could be increased through the use of a stronger impinging jets source. This can be accomplished by increasing the diameter of the impinging jets.

The sound power in the duct was estimated using only 19 points and assuming azimuthal uniformity as depicted in Figure 4.9(a). A more accurate estimation of the sound power in the duct can be obtained by increasing the number of measurement locations in the measurement plane. The validity of the sound power measurement used in this study can also be assessed by comparing with other in-duct methods of sound power measurement. One alternative example of measuring sound power in a duct involves circumferentially averaging the sound pressure level in the duct at a fixed radius. This procedure is a standard provided in ISO-5136, which can be used to compare and validate the current method.

Near-field effects were not rigorously considered in the present study, however, these effects are assumed to be inherent in the current model through the hole interaction and end correction terms. Although these simplifications have been shown to predict the insertion loss of perforated plates over a wide range of bias flow speeds, the current theory can be made more accurate by including higher order modes of pressure fluctuations at the sudden area changes upstream and downstream surfaces of the contraction.

In most of the experiments, the insertion loss was shown to increase monotonically with increasing upstream Mach number. However, for low porosity plates, the increase in perforation Mach number $M_2 \geq 0.25$ for perforations with open area ratio of about 0.23 resulted in a saturation and decrease in insertion loss. It is assumed that the pressure fluctuations due to bias flow become strong enough to overcome the additional attenuation at lower perforation Mach number. Obtaining additional experimental insertion loss data for the perforations of higher porosity validate this assumption, and would therefore more clearly establish the Mach number limit at which the current bias flow model is valid.

BIBILIOGRAPHY

[1] G. C. G. Hofmans, R. J. J. Boot, P. P. J. M. Durrieu, Y. Auregan, and A. Hirschberg, "Aeroacoustic response of a slit-shaped diaphragm in a pipe at low Helmholtz number, 1: Quasi-steady results," *Journal of Sound and Vibration*. Vol. 244, No. 1**,** pp. 35-56, 2001.

[2] V. Phong, S. Taghavi Nezhad, F. Liu, and D. Papamoschou, "Noise reduction of a turbofan bleed valve," AIAA Paper 2012-0681, January 2012.

[3] M. J. T. Smith, *Aircraft Noise* (Cambridge University Press, New York, 1989), Chap. 4, pp. 141.

[4] I. B. Crandall, *Theory of Vibration System and Sound* (Van Nostrand, New York, 1926), pp. 229 et seq.

[5] M. L. Munjal, *Acoustics of Ducts and Mufflers With Application to Exhaust and Ventilation System Design* (John Wiley & Sons Inc., New York, 1987), Chap. 1, pp. 9-12

[6] L. L. Beranek and I. L. Vér, *Noise and Vibration Control Engineering: Principles and Applications* (John Wiley & Sons Inc., 1992), Chap. 7, pp. 367-374.

[7] L. E. Kinsler, A. R., Frey, A. B. Coppens, J. V. Sanders, *Fundamentals of Acoustics* (John Wiley & Sons Inc., New York, 1982), Chap. 12, pp. 303, Chap. 6, pp. 125.

[8] A. D. Pierce, *Acoustics: An Introduction to Its Physical Principles and Applications* (McGraw-Hill Inc., 1981), Chap. 7, pp. 350-353.

[9] Lord Rayleigh the Third, *The Theory of Sound, Volume II* (Macmillan, Dover Publications, New York, 1945 ed.), Chap. 14, pp. 162-169.

[10] M. S. Howe, *Acoustics of Fluid-Structure Interactions* (Cambridge University Press, New York, 1998), Chap. 5, pp. 354-368.

[11] V. A. Fok, "Teoreticheskoe issledovanie provodimosti kruglogo otverstiya v perogorodke, postavlennoi poperek truby (Theoretical study of the conductance of a circular hole, in a partition across a tube)," *Doklady Akademii Nauk SSSR*, Vol. 31, No. 9, pp. 875-878, 1941.

[12] V. S. Nesterov, "An experimental study of the acoustical conductivity of a circular orifice in a partition placed across a tube," *Doklady Akademii Nauk SSSR*, Vol. 31, No. 9, pp. 879-882, 1941.

[13] U. Ingard, "On the theory and design of acoustic resonators," *Journal of the Acoustical Society of America*. Vol. 26, No. 6, pp. 1037-1061, 1953.

[14] J. Christensen, L. Martin-Moreno, and F. J. Garcia-Vidal, "Theory of resonant acoustic transmission through subwavelength apertures," *Physical Review Letters*, Vol. 101, No. 1, pp. 1-4, 2008

[15] B. Hou, J. Mei, M. Ke, W. Wen, Z. Liu, J. Shi, and P. Sheng, "Tuning Fabry-Perot resonances via diffraction evanescent waves," Physical Review B., Vol. 76, No. 5, pp. 1-6, 2007

[16] B. Hou, J. Mei, M. Ke, Z. Liu, J. Shi, and W. Wen, "Experimental determination for resonance-induced transmission of acoustic waves through subwavelength hole arrays," Journal of Applied Physics, Vol. 104, No. 1, pp. 1-5, 2008

[17] K. S. Hebbar, K. Sridhara, and P. A. Paranjpe, "Performance of Conical Jet Nozzles in Terms of Discharge Coefficient," Journal of the Aeronautical Society of India, , Vol. 22, No. 1, pp. 3-9, 1970

[18] J. H. Lienhard V and J. H. Lienhard IV, "Velocity coefficients for free jets from shar-edged orifices," Journal of Fluids Engineering, Vol. 108, pp. 13-17, 1984

[19] Y. Torizumi, N. Hirayama, and T. Maeda, "Flow characteristics and methods of flow calculation of high-speed compressible flow through pipe orifices," Bulletin of the Japan Society of Mechanical Engineers, Vol. 211, pp. 57-63, 1984

[20] G. K. Batchelor, *An Introduction to Fluid Mechanics*, (Cambridge University Press, New York, 1967), Chap. 6, pp. 493-497

[21] A. H. Shapiro, *The Dynamics and Thermodynamics of Compressible Fluid Flow*, (The Ronald Press Co., 1953), Chap. 11, pp. 358-359.

[22] A. J. W. Smith, *Pressure Losses in Ducted Flows*, (Butterworth & Co., 1971), Chap. 4, pp. 135-188.

[23] I. E. Idelchik, *Handbook of Hydraulic Resistance 2nd Ed.*, (Hemisphere Publishing Ca., 1986), Chap. 4, pp. 135-188.

[24] D. S. Miller, *Internal Flow Systems 2nd Ed.*, (British Hydrodynamics Research Association, 1978), Chap. 14, pp. 260-265.

[25] P. L. Smith and M. Van Winkle, "Discharge coefficients through perforated plates at Reynolds numbers of 400 to 3,000," *American Institute of Chemical Engineers Journal*, Vol. 4, No. 3, pp. 266-268, 1958

[26] P. A. Kolodzie and M. Van Winkle, "Discharge coefficients through perforated plates," *American Institute of Chemical Engineers Journal*, Vol. 3, No. 3, pp. 266-268, 1957

[27] P. Mungur and G. M. L. Gladwell, "Acoustic wave propagation in a sheared fluid contained in a duct," *Journal of Sound and Vibration*. Vol. 9, No. 1, pp. 28-48, 1969

[28] D. Ronneberger, "Experimental investigations of the acoustic reflection coefficient of discontinuous changes of cross section in tubes with air flow," *NASA TT F-14222*. 1972

[29] R. J. Alfredson and P. O. A. L. Davies, "Performance of exhaust silencer components," *Journal of Sound and Vibration*. Vol. 15, No. 2, pp. 175-196, 1970

[30] P. O. A. L. Davies, "Practical flow duct acoustics," *Journal of Sound and Vibration*. Vol. 124, No. 1, pp. 91-115, 1987

[31] A. Cummings, “Sound transmission at sudden area expansions in circular ducts, with superimposed mean flow,” *Journal of Sound and Vibration*. Vol. 38, No. 1, pp. 149-155, 1974

[32] P. Durrieu, G. Hofmans, G. Ajello, R. Boot, Y. Aurégan, A. Hirschberg, and M.C.A.M. Peters, “Quasisteady aero-acoustic response of orifices,” *Journal of the Acoustical Society of America*. Vol. 110**,** No. 4, pp. 1859-1872, 2001

[33] M. S. Howe, “On the theory of unsteady high Reynolds number flow through a circular aperture,” *Proceedings of the Royal Society of London*, Vol. 366, pp. 205-223, 1979

[34] M. S. Howe, “The dissipation of sound at an edge,” *Journal of Sound and Vibration*, Vol. 70, No. 3, pp. 407-411, 1980

[35] D. W. Bechert, “Sound absorption caused by vorticity shedding, demonstrated with a jet flow,” *Journal of Sound and Vibration*, Vol. 70, No. 3, pp. 389-405, 1980

[36] I. J. Hughes and A. P. Dowling, “The absorption of sound by perforated linings,” *Journal of Fluid Mechanics*, Vol. 218, pp. 299-335, 1990

[37] J. D. Eldredge and A. P. Dowling, “The absorption of axial acoustic waves by a perforated liner with bias flow,” *Journal of Fluid Mechanics*, Vol. 485, pp. 307-335, 2003

[38] Y. Fukumoto and M. Takayama, “Vorticity production at the edge of a slit by sound waves in the presence of a low Mach number bias flow,” *Physics of Fluids A.* Vol. 3, No. 12, pp. 3080-3083, 1991

[39] A. P. Dowling and I. J. Hughes, “Sound absorption by a screen with a regular array of slits,” *Journal of Sound and Vibration*, Vol. 156, No. 3, pp. 387-405, 1991

[40] J. C. Wendoloski, “Sound absorption by an orifice plate in a flow duct,” *Journal of the Acoustical Society of America*, Vol. 104, No. 1, 1998

[41] X. Jing and X. Sun, “Experimental investigation of perforated liners with bias flow,” *Journal of the Acoustical Society of America*. Vol. 105. No. 5. 1999

[42] X. Jing and X. Sun, "Effect of plate thickness on impedance of perforated plates with bias flow," *AIAA Journal*, Vol. 38. No. 1. pp. 1573-1578 (2000).

[43] V. Bellucci, P. Flohr, and C. O. Paschereit, "Numerical and experimental study of acoustic damping generated by perforated screens," *AIAA Journal*, Vol. 42, No. 8, pp. 1543-1549, 2004

[44] S-H. Lee, J-G. Ih and K. S. Peat, "A model of acoustic impedance of perforated plates with bias flow considering the interaction effect*," Journal of Sound and Vibration*, Vol. 303, pp. 741-752, 2007

[45] L. J. Sivian, "Acoustic impedance of small orifices," *Journal of the Acoustical Society of America*, Vol. 7, No. 2, pp. 94-101, 1935

[46] U. Ingard and S. Labate, "Acoustic circulation effects and the nonlinear impedance of orifices," *Journal of the Acoustical Society of America*, Vol. 22, No. 2, pp. 211-218, 1950

[47] U. Ingard and H. Ising, "Acoustic nonlinearity of an orifice," *Journal of the Acoustical Society of America*, Vol. 42, No. 1, pp. 6-17, 1967

[48] K. T. Chen, "Study on the acoustic transmission loss of a rigid perforated screen," *Applied Acoustics*, Vol. 47, No. 4, pp. 303-318, 1996

[49] R. B. Tayong, T. Dupont, and P. Leclaire, "Experimental investigation of holes interaction effect on the sound absorption coefficient of micro-perforated panes under high and medium sound levels," *Applied Acoustics*, Vol. 72, No. 10, pp. 777-784, 2011

[50] T. H. Melling, "The acoustic impedance of perforates at medium and high sound pressure levels," *Journal of Sound and Vibration*, Vol. 29, No. 1, pp. 1-65, 1973

[51] N. Atalla and F. Sgard, "Modeling of perforated plates and screens using rigid frame porous models," *Journal of Sound and Vibration*, Vol. 303, pp. 195-208, 2007

[52] Y. Champoux and J. F. Allard, "Dynamic tortuosity and bulk modulus in air-saturated porous media," *Journal of Applied Physics*, Vol. 70, No. 4, pp. 1975-1979, 1991

[53] J. F. Allard, *Propagation of sound in porous media: Modeling sound absorbing materials* (Elsevier, New York, 2009), Chap. 5, pp. 90.

[54] L. Jaouen and F.-X. Bécot, "Acoustical characterization of perforated facings," *Journal of the Acoustical Society of America*, Vol. 129, No. 3, pp. 1400-1406, 2011

[55] J. F. Betts, *Experiments and Impedance Modeling of Liners Including the Effect of Bias Flow*, Ph.D. thesis. Virginia Polytechnic Institute. 2000

[56] S. Mendez and J. D. Eldredge, "Acoustic modeling of perforated plates with bias flow for Large-Eddy Simulations," *Journal of Computational Physics*, Vol. 228, No. 13, pp. 4757-4772. 2009

[57] H. Aygun and K. Attenborough, "The insertion loss of perforated porous plates in a duct without and with mean air flow," *Applied Acoustics*, Vol. 69, No. 6, pp. 506-513, 2008

[58] J. E. Ffowcs Williams, and A. P. Dowling, *Sound and Sources of Sound* (Halsted Press, New York, 1983), Chap. 3, pp. 65-67.

[59] H. Rouse and A.-H. Abul-Fetouh, "Characteristics of irrotational flow through axially symmetric orifices," *Journal of Applied Mechanics*. Vol. 17, No. 50, pp. 421-426, 1950

[60] C. H. Gerhold, and L. R. Clark, "Database of inlet and exhaust noise shielding for wedge-shaped airframe," *NASA/TM-2001-210840*, April 2001.

[61] M. O. McKinney, and J. Scheiman, "Evaluation of turbulence reduction devices for the Langley 8-Foot Transonic Pressure Tunnel," *NASA/TM-81792*, June (1981)

[62] K. Myers, *Design of a Catenoidal Shaped Anechoic Termination* (Master's Thesis, Western Michigan University, 2012).

[63] ISO 5136 2003, *International Organisation for Standardization, Geneva, Switzerland, International Standard.* Acoustics – Determination of sound power radiated into a duct by fans and other air-moving devices – In-duct method.

[64] W. Neise and F. Arnold, “On sound power determination in flow ducts,” *Journal of Sound and Vibration*, Vol. 244, No. 3, pp. 481-503, 2001.

[65] A. Savitzky, and M. J. E. Golay, “Smoothing and differentiation of data by simplified least squares procedures,” Anal. Chem. **36**, pp. 1627-1639 (1964).

[66] P. M. Morse, and U. K. Ingard, *Theoretical Acoustics* (McGraw-Hill Inc., New York, (1968), Chap. 9, pp. 509-513

[67] E. J. Rice, M. F. Heidmann, and T. G. Sofrin, “Modal propagation angles in a cylindrical duct with flow and their relation to sound absorption,” NASA/TM-79030, January 1979

[68] H. Estrada, P. Candelas, A. Uris, F. Belmar, F. Javier García de Abajo, and F. Meseguer, “Influence of lattice symmetry on ultrasound transmission through plates with subwavelength aperture arrays,” *Applied Physics Letters*, Vol. 95, No. 5, 2009

[69] T. J. Mueller, C. S. Allen, W. K. Blake, R. P. Dougherty, D. Lynch, P. T. Soderman, and J. R. Underbrink. *Aeroacoustic Measurements*. Springer-Verlag Berlin Heidelberg. Ch. 1. pp 3-13, 2002

[70] P. Testud, Y. Aurégan, P. Moussou, and A. Hirschberg. “The whistling potentiality of an orifice in a confined flow,” *Journal of Sound and Vibration*. Vol. 325. pp 769-780, 2009

[71] R. Lacombe, S. Föller, G. Jasor, W. Polifke, Y. Aurégan, and P. Moussou. “Identification of aero-acoustic scattering matrices from large eddy simulation: Application to whistling orifices in duct,” *Journal of Sound and Vibration*. Vol. 332, No. 20, pp 5059-5067, 2013

Appendix A

NON-ISENTROPIC DENSITY FLUCTUATIONS

Assuming adiabatic flow, the first and second law of thermodynamics

$$de = Tds - pd\left(\frac{1}{\rho}\right) \tag{A.1}$$

Further assuming a thermally perfect gas, Equation A.1 can be rewritten as

$$c_v dT = Tds - pd\left(\frac{1}{\rho}\right)$$

$$\frac{dT}{T} = \frac{ds}{c_v} + (\gamma - 1)\frac{d\rho}{\rho} \tag{A.2}$$

From the equation of state

$$\frac{dp}{p} - \frac{d\rho}{\rho} = \frac{dT}{T} \tag{A.3}$$

Combining Equation A.2 and A.3

$$\frac{ds}{c_v} = \frac{dp}{p} - \gamma\frac{d\rho}{\rho} \tag{A.4}$$

Rewriting Equation A.4 in terms of acoustic perturbations

$$\frac{s'}{c_v} = \frac{p'}{p} - \gamma\frac{\rho'}{\rho} \tag{A.5}$$

Without entropy fluctuations, $s' = 0$ and Equation A.5 becomes the usual expression for the speed of sound. With entropy fluctuations, however, the density fluctuations

$$\rho' = \frac{p' - \rho T(\gamma - 1)s'}{c^2} \tag{A.6}$$

Appendix B

PITOT PRESSURE PROFILES

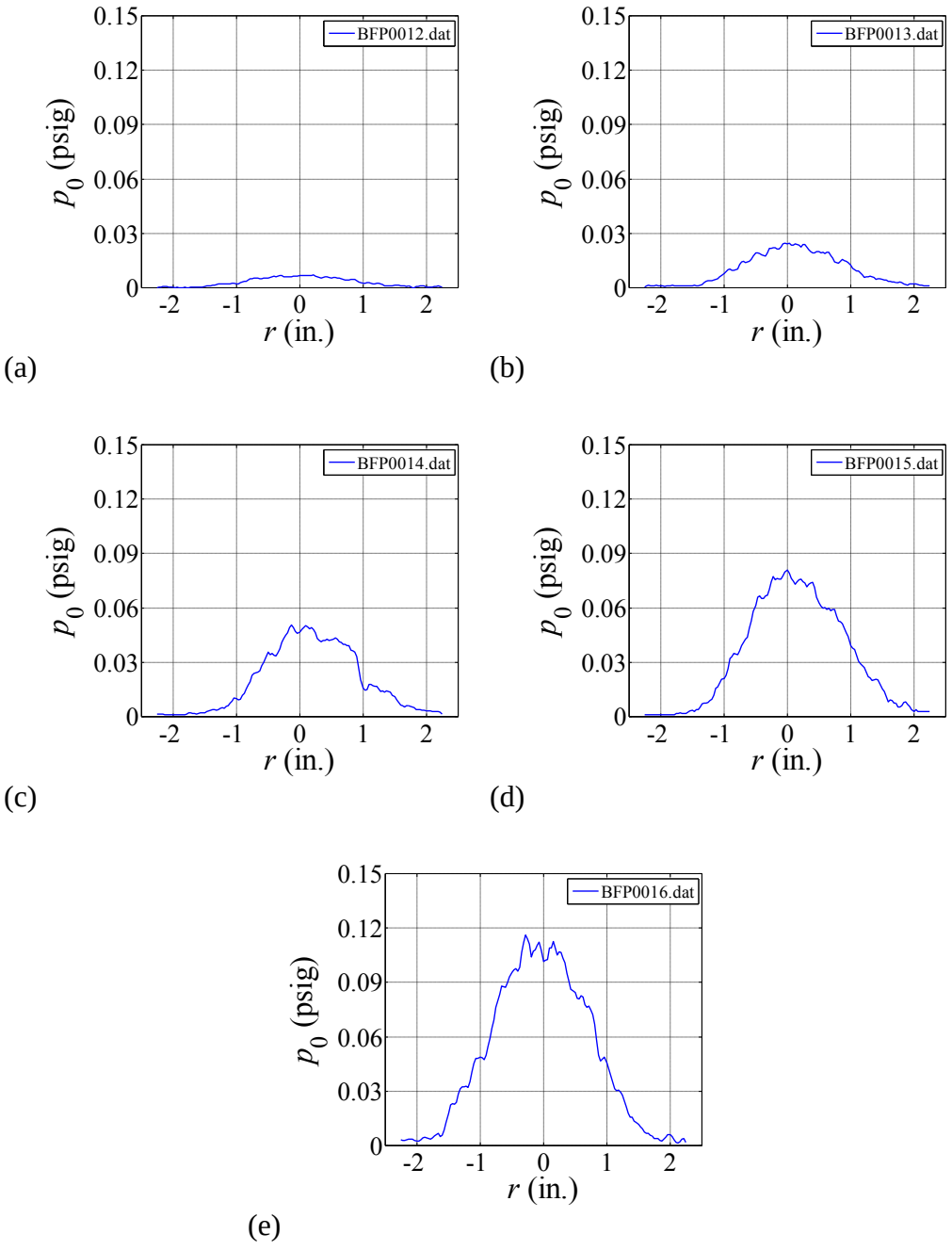

Figure B.1: Pitot pressure profile along the measurement axis for Plate 1.

(a) $M_1 = 0.02$; **(b)** $M_1 = 0.04$; **(c)** $M_1 = 0.06$; **(d)** $M_1 = 0.08$; **(d)** $M_1 = 0.1$.

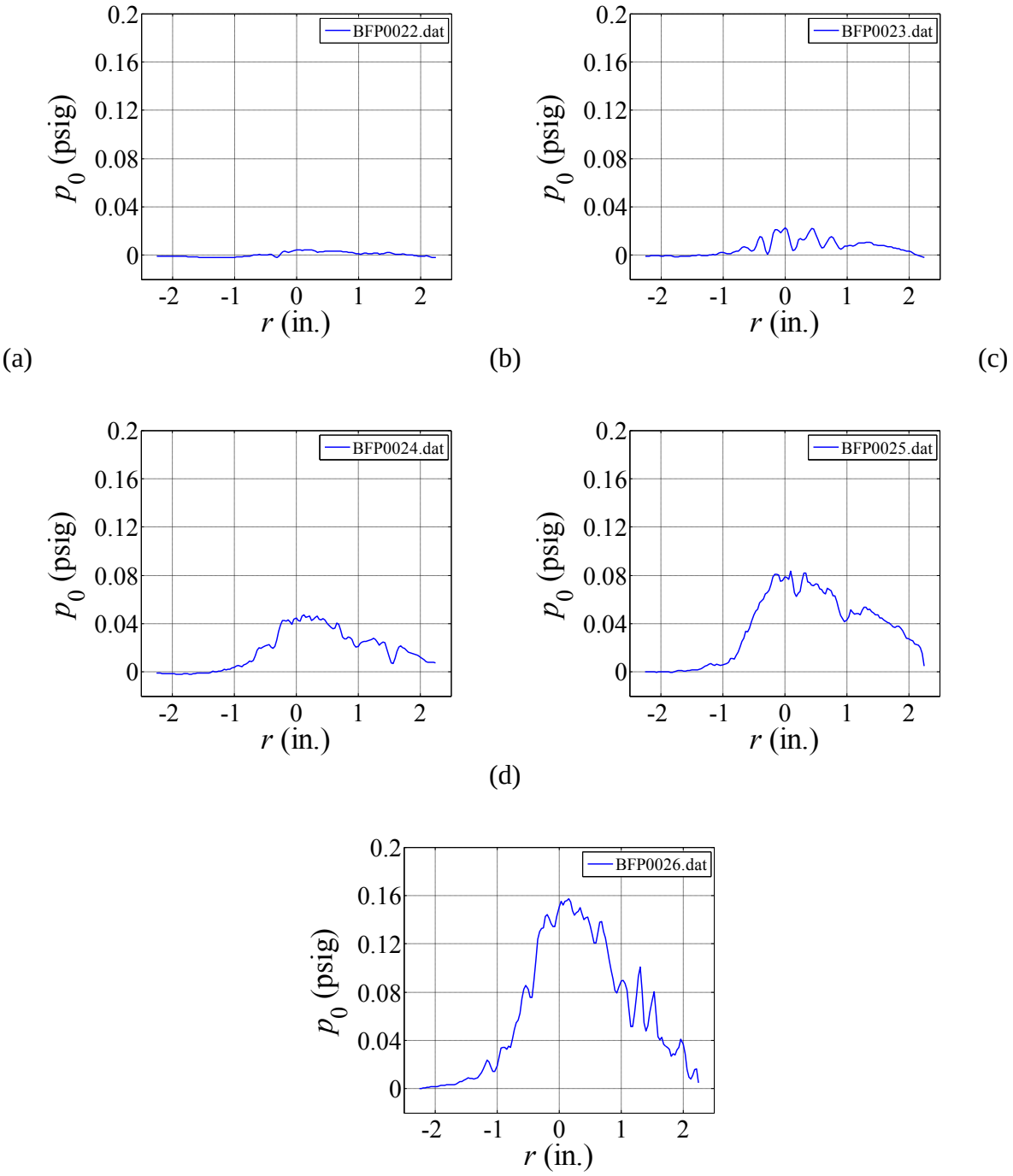

Figure B.2: Pitot pressure profile along the measurement axis for Plate 2.

(a) $M_1 = 0.02$; **(b)** $M_1 = 0.04$; **(c)** $M_1 = 0.06$; **(d)** $M_1 = 0.08$; **(d)** $M_1 = 0.1$.

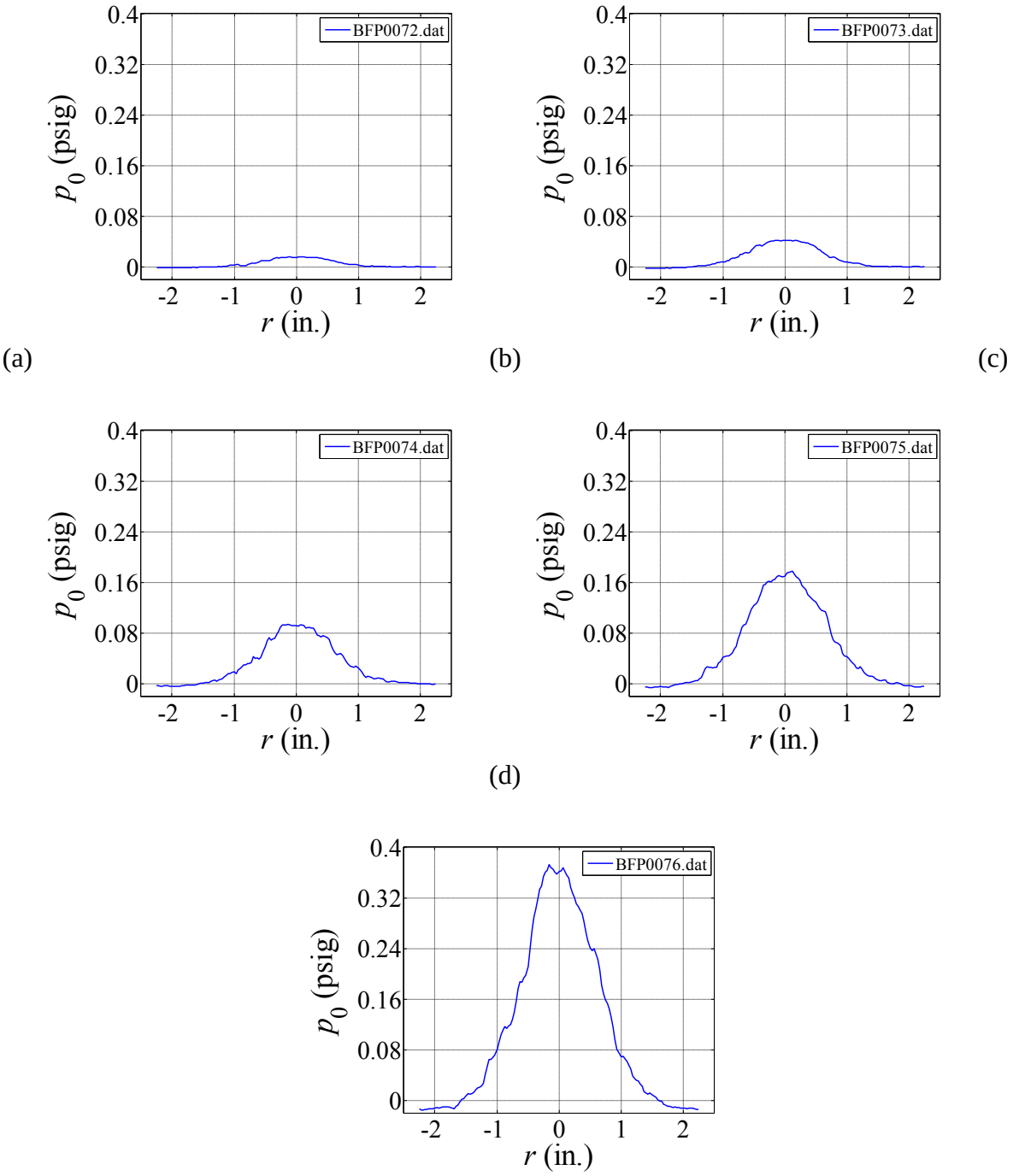

Figure B.3: Pitot pressure profile along the measurement axis for Plate 7.

(a) $M_1 = 0.02$; **(b)** $M_1 = 0.04$; **(c)** $M_1 = 0.06$; **(d)** $M_1 = 0.08$; **(d)** $M_1 = 0.1$.

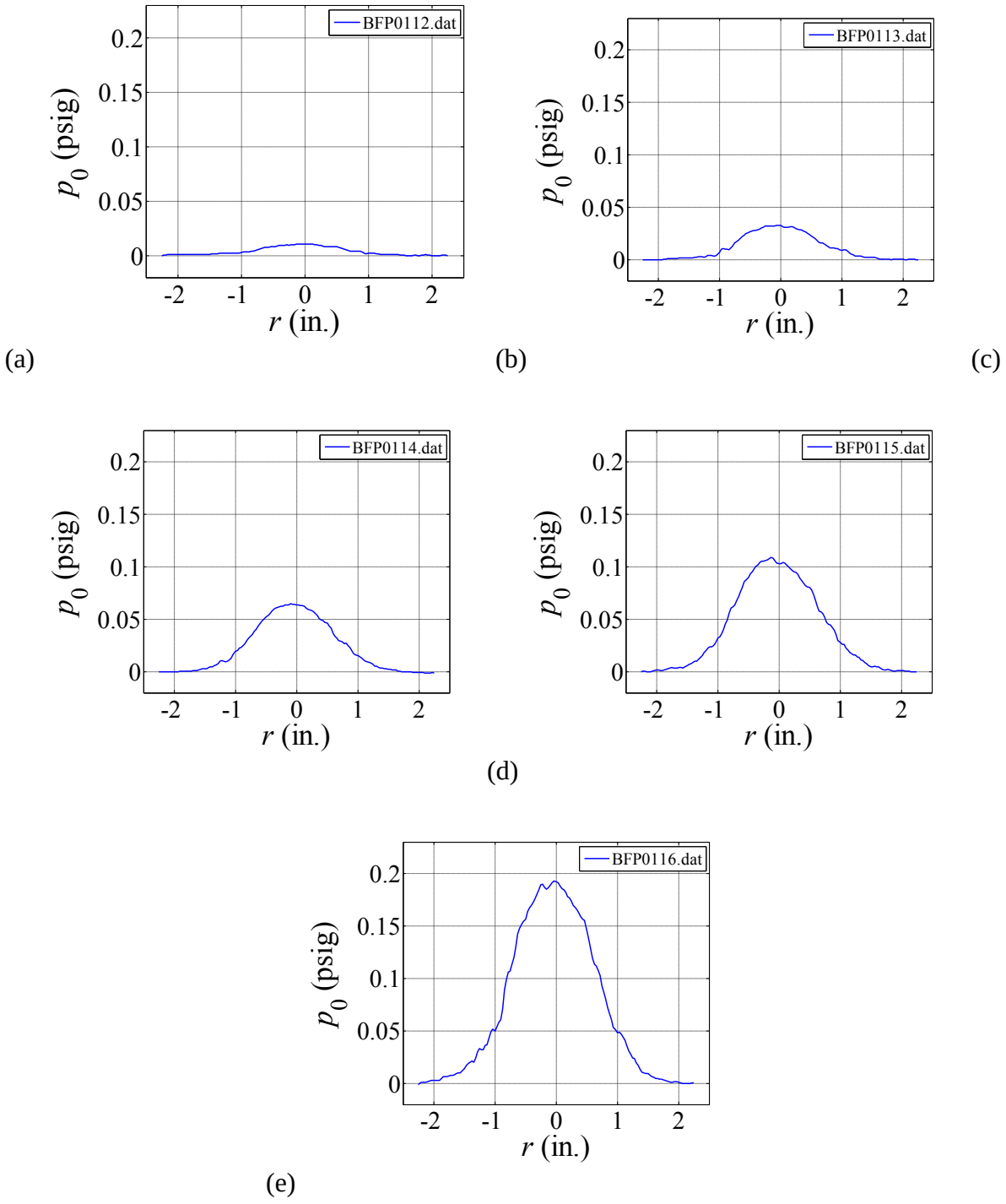

Figure B.4: Pitot pressure profile along the measurement axis for Plate 11.

(a) $M_1 = 0.02$; **(b)** $M_1 = 0.04$; **(c)** $M_1 = 0.06$; **(d)** $M_1 = 0.08$; **(d)** $M_1 = 0.1$.